PREDICTION OF SEISMIC DAMAGE

IN REINFORCED CONCRETE FRAMES

by

HOOSHANG BANON

B.S., University of Illinois at Urbana-Champaign
(1976)

S.M., Massachusetts Institute of Technology
(1978)

SUBMITTED IN PARTIAL FULFILLMENT
OF THE REQUIREMENTS FOR THE
DEGREE OF

DOCTOR OF SCIENCE

at the

MASSACHUSETTS INSTITUTE OF TECHNOLOGY

June 1980

Signature of Author _____
Department of Civil Engineering
May 9, 1980

Certified by _____
John M. Biggs

and _____
H. Max Irvine
Thesis Supervisors

Accepted by _____
C. Allin Cornell
Chairman, Department Committee

PREDICTION OF SEISMIC DAMAGE IN REINFORCED CONCRETE FRAMES

by

HOOSHANG BANON

Submitted to the Department of Civil Engineering
on May 9, 1980 in partial fulfillment of the
requirements for the degree of Doctor of Science

ABSTRACT

In practice, damage in reinforced concrete buildings is qualitatively measured in terms of ductility demands. In the present study a more rigorous model of member damage in reinforced concrete buildings is set up. Analytical models for inelastic behavior of reinforced concrete members are used to analyze a set of static cyclic load tests. Other damage indicators, such as dissipated energy and cumulative plastic rotation, are measured for each test. Results for the sample are then used to develop a stochastic model of damage in reinforced concrete members. Final results are in terms of probabilities of local failure in a building frame subjected to a given earthquake. A model for computing the system reliability as a function of correlation between member resistances is also presented.

Thesis Supervisors: John M. Biggs

Title: Professor of Civil Engineering

H. M. Irvine

Title: Associate Professor of Civil Engineering

ACKNOWLEDGEMENTS

This dissertation was written under the supervision of Professors John M. Biggs and H. Max Irvine. The stochastic model of damage was developed under the guidance of Professor Daniele Veneziano. The author wishes to express his sincere appreciation to Professors Biggs, Irvine, and Veneziano for their support and enthusiasm.

My appreciation is extended to my sister Shida, who has drawn all the figures and given me moral support. Many friends and colleagues at M.I.T. have assisted me during this study, and my grateful thanks are extended to Apostolos Papageorgiou, Shi-Sheng Lai, Carlos Llorente, Hany El-Khoraibie, Joseph Burns, and Roger Graves. My thanks to Mrs. J. Malinofsky, who has done an excellent job in typing this manuscript.

This research was made possible under Grant No. ENV77-14174 from the National Science Foundation.

TABLE OF CONTENTS

LIST OF FIGURES

LIST OF TABLES

NOTATION

A_g	Gross Section Area
A_s, A_s'	Area of Steel
A_{st}	Area of Stirrup
a	Parameter in the Hazard Function
b	Section Width
C	Compressive Load, Also Coefficient in the Code Formula for Base Shear
$\underset{\sim}{C}$	Damping Matrix
C_c	Concrete Compressive Force
C_s	Steel Compressive Force
D	Diameter of Reinforcement
$\underline{D}$	Given Point on D_1-D_2 Plane
D_f	Failure Point on D_1-D_2 Plane
D_1, D_2	Pair of Damage Indicators
DR	Damage Ratio
d, d_i, d_j	Distance along 45° Line on D_1-D_2 Plane
d,d'	Effective Depth for Steel Reinforcement
E_n	Normalized Dissipated Energy
E_o, E_s	Young's Modulus for Steel
E_{sh}	Strain Hardening Modulus for Steel
E_{st}	Young's Modulus for Stirrups
E_t	Total Dissipated Energy
EI,$(EI)_1$,$(EI)_2$	Section Stiffness
e	Eccentricity of Axial Load
$\underset{\sim}{F}$	Flexural Flexibility Matrix
F_t	Splitting Force

$F_D(d)$	CDF of Distance d
$F_S(s)$	CDF of Distance along Failure Path s
f_c	Concrete Stress
f'_c	Peak Stress for Concrete
$f_A(a)$	PDF of parameter a in the Hazard Function
$f_S(s)$	PDF of Distance along Failure Path s
$f_S(s\|a)$	Conditional PDF of s Given a
h	Height of Section Measured from Neutral Axis
K	Seismic Coefficient Depending on Type of Structure
$\underset{\sim}{K}_a$	P-δ Modification Matrix
K_f	Flexural Stiffness
$\underset{\sim}{K}_g$	Element Stiffness Matrix in Global Coordinates
K_i, K_j	Flexural Hinge Stiffnesses
$\underset{\sim}{K}_L$	Element Stiffness Matrix in Local Coordinates
K_o	Initial Stiffness
K_r	Reduced Secant Stiffness
$\underset{\sim}{K}_t$	Tangent Stiffness Matrix
k	Parameter in the Extreme Type III Distribution
L	Likelihood Function
L_d	Development Length
ℓ, ℓ_1, ℓ_2	Member Length
ℓ_i	Realization of Length along Failure Path i
$\underset{\sim}{M}$	Mass Matrix
M, M_A, M_B	External Moment
M_{cr}	Cracking Moment
M_i, M_j	External Moments at Nodes i,j

M_{el}	Pseudo Elastic Moment
M_{max}	Maximum Moment
M_u	Ultimate Moment
M_y	Yield Moment
M_1, M_2, M_n	Story Masses
m_a	Mean Value of a
m_d	Mean Value of d
NCR	Normalized Cumulative Rotation
P_a	Axial Load
P_b	Balanced Point Axial Load
P_i, P_j	Axial Loads at Nodes i,j
P_i	Probability of Failure for Member i
P_s	System Reliability
P_s^L	Lower Bound on System Reliability
P_s^u	Upper Bound on System Reliability
p	Ratio of Second Slope to Initial Stiffness in m-ϕ Curve
r	Specified Coordinate on D_1-D_2 Plane
s	Distance along Failure Path on D_1-D_2 Plane
T	Tension Load
$\underset{\sim}{T}$	Transformation Matrix
T_s	Steel Tensile Force
u	Bond Stress, Also Parameter of the Extreme Type III Distribution
V	Base Shear, also Member Shear Load
V_{cr}	Contribution of Concrete to Shear Load
V_i, V_j	Shear at Nodes i, j

V_{st}	Contribution of Steel to Shear Load
W	Total Weight of Structure
X_i, X_n	Distance from Joint Face to Stirrups i, n
X_1, X_2	Parameters of the Regression Model
Z	Seismic Coefficient Depending on Site
Z(0,1)	Stochastic Damage Process
α, β	Parameters Used in the Modified Takeda Model
γ_{sr}	Shear Rotation
Δ, δ	Displacement
ΔL, ΔL_n, ΔL_u	Crack Opening
δ_{max}	Maximum Displacement
ε_c	Concrete Strain
ε_i, ε_n	Strain for Stirrups i,n
ε_m	Concrete Strain at Minimum Concrete Stress
ε_o	Concrete Strain at Maximum Concrete Stress
ε_s	Steel Strain
ε_{sh}	Strain Hardening Strain
ε_u	Ultimate Steel Strain
θ_{max}	Maximum Rotation
θ_o	Plastic Rotation
θ_p	Permanent Set Rotation
θ_u	Ultimate Rotation
θ_y	Yield Rotation
$\lambda_X(x)$	Hazard Function (General for x)
μ_p	Permanent Set Ductility

μ_θ	Rotation Ductility
μ_ϕ	Curvature (Moment) Ductility
ρ	Correlation between Member Resistances
σ_a	Axial Stress, Also Standard Deviation of a
σ_s, σ_s'	Steel Stress
σ_t	Tensile Stress
σ_y	Yield Stress
τ	Shear Stress
τ_{avg}	Average Shear Stress
τ_{cr}	Shear Stress at Concrete Cracking
ϕ, ϕ_A, ϕ_B	Curvature
ϕ_{max}	Maximum Curvature
ϕ_o	Plastic Curvature
ϕ_y	Yield Curvature

CHAPTER I - INTRODUCTION

1.1 Objective

The objective of the present work is to identify local damage in reinforced concrete frames on the basis of an inelastic dynamic analysis. Since the prediction of damage has an inherent uncertainty associated with it, probabilistic models have been used for this purpose. Final results are then presented in terms of probabilities of local damage for each member which shows inelastic behavior. In this study, damage is defined in terms of the ability of a member to carry loads. Thus, the prediction reveals if a member is able to carry loads after it has gone through several inelastic cycles. Results of experimental cyclic load tests are used to set up a stochastic model of damage. This model would allow the engineer to check the safety of a building frame using parameters other than peak ductility.

The immediate application of this work is in probabilistic inelastic dynamic analysis of structures. The models of local damage may be used to modify the stiffness matrix of a structure during an inelastic dynamic analysis. A simulation technique will then result in probability distributions of displacements or member end forces.

1.2 Scope

Analytical techniques which can predict the behavior of reinforced concrete structures under earthquakes have been continually refined over the past few years. There are also many experimental results, either static or dynamic, which can be used to verify existing models. However,

little attention has been given to the prediction of damage in reinforced concrete structures. There are two main obstacles to the prediction of damage. First, it is difficult to quantify damage in a structure, and secondly, the prediction has an inherent uncertainty associated with it. It is obvious that one has to use a probabilistic approach to carry out such a task. Whitman et al. (58, 59) attempted to quantify damage into six different states. Then from observations after the San Fernando earthquake, a "Damage Probability Matrix" was set up. This matrix related the damage states with Modified Mercalli Intensity (MMI) of an earthquake, thus assigning probabilities to each element of the matrix. Blume et al. (10, 11) presented a relationship between damage in a member, in terms of the total replacement cost, peak computed ductility, and the member ultimate ductility (at failure). Using the random vibration approach, Lai (33) calculated the probability of exceedance of a ductility level, and then used Blume's results to estimate damage. Unfortunately, very little further research has been done on the subject.

This work is an attempt to set up a more rigorous model of damage in reinforced concrete frames. Only one state of damage, namely the failure state or excessive damage, is considered in this study. It has long been realized that peak ductility alone can not explain damage in concrete structures. However, up to now, peak ductility has been used as the most widespread measure of damage in practice. Other parameters, such as cumulative ductility and energy dissipation, have received attention also (12). But the question still remains as to what these paraeters mean in terms of predicting damage in structures. Chapter II reviews analytical models which are used to study the inelastic behavior

of reinforced concrete frames. A set of experimental cyclic load tests is then chosen as a sample. Analysis of each test, and comparisons between analytical and experimental results, are presented in Chapter III. Chapter IV uses the results of the tests to set up a stochastic model of failure in members. The method is then employed in inelastic dynamic analysis of reinforced concrete frames in Chapter V. Chapter VI draws up a set of recommendations and conclusions based on the results.

1.3 Previous Work

Reinforced concrete frames and shear walls have long been used as lateral load resisting elements in seismic areas. During the past two decades, researchers in earthquake engineering have focused heavily on studying the behavior of reinforced concrete structures under earthquake loads. Because of the development of new computers, it has become possible to employ more complex numerical techniques to model the behavior of reinforced concrete elements under seismic loads. In the meantime, the experiments on reinforced concrete frames and shear walls have become more sophisticated, and the results of such experiments enable researchers to refine the analytical models. It is now widely accepted that reinforced concrete structures are suitable for seismic zones, if they have been designed and built according to the codes and procedures developed for seismic areas. These new seismic codes attempt to use analytical and experimental research to set up aseismic design procedures. Although the codes specify an equivalent static load to design the structure, the new ATC recommendations have realized the need for carrying out a dynamic analysis. It seems that an elastic dynamic analysis will be integrated

at the design stage in the near future. In studying the behavior of reinforced concrete structures under cyclic loads, researchers have long realized the need for employing inelastic models. Although such models have limited value to the designer, they are valuable analytical tools once the design stage is completed.

Two of the characteristics of reinforced concrete elements are loss of stiffness and strength, which can be explained only by relatively sophisticated inelastic models. Most of the early work in inelastic analysis of concrete structures was based on bilinear systems. However, it was soon realized that reinforced concrete elements do not offer the large energy dissipation capacity which is inherent in a bilinear system (17). A more general stiffness-degrading model for reinforced concrete was first introduced by Clough (14). This model has the advantage over the bilinear model that the loading stiffness is modified as peak rotation increases. Anagnostopoulos (1) suggested changes to Clough's model to reduce the unloading stiffness. He also compared peak ductilities of single-degree-of-freedom systems having different inelastic characteristics. Takeda (54) developed a nonlinear model which can closely reproduce the behavior of reinforced concrete elements in flexure. The model has a trilinear envelope curve, and it is designed to dissipate energy at low cycles once the cracking point is exceeded. Takayanagi (53) and Emori (18) later introduced modifications into the Takeda model to take into account the slippage and shear pinching effects. Saiidi (51) introduced a nonlinear hysteresis model which is designed to follow the behavior of a reinforced concrete frame if it was modeled as a single-degree-of-freedom system.

One of the most widely used methods of stiffness formulation to study the inelastic behavior of structures is the shear beam model. This model has a serious shortcoming, and that is the lack of interaction between story levels. Takizawa (55) has compared three different shear beam models with a more generalized model, which raises questions about the accuracy of shear beam models. Piqué (49) used an incremental lateral static load to find the stiffness characteristics of each story. It was discovered that the shape of the lateral load does not alter story load-deflection curves significantly. Although the method is a refinement of the shear beam model, the problem is much more complex when a building is subjected to cyclic loads.

For a more complete analysis of reinforced concrete structures, four classes of models are available for setting up the stiffness matrix of each element. These models are the Single Component Model, the Dual Component Model, the Fiber Model, and various Finite Element Models. The Dual Component Model was first introduced by Clough and Benuska (15), and uses an elastic element and an elasto-plastic element in parallel. Giberson (21) studied the Single Component Model, in which the inelastic behavior is lumped at the two ends of the member. He also compared the Single Component Model and the Dual Component Model, and outlined the advantages and limitations of both models. Because of the fact that the Dual Component Model can reproduce only bilinear behavior, it has not been used in inelastic analysis of reinforced concrete structures. Anderson et al. (2) used the Single Component Model in conjunction with four different degrading hinge hysteresis models to analyze ductility levels of a ten-story reinforced concrete building. Aziz (5) employed both the

Single Component Model and the Dual Component Model and compared ductility levels for selected buildings. Otani (41) developed an inelastic beam element which takes into consideration the location of the point of contraflexure. Assuming that the member is made up of two cantilevers, he applied the Takeda model to load-deflection curves for each cantilever. He also modeled slippage of the reinforcing bars as flexible springs at the two ends of the member. Kŭstŭ (32) used a set of cyclic load tests to study inelastic shear deformations of reinforced concrete columns. He used flexible springs at the two ends of the member to incorporate the shear deformations.

The other class of analytical models used for stiffness formulation of reinforced concrete members is the so-called "Fiber Model." In this case, the section is divided into many fibers, and from the constitutive laws for steel and concrete moment-curvature of the section at any load level may be determined. Then, by integration along the member length, its stiffness matrix is formulated. Park et al. (45) used the Fiber Model for a simple reinforced concrete member under cyclic loads. Latona (34) applied the Fiber Model to steel frames, and Mark (39) extended its application to reinforced concrete frames. One of the major considerations in using the Fiber Model is the high cost of an analysis.

Finally, Finite Element Models have been used to analyze reinforced concrete walls, panels, or slabs. However, because of the large number of degrees of freedom in a finite element analysis, the cost of an inelastic dynamic analysis is high. Thus, use of the Fiber Model or Finite Element Models in inelastic dynamic analysis of reinforced concrete frames has been rather limited.

Analytical models which are developed for analysis of reinforced concrete structures can be substantiated only on the basis of experimental test results. Many static cyclic load tests on frame subassemblages and walls have been used for such purposes. Although there may seem to be many differences in the response of a member under dynamic loads and under static loads, static tests have provided researchers with valuable information about the stiffness characteristics of reinforced concrete beams and columns. Many such tests are used in this work, and each test is discussed in detail in Chapter III. Dynamic tests of structures on the shaking table can also reveal information about the inertia and damping forces generated under earthquake motions. Many dynamic test results of reinforced concrete frames have become available during the past few years (16, 22, 25, 26, 40, 41). However, it should be realized that it is much more difficult to extract information from dynamic tests.

The models used in this work are limited to the two-dimensional (2-D) analysis of reinforced concrete frames. In recent years, attention has been given to the response of reinforced concrete members under biaxial states of stress. Some tests on biaxial loading of members have been carried out (4, 28, 44), and these results may be used to develop 3-D analytical models for inelastic analysis of reinforced concrete frames, although this is not pursued herein.

CHAPTER II - ANALYTICAL MODELS

2.1 Introduction

Modeling the inelastic behavior of reinforced concrete elements is a difficult task. Both stiffness and strength degradation are usually observed in beams and columns. Other phenomena, such as pinching of hysteresis loops, may occur because of high shear forces or slippage of steel bars. In modeling the inelastic behavior of reinforced concrete elements, it is important to take all of these effects into account. As previously discussed in Chapter I , there are many models available for the stiffness formulation of a member. Excessive cost of analysis makes the Fiber Model and various Finite Element Models less attractive. If one is interested only in peak ductility levels, a simple bilinear point hinge (Single Component Model) may be used. However, it is felt that if damage in a member is to be predicted by just a few parameters, it is imperative that those parameters be accurately calculated. Since the stochastic models of failure presented in Chapter IV use damage indicators described in Section 2.7, the inelastic models used are intended to give the best estimates of these parameters. A Single Component Model (21) was chosen for this purpose, and an extension of the model was developed to analyze non-symmetric reinforced concrete sections.

There are three main components of deformation in a reinforced concrete element which are due to flexure, shear, and slippage of bars. Each one of these components is considered separately in this work. Hysteresis curves for shear and slippage are set up, and they are introduced as flexible springs at the two ends of a member. Reinforced concrete is a

rather unpredictable material, and the objective here is to use models which can reproduce inelastic behavior of elements after many cycles. However, modeling is only a means to the end, which is the prediction of damage in a given member.

The general-purpose computer program DRAIN-2D, written by Kanaan and Powell (30), is used in this study. The program is intended for 2-D analysis of structural frames and walls. The Single Component Model with stiffness-degrading Takeda model at its two ends was added to DRAIN-2D by Litton (36). In this study many modifications were made to the program to allow both static and dynamic analysis of frames. Also, the extended Single Component Model (Section 2.3c) and the shear and slippage hysteresis curves were added as new elements to the computer program.

2.2 Material Constitutive Laws

a) Steel

The steel stress-strain relationship may be approximated in different ways. The strain-hardening characteristic of steel and the Baushinger effect can best be represented by the Ramberg-Osgood model (29). Since the steel stress-strain relationship is used to find the moment-curvature of a section, use of the Ramberg-Osgood model is not warrented. Instead, a more simple multilinear approximation has been used. The curve in Fig. 2.1 represents an elastic portion, a flat segment, and the strain hardening, respectively.

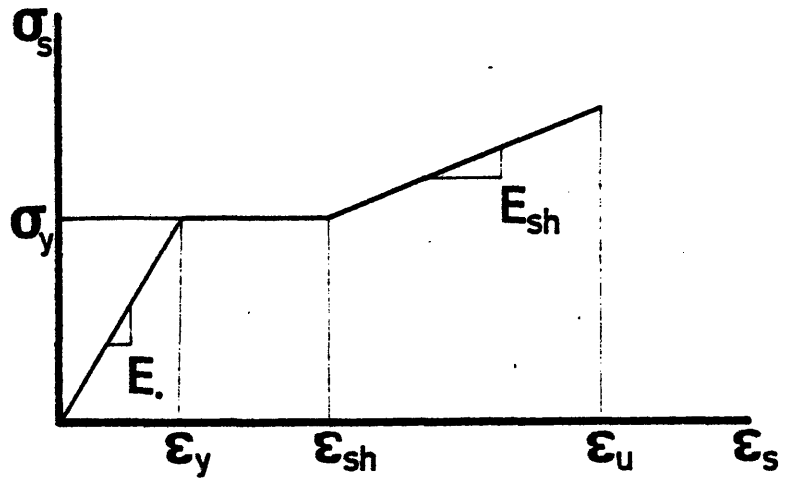

FIG. 2.1 - STRESS-STRAIN RELATIONSHIP FOR STEEL REINFORCEMENT

$$\sigma_s = E_o \varepsilon_s \qquad \varepsilon_s \leq \varepsilon_y \qquad (2.1a)$$

$$\sigma_s = \sigma_y \qquad \varepsilon_{sh} > \varepsilon_s > \varepsilon_y \qquad (2.1b)$$

$$\sigma_s = \sigma_y + E_{sh} (\varepsilon_s - \varepsilon_{sh}) \qquad \varepsilon_u \geq \varepsilon_s \geq \varepsilon_{sh} \qquad (2.1c)$$

In reality, the curve has an unloading portion, and also steel fails at its ultimate strain. Steel reinforcement in a section will not usually undergo such large deformations, and, in any event, the concrete would fail before that stage could be reached. So ultimate strain in this study corresponds to the point of peak stress of experimental stress-strain curves. The same relationships apply both in tension and compression.

b) Concrete

Unlike steel, concrete shows very different behavior under tension and compression. Although concrete has roughly 10 percent of its compressive strength in tension, its tensile strength can be safely neglected.

It is obvious that a section will crack after the first few cycles, and there would be no tensile contribution after that point. Concrete also shows a different behavior when confined (Fig. 2.2). Behavior of confined and unconfined concrete, up to peak concrete stress (f'_c) is almost the same, but their unloading slopes are different (31). In general, the unloading slope depends on the degree of confinement by web reinforcement (Fig. 2.2b).

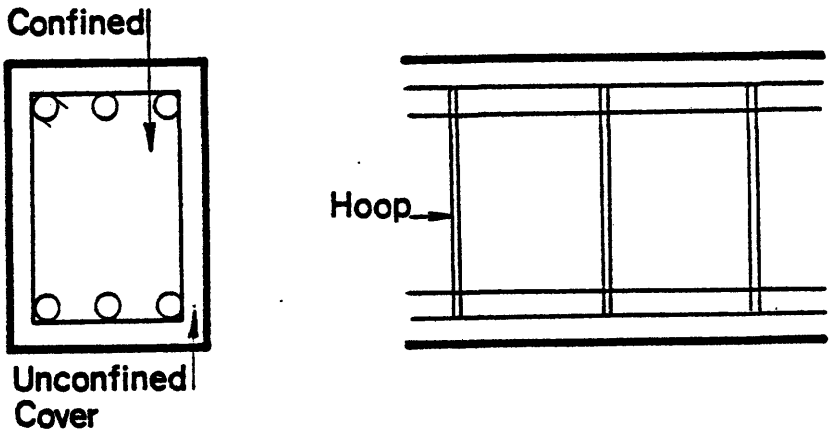

(a)

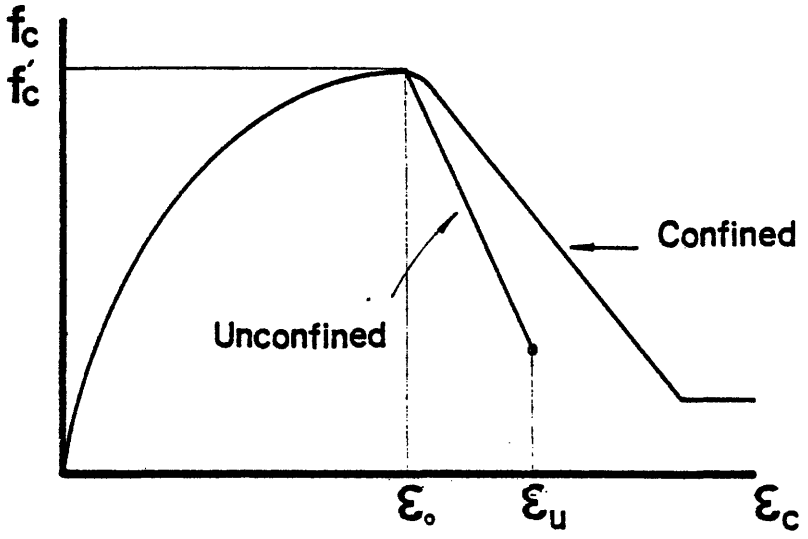

(b)

FIG. 2.2 - STRESS-STRAIN RELATIONSHIP FOR CONFINED AND UNCONFINED CONCRETE

If a more elaborate analysis is to be carried out, contributions of unconfined concrete cover and the confined concrete in a section must be calculated separately. Concrete when properly confined can carry compressive forces well beyond its unconfined ultimate strain. However, it is important to note that the overall behavior of a section is dominated by steel, and any reasonable approximation in concrete stress-strain curve will have little effect on moment-curvature relationships. Adopted stress-strain relationship for concrete is shown in Fig. 2.3.

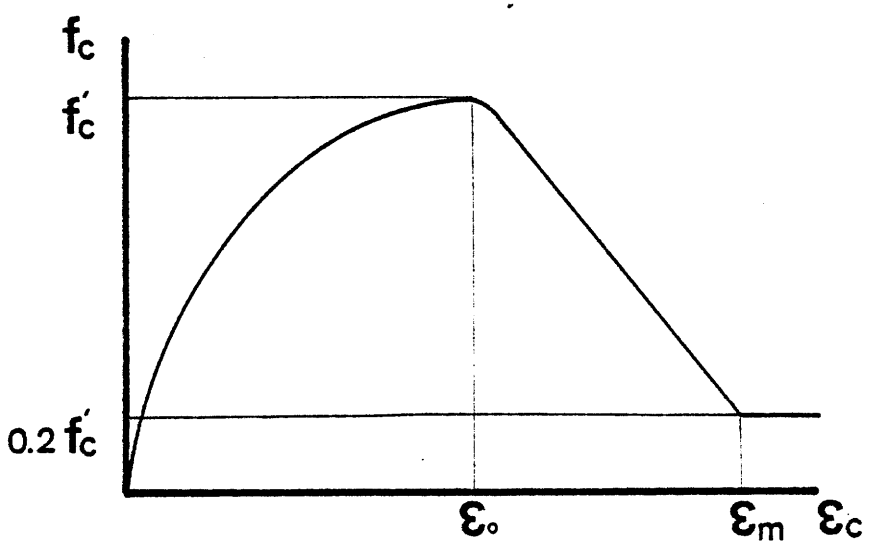

FIG. 2.3 - STRESS-STRAIN RELATIONSHIP ADOPTED FOR CONCRETE

$$f_c = f'_c \left[2 \left(\frac{\varepsilon_c}{\varepsilon_o}\right) - \left(\frac{\varepsilon_c}{\varepsilon_o}\right)^2\right] \qquad \varepsilon_c \leq \varepsilon_o \qquad (2.2a)$$

$$f_c = f'_c \left[1 - Z \left(\varepsilon_c - \varepsilon_o\right)\right] \qquad \varepsilon_o < \varepsilon_c < \varepsilon_m \qquad (2.2b)$$

$$f_c = 0.2\, f'_c \qquad \varepsilon_c \geq \varepsilon_m \qquad (2.2c)$$

Thus a uniform curve is assumed, and concrete is allowed to carry compressive forces beyond its ultimate strain. The parameter Z defines the unloading slope, and a method of estimating it is suggested by Kent and Park (31). In this work, Z is assumed to have a constant value of 200. As mentioned before, such an approximation will not affect the calculated moment-curvature relationship of a section appreciably.

2.3 Flexural Deformation

a) Moment-Curvature Behavior of a Section

Once concrete and steel stress-strain curves are determined, it is then possible to calculate the moment-curvature relationship for a section. Fig. 2.4a shows a reinforced concrete T section with longitudinal steel bars at top and bottom. The section is divided into many longitudinal fibers. Equilibrium is satisfied by

$$\Sigma T - \Sigma C + P_a = 0 \quad , \qquad (2.3)$$

where T and C are tensile and compressive forces, and P_a is the axial load. Assuming that plane sections remain plane, strain distribution over the section is drawn (Fig. 2.4b). Then from material constitutive

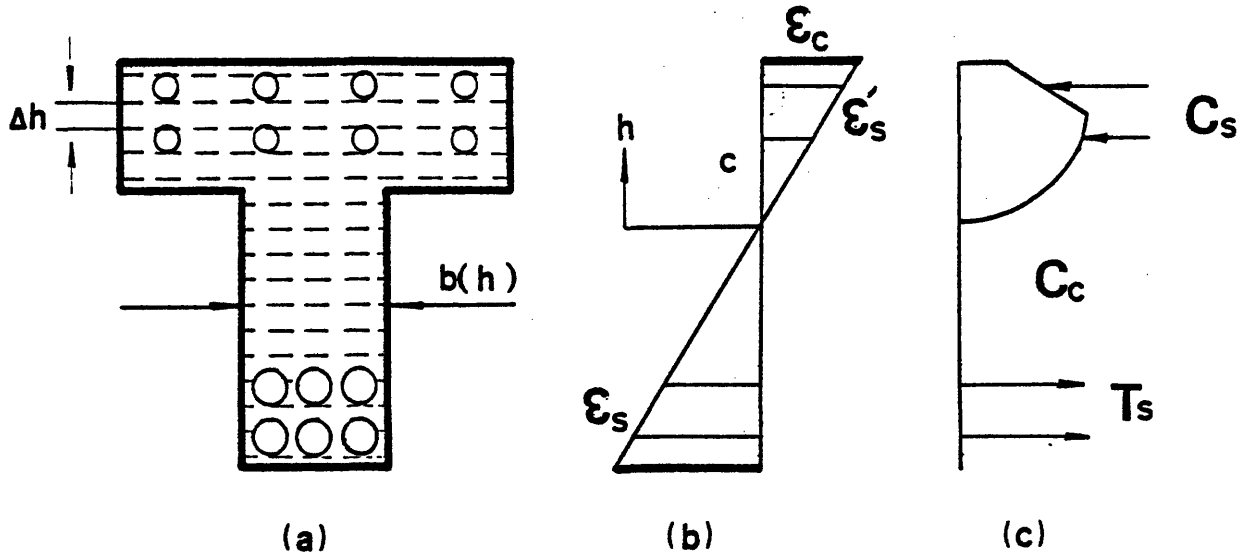

FIG. 2.4 - CONCRETE AND STEEL STRESS AND STRAIN DIAGRAMS FOR A REINFORCED CONCRETE T-SECTION

laws, stresses are calculated. Finally, tensile and compressive forces are determined (Fig. 2.4c).

$$T_s = A_s \sigma_s \qquad (2.4a)$$

$$C_s = A'_s \sigma'_s \qquad (2.4b)$$

$$C_c = \sum f_c(h)\, b(h)\, \Delta h \qquad (2.4c)$$

Since equilibrium is not automatically satisfied, a trial and error procedure is needed. Analysis is started by assuming values for strain in the concrete (ε_c) or steel (ε_s), and modifying the distance c in Fig. 2.4b until equilibrium is satisfied. The external moment acting on the section is then calculated

$$M = \sum f_c(h)\, b(h) h\, \Delta h + \sum T_s h + \sum C_s h - P_s\, e \quad , \qquad (2.5)$$

where e is eccentricity of the axial load (P_a). The curvature is simply

(Fig. 2.4b),

$$\phi = \frac{\varepsilon_s + \varepsilon_c}{d} \tag{2.6}$$

The first point of interest in the moment-curvature diagram (Fig. 2.5) is yielding of tensile reinforcement. The curve usually exhibits a relationship which is nearly linear up to yield point. If there is more than one layer of steel, yield point is defined to be when tensile steel yield strain is reached at an average depth. Section stiffness (EI) is the slope of the M-ϕ curve. Other points on the curve may be defined by setting concrete strain (ε_c). Various values of concrete strain have been suggested. Key point is that if a bilinear moment-curvature relationship for a section is assumed, the second slope becomes very sensitive to the assumed concrete peak strain (Fig. 2.5). Also, a bilinear assumption does not hold at high concrete strains, because the curve starts to drop off after reaching its peak. Axial load in a member also greatly modifies

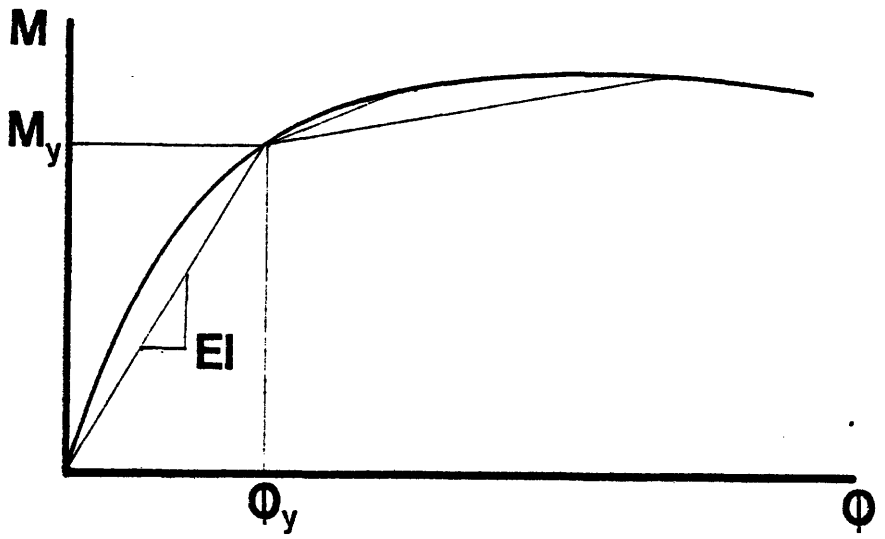

FIG. 2.5 - MOMENT-CURVATURE RELATIONSHIP FOR A REINFORCED CONCRETE SECTION

the shape of the moment-curvature relationship (Fig. 2.6). Moderate axial load on a member increases its yield moment and initial section stiffness, but it limits the capacity of a member to sustain high strains. When a building is subjected to dynamic loads, axial loads in the columns change at each time step. Variations of axial load around the average axial load (which is equal to the dead load) may be quite significant for perimeter columns. The calculated moment-curvature relationships represent an average behavior for members with axial load.

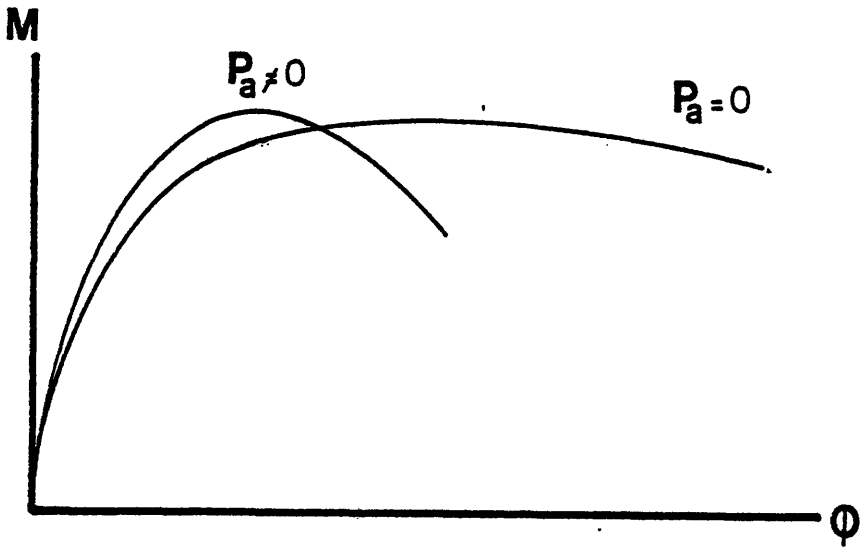

FIG. 2.6 - MOMENT-CURVATURE RELATIONSHIP FOR SECTIONS WITH AXIAL LOAD (P_a) AND WITHOUT AXIAL LOAD

b) The Single Component Model

The Single Component Model is used in this work for the stiffness formulation of reinforced concrete elements. The model consists of an elastic element with two hinges at its two ends. Thus, all inelastic rotations within a member length are lumped at these two points. In order to estimate the characteristics of these two hinges, moment distribution along a member must be predetermined. The assumption is that dead loads are negligible, and member end moments are of the same magnitude and opposite signs. This assumption is not always justified, but we employ it anyway. In reality, the yield condition at one end of a member depends on rotation at the other end. In fact, curvature distribution along a member changes for different loading conditions. Consider the two loading conditions shown in Fig. 2.7a (43). In Case I the two end moments are equal, and the point of contraflexure is in the middle, and in case II there is moment only at one end of the member. Figures 2.7b and 2.7c show curvature diagrams along the member for cases I and II respectively. It

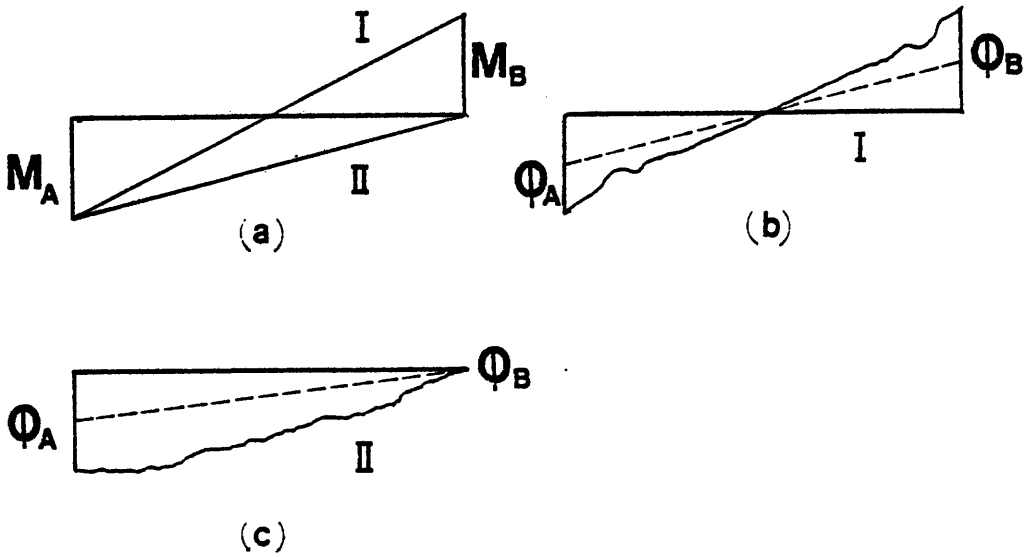

FIG. 2.7 - MOMENT AND CURVATURE DIAGRAMS FOR TWO DIFFERENT LOADING CONDITIONS

may be observed that inelastic rotation at one end of the member is very much dependent on curvature distribution and loading condition at the other end.

The antisymmetric moment distribution assumption is fairly accurate for girders. It may be argued that even if one end of a member reaches its yield condition, the moment at that end can not increase at the same rate, and this gives the moment at the other end the chance to reach yield also. The assumption is less valid for columns where the effect of axial load becomes important.

Figures 2.8a and 2.8b show the two end moments, and the assumed moment distribution shape for the Single Component Model. Since the point of contraflexure is in the middle, each half of the member may be viewed as a cantilever (Fig. 2.8c). Assuming a bilinear M-ϕ diagram for the section,

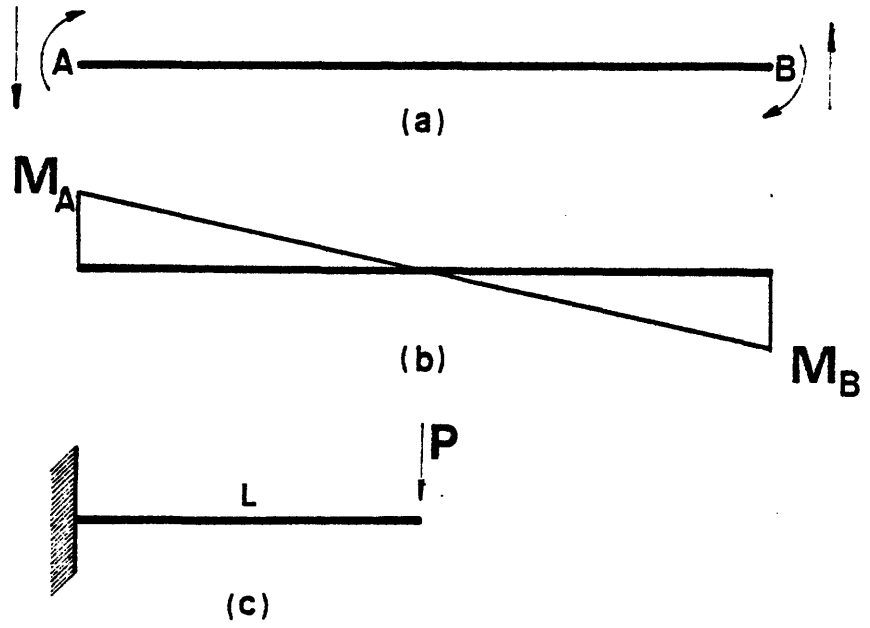

FIG. 2.8 - MOMENT DISTRIBUTION AND CANTILEVER ANALOGY FOR THE SINGLE COMPONENT MODEL

it is possible to match the end displacement of the half-length cantilever with that of the model. The model in this case is an elastic element with a hinge at its end. This approach is discussed in more detail in Appendix A. This may be viewed as an approximation to the true behavior of an element, and the following illustrates some of the factors which affect our results.

i) Plane sections do not remain plane, and the assumption may be justified only for segments of a member in between perpendicular flexural cracks.

ii) If shear is relatively high, interaction between shear and flexure in hinging zones adds to the complexity of member behavior.

iii) The M-ϕ diagram is not bilinear, and the unloading portion of the curve becomes important at higher ductilities.

iv) Even the assumption of a bilinear M-ϕ diagram does not mean that the P-δ curve of the half-length cantilever is bilinear (Appendix A). The second slope of the P-δ curve is very sensitive to the peak strain assumed for concrete.

After analyzing many cyclic load tests of cantilevers, it was found that the above approach results in a second slope on the P-δ curve which is too high and can not be reached in experiments. This is especially true if a member is subjected to increasing levels of cyclic loads. On the basis of experimental evidence, it was decided to put a 3 percent limit on the second slope of the cantilever P-δ curve (see Chapter III).

The two hinges at the two ends of an elastic element in the Single Component Model represent flexural inelastic behavior of a member. Hysteresis curves for moment-rotation of these hinges are assumed to follow the

Takeda model (54). The model is described in Appendix B. A modified version of the Takeda model with a bilinear primary curve is used in this study. Thus the bilinear primary curve is completely defined by yield point and second slope of the P-δ curve for the half-length cantilever.

Flexural hinges in a Single Component Model are initially infinitely stiff, so they do not affect the behavior of a member before yielding. Once they yield, their flexibilities are added to the rotation flexibility matrix of the elastic member.

$$\underset{\sim}{F} = \begin{bmatrix} \frac{\ell}{3EI} + \frac{1}{K_i} & \frac{-\ell}{6EI} \\ \frac{\ell}{-6EI} & \frac{\ell}{3EI} + \frac{1}{K_j} \end{bmatrix} , \qquad (2.7)$$

where K_i and K_j are stiffnesses of the flexural hinges.

One advantage of the Single Component Model is that the stiffness matrix of an element is modified only when there is a change of stiffness in one of the two hinges. This means that the global stiffness matrix is not necessarily modified at each time step, and this greatly reduces the computational time.

c) Non-symmetric Reinforced Concrete Sections

In design of earthquake-resistant reinforced concrete frames, codes usually specify that the positive moment capacity of a girder has to be no less than 50 percent of its negative moment capacity. This means that, unlike many experiments which use symmetric concrete sections, most members in a real building have different areas of steel at top and bottom.

Furthermore, both yield moment and stiffness of a non-symmetric section differ in the two loading directions (Fig. 2.9). This is also true of T-sections, which are commonly used in reinforced concrete structures, and in beam-slab construction, where the slab would partly contribute to moment resistance of the beam in both directions.

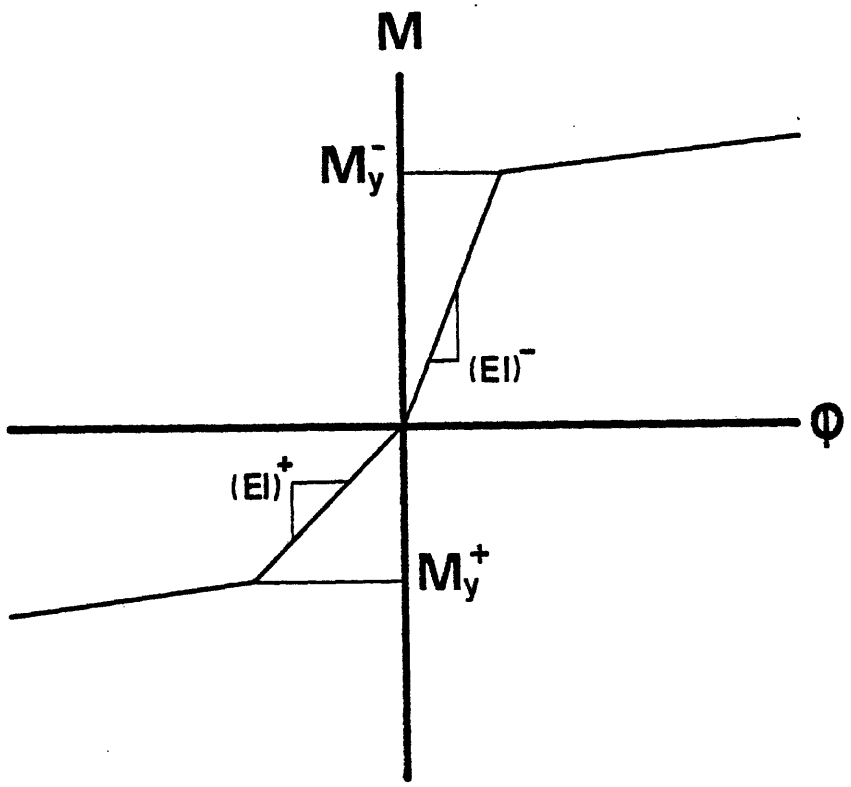

FIG. 2.9 - MOMENT-CURVATURE RELATIONSHIP FOR A NON-SYMMETRIC SECTION

A simple method of analyzing such sections is to use an average stiffness, and to have different yield moments in negative and positive directions for the Takeda model. This results in an overestimate of stiffness in the positive direction and an underestimate in the negative direction. The difference may be drastic for T-sections. A different element was

developed in this work to model such members. This element is a Single Component Model, but it has different properties, as explained below.

Consider a member acted upon by two end moments (Fig. 2.10a) of opposite signs. The point of contraflexure divides the element into two segments. Consider what happens before any yielding has taken place. The two segments denoted by ℓ_1 and ℓ_2 would exhibit different stiffnesses (Fig. 2.10b). The model consists of two elements connected at point C and two hinges at its two ends. Neglecting cracking, this element's behavior would be very similar to actual behavior of the member. Once yielding occurs, our analytical model deviates from the real behavior because the effect of the point of contraflexure on hinge properties is not taken into account. The Takeda model for two end hinges is also modified to have different stiffnesses in the two directions. A more consistent approach would be to apply the Takeda model on the two segments, assuming that each one acts as a cantilever. Such an approach has been used by Otani (41).

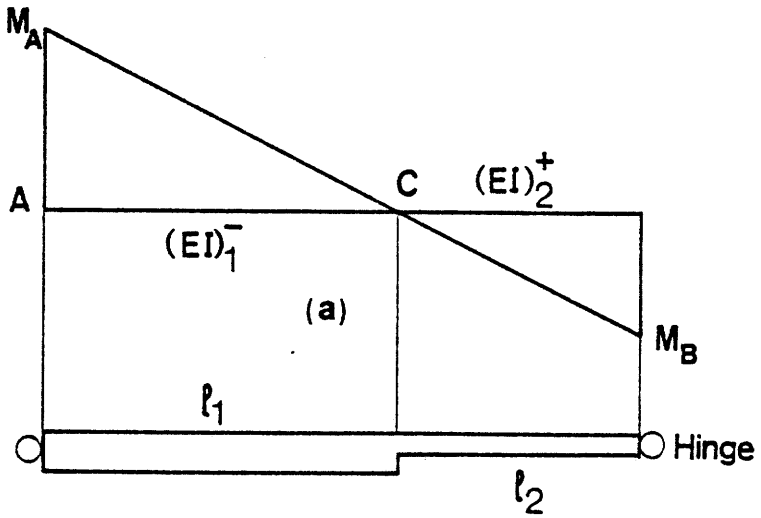

FIG. 2.10 - MOMENT DISTRIBUTION AND STIFFNESS FOR A NON-SYMMETRIC SECTION.

In order to set up the stiffness matrix of this element, length of each segment is computed from end bending moments. Here it is assumed that the point of contraflexure does not move in a small time step, (Δt). Otherwise an iteration procedure has to be used to find its exact location. However, changes in the location of the point of contraflexure may be very large when the two end moments are small, which would make the iteration non-convergent. Once length of each segment and its stiffness properties are known, it is possible to condense out the degrees of freedom of point C and to find the stiffness matrix of combined element. Assuming segments of lengths ℓ_1 and ℓ_2 and stiffness values of $(EI)_1$ and $(EI)_2$, the flexural stiffness matrix of this model may be written as follows.

$$K = \begin{bmatrix} \frac{4(EI)_1}{\ell_1} & 0 \\ 0 & \frac{4(EI)_2}{\ell_2} \end{bmatrix} - \frac{1}{Det} \begin{bmatrix} K_{11} & K_{12} \\ K_{21} & K_{22} \end{bmatrix} \tag{2.8a}$$

$$K_{11} = \frac{48(EI)_1^3}{\ell_1^5} + \frac{144(EI)_1^2(EI)_2}{\ell_1^3\ell_2^2} + \frac{144(EI)_1^2(EI)_2}{\ell_1^4\ \ell_2} + \frac{48(EI)_1^2(EI)_2}{\ell_1^2\ \ell_2^3} \tag{2.8b}$$

$$K_{12} = \frac{-24(EI)_1^2(EI)_2}{\ell_1^4\ell_2} - \frac{72(EI)_1^2(EI)_2}{\ell_1^3\ell_2^2} - \frac{72(EI)_1(EI)_4^2}{\ell_1^2\ell_2^3} - \frac{24(EI)_1(EI)_2^2}{\ell_1\ell_2^4} \tag{2.8c}$$

$$K_{22} = \frac{48(EI)_2^3}{\ell_2^5} + \frac{144(EI)_1(EI)_2^2}{\ell_1^2\ell_2^3} + \frac{144(EI)_1(EI)_2^2}{\ell_1\ell_2^4} + \frac{48(EI)_1(EI)_2^2}{\ell_1^3\ell_2^2} \tag{2.8d}$$

$$K_{21} = K_{12} \tag{2.8e}$$

$$Det = \frac{12(EI)_1^2}{\ell_k^4} + \frac{12(EI)_2^2}{\ell_2^4} + \frac{48(EI)_1(EI)_2}{\ell_1^3\ell_2} + \frac{48(EI)_1(EI)_2}{\ell_1\ell_2^3} + \frac{72(EI)_1(EI)_2}{\ell_1^2\ell_2^2} \tag{2.8f}$$

The 2 x 2 stiffness matrix is easily inverted to find the flexibility matrix. Finally, the effect of two end hinges is added to the diagonals of the flexibility matrix (Eq. 2.7). One advantage of this method over the Connected-Two-Cantilever Method is that the stiffness matrix is symmetric. However, in both cases the stiffness matrix of an element has to be assembled at each time step, which adds appreciably to the cost of analysis.

2.4 Slippage of Reinforcement

a) Physical Characteristics of Slippage

One of the components of element deformation in reinforced concrete members is due to slippage of main longitudinal reinforcement. Figure 2.11 shows the mechanism of rotation. A vertical crack at the joint crosses the tensile reinforcement, and the section rotates around its neutral axis. Loss of bond between steel and concrete in the joint causes any

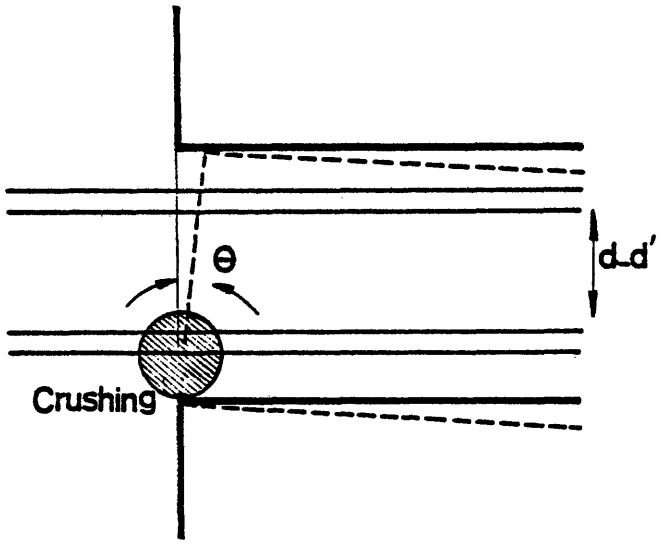

FIG. 2.11 - FIXED END ROTATION DUE TO SLIPPAGE OF LONGITUDINAL REINFORCEMENT

steel elongation to be transferred to the crack. Also, concrete in the compression zone starts to crush once any fixed end rotation has occurred. The following treatment of the problem makes two simplifying assumptions. First, a section is assumed to rotate around its compressive steel. In most reinforced concrete sections the location of the neutral axis will not be far from compressive reinforcement. Second, any cracking and crushing is assumed to occur outside the joint area; thus no damage in the joint is allowed. This implies that satisfactory detailing of the joint has been achieved. In order to estimate any fixed end rotation, steel development length has first to be calculated. Figure 2.12 is a diagram of concrete bond stress and steel stress along steel development length (L_d). Bond stress (u) is assumed to be constant along development length, whereas steel strain (σ_s) changes linearly (41). An inherent assumption in this approach is that the embedment length is long enough

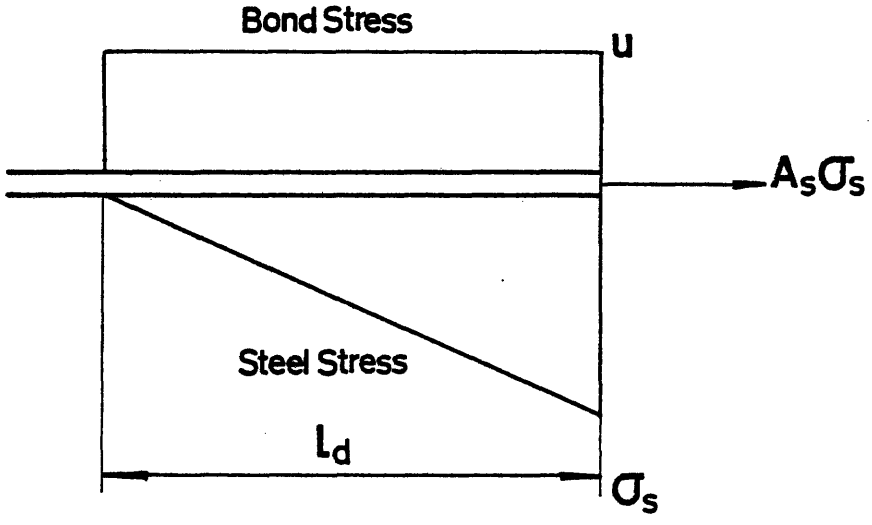

FIG. 2.12 - CONCRETE BOND STRESS AND STEEL STRESS ALONG THE DEVELOPMENT LENGTH

so that steel development length can be obtained. This is the basis of the "joint problem" in reinforced concrete. For equilibrium to be satisfied, the following relationship must hold:

$$\pi D u L_d = A_s \sigma_s \quad , \tag{2.9}$$

where D is the diameter of steel reinforcement. An approximate formula is used to estimate the bond stress (u).

$$u = 6.5 \sqrt{f'_c} \quad . \tag{2.10}$$

Assuming that all steel elongation is transferred to the crack, the opening length (ΔL) at the level of tensile steel is computed.

$$\Delta L = \frac{L_d \sigma_s}{2E_s} \quad . \tag{2.11}$$

Substituting for development length L_d, and the area of steel (A_s) in Eq. (2.11), the crack opening length is written as follows:

$$\Delta L = \frac{1}{8} \frac{D}{E_s u} \sigma_s^2 \quad , \tag{2.12}$$

where E_s is Young's modulus for steel. Fixed end rotation of the member is simply

$$\theta = \frac{\Delta L}{d - d'} \quad . \tag{2.13}$$

Assuming the following relationship between steel stress and member end moment,

$$\frac{\sigma_s}{\sigma_y} = \frac{M}{M_y} \quad . \tag{2.14}$$

Fixed end rotation at the yield point of tensile reinforcement is computed by

$$\theta_y = \frac{1}{8} \frac{D}{E_{su}} \frac{\sigma_y^2}{d - d'} \quad . \tag{2.15}$$

Using the steel stress-strain diagram (Fig. 2.1), steel stresses and steel strain along the new development length at ultimate steel stress (σ_u) may be determined. Figures 2.13a and 2.13b show such diagrams, where area under the strain curve represents the crack opening.

$$\Delta L_u = \frac{1}{2} (L_d)_u \left(1 - \frac{\sigma_y}{\sigma_u}\right)(\varepsilon_u + \varepsilon_{sh} - \varepsilon_y) + \frac{1}{2} L_d \varepsilon_y \tag{2.16}$$

$$\theta_u = \frac{\Delta L_u}{d - d'} \tag{2.17}$$

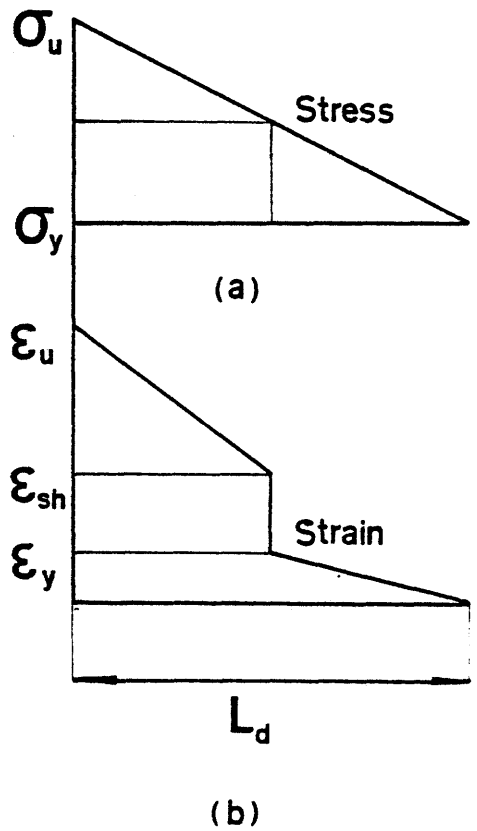

FIG. 2.13 - ULTIMATE STEEL STRESS AND STRAIN ALONG THE DEVELOPMENT LENGTH

Figure 2.14 represents the moment-rotation relationship for a monotonically increasing load. Since there is no crack opening up to cracking moment (M_{cr}), the curve has infinite stiffness in the beginning. Two other points on the curve are determined by yielding and ultimate stress of tensile reinforcement. In this study, a bilinear approximation to this trilinear curve is used.

The moment-rotation primary curve (Fig. 2.14) may then be used to set up a hysteresis curve of slippage. The proposed hysteresis curve is based on experimental results in Chapter III, and also on physical consideration of slippage.

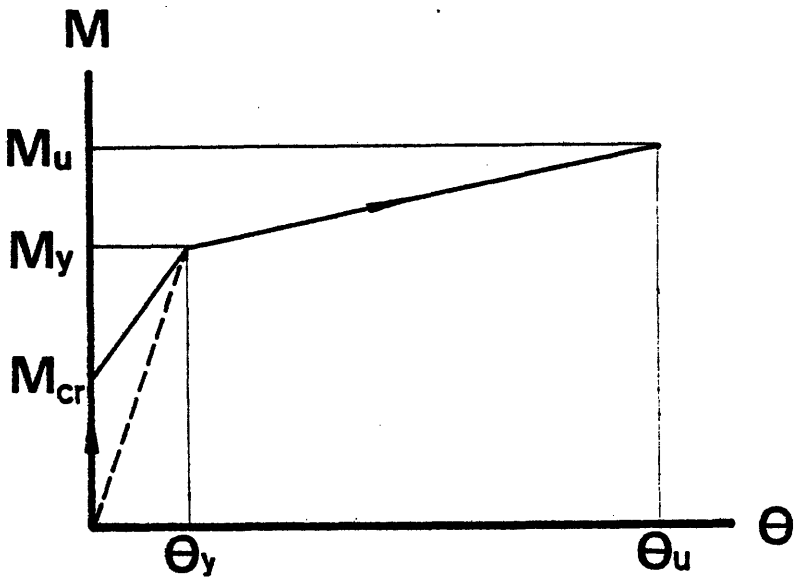

FIG. 2.14 - MOMENT-ROTATION PRIMARY CURVE FOR SLIPPAGE OF REINFORCEMENT

b) Hysteretic Behavior under Cyclic Loads

Using yield and ultimate points of tensile reinforcement, a bilinear curve for fixed end rotation of a member under an increasing monotonic

load may be set up. If the load is then reversed, initial unloading stiffness will be very high. However, as moment passes through zero the crack stays open, mainly due to residual plastic strain in steel. Little moment can be applied in the opposite direction until the crack is fully closed, except for what the compression steel may take. This is why a pinched behavior is observed when there is considerable steel slippage. The proposed hysteresis model is shown in figure 2.15. Slippage hysteretic behavior is defined by a set of 8 rules, which are identified in the figure by their corresponding numbers.

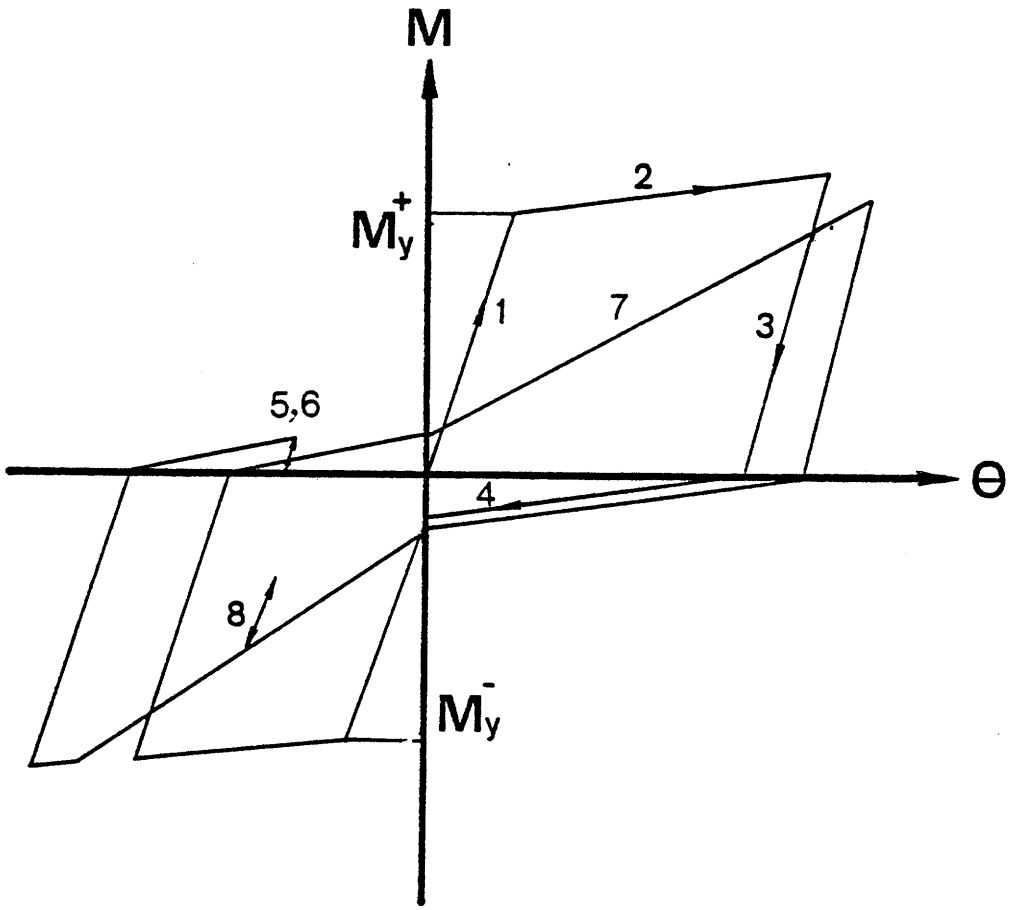

FIG. 2.15 - MOMENT-ROTATION HYSTERETIC BEHAVIOR FOR SLIPPAGE OF REINFORCEMENT

1 - Moment-rotation due to slippage is elastic up to the yield point.

2 - Once the yield point is exceeded, loading proceeds on the second slope of the primary bilinear curve.

3 - Unloading from the second slope is parallel to the elastic slope.

4 - Once the unloading stage is finished, the crack has then to be closed. Stiffness of this part may be taken as a percentage of the second slope of the primary curve. A 50-percent value is used in this study.

5 - If the direction of moment changes while closing the crack (rule 4), an unloading slope equal to the elastic slope is used.

6 - If the direction of moment changes while in rule 5, loading will be on the same curve until the previous point in rule 4 is reached. Then it will continue according to rule 4.

7 - Once the crack is closed, loading will be towards the previous maximum point in the opposite direction. In addition, a strength degradation feature has also been built into the model. Thus, instead of loading towards the point of maximum rotation, a new maximum rotation is defined as follows:

$$\theta_{max} = \frac{\theta_{max}}{\alpha} \tag{2.18}$$

Parameter α is an input to the model. A value of α equal to 0.8 is used for some of the experiments, resulting in strength degradation which is typical of such hysteresis curves. (See Chapter III).

8 - If the direction of the moment changes while unloading (rule 3), loading will be on the same curve until the previous intermediate point is reached.

2.5 Shear Deformation

In most analytical studies of reinforced concrete structures, shear deformation is assumed to be elastic. This means that a modified shear stiffness (GA) is used to correct the stiffness matrix of a member. Recent tests of reinforced concrete members where shear deformations were measured reveal that shear deformation has an inelastic behavior which is quite different from flexural behavior (32, 38). These tests show that most of the shear deformation occurs at both ends of a member where flexural deformation is also important. This is mainly due to propagation of inclined cracks at the ends of a member. The mechanism of opening and closing of such cracks is very similar to the slippage of reinforcement at joint interface.

Shear forces are transferred across cracks (Fig. 2.16) by three mechanisms (27). The most important mechanism of shear transfer in

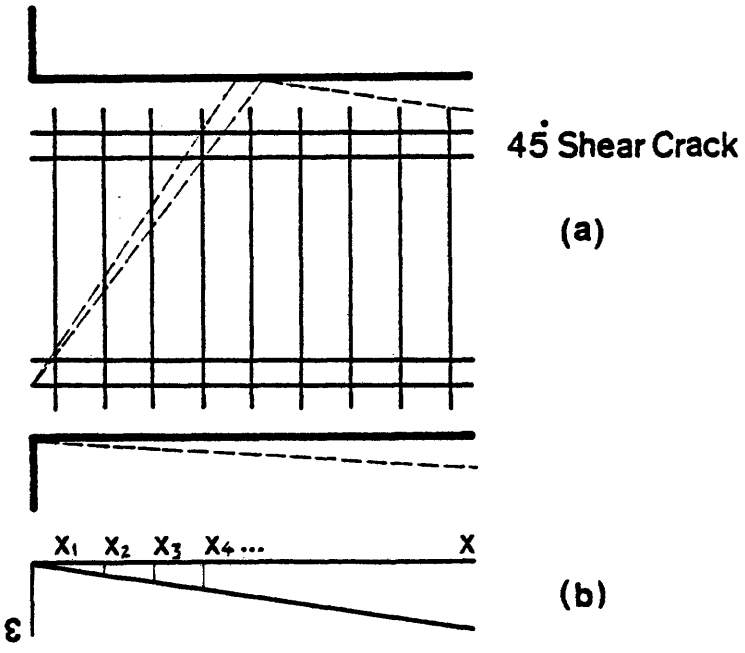

FIG. 2.16 - 45° CRACK OPENING AND STRAIN DISTRIBUTION FOR STIRRUPS ACROSS CRACK

reinforced concrete members is by web reinforcement and its contribution to shear resistance, may be estimated with reasonable accuracy. The contribution of concrete to shear resistance may be divided into two categories. The first is frictional and bearing forces across cracks generated by tangential shear displacement, and the second is contribution of concrete to shear resistance in the compression zone. The former category is generally known as interface shear or aggregate interlock. Finally, dowel action, which is activated by relative movement of the two ends of steel, also contributes to shear resistance.

The model that is adopted here was originally proposed by Küstü (32). This model is a simplification of real behavior, because it neglects the contribution of dowel action to shear resistance. Only minor changes to the original mdoel were made in this study. However, it is felt that better estimates of the contribution of concrete, and the inclusion of dowel action, would result in a fairly accurate model.

Figure 2.16a shows an inclined crack opening at the end of a reinforced concrete member. Such cracks are initiated when the resultant of flexural and shearing stresses exceeds the tensile strength of concrete. Here, it is assumed that a 45-degree crack propagates through the member, and there is a rotation around compressive reinforcement. Assuming that the crack opens linearly, strain distribution of stirrups along the crack will also be linear. Taking strain in the farthest stirrup from the joint as the control point (ε_n), crack opening may be estimated by

$$\Delta L_n = \varepsilon_n L_d \quad , \tag{2.19}$$

where L_d is development length on each side of the stirrup. As in the

slippage model, a linear steel stress along the development length is assumed. Shear rotation (γ_{sr}) is thus given by

$$\gamma_{sr} = \frac{\Delta L_n}{X_n} \tag{2.20}$$

Distance X_n is from joint interface to the control stirrup (Fig. 2.16b). Strains in all other stirrups and their contribution to shear resistance may also be estimated.

$$\varepsilon_i = \frac{X_i}{X_n} \varepsilon_n \tag{2.21}$$

$$F_i = \frac{X_i}{X_n} \varepsilon_n E_{st}(A_{st})_i \quad , \tag{2.22}$$

where F_i is the contribution of the i^{th} stirrup, E_{st} is Young's modulus, and A_{st} is the area of each stirrup. Total resistance offered by stirrups is then

$$V_{st} = \sum_{i=1}^{n} \frac{X_i}{X_n} \varepsilon_n E_{st}(A_{st})_i \quad . \tag{2.23}$$

It is more difficult to estimate interface shear transfer. In fact, concrete transfers most of the shear before any cracking occurs. However, most of the load is transferred to stirrups and the dowel mechanism once inclined cracks propagate across a member. Axial load in a member affects opening of the crack and increases interface shear transfer. It may be noted that aggregate interlock will be markedly reduced after a member is subjected to load reversals. This is a primary cause of strength degradation observed in shear hysteresis curves. In order to estimate the contribution of concrete to shear resistance, the elastic

cracking load is calculated. Figure 2.17 shows Mohr's circle for concrete at the cracking stage. At this point, tensile stress is equal to cracking stress (σ_t). Knowing the magnitudes of axial stress (σ_a) and tensile stress (σ_t), the cracking shear stress (τ_{cr}) may be calculated:

$$\tau_{cr} = \sqrt{\sigma_t^2 - \sigma_t \sigma_a} \quad . \tag{2.24}$$

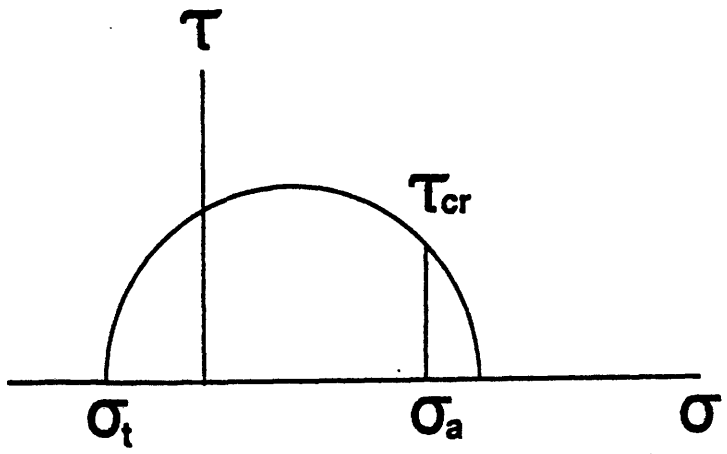

FIG. 2.17 - MOHR'S CIRCLE AT SHEAR CRACKING STAGE

Assuming a parabolic distribution of shear across the section, cracking shear stress is related to average shear stress (τ_{avg}).

$$\tau_{cr} = \frac{3}{2} \tau_{avg} \quad . \tag{2.25}$$

Multiplying Eq. (2.24) by gross area of the section (A_g), and then substituting total forces for stresses and τ_{avg} for τ_{cr} from Eq. (2.25), the cracking shear force (V_{cr}) is estimated.

$$V_{cr} = \frac{2}{3} \sqrt{F_t^2 - P_a F_t} \quad , \tag{2.26}$$

where P_a is axial load on the member and $F_t = A_g \sigma_t$ is the value of the

splitting force. The following relationship is used to determine σ_t:

$$\sigma_t = - 1.5 \sqrt{f'_c} \quad . \tag{2.27}$$

It may be observed that this is only 20% of the suggested code value of concrete tensile strength. This is to take into account the fact that most of the shear is transferred to steel once there is any crack opening. Total shear resistance may be written as

$$V = V_{cr} + V_{st} \quad . \tag{2.28}$$

Using the yield point of the control stirrup, one point on the shear deformation curve is identified. In order to locate another point on such a curve, the ultimate steel strain for the control stirrup is considered. Using the steel stress-strain diagram (Fig. 2.1), the crack opening at the control point is computed.

$$(\Delta L_n)_u = L_d \left(1 - \frac{\sigma_y}{\sigma_u}\right)(\varepsilon_u + \varepsilon_{sh} - \varepsilon_y) + L_d \varepsilon_y \quad . \tag{2.29}$$

It is also possible to find strain and thus stress in each one of the stirrups using the linear crack opening assumption. Again, a trilinear shear-rotation curve would result which may be approximated by a bilinear curve. Assuming that the point of contraflexure is in the middle, it is possible to use a moment-rotation curve instead of a shear-rotation curve. Thus, inelastic shear deformations may be lumped at the end of the member.

In this study, the same hysteresis model was used for both slippage and shear deformations (Fig. 2.15). Shear hysteresis curves usually show more pinched behavior and strength degradation than slippage curves. In

order to refine the proposed hysteresis model, more experiments on members with high shear forces must be carried out. Because of the interaction of shear and flexural deformations in the hinging zone, it is difficult to isolate shear deformations in cyclic load tests.

2.6 Method of Analysis

a) Assumptions

The following set of assumptions were made in the analysis of reinforced concrete subassemblages or frames. Some of these items are discussed in more detail in the next few sections.

- A member is idealized by an elastic element with two hinges representing flexural deformation at its two ends. Other springs representing slippage of reinforcement or inelastic shear deformation are also added to the ends of the member when necessary. Different components of deformation (flexure, shear, and slippage) are assumed to act independently.
- Only the two-dimensional deformation of members is considered, and all members lie in the plane of loading.
- Axial deformation in girders is neglected, causing all nodes in one floor to have the same horizontal displacement.
- Secondary P-δ effects are taken into account (2.6e).
- The effect of finite joint size has been considered by transformation of the element stiffness matrix. Joints themselves are taken to be infinitely rigid.
- Masses are lumped at the nodes only (2.6b)
- The base of the structure is assumed to be infinitely rigid.

b) Mass Matrix

Although mass in a structure is distributed along each one of the members, for practical reasons masses are concentrated at the nodes. Only translational masses were considered here, and rotational inertia has been ignored. Furthermore, since all the nodes in one floor are assumed to have the same horizontal displacement, the mass matrix may be written as follows:

$$\underset{\sim}{M} = \begin{bmatrix} M_1 & & & \\ & M_2 & & \\ & & \ddots & \\ & & & M_n \end{bmatrix} \quad . \tag{2.30}$$

[M] is the diagonal mass matrix, and the elements of the matrix represent story masses. These assumptions should have less effect on lower modes of the structure.

c) Stiffness Matrix

Since a 2-D analysis is being considered, each node has two translational and one rotational degrees of freedom. Once the member stiffness matrix is set up, and it is modified for finite joint size, it must then be transformed into a global coordinate system. This is done using the transformation matrix $\underset{\sim}{T}$.

$$\underset{\sim}{K}_g = \underset{\sim}{T}^T \underset{\sim}{K}_L \underset{\sim}{T} \quad . \tag{2.31}$$

This matrix can be readily inserted into the global stiffness matrix. Since all the elements in this work have symmetrical stiffness matrices, only half of the total stiffness matrix needs to be set up. Springs repre-

senting shear or slippage deformations were treated as individual elements in this study. In fact, it is possible to condense out all the degrees of freedom at mid-points, and assemble a 6 x 6 stiffness matrix including effects of flexure, shear, and slippage.

During an inelastic dynamic analysis, the change of stiffness within a time step results in unbalanced loads at some of the nodes. This means that equilibrium at these nodes is not satisfied. An iteration procedure may be used to converge to an equilibrium condition, but convergence to the right results can not be guaranteed. In this study, unbalanced loads are added, with an opposite sign, to the load vector at the next time step. If magnitudes of these unbalanced loads are not high, results will be satisfactory.

d) Damping Matrix

Viscous damping forces are added to the equations of motion to model non-structural damping, friction, and other damping effects. On the one hand, damping in a structure is not necessarily of viscous form, and this is done only for convenience; and on the other hand, it is very difficult to estimate a value of viscous damping for reinforced concrete structures.

It is usually assumed that the structure's damping matrix is proportional to mass matrix, or stiffness matrix, or a combination of the mass and stiffness matrices. After studying many dynamic tests of structures on shaking tables, it was found that most of the response of these prototype structures is in the first mode. This is in part due to the fact that higher modes are more heavily damped than the first mode of the structure. Thus it was decided to use a damping matrix which is proportional to the stiffness matrix only, because this produces higher damping in the

higher modes.

$$\underset{\sim}{C} = a\ \underset{\sim}{K}_t \quad , \tag{2.32}$$

where $\underset{\sim}{K}_t$ is the tangent stiffness matrix of the structure. The method is shown to cause more damping as natural frequencies of the structure become higher. It also takes into account softening of the structure and the increase in natural period of a building.

e) P-δ Effect

Axial loads on a member produce secondary moments which tend to increase inelastic deformations. Since the two ends of girders in this study are assumed to have the same horizontal translations, no axial force is induced in girders. However, axial loads may become important for lower columns of a building. A more complete theory of stability of columns may be found in the work by Aziz (5). Here, a linear solution to the problem has been used, and it is also assumed that axial load on columns stays constant during the strong-motion duration. A more complete analysis would be to allow axial loads to change, but this requires that the stiffness matrix of the structure be modified at each time step. Here, corresponding shear terms in the element stiffness matrix are modified by the following matrix $\underset{\sim}{K}_a$.

$$\underset{\sim}{K}_a = \frac{P_a}{L}\begin{bmatrix} 1 & -1 \\ -1 & 1 \end{bmatrix} \tag{2.33}$$

It is also necessary to take axial load into account when considering equilibrium of the element. Thus, shear at each end of the member is modified for the P-δ effect. (Fig. 2.18).

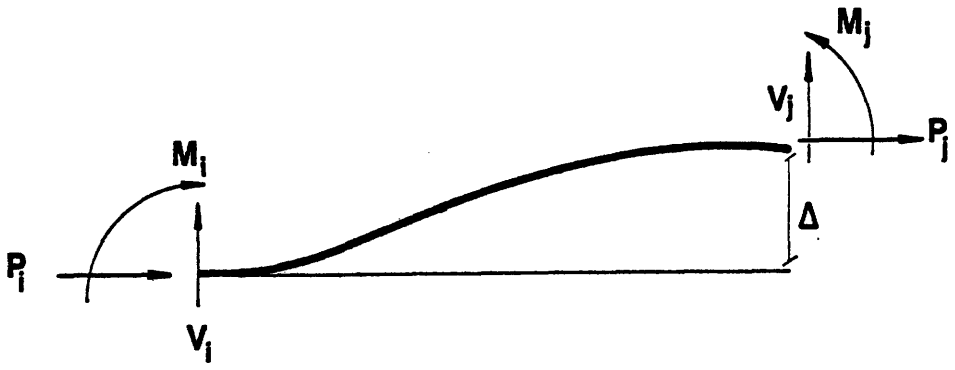

FIG. 2.18 - ELEMENT END FORCES

$$V_i = \frac{-M_i + M_j + P_i \Delta}{L} \tag{2.34a}$$

$$V_j = \frac{M_i - M_j + P_j \Delta}{L} \tag{2.34b}$$

2.7 Damage Indicators

When a reinforced concrete building is subjected to strong ground motions, it is expected that some members will undergo considerable inelastic behavior. Then, the important issue is not the prevention of such an inelastic behavior, but rather the prediction of damage given that some members have behaved inelastically. A parameter which is frequently used in practice to identify damage is peak ductility. There are many definitions of ductility. Even assuming that peak ductility can be computed without uncertainty, it is obvious that this parameter by itself can not predict the state of damage in a member. Other parameters such as cumulative ductility and energy dissipation have recently been given attention (12). Since the present work is intended to develop an alternative method of damage prediction, a survey of different definitions of damage indicators and their applicability in analysis of reinforced concrete structures is presented.

The most widely used definition of ductility is the ratio of maximum rotation (θ_{max}) to yield rotation (θ_y) (Fig. 2.19).

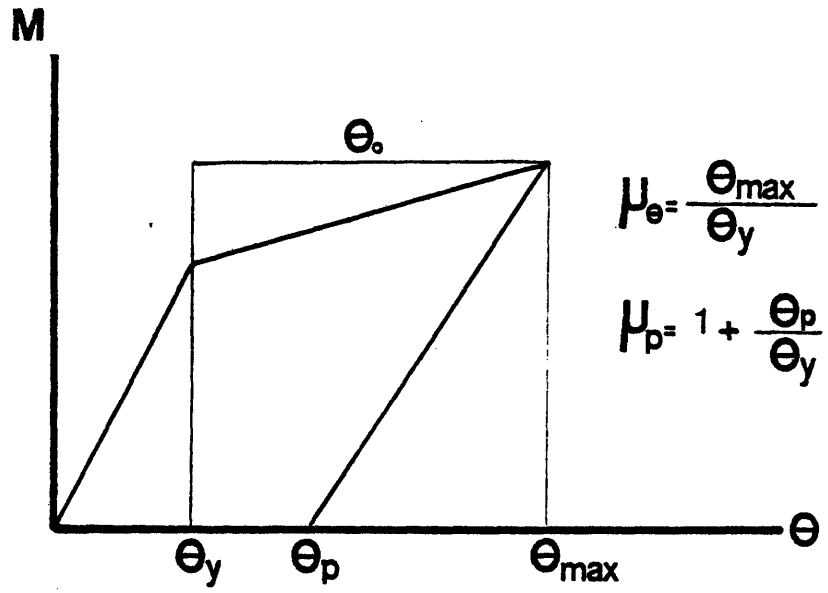

FIG. 2.19 - DEFINITIONS OF ROTATION DUCTILITY AND PERMANENT SET DUCTILITY

$$\mu_\theta = \frac{\theta_{max}}{\theta_y} \quad . \tag{2.35}$$

In order to estimate θ_y, anti-symmetric bending of a structural element has to be assumed.

$$\mu_\theta = 1 + \frac{\theta_o}{\theta_y} = 1 + \frac{\theta_o}{M_y L/6EI} \tag{2.36}$$

The shortcomings of assuming the point of contraflexure to be at midspan have been discussed before (Section 2.3b). Ductility may also be defined as the ratio of permanent plastic rotation (θ_p) to yield rotation plus one (Fig. 2.19).

$$\mu_p = 1 + \frac{\theta_p}{\theta_y} = 1 + \frac{\theta_p}{M_y L/6EI} \tag{2.37}$$

If the element does not have a well-defined yield point, such as the

one shown in Fig. 2.20, then both of these definitions fail. Also in many stiffness degrading systems, permanent set, which is used in the second definition (θ_p), may only slightly increase, while the rate of damage is increasing (Fig. 2.20). This is due to degradation of the unloading stiffness. In light of such an observation, μ_θ seems to be superior to μ_p.

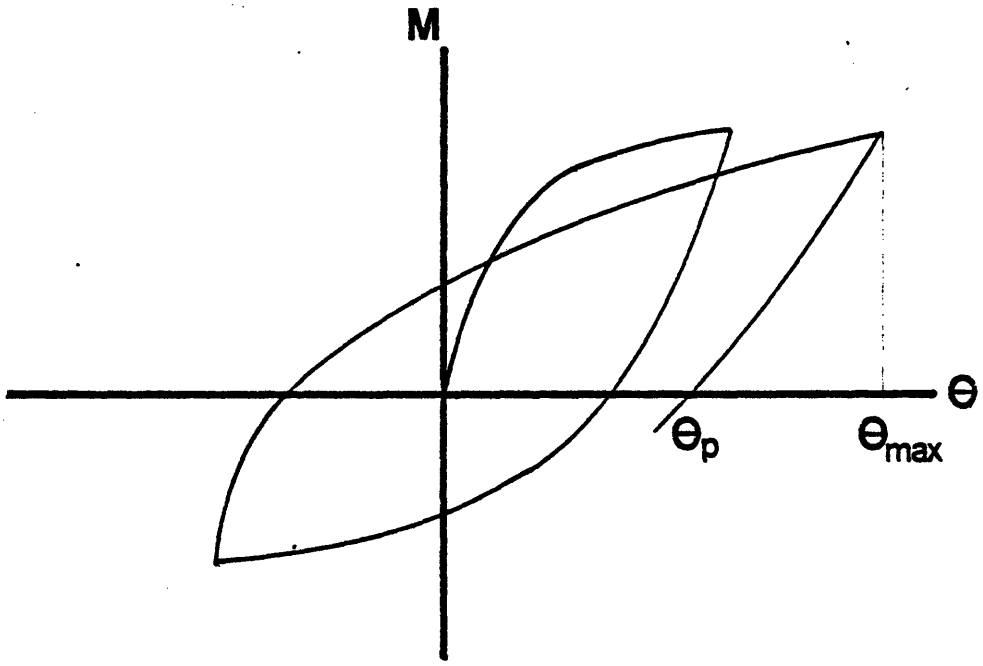

FIG. 2.20 - HYSTERESIS CURVE FOR A CURVILINEAR SYSTEM

The third definition of ductility is based on curvature, and it is intended to eliminate the need for assuming antisymmetric bending of an element. Figure 2.21 shows the moment-curvature relationship for the end section of a member. Curvature ductility is defined as the ratio of moment that would be developed if the member had remained elastic (M_{el}) to yield moment (M_y).

$$\mu_\phi = \frac{M_{el}}{M_y} = \frac{\phi_{max}}{\phi_y} = 1 + \frac{\phi_o}{\phi_y} . \qquad (2.38)$$

If a bilinear moment-curvature relationship is assumed, then curvature ductility may be written as follows.

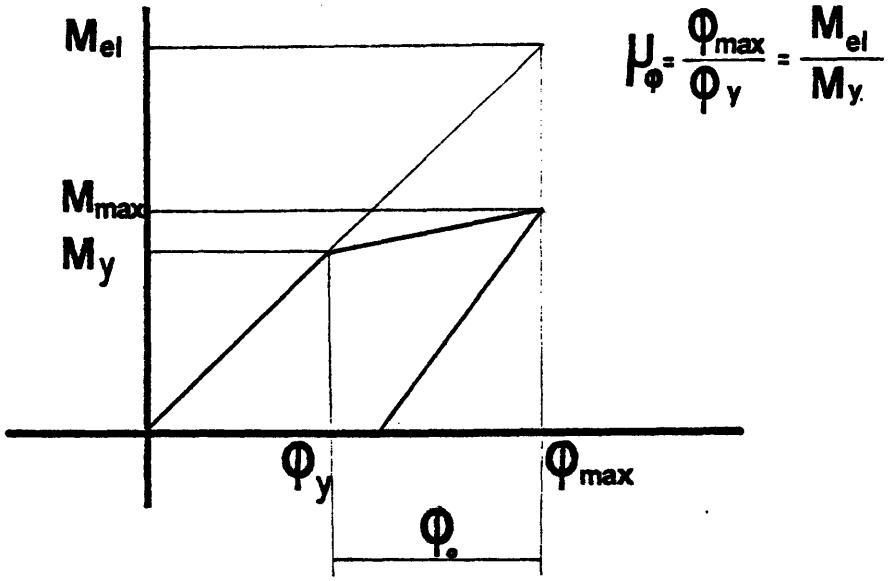

FIG. 2.21 - CURVATURE DEFINITION OF DUCTILITY

$$\mu_\phi = 1 + \frac{M_{max} - M_y}{p\, M_y} \quad , \tag{2.39}$$

where p is the ratio of second stiffness to initial elastic stiffness. This eliminates the need for computing curvatures which are not accessible in the Single Component Model. Using Eq. (2.39), curvature ductilities were estimated for all the experiments in Chapter III. For non-symmetric sections, the ratio (p) may be quite different in the two loading directions. Although the method is expected to give good estimates of curvature ductilities, the utility of this definition of ductility in predicting damage is questionable. The fact is that curvature ductility is valid only for the worst section of the member, and it does not reflect the extent of inelastic rotations along the member length.

Another interesting idea for prediction of damage was first proposed by Sozen (37). A reduced secant stiffness (K_r) at maximum displacement is computed, and the ratio of initial stiffness (K_0) to this reduced stiffness is called "damage ratio" (DR). (Fig. 2.22).

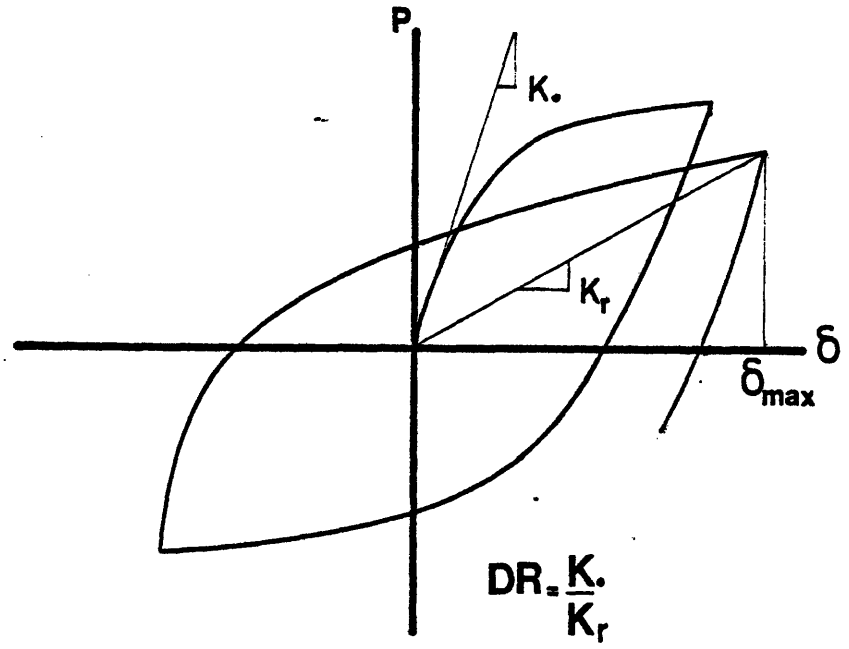

FIG. 2.22 - DEFINITION OF DAMAGE RATIO

$$DR = \frac{K_o}{K_r} \quad . \tag{2.40}$$

This definition eliminates the need for computing yield displacements. The definition may be applied to the half-length cantilever of the Single Component Model. Therefore, the initial slope of the P-δ curve of a cantilever of length L/2 including shear and slippage flexibilities is as follows:

$$K_o = \frac{1}{\frac{L^3}{24EI} + \sum_i \frac{L^2}{4K_i}} \quad , \tag{2.41}$$

where K_i is the stiffness of slippage or shear springs. One advantage of damage ratio over other ductility definitions is that both load and displacement are taken into account. For example, if there is any strength degradation in the model, DR would reflect that, but other definitions of ductility will not.

In this study, a modified definition of damage ratio was adopted. This is called "flexural damage ratio" (FDR) and it is the ratio of initial flexural stiffness of the member (K_f) to its reduced secant stiffness.

$$FDR = \frac{K_f}{K_r} \quad , \tag{2.42}$$

where flexural member stiffness is simply

$$K_f = \frac{24EI}{L^3} \quad . \tag{2.43}$$

The reason for excluding effects of shear and slippage from the damage ratio definition is the uncertainty in modeling those deformations. Flexural stiffness (EI) of the section can be estimated with a higher degree of accuracy (Section 2.3a). It may be noted that the stochastic models of failure which are presented in Chapter IV can use either one of the two definitions of damage ratio. However, it is felt that the flexural damage ratio introduced here has less uncertainty associated with it.

All parameters introduced to this point lack one important feature, and that is the cumulative effect of inelastic behavior on the state of damage in a member. It must be realized that (low cycle) fatigue type damage is possible under earthquake excitations. Two other useful parameters may be added, namely, cumulative plastic rotation and dissipated energy.

Normalized cumulative rotation (NCR) is defined as the ratio of the sum of all plastic rotations in a hinge, except for unloading parts, to yield rotation

$$NCR = \frac{\Sigma\theta_o}{\theta_y} = \frac{\Sigma\theta_o}{M_y L/6EI} \tag{2.44}$$

Dissipated energy in a Single Component Model may also be easily computed

by integrating the area under the moment-rotation curve for each inelastic spring

$$E_t = \oint M\,\theta\,d\theta \quad . \tag{2.45}$$

This energy is then normalized in terms of the maximum elastic flexural energy that may be stored in a member when it is subjected to antisymmetric bending.

$$E_n = \frac{E_t}{\frac{1}{2} M_y \theta_y} = \frac{E_t}{M_y^2 L/12EI} \quad . \tag{2.46}$$

Even though this definition of normalized dissipated energy (E_n) is dependent on the location of point of contraflexure, it is especially useful in terms of indicating the overall cyclic inelastic rotations in a member. Once energy is evaluated for each inelastic spring, a backward pass is made to ensure that it is a non-decreasing function, i.e., local fluctuations in the function are eliminated.

This chapter has dealt with models of inelastic behavior of reinforced concrete members. Flexure, shear, and slippage of reinforcement were identified as main sources of deformation, and models of their hysteretic behavior were presented. A Single Component Model with the Takeda model for hysteretic behavior of its hinges was used for flexure. An extension of the model was developed for non-symmetric reinforced concrete sections. Making simplifying assumptions, hysteresis models were also introduced for shear and slippage. Next, parameters which are used for prediction of damage were identified. Among them peak ductility is the most commonly used parameter. Others, such as dissipated energy and cumulative plastic rotation have recently been given attention. Flexural damage ratio is thought to be a useful indicator of damage. Chapter III deals

with analysis of a set of static cyclic load experiments. Models described in this chapter are used for this purpose. All of the damage indicators introduced in this chapter are calculated for each experiment. Results are then used to develop a stochastic model of damage in Chapter IV.

CHAPTER III - INVESTIGATION OF CYCLIC LOAD TESTS

3.1 Introduction

Along with the development of better analytical techniques to model inelastic behavior of reinforced concrete structures, there has also been a growing interest in experiments simulating earthquake loads on these structures. Both static tests and dynamic shaking table tests of reinforced concrete structures have been used to check or develop models of inelastic behavior. The purpose for developing analytical models in this study (see Chapter II) is twofold. First, the models are necessary to compute the damage parameters for each test; and second, the models are needed to apply the method of predicting damage in a real frame.

The experiments which are reported in this chapter are all cyclic load tests on single members or frame subassemblages. The idea is to isolate one part of a frame and then simulate the same type of deformations that it might experience under earthquake loads. Although some of the tests reported here also include analytical results, no effort has been made to compare them with analytical results of this study. Reasons for choosing cyclic load tests rather than dynamic shaking table tests are as follows:

- Static cyclic load tests are usually controlled by displacement magnitudes. In these tests, it is possible to measure both loads and displacements at various points accurately. Stiffness and strength variations in a specimen are recorded in static tests, and the accuracy of analytical models is easily checked. On the other hand, dynamic tests can not be closely controlled, and they do not offer accurate results.

- Quantities such as shear deformations, fixed end rotations due to bar slippage, and steel strains which are measured in most static cyclic load tests are not easily accessible in dynamic tests.

- There are many cyclic load tests available, but the number of dynamic tests is still limited.

However, it should be kept in mind that inertia and damping forces are absent in cyclic load tests. These tests provide us with information on hysteretic behavior and energy dissipation capacity in a member. Also, there are other aspects of loading, such as the rate of loading in static tests, which are not compatible with true earthquake environment. Thus, when one extrapolates the results of cyclic load tests to inelastic dynamic behavior of buildings, some uncertainty is being introduced. Although many static cyclic load tests are available in the literature, most of them do not represent the true behavior of reinforced concrete buildings under earthquake loads. One problem with many of these tests is the scale of a specimen, and it was decided to use only large-scale specimens in this study. Integrity of the beam-column joint is another important consideration. Joints must be designed to withstand all combinations of loads transmitted to them by adjoining members with minimum damage. Analytical models used to study inelastic behavior of frames usually assume that the joint is infinitely stiff. Some members in the experiments were excluded from the sample because either they were not tested to failure or the specimen did not meet one of the above requirements. A total of 32 specimens from eight different sets of experiments were included in the sample. The sample is rather small, and a bigger sample size would help to better estimate the parameters of the stochastic model of failure which is developed in

the next chapter. It is also possible to include some more specimens from the experiments which are described in the next section. In particular, five more specimens in the experiments by Atalay and Penzien (3) may be added to the sample.

All experiments in the sample are described in the next section. It is important that analytical models yield good estimates of damage indicators which are used to develop a stochastic model of damage. This is discussed for each experiment, and also experimental and analytical results are compared when possible. Since the goal of the present work is to predict damage in a member, the state of "excessive damage" had to be defined. This is done in terms of load-carrying capacity of a member. In most of the experiments, failure was a rather sudden phenomenon; i.e., the load-carrying capacity dropped very fast once excessive damage had occurred. On the other hand, some of the laboratory tests of the specimens showed a slow failure process. In these cases, a member is assumed to be badly damaged when there is more than 80 percent deviation between the experimental load and the computed analytical load. This method assumes that a member follows the analytical model until an unexpected mode of failure causes a deviation between the two results. Some judgement has been used to define failure point for specimens which showed gradual failure. However, computed values of damage indicators at failure are not expected to be too sensitive to definition of failure. Even though some members were able to carry several more cycles of load past their theoretical failure point, for all practical purposes these members may be assumed to have failed.

3.2 Experimental Data

a) Atalay-Penzien

These sets of tests were designed to study behavior of reinforced concrete columns under high axial and flexural loads (3). A total of 12 specimens were built and tested for this purpose. All specimens had a length of 11 ft and 12 x 12-inch cross sections (Fig. 3.1). Variables in these tests were magnitude of axial load, percentage of transverse reinforcement, and rate of loading. The specimen represents two columns of a high-rise building in between their inflection points, which are assumed to be at their mid-points. Although seismic loads in a building would cause columns to deform in double curvature, this type of test setup was used for simplicity. Longitudinal reinforcement for each specimen consisted of two #7 bars at top and bottom with an average yield stress of 55.2 ksi. These bars were welded to two steel plates in the joint to limit their slippage. Transverse reinforcement was #3 bars with a spacing of three inches for odd-numbered specimens and five inches for even-numbered specimens. Axial load on members was 60 kips for specimens 1-4, 120 kips for specimens 5-8, and 180 kips for specimens 9-12. These represent 25 percent, 50 percent, and 75 percent of the balanced point axial load, respectively.

Two sets of displacements of 20 cycles each were applied to the joint of each specimen. Because of high span-to-depth ratio, shear deformations were not important. Only five specimens were considered in this study (4, 7, 8, 11, 12). These five specimens were tested under higher strain rates. Experimental and analytical load deflection curves for these specimens appear in Figs. 3.2 - 3.6. In the following figures, (a)-figures

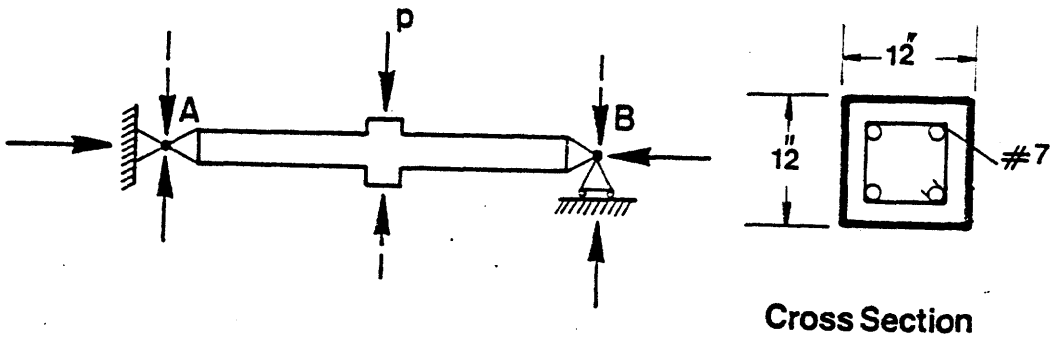

Fig. 3.1 - Test Set-up and Section Properties for the Expetiment by Atalay-Penzien

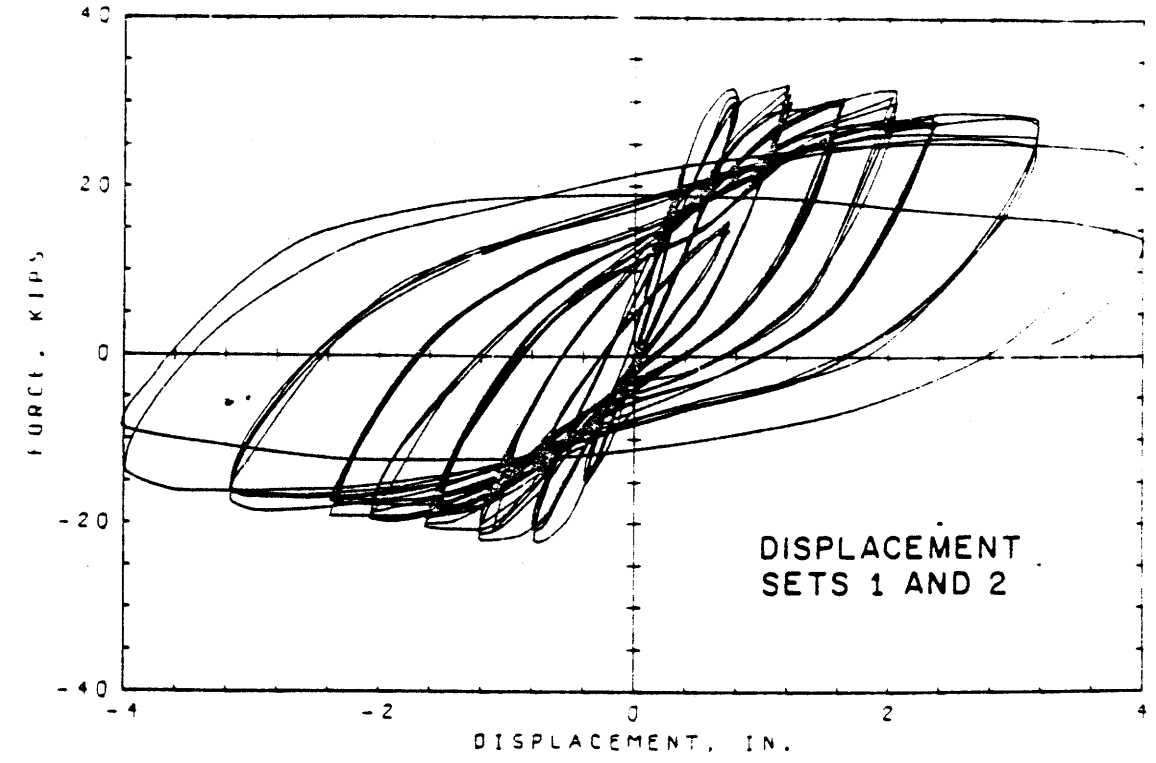

(a)

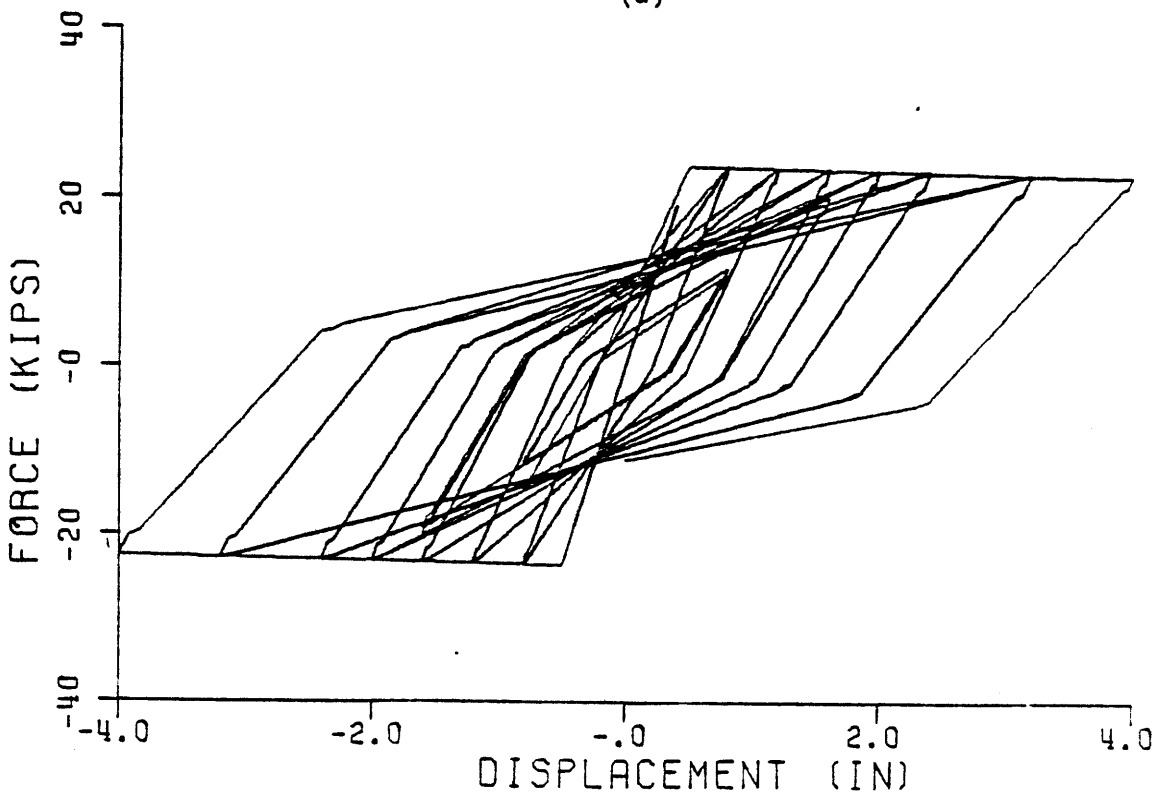

(b)

Fig. 3.2 - Experimental and Analytical Load-Deflection Curves for Specimen 4 in the Experiment by Atalay-Penzien

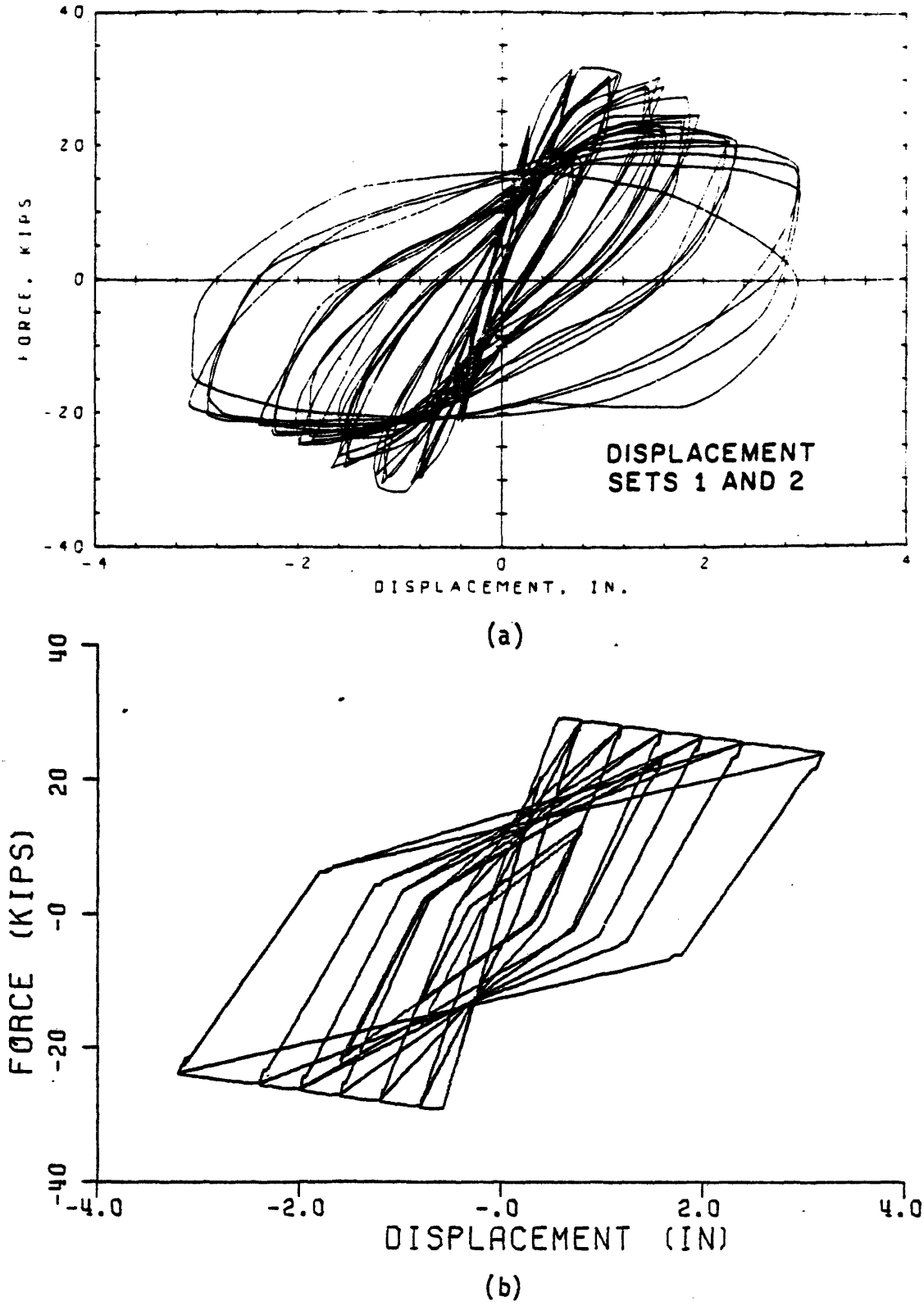

Fig. 3.3 - Experimental and Analytical Load-Deflection Curves for Specimen 7 in the Experiment by Atalay-Penzien

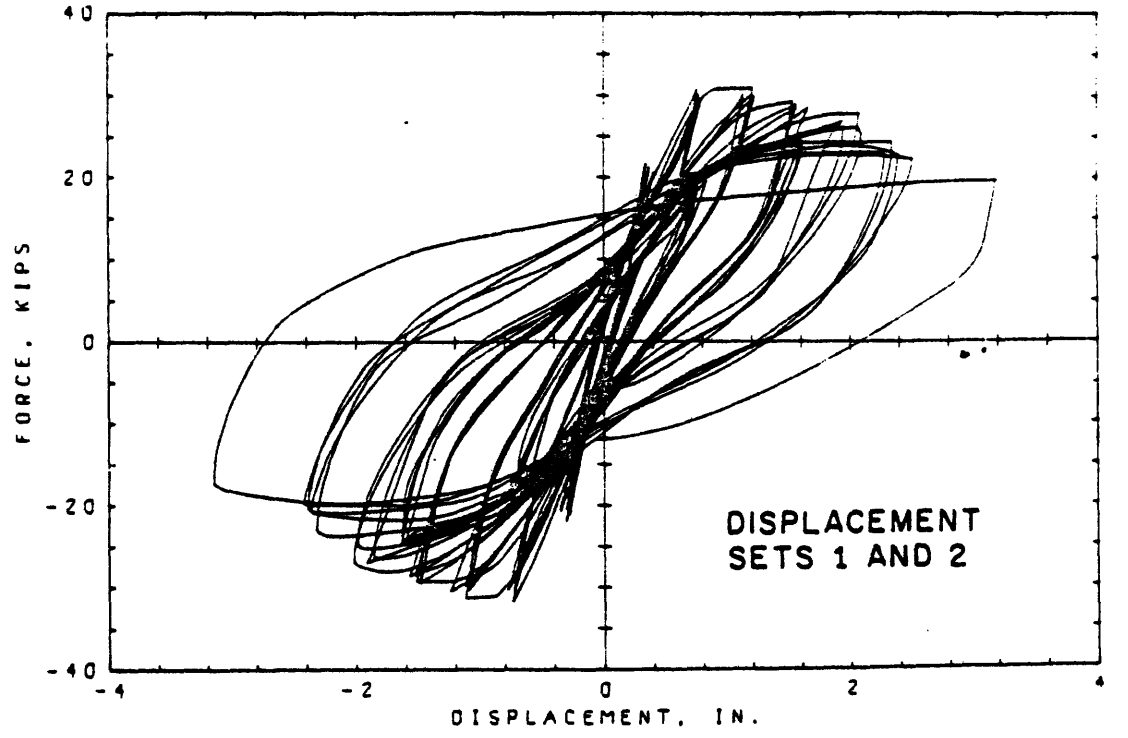

(a)

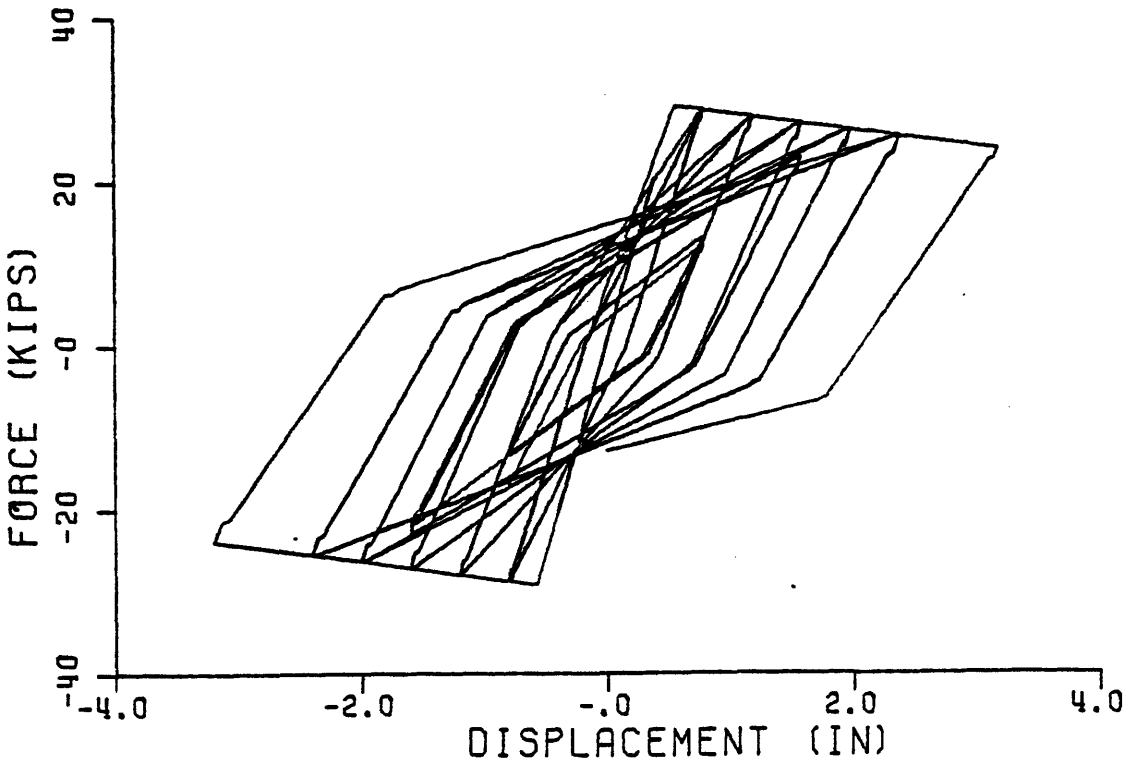

(b)

Fig. 3.4 - Experimental and Analytical Load-Deflection Curves for Specimen 8 in the Experiment by Atalay-Penzien

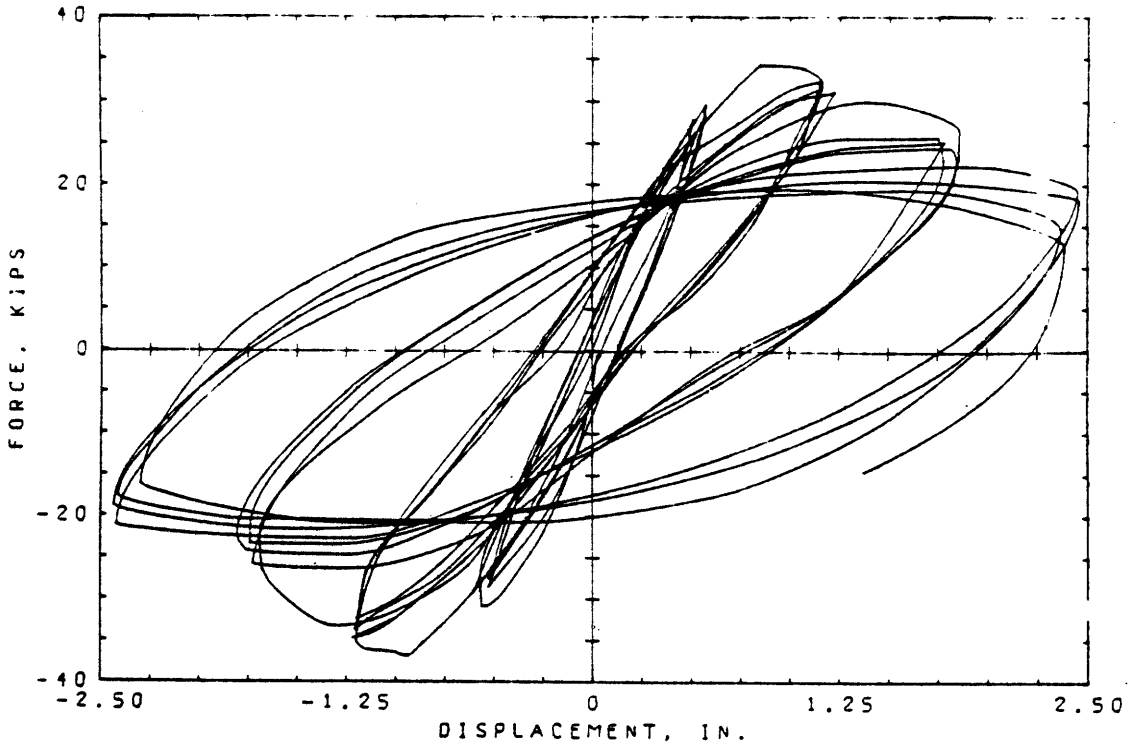

(a)

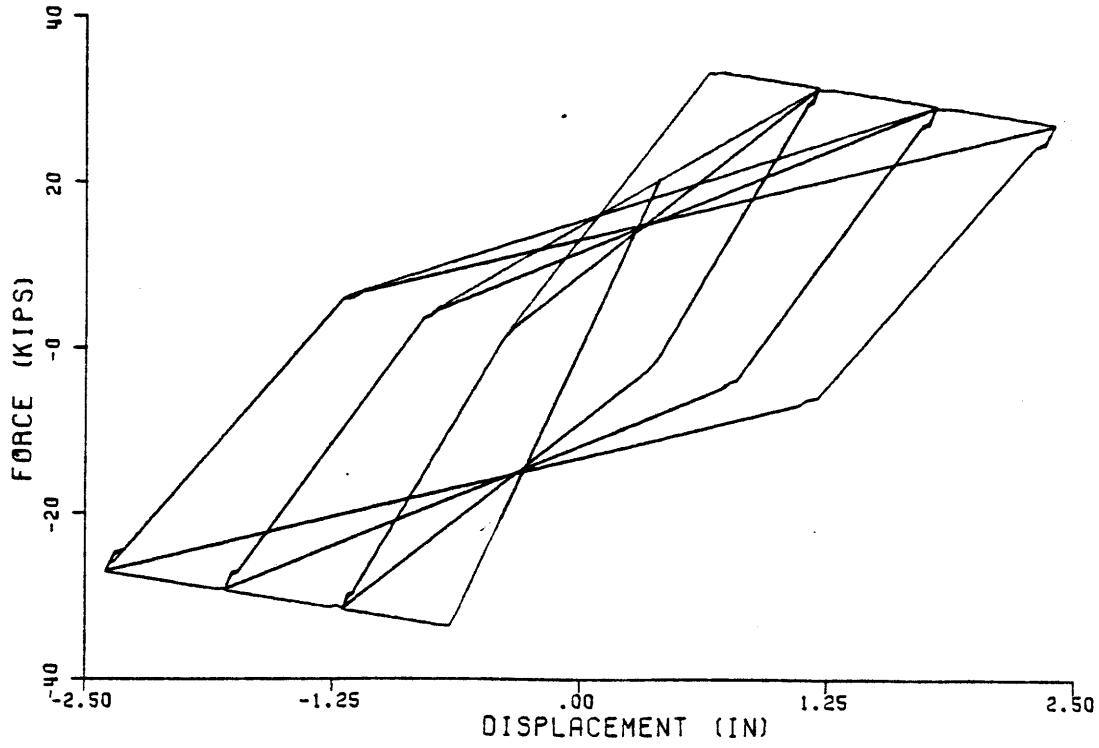

(b)

Fig. 3.5 - Experimental and Analytical Load-Deflection Curves for Specimen 11 in the Experiment by Atalay-Penzien

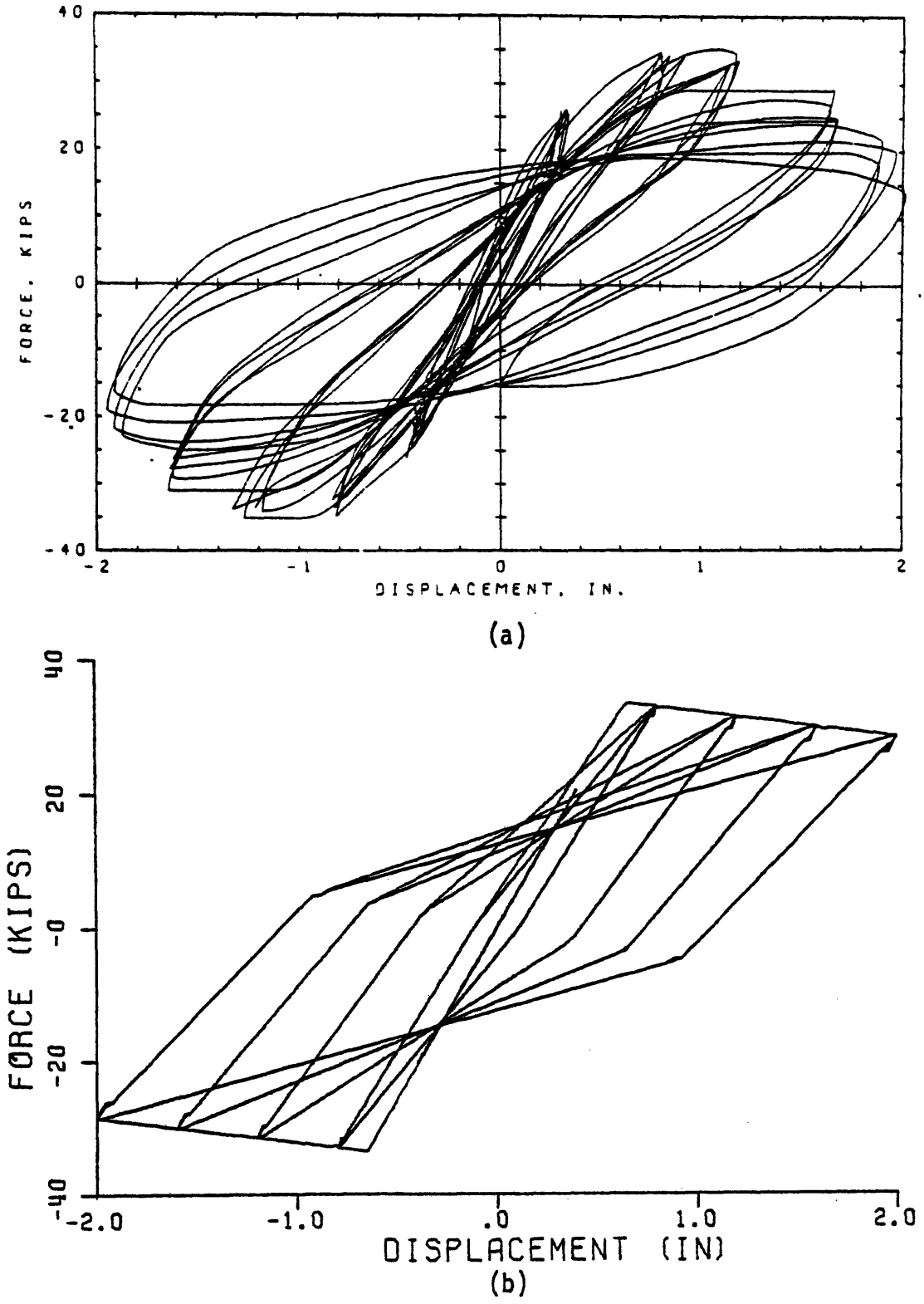

Fig. 3.6 - Experimental and Analytical Load-Deflection Curves for Specimen 12 in the Experiment by Atalay-Penzien

are laboratory test results and (b)-figures are analytical curves. These columns, in general, exhibited stable hysteretic behavior up to their failure points. The P-δ effect for these specimens is very pronounced. Computed damage parameters for these specimens are listed in Table 3.3 (specimens A4 - A12). The damage indicators are computed according to their definitions in Chapter II. The last two columns in the table are the ratio of peak shear stress (τ) over square root of concrete strength ($\sqrt{f'_c}$), and the ratio of axial load (P_a) over the balanced point axial load (P_b). An examination of damage indicators for these specimens shows that columns with higher axial loads dissipated less energy and also had lower values of flexural damage ratios at failure. Displacement ductilities, which are equal to rotation ductilities in this case, were measured to be 5.5, 3.4, 3.6, 2.9 and 2.1 for these five specimens. A comparison with ductilities in Table 3.3 shows that these are somewhat less than computed ductilities. Since the flexural deformation is by far the dominant mode of deformation, the match between ductilities was the best among all experiments in the sample. This is due to the fact that elastic flexural stiffness of a member may be calculated accurately.

b) Bertero-Popov-Wang

These experiments explored the means of minimizing damage in reinforced concrete beams under very high shear forces (7). Two cantilever beams, each 78 inches long, were built for this purpose (Fig. 3.7). Specimen 33 was reinforced with six #9 bars at top and bottom, and two #4 bars were put in the middle of the section along with cross ties to prevent bulging. Shear reinforcement in this specimen consisted of #3 bars

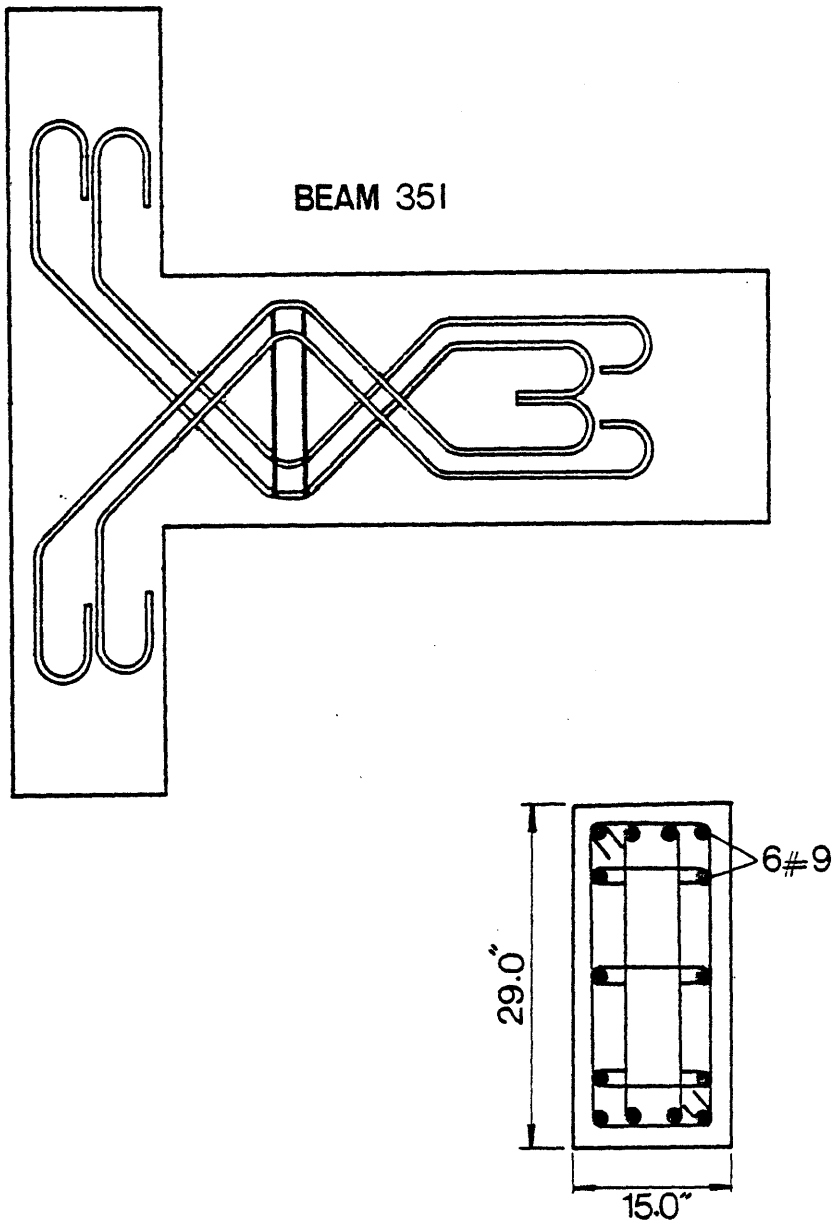

Fig. 3.7 - Test Set-up and Section Properties for the Experiment by Bertero-Popov-Wang

at an interval of 3 inches. Specimen 35I was designed to resist ultimate shear by means of eight #6 inclined bars (Fig. 3.7). The scheme provided maximum efficiency for transfer of shear forces across inclined cracks (48). Inclined bars were assembled together using short bars which were welded to them. The result was a well confined concrete, and also buckling of steel bars was prevented. Longitudinal steel for both specimens was welded to a steel plate at the reaction frame, thus preventing any fixed end rotation due to slippage.

Loading was controlled by magnitude of peak ductility such that larger cycles would have an increase of 1 in displacement ductility. Because of special design of specimen 35I, no shear deformation was considered in its analysis. Strength degradation was neglected in analysis of specimen 33. Experimental and analytical curves for the two specimens (Figs. 3.8 and 3.9) are in good agreement. Specimen 33 shows pinching of hysteresis loops due to shear deformations. Experimental yield moments are roughly ten percent higher than analytical yield moments. Experimental ductilities for specimens 33 and 35I were 5 and 6 respectively, which are much lower than computed values (12.9 for specimen W33 and 16.8 for specimen W35I in Table 3.3). This is a direct result of an overestimate in elastic member stiffnesses which is observed in most experiments. Total energy dissipated in experiments was 6470 k-in (E_n = 377) for specimen 33, and 9510 k-in (E_n = 555) for specimen 35I. Since theoretical failure points were reached before the end of tests, these may be viewed as upper bounds on normalized energy values listed in Table 3.3 (269, 457). A very fast progressive failure was observed in both specimens. Specimen 35I has the highest normalized dissipated energy in the sample.

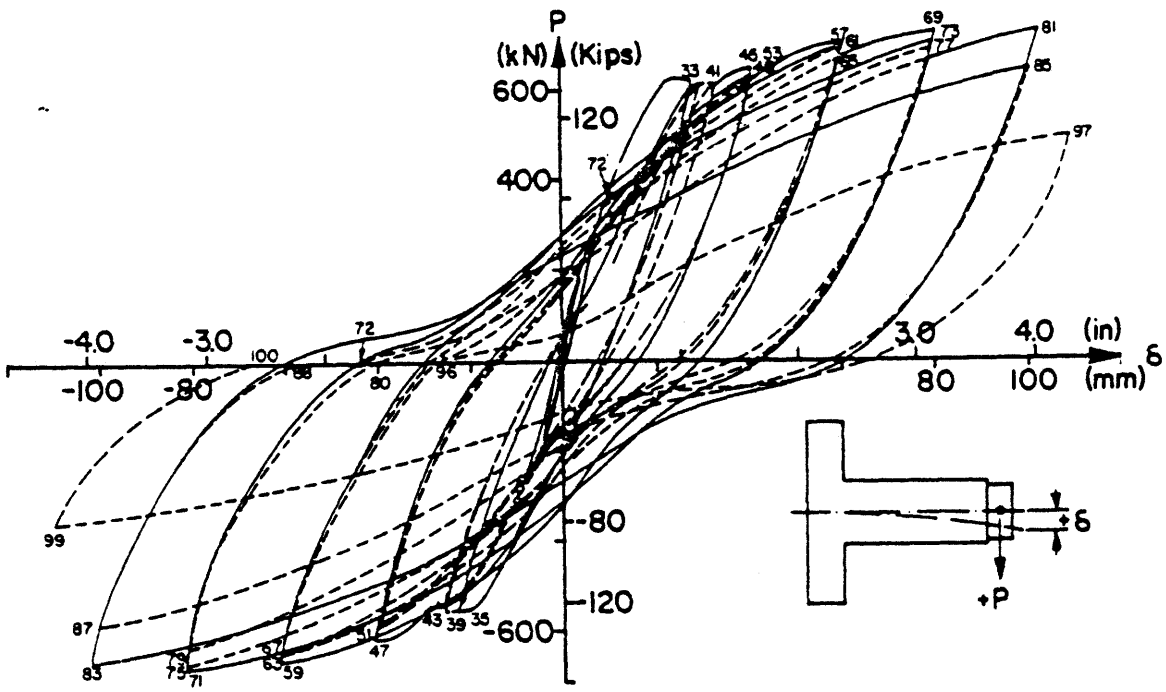

(a)

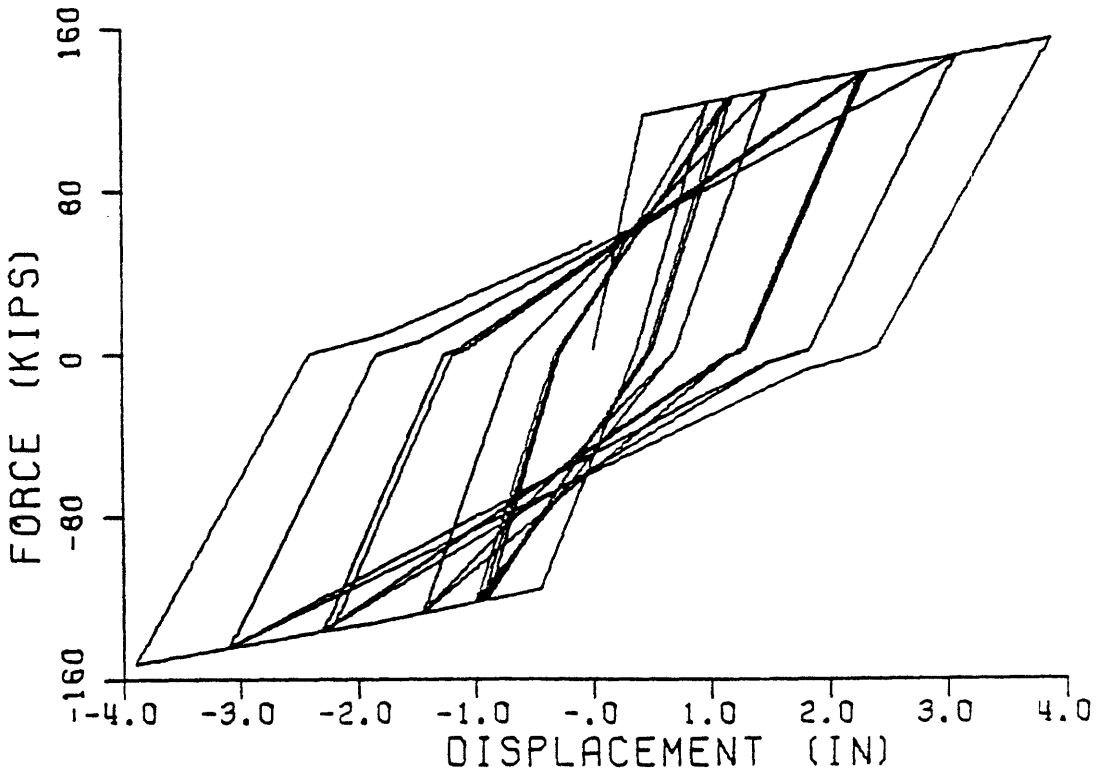

(b)

Fig. 3.8 - Experimental and Analytical Load-Deflection Curves for Specimen 33 in the Experiment by Bertero-Popov-Wang

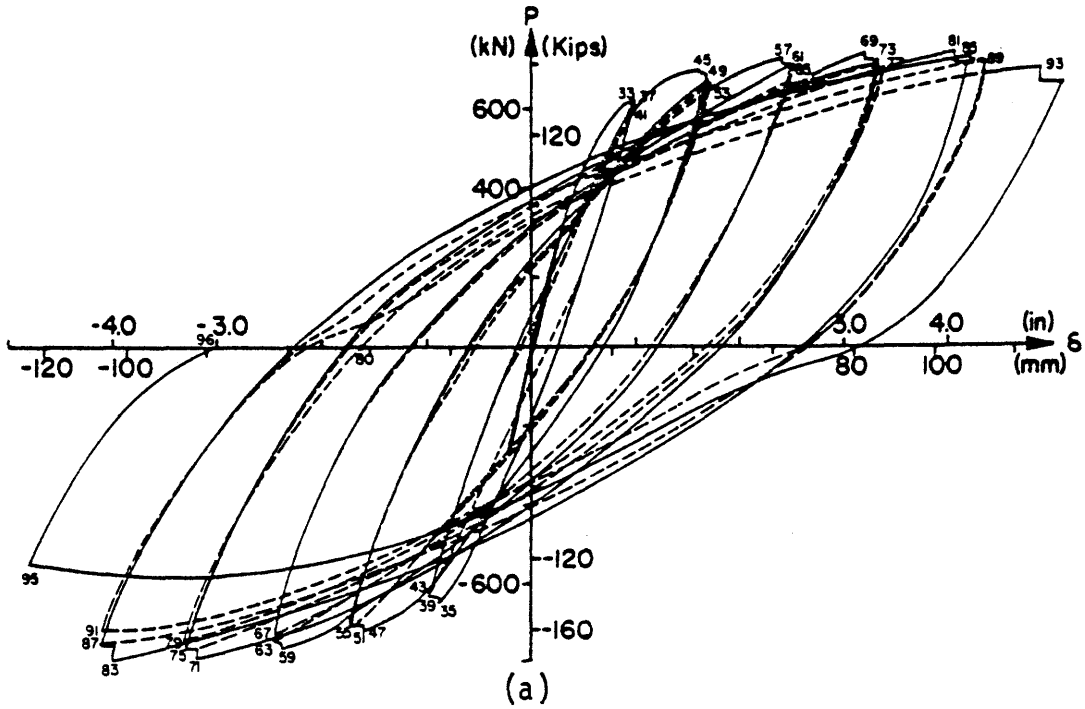

(a)

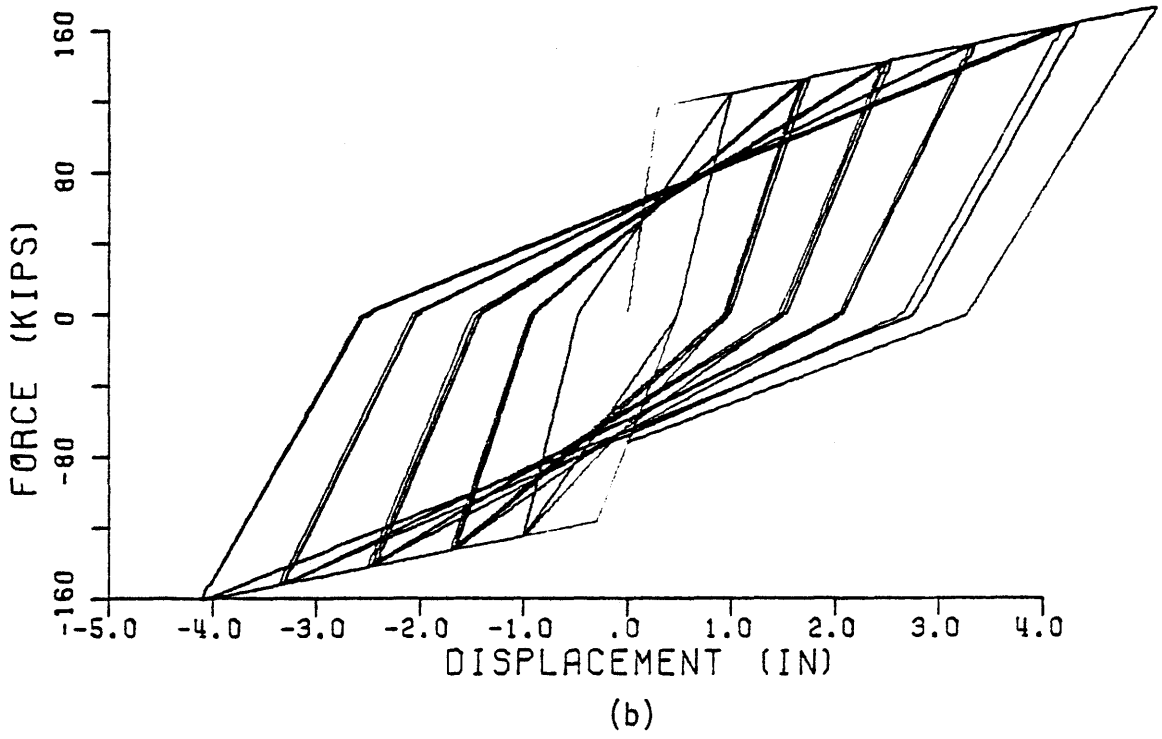

(b)

Fig. 3.9 - Experimental and Analytical Load-Deflection Curves for Specimen 35I in the Experiment by Bertero-Popov-Wang

c) Fenwick-Irvine

These tests, carried out at the University of Auckland, New Zealand, were designed to investigate the adequacy of existing codes for joint design (19). Four beam-column joint specimens were built and tested under simulated earthquake loads (Fig. 3.10). A useful discussion of mechanisms of shear resistance in a joint appears in the paper. In this study, only two of the specimens were considered. Unit 1 was designed according to ACI code and Committee 352 recommendations, and unit 4 was designed to control yielding of steel in joint zones and to prevent slippage of bars. Bond plates were welded to longitudinal steel reinforcement of unit 4, being designed to transmit all forces into the joint. To prevent yielding of longitudinal bars in between the two bond plates, additional bars were fillet-welded onto the reinforcement in between plates. SI units were used for the original report, and analytical results are also presented in the same units. Cross sections of beams and columns for the two units is shown in Fig. 3.10. Deformed steel bars of 20-mm diameter (D20) and 24-mm diameter (D24) were used as main longitudinal reinforcement. Additional D16 bars were also placed in columns. Concrete strengths for units 1 and 4 were 42.9 MPa (6200 ksi) and 40.4 MPa (5860 psi), respectively.

Experiment was displacement controlled, and loads of equal magnitude were applied at a distance of 1.425 m from the joint centerline in opposite directions (Fig. 3.10). Displacements of beams were measured at a distance of 1.25 m from the joint centerline. Two cycles of displacement ductilities of 2, 4, 6, 8, etc. were applied on beams until member failure was reached. Experimental and analytical load-deflection curves are

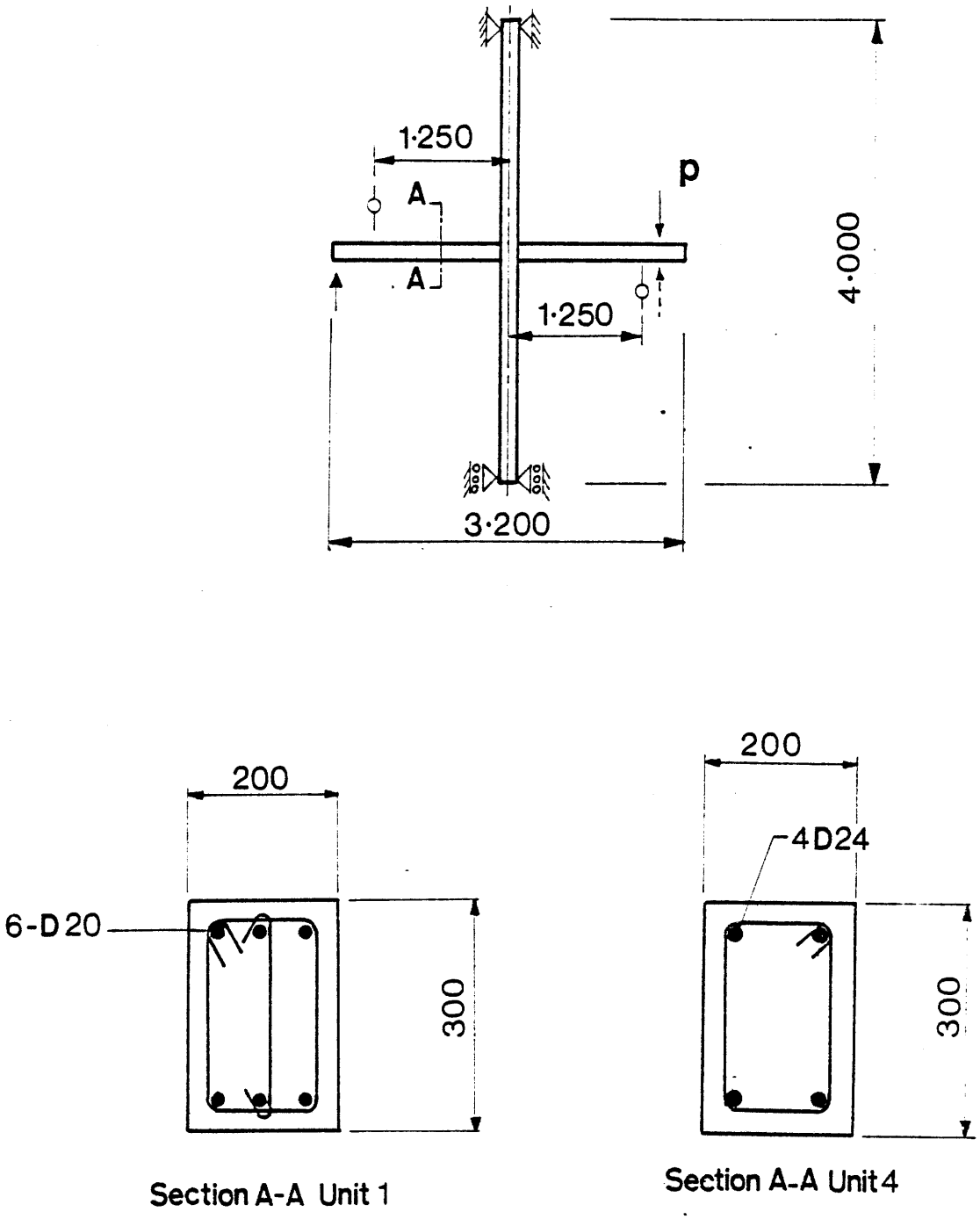

Fig. 3.10 - Test Set-up and Section Properties for the Experiment by Fenwick-Irvine

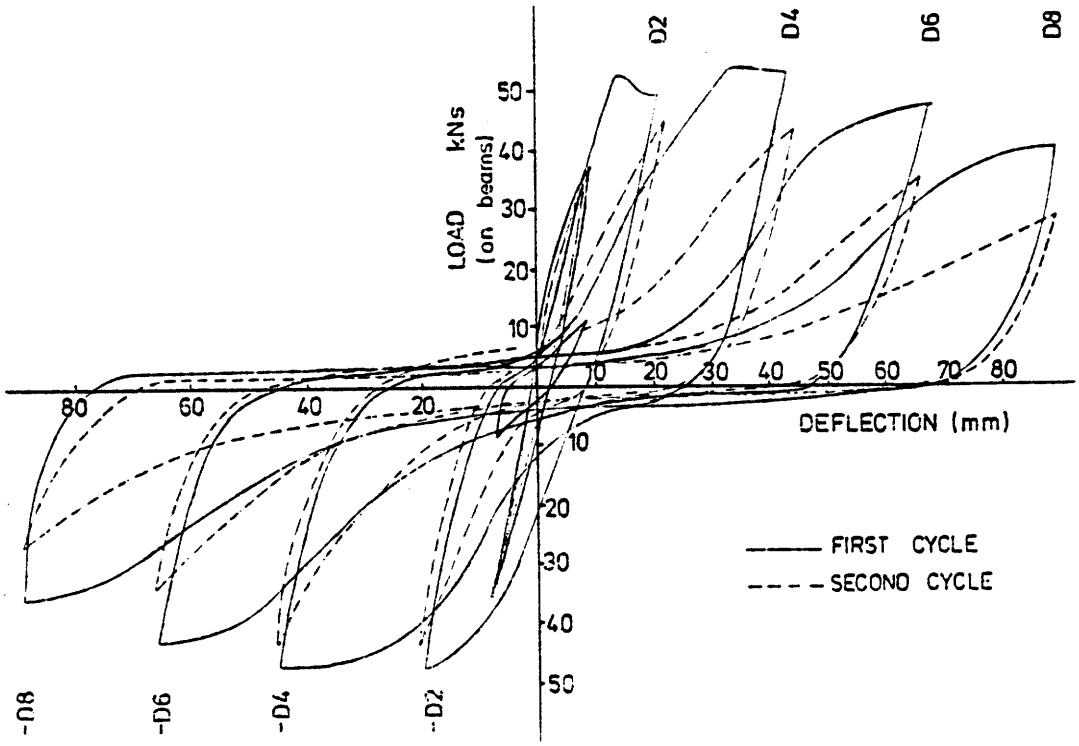

(a)

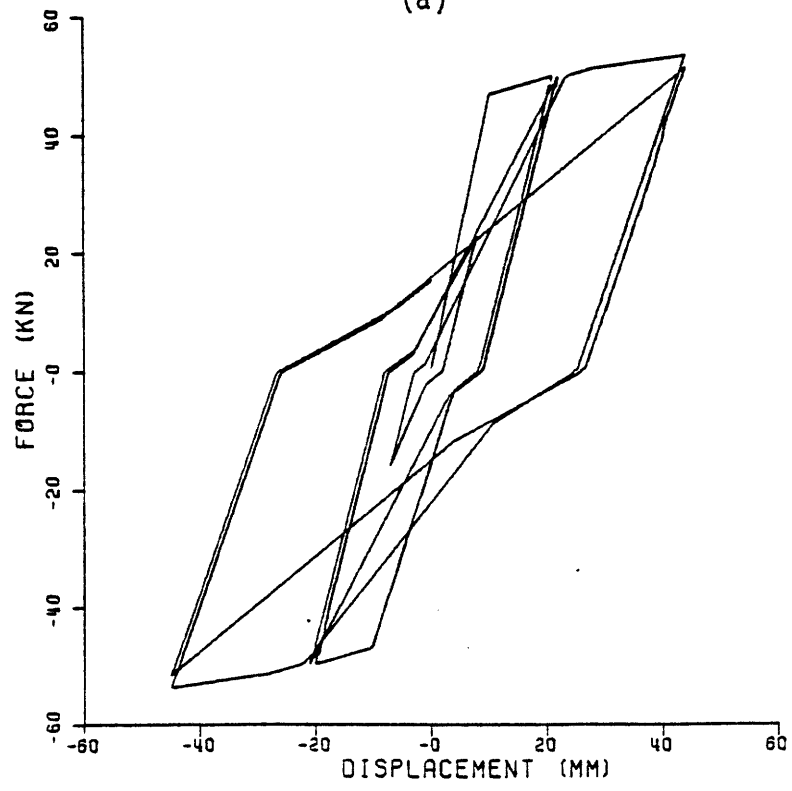

(b)

Fig. 3.11 - Experimental and Analytical Load-Deflection Curves for Unit 1 in the Experiment by Fenwick-Irvine

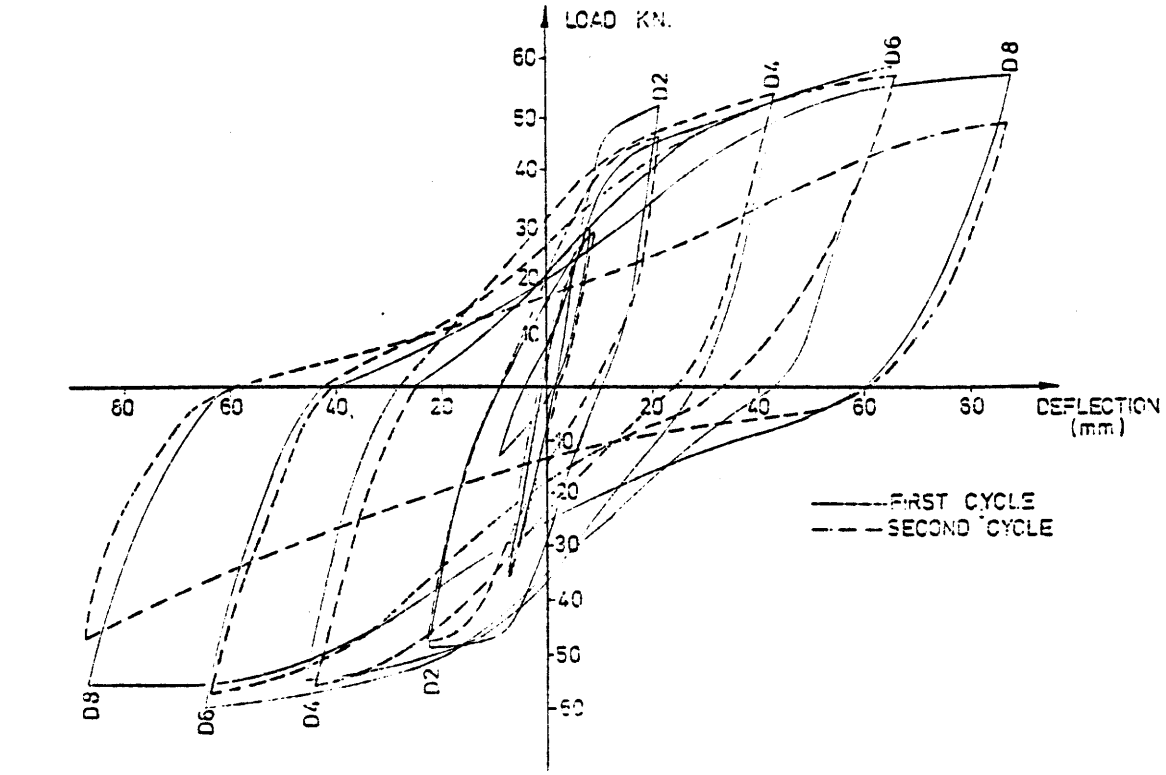

(a)

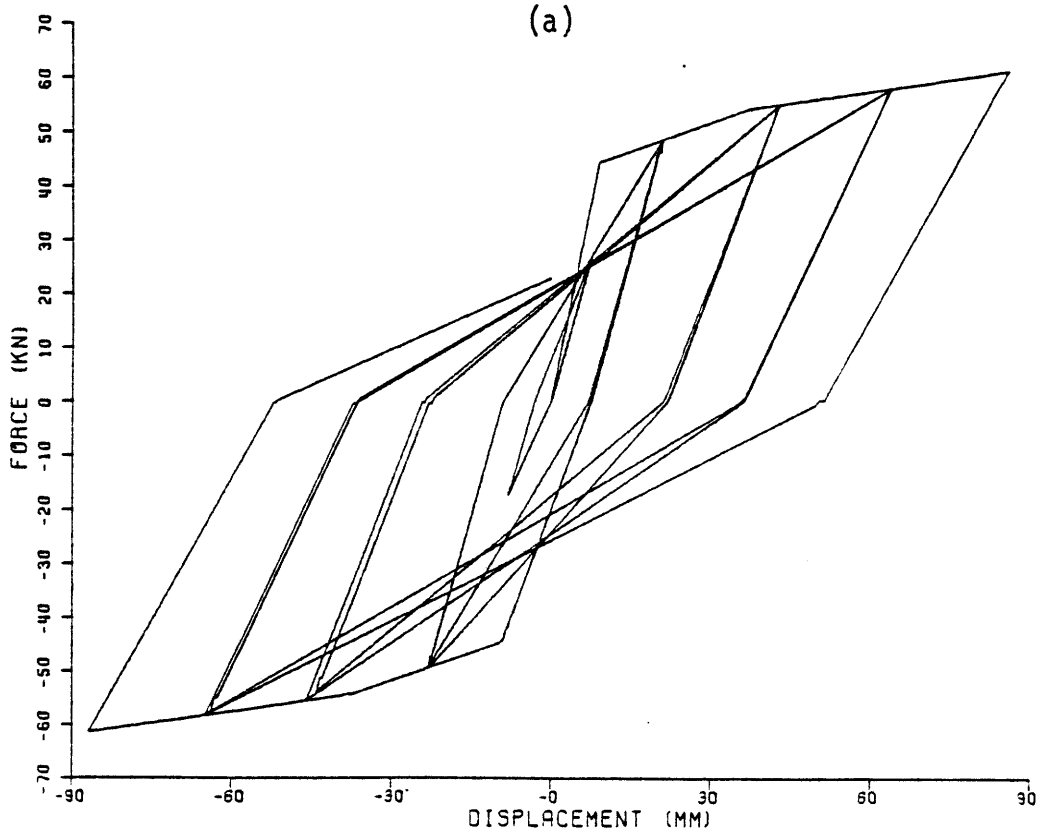

(b)

Fig. 3.12 - Experimental and Analytical Load-Deflection Curves for Unit 4 in the Experiment by Fenwick-Irvine

shown in Figs.3.11 and 3.12. The joint in unit 1 suffered more severe damage, and this is clearly seen from its strength degradation. On the other hand, hysteresis loops for unit 4 are very stable, and the specimen did not fail until a displacement ductility of 8 was reached. Although columns were designed to stay elastic, analysis indicated some yielding in columns of unit 4. Measurements in the experiment also revealed some yielding in unit 4 columns, which finally led to joint deterioration and specimen failure. Peak loads were listed for each cycle and compared well with analysis. Failure of unit 1 is very gradual, and the theoretical failure point was reached long before the experimental failure point. On the contrary, unit 4 had very fast progressive failure after a displacement ductility of 8. The overall match between experimental and analytical results is fair for unit 1 and very good for unit 4. Computed values of damage indicators for these two specimens are listed in Table 3.3 (specimens F1, F4).

d) Hanson-Conner

This is one of the early series of tests on full size reinforced concrete specimens carried out by Portland Cement Association (23). The main purpose of the experiment was to study the adequacy of joint reinforcement designs for cyclic loads. Three types of joints were chosen for testing, namely, a corner joint, an edge joint, and an interior joint. The two interior joints were not included in the sample, because one developed serious joint cracking and the other one was not loaded to failure. Test setup and section properties for the corner joint (specimen no. 7) and the interior joint (specimen no. 9) appear in Fig. 3.13. Grade 40 reinforce-

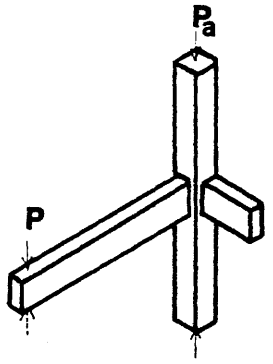

EDGE BEAM
SPECIMEN 7

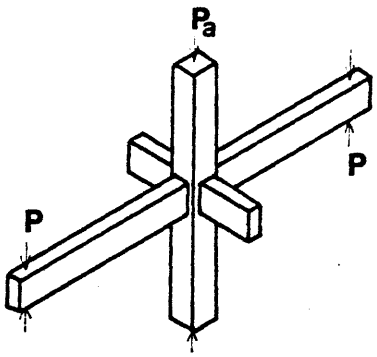

INTERIOR BEAM
SPECIMEN 9

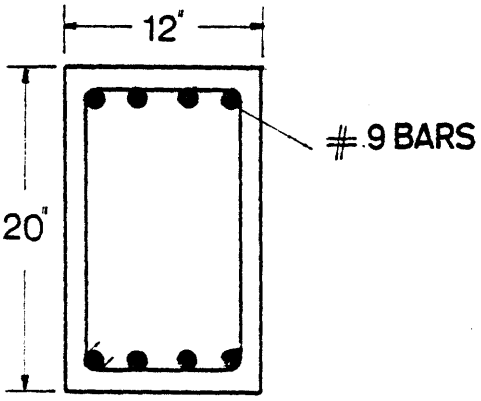

Beam Section

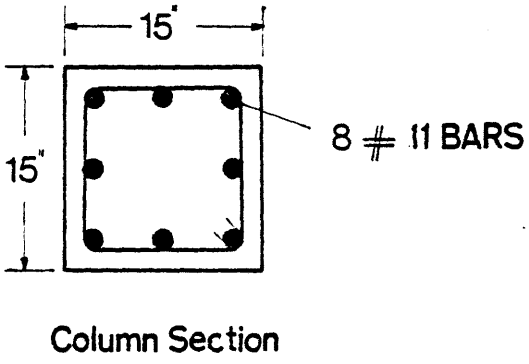

Column Section

Fig. 3.13 - Test Set-up and Section Properties for the Experiment by Hanson-Conner

ment was used for all specimens. Concrete in beams and columns had different properties, and f'_c ranged from 3800 psi to 6000 psi.

After putting a load of 640 kips on columns, beams were subjected to cyclic deflections. Because of high value of span length to depth ratio, shear deformations were found to be negligible for all members. Slippage of longitudinal reinforcement was considered in the analysis of these specimens. Deflections of the beams were intended to produce displacement ductility levels of 2.5 to 5.0. Computed beam ductility demands are 6.5 and 10.5 for specimens 7 and 9 respectively (H7 and H9 in Table 3.3). Although specimen no. 7 showed some yielding in the negative loading direction, the analysis did not indicate any yielding in that direction (Figs. 3.14 and 3.15). Comparison of energy dissipation and damage ratio for these two specimens with the rest of the sample (Table 3.3) reveals that these specimens behaved poorly. The main reason is that the overall design of these two specimens was less than satisfactory.

e) Ma-Bertero-Popov

This set of experiments was conducted at the University of California, Berkeley (38). A total of nine members were tested to study behavior of reinforced concrete members near the column face. The model (Fig. 3.16) represents, in half scale, lower story girders of a 20-story ductile moment-resisting reinforced concrete frame. All specimens were cantilever beams supported by a large block. Six rectangular sections (R1-R6) and three T-sections (T_1-T_3) were tested. Cross-sectional characteristics of these specimens are sketched in Fig. 3.16. Three pairs of beams (R1

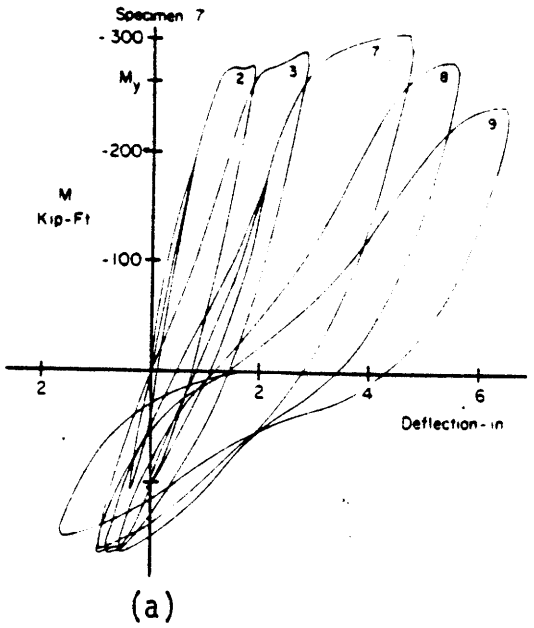

(a)

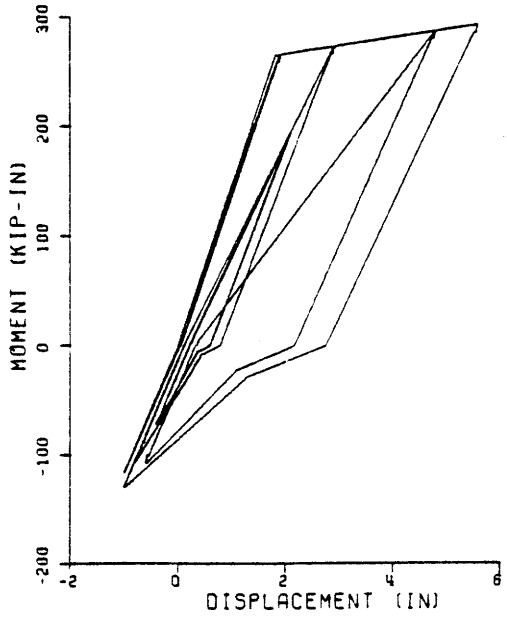

(b)

Fig. 3.14 - Experimental and Analytical Load-Deflection Curves for Specimen 7 in the Experiment by Hanson-Conner

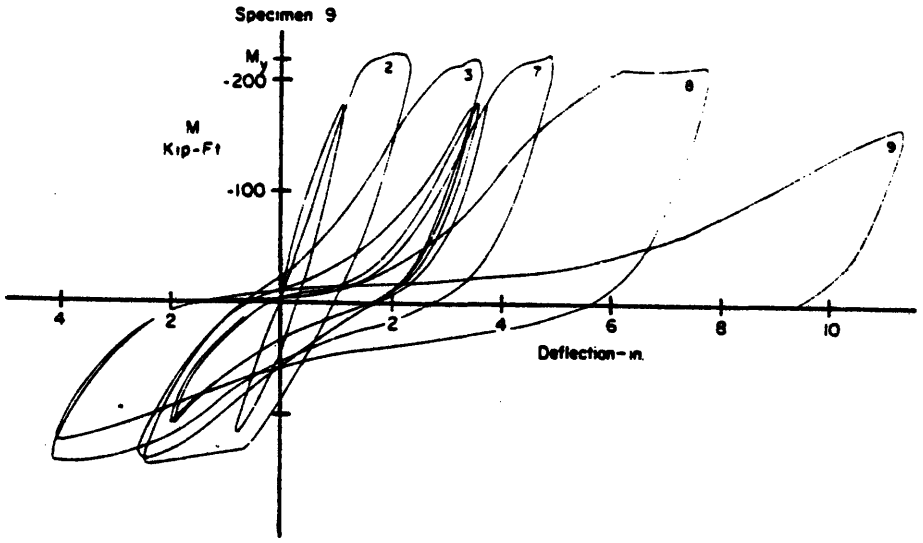

(a)

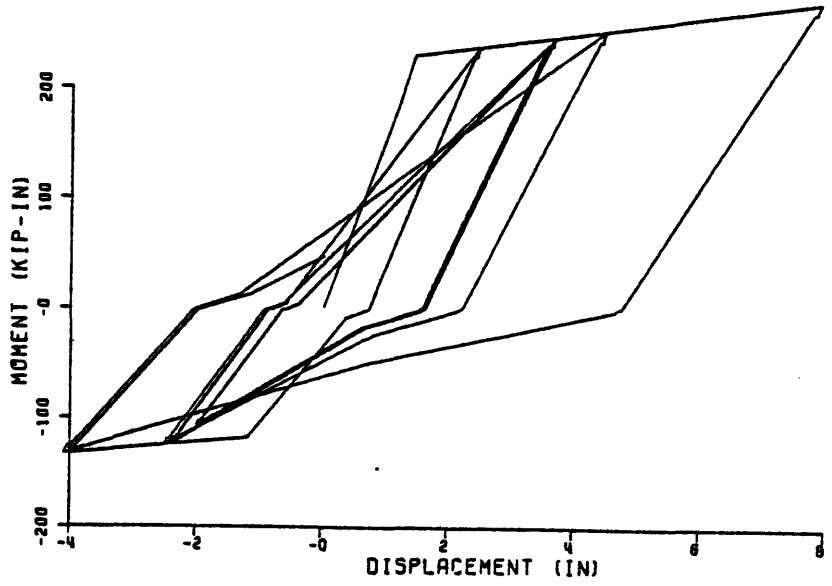

(b)

Fig. 3.15 - Experimental and Analytical Load-Deflection Curves for Specimen 9 in the Experiment by Hanson-Conner

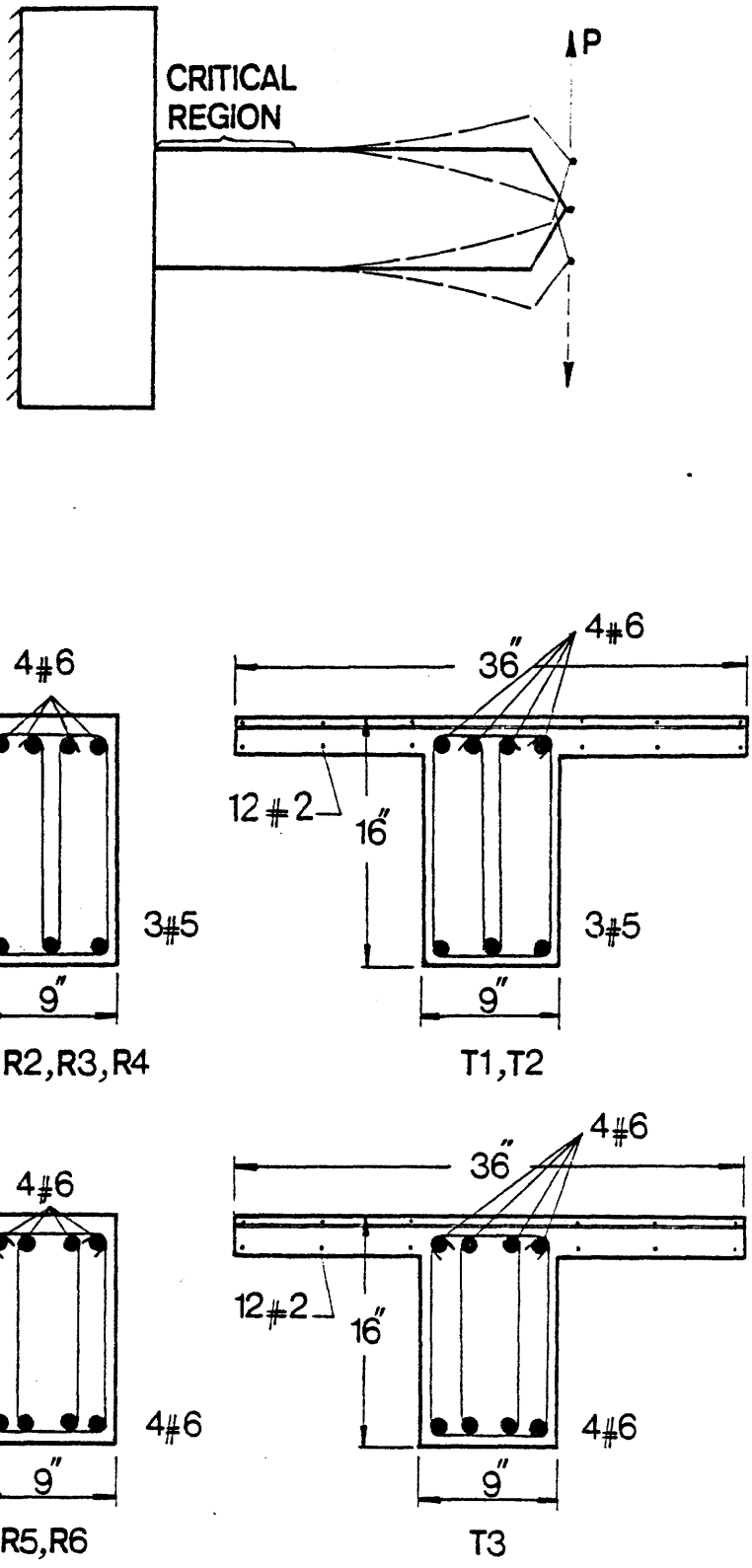

Fig. 3.16 - Test Set-up and Section Properties for the Experiment by Ma-Bertero-Popov

and R2, R3 and R4, T1 and T2) were made identical to study the effect of different loading conditions on inelastic behavior of specimens. All of the specimens have four #6 bars at the top and four #6 bars or three #5 bars (All G60) at the bottom. Thus some of the sections had roughly 50 percent of their negative moment capacity in positive direction. Shear reinforcement consisted of #2 ties at 3 1/2 inches, and in T-sections #2 deformed bars were also used in the top flange, representing the contribution of floor slab to moment capacity of the section. All specimens had a span length of 62.5 inches, except for specimen R5, which had a length of 38.5 inches. Concrete strength (f'_c) for beams ranged from 4190 psi to 5070 psi. Material properties were found by testing both steel and concrete.

Shear deformations only were considered for specimen R5. The Non-Symmetric Single Component Model (Section 2.3c) was used to model flexural deformations of specimens which had different amounts of steel at top and bottom. It may be noted that in this case the point of contraflexure is fixed, and this model becomes the same as Otani's model (42), i.e., the inconsistency between assumed location of point of contraflexure and its actual location may be eliminated by adjusting the hinge characteristics. Slippage of reinforcement was not included, because it was felt that concrete block behind the cantilever and well-anchored longitudinal steel would result in negligible slippage.

Experimental and analytical load-deflection curves appear in Figs. 3.17 through 3.25. Except for specimens R4 and T2, all of the other beams were subjected to increasing displacement ductilities. Failure of all members was a rather quick event, i.e., all members showed progressive

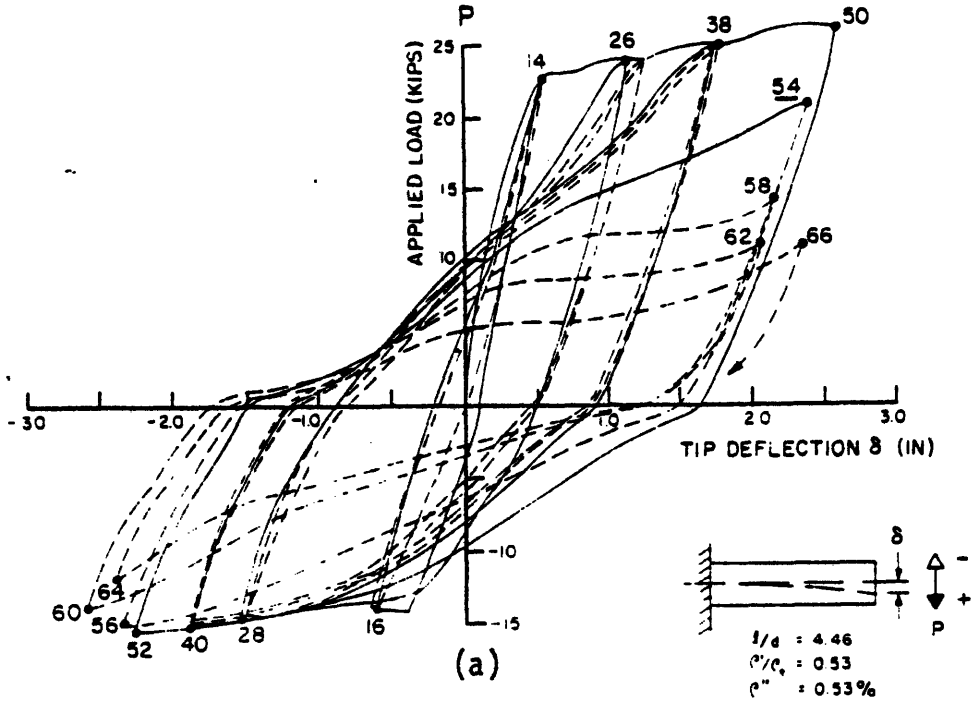

(a)

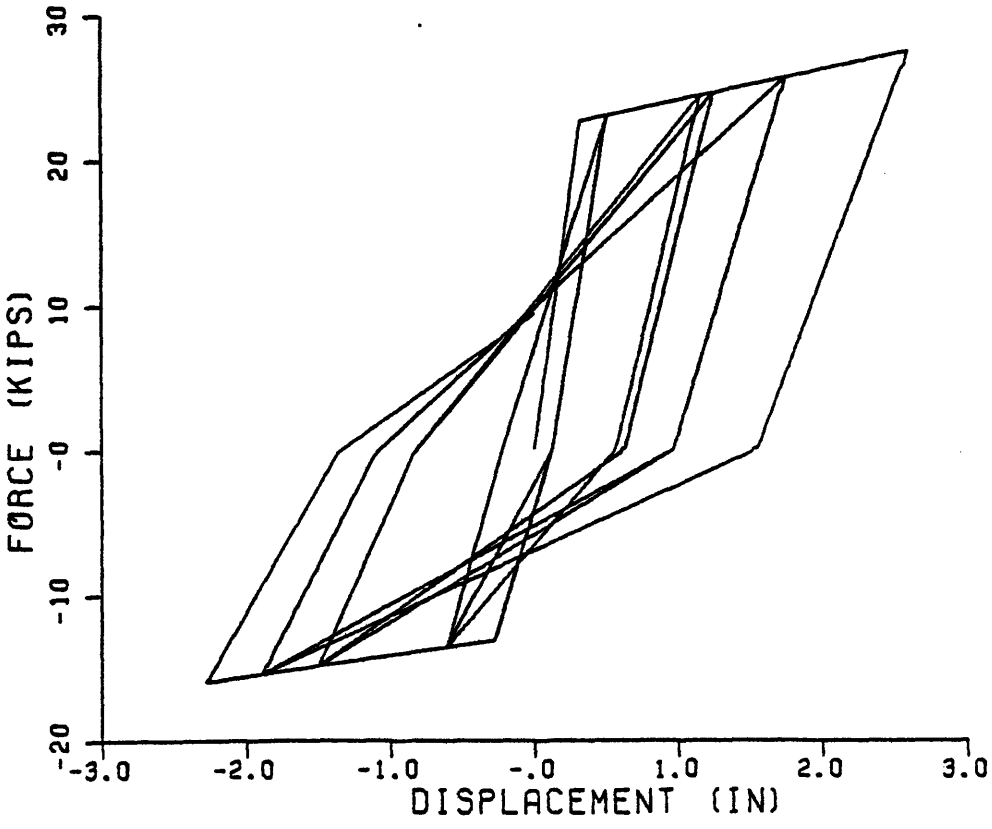

(b)

Fig. 3.17 - Experimental and Analytical Load-Deflection Curves for Specimen R1 in the Experiment by Ma-Bertero-Popov

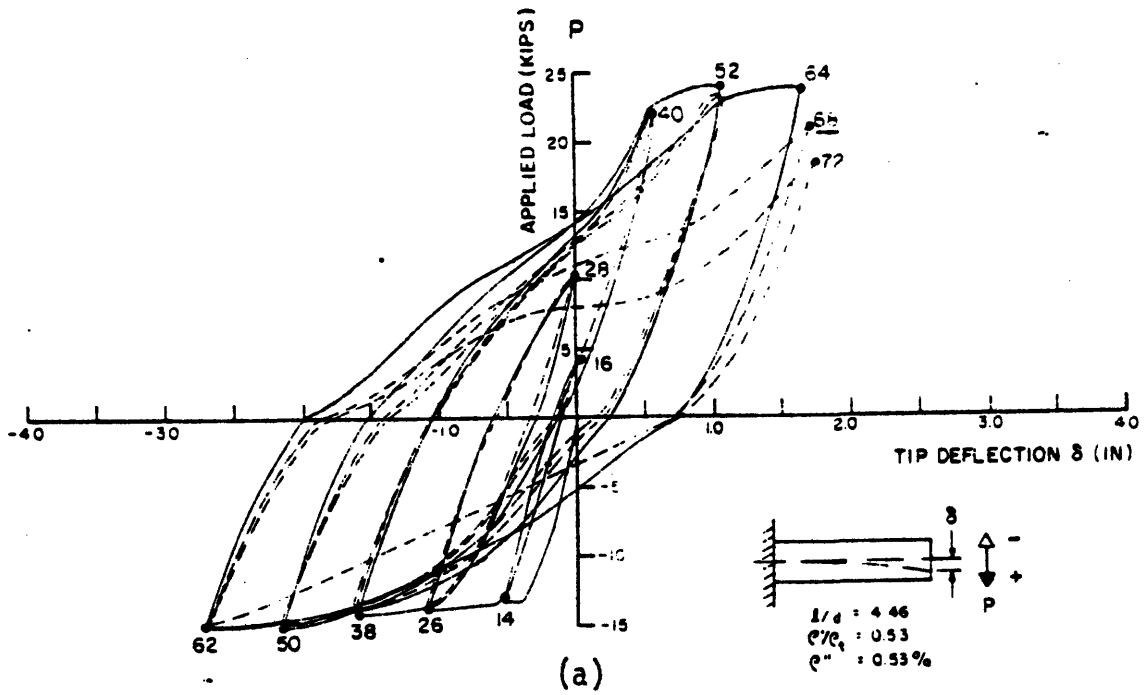

(a)

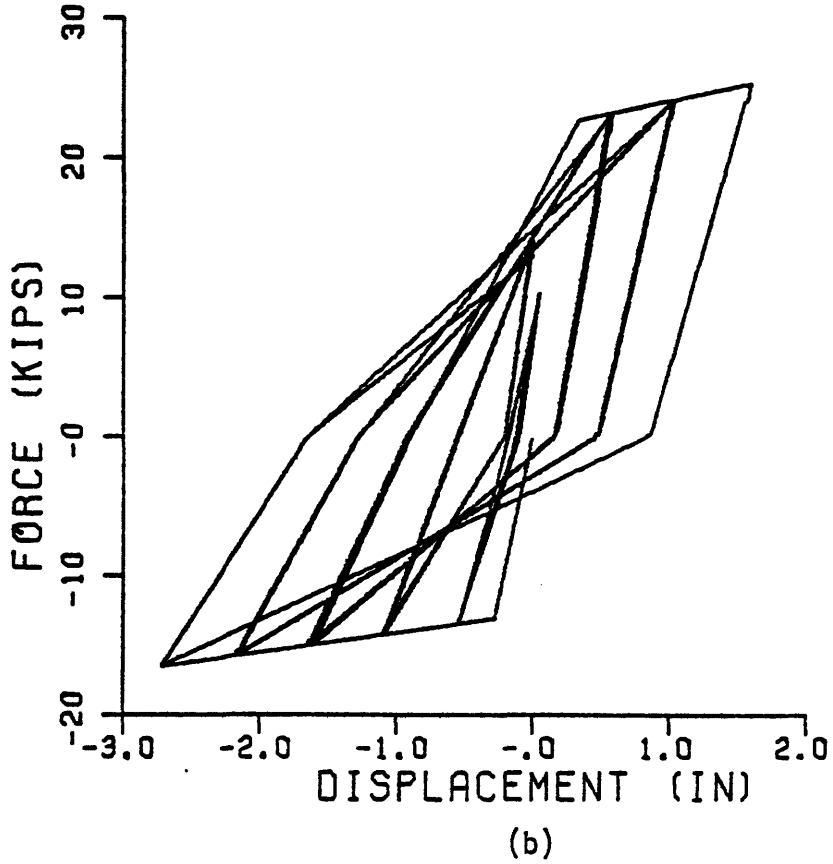

(b)

Fig. 3.18 - Experimental and Analytical Load-Deflection Curves for Specimen R2 in the Experiment by Ma-Bertero-Popov

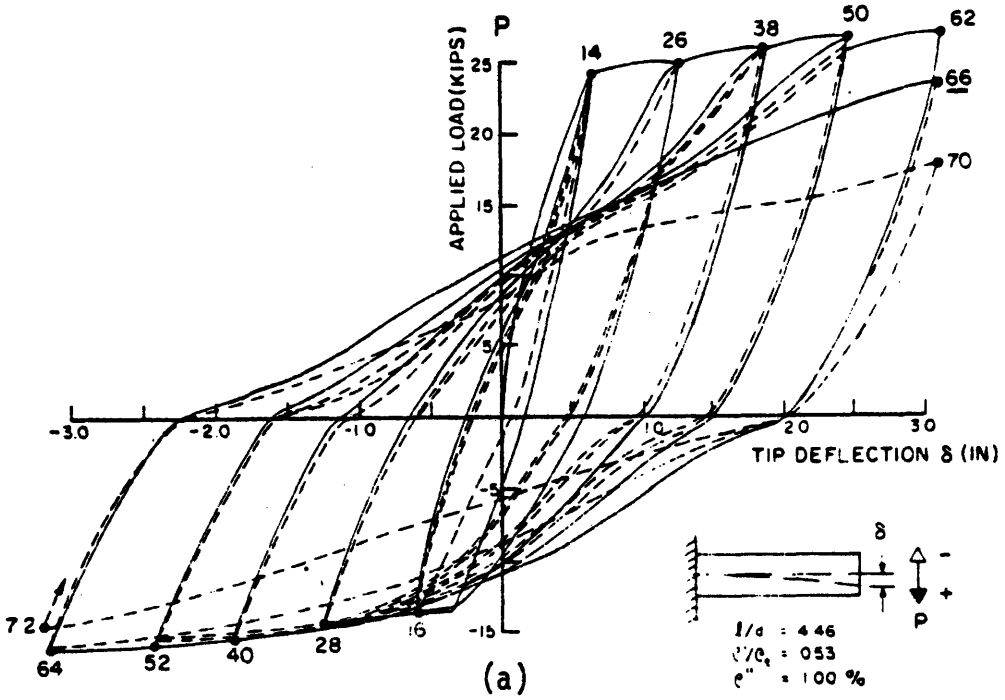

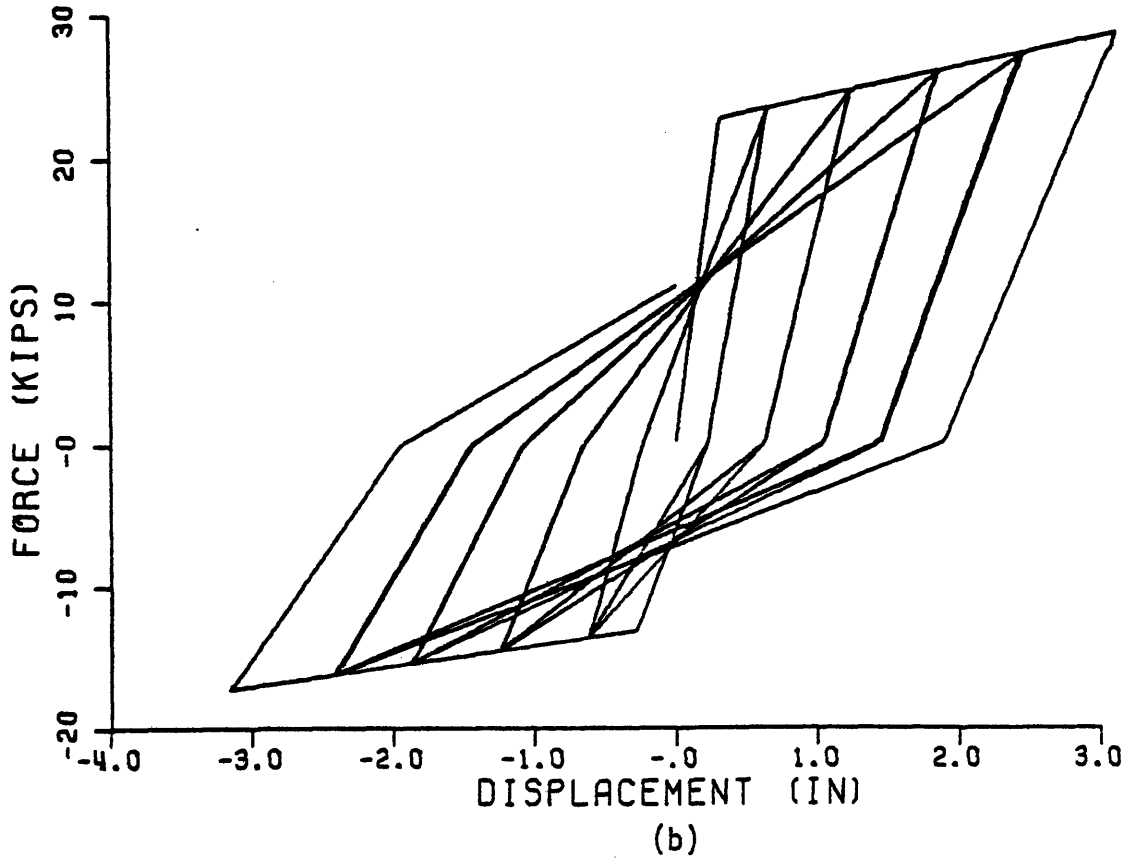

Fig. 3.19 - Experimental and Analytical Load-Deflection Curves for Specimen R3 in the Experiment by Ma-Bertero-Popov

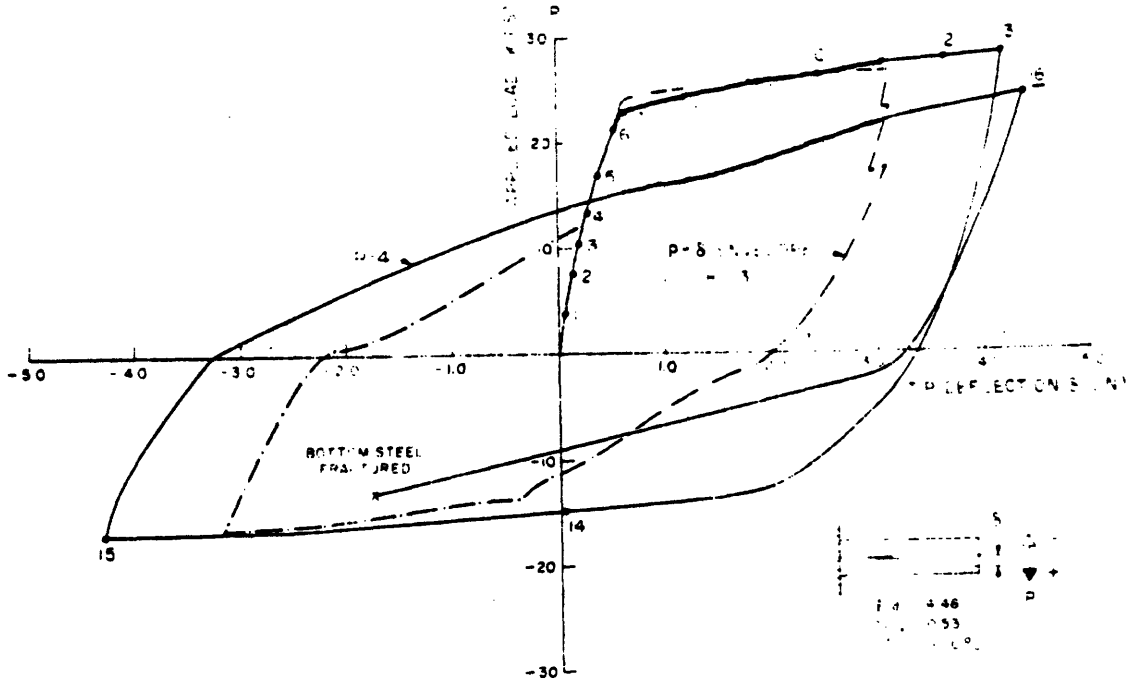

(a)

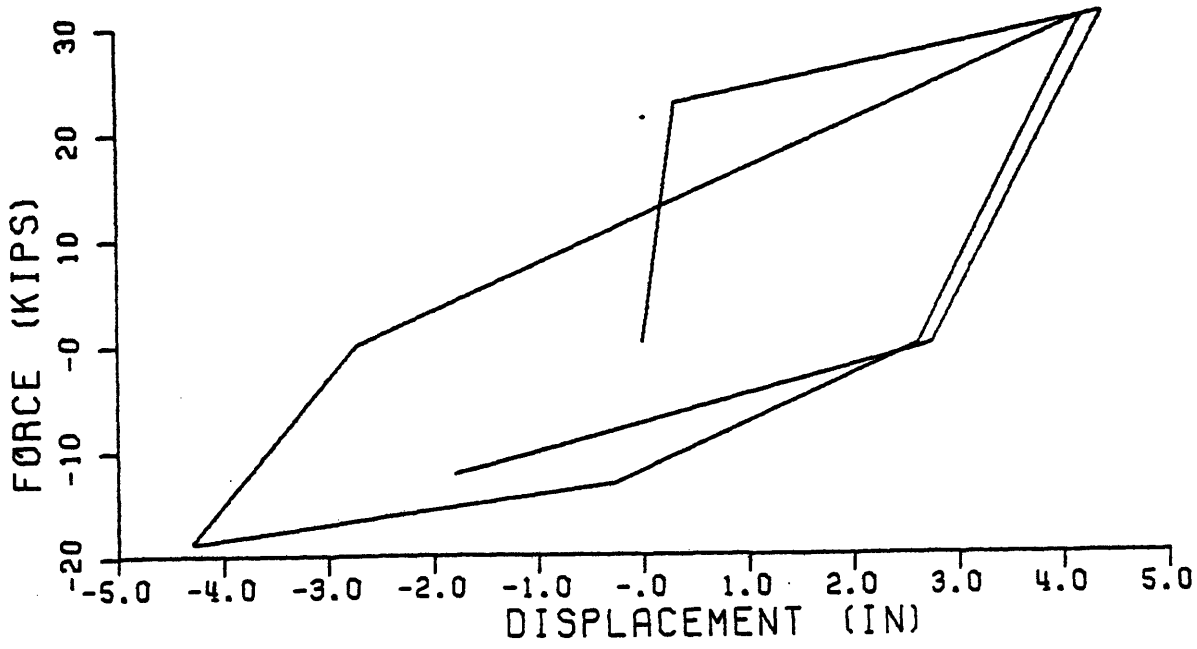

(b)

Fig. 3.20 - Experimental and Analytical Load-Deflection Curves for Specimen R4 in the Experiment by Ma-Bertero-Popov

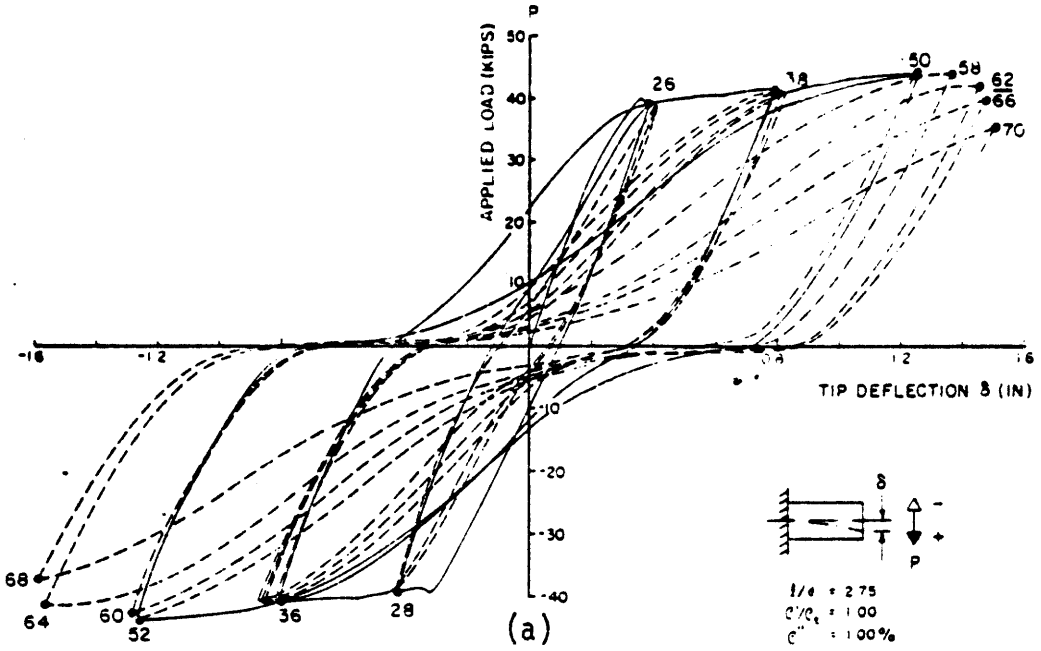

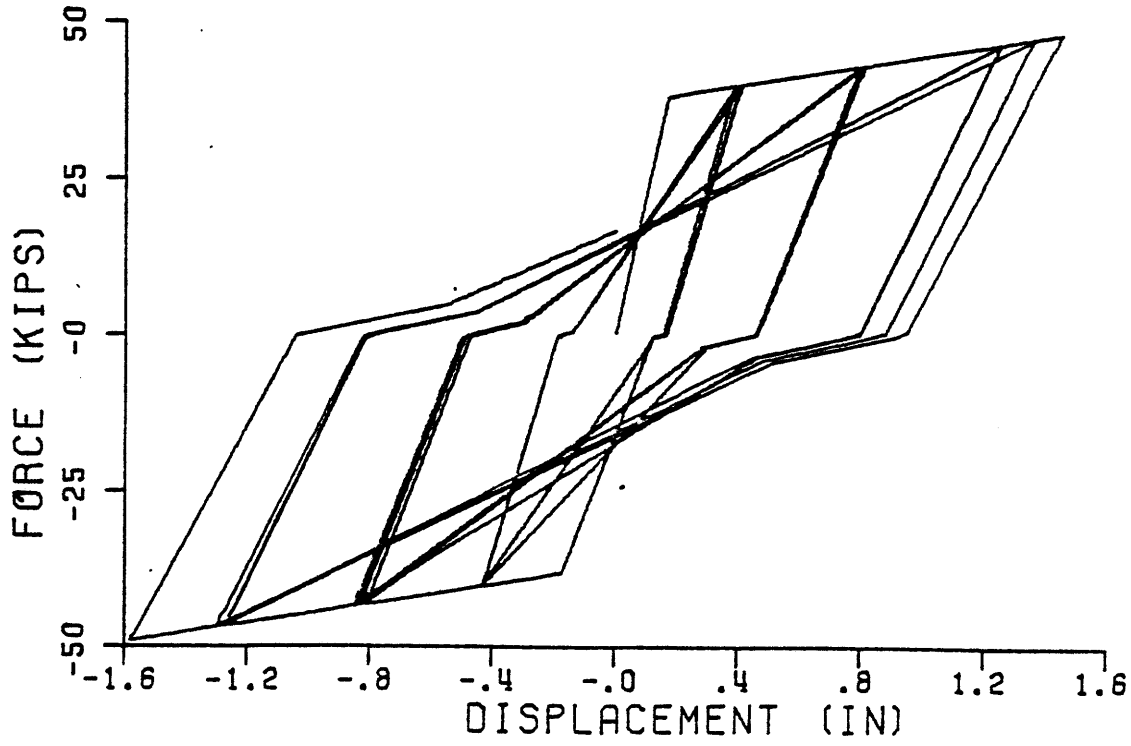

Fig. 3.21 - Experimental and Analytical Load-Deflection Curves for Specimen R5 in the Experiment by Ma-Bertero-Popov

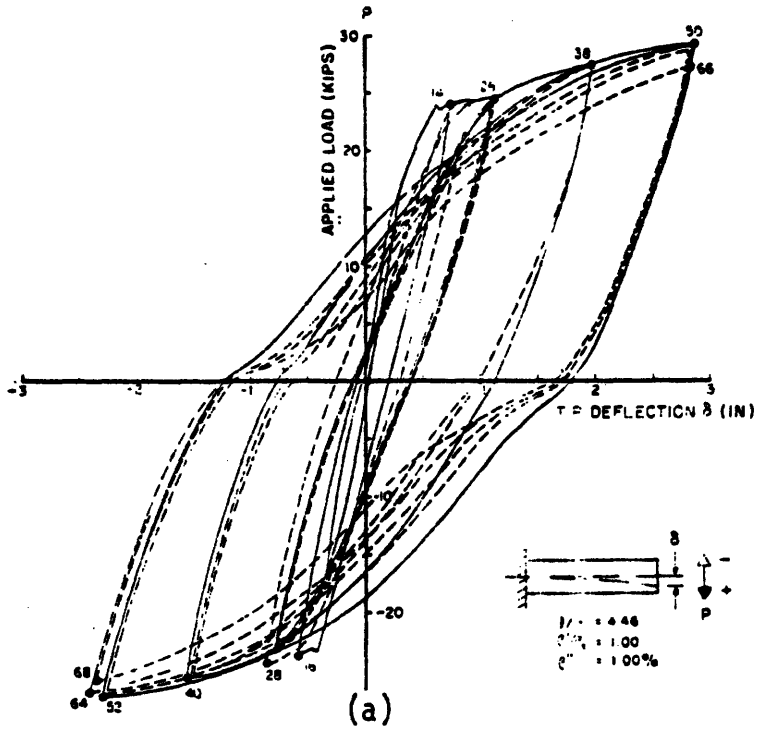

(a)

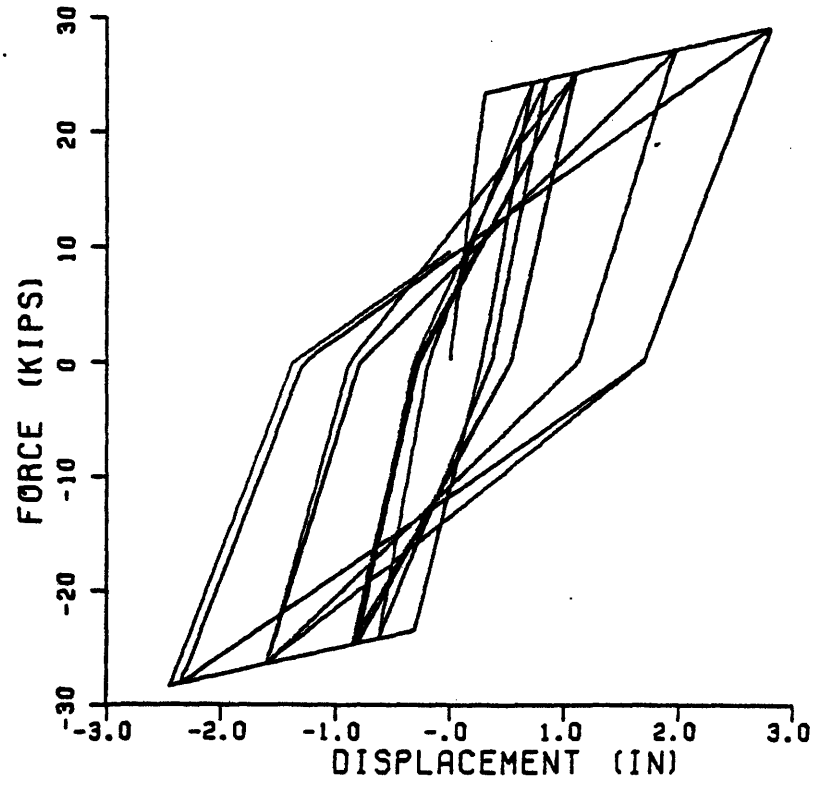

(b)

Fig. 3.22 - Experimental and Analytical Load-Deflection Curves for Specimen R6 in the Experiment by Ma-Bertero-Popov

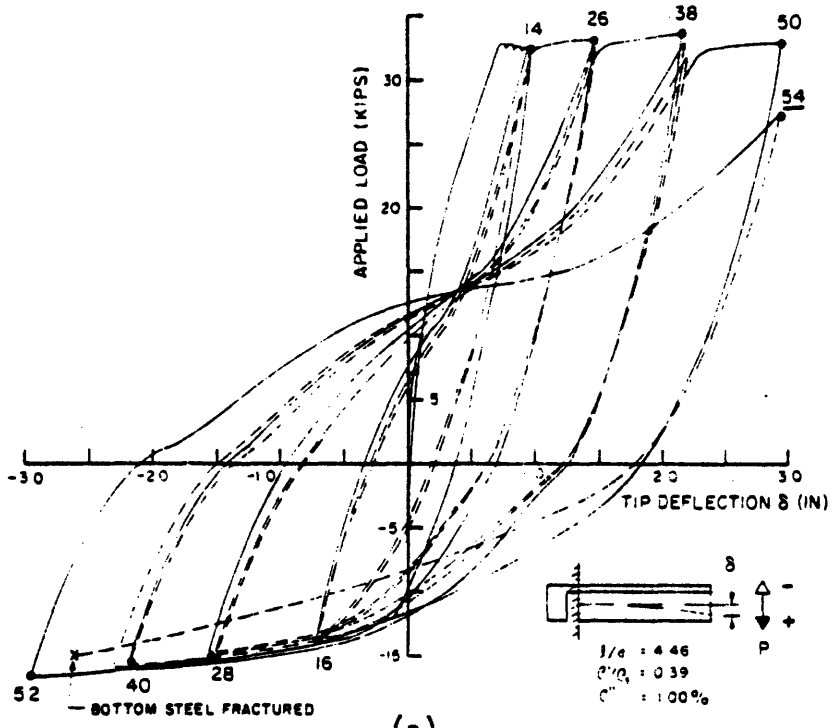

(a)

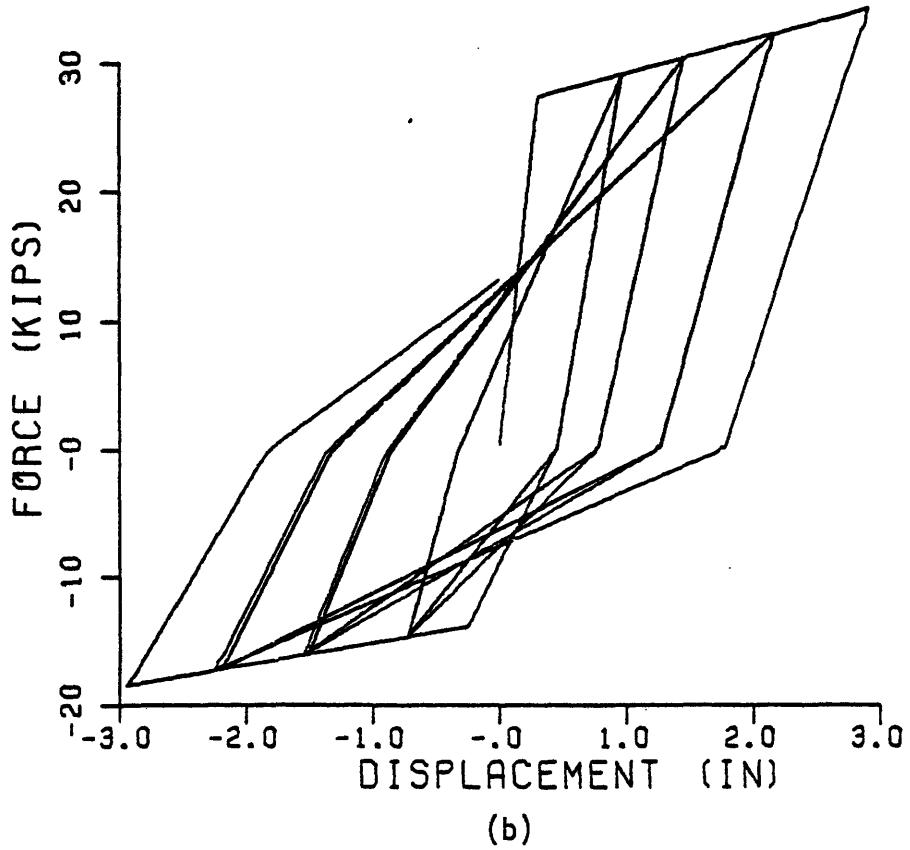

(b)

Fig. 3.23 - Experimental and Analytical Load-Deflection Curves for Specimen T1 in the Experiment by Ma-Bertero-Popov

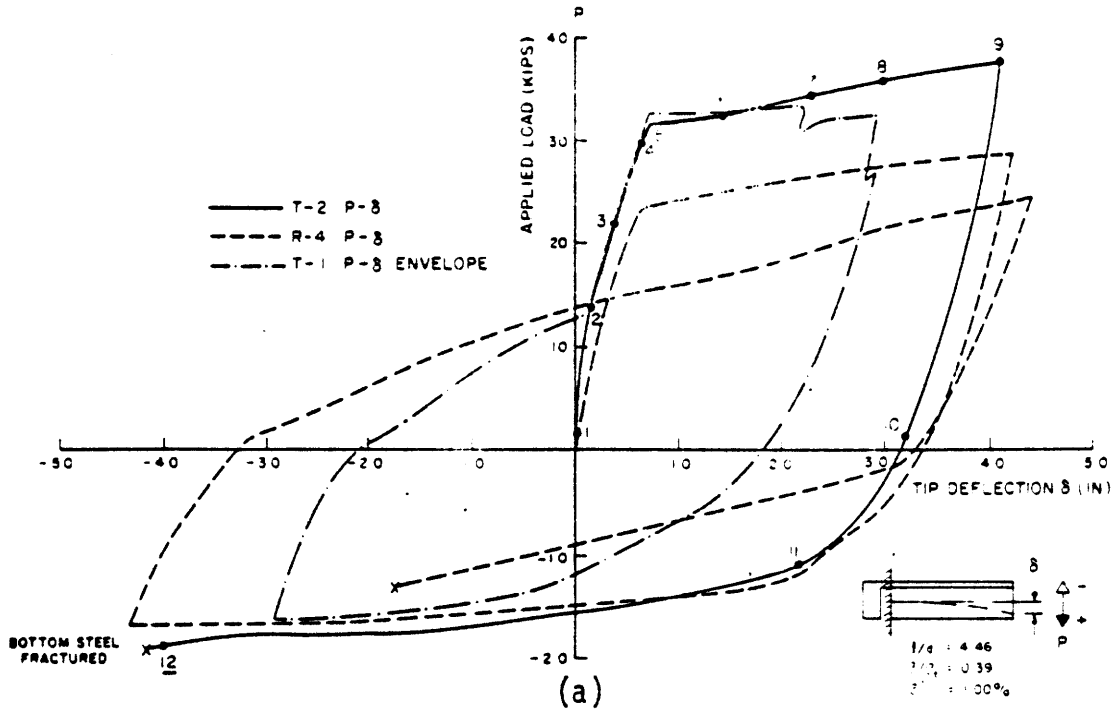

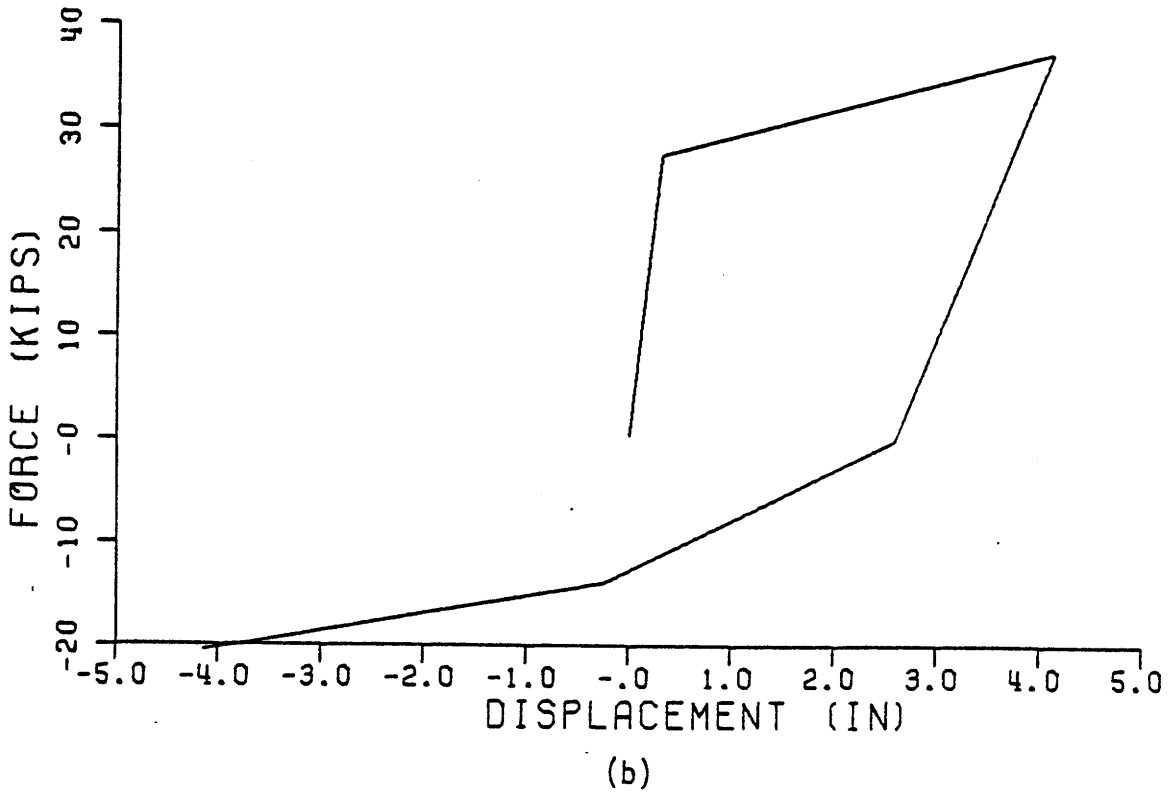

Fig. 3.24 - Experimental and Analytical Load-Deflection Curves for Specimen T2 in the Experiment by Ma-Bertero-Popov

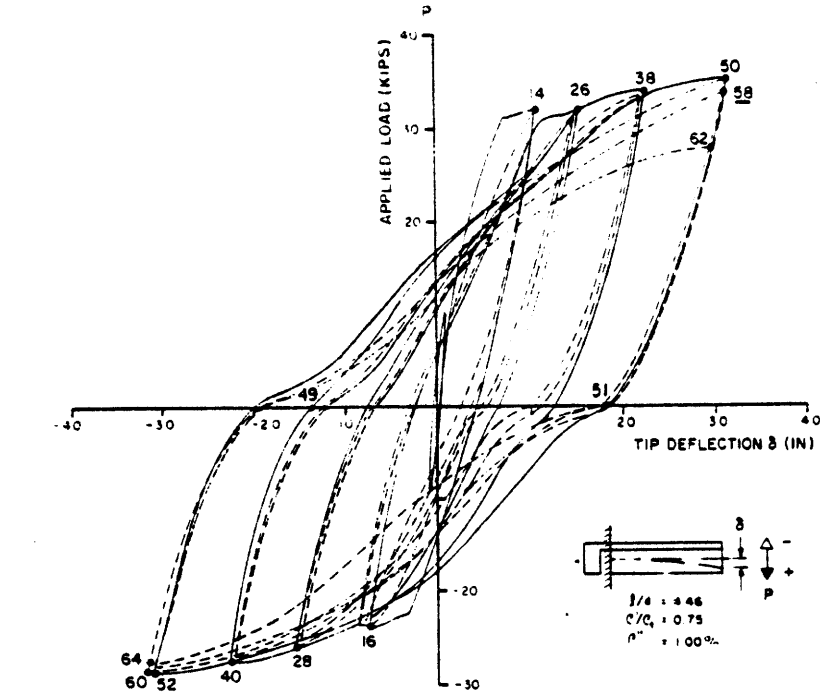

(a)

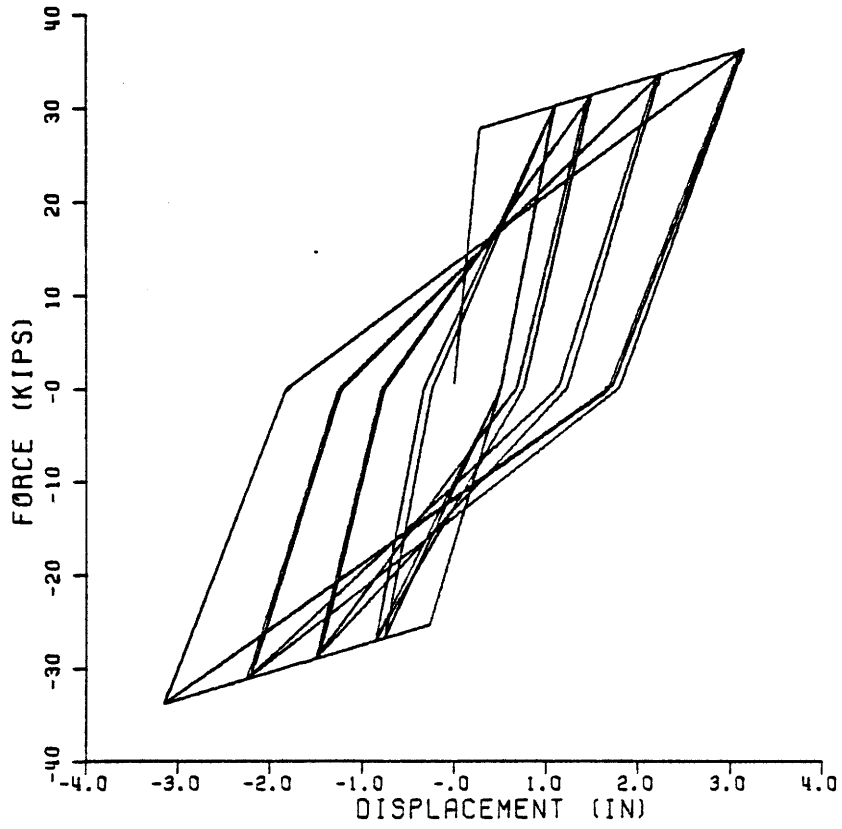

(b)

Fig. 3.25 - Experimental and Analytical Load-Deflection Curves for Specimen T3 in the Experiment by Ma-Bertero-Popov

damage in terms of their load-carrying capacity once failure was initiated and failed soon after. There is very good agreement between analytical and experimental hysteresis loops for all members. On the other hand, even though there is good match between yield loads, computed yield displacements are much lower than experimental yield displacements. Some of the damage indicators which were measured in these experiments are shown in Table 3.1. A comparison of this table with Table 3.3 reveals that computed ductilities are higher than experimental values. Curvature ductility in these tests was measured in the critical hinging zone of members, taken to be half the effective depth. Experimental energy dissipation values represent the total energy dissipated until each test was terminated; thus they are upper bounds to the computed values of energy dissipation. Except for specimen R5, there is very good agreement between dissipated energy values. A comparison of computed energy dissipation and damage ratio for these specimens with the rest of the sample (Table 3.3) shows that these specimens behaved rather well. Specimens R4 and T2 did not dissipate much energy because they were failed under high ductilities. Specimen R5, even though it was subjected to high shear forces, has high damage ratio and energy dissipation. This suggests that if a member is well designed, it can perform well under both flexure and shear.

f) Popov-Bertero-Krawinkler

The objective of this experiment was to study strength, ductility, and energy absorption capacity of reinforced concrete beams under high flexural and shear loads (50). A total of three cantilever beams were tested, but only one (beam 43) which had adequate shear reinforcement was considered here. This cantilever beam had a length of 78 inches and a

cross-sectional area of 15 x 29 inches (Fig. 3.26). Main longitudinal reinforcement consisted of six #9 bars (G60). Shear reinforcement consisted of #4 bars at 3-inch spacing. Concrete strength (f'_c) for this beam was 5000 psi.

Since the main longitudinal reinforcement was welded to a T-beam at the fixed end of the cantilever, no slippage of bars was observed. On the other hand, shear deformation was important, and it was considered in analysis. Experimental and analytical load-deflection curves are shown in Fig. 3.27. The computed peak load is 135 kips, which is 15 percent lower than the experimental peak load. Peak rotation ductility (μ_θ) as measured in the experiment is 6.2, which is less than half the computed ductility value (14.4 for specimen P43 in Table 3.3). Average curvature ductility (μ_ϕ) and normalized cumulative rotation for the critical section (hinging zone) were measured to be 11.0 and 185 respectively. Normalized cumulative ductility is in good agreement with the computed value (225, Table 3.3) from the Single Component Model. It may be noted that the computed cumulative rotation takes into account not only the hinging zone but also inelastic rotations along the rest of the member. Failure of this beam was fast, and once the load started to decrease, only one more cycle caused ultimate failure. Overall, there is good match between experimental and analytical parameters and curves.

g) Scribner-Wight

The purpose of these tests (52) was to investigate effects of longitudinal reinforcement at mid-depth on strength and stiffness degradation of reinforced concrete members. A second objective of the experiments was to study the beam-column joint behavior under high shear and flexural

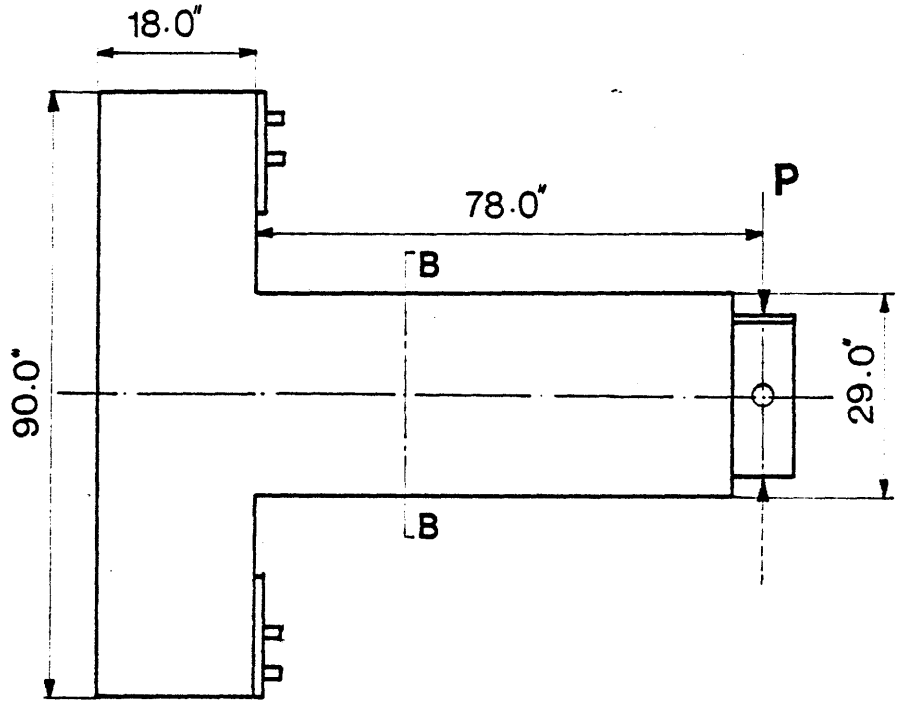

BEAM 43

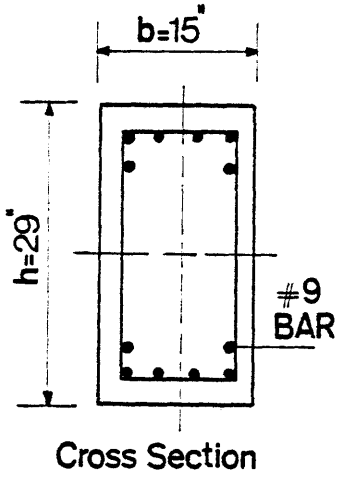

Cross Section

Fig. 3.26 - Test Set-up and Section Properties for the Experiment by Popov - Bertero - Krawinkler

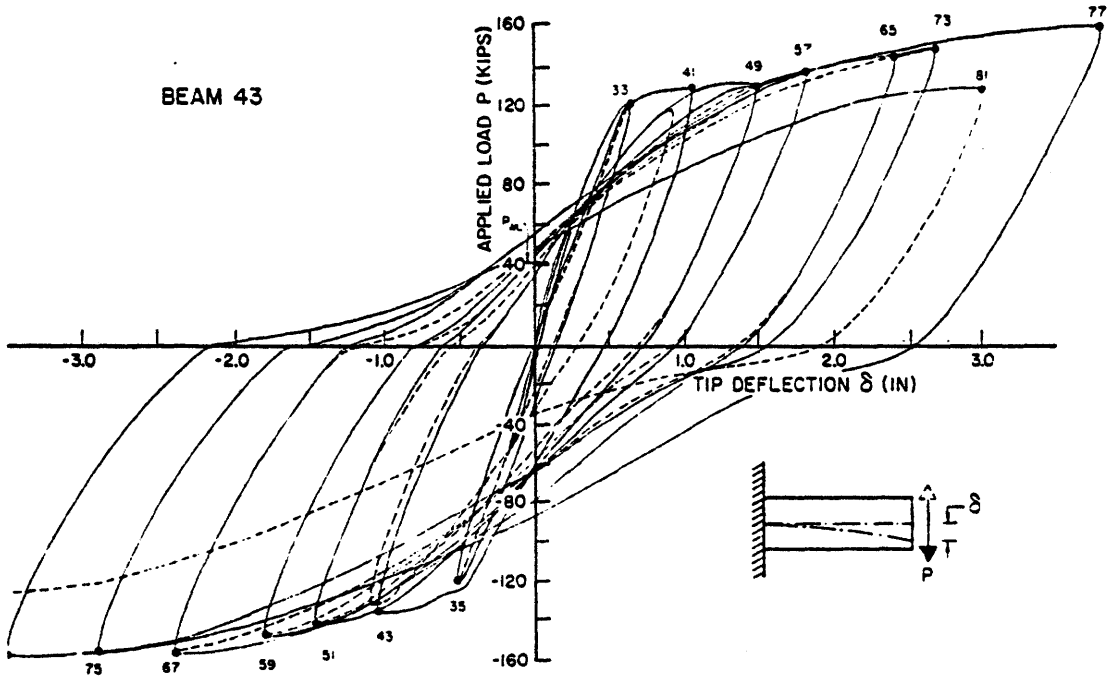

(a)

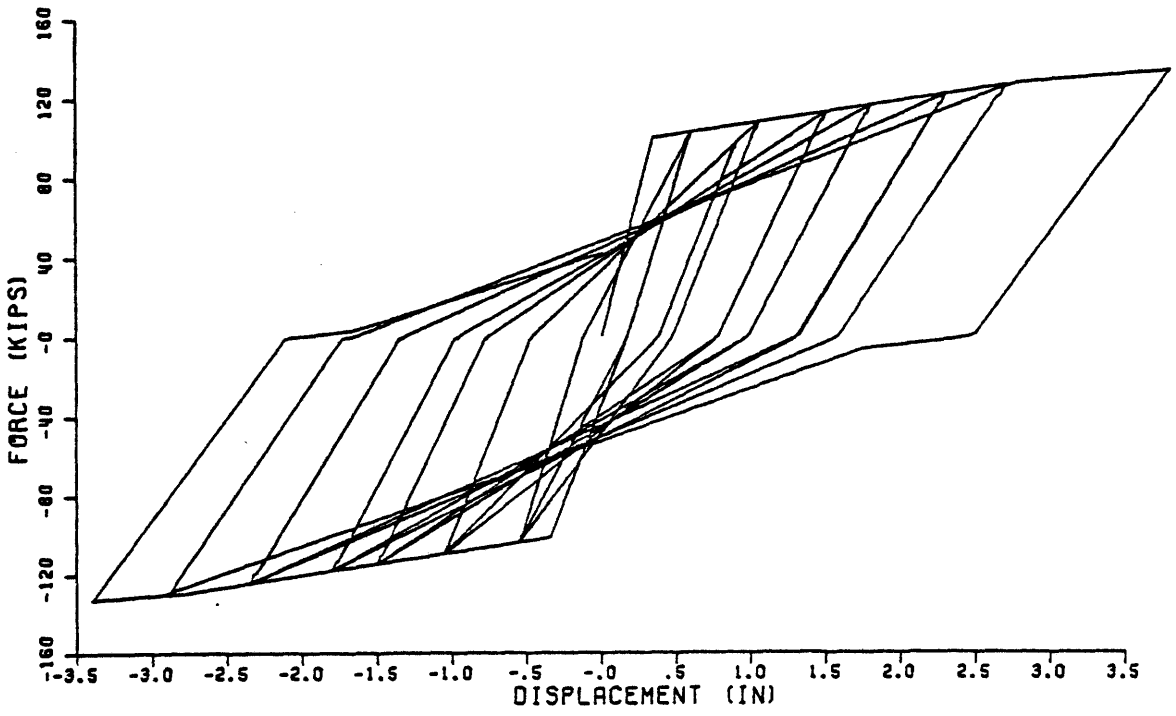

(b)

Fig. 3.27 - Experimental and Analytical Load-Deflection Curves for Specimen 43 in the Experiment by Popov-Bertero-Krawinkler

loads. A schematic representation of the test setup is shown in Fig. 3.28. The assembly represents an exterior beam-column joint in a tall building. A total of 12 specimens, 8 half size (Group I) and 4 full size (Group II) were tested.

Beam and column cross sections are also shown in Fig. 3.28. Beam cross sections were 8 x 10 inches or 8 x 12 inches for Group I, and 10 x 14 inches for Group II. Main longitudinal reinforcement for beams ranged from 1.27 percent to 2.62 percent. Transverse reinforcement in beams ranged from 0.63 percent to 1.1 percent. Grade 40 reinforcement was used for all beams, except for specimen number 7, and Grade 60 reinforcement was used for all columns. Intermediate longitudinal reinforcement was used in half of the specimens, namely, the even-numbered specimens. This is shown in beam cross-sectional areas in Fig. 3.28. It consisted of four steel bars in two layers, and extra transverse reinforcement was used to confine the concrete inside. The area of intermediate longitudinal reinforcement (A_i) was roughly 25 percent of the total compressive and tensile reinforcement areas ($A_s + A_s'$). Intermediate reinforcement, shown as dashed lines in Fig. 3.28, extended a distance of twice the effective depth plus a development length of 12 bar diameters. Axial load (P_a) on columns was 40 kips for group I specimens and 100 kips for group II specimens. Axial load affected only the stiffness characteristics of columns, but it had no effect on inelastic behavior of connecting beams.

In modeling the inelastic behavior of specimens, only flexural and shear deformations were considered. Analytical and experimental load deflection curves for specimens 3 - 12 are in Figs. 3.29 through 3.38. Specimens 1 and 2 exhibited only flexural deformations, and since they

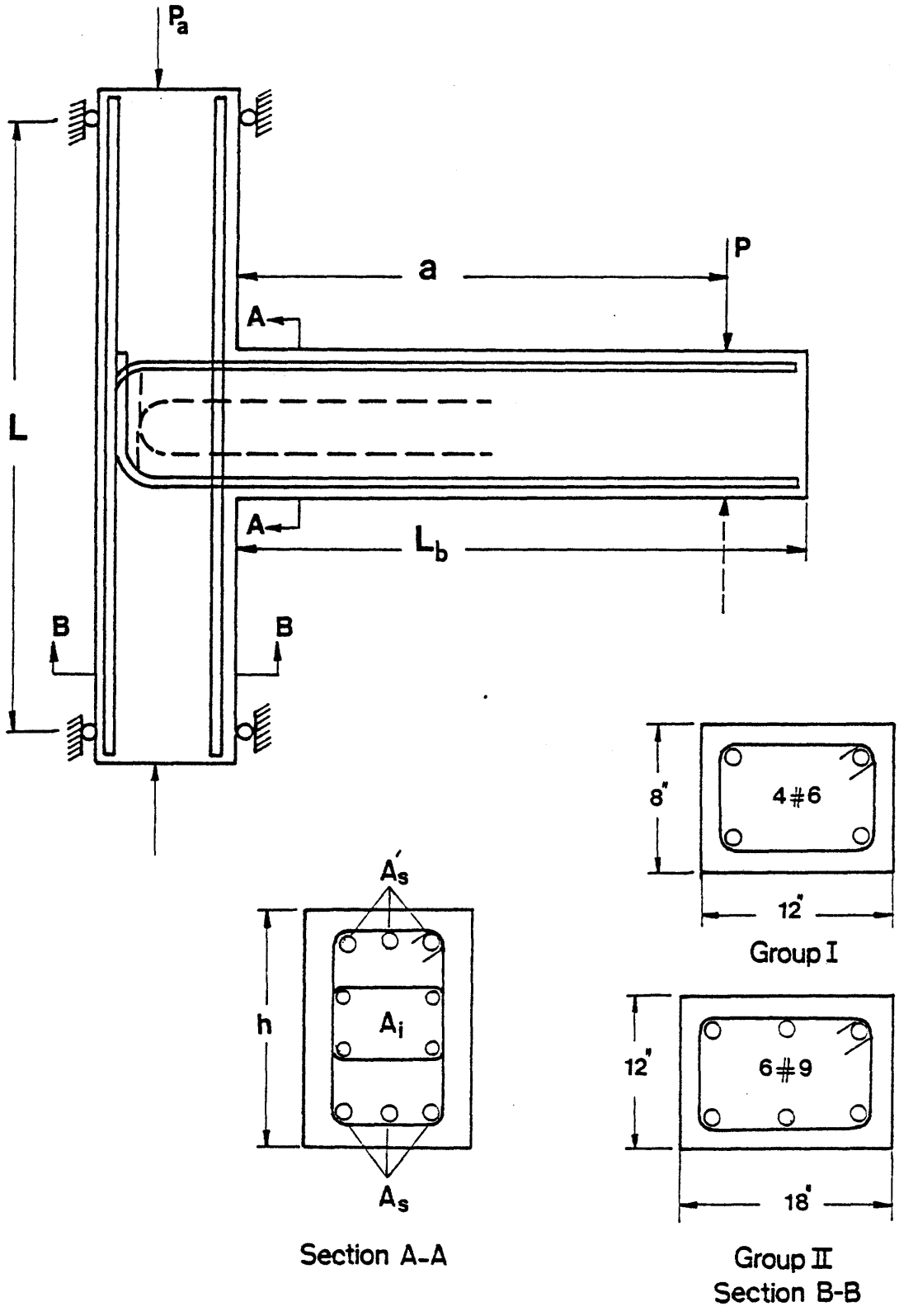

Fig. 3.28 - Test Set-up and Section Properties for the Experiment by Scribner-Wight

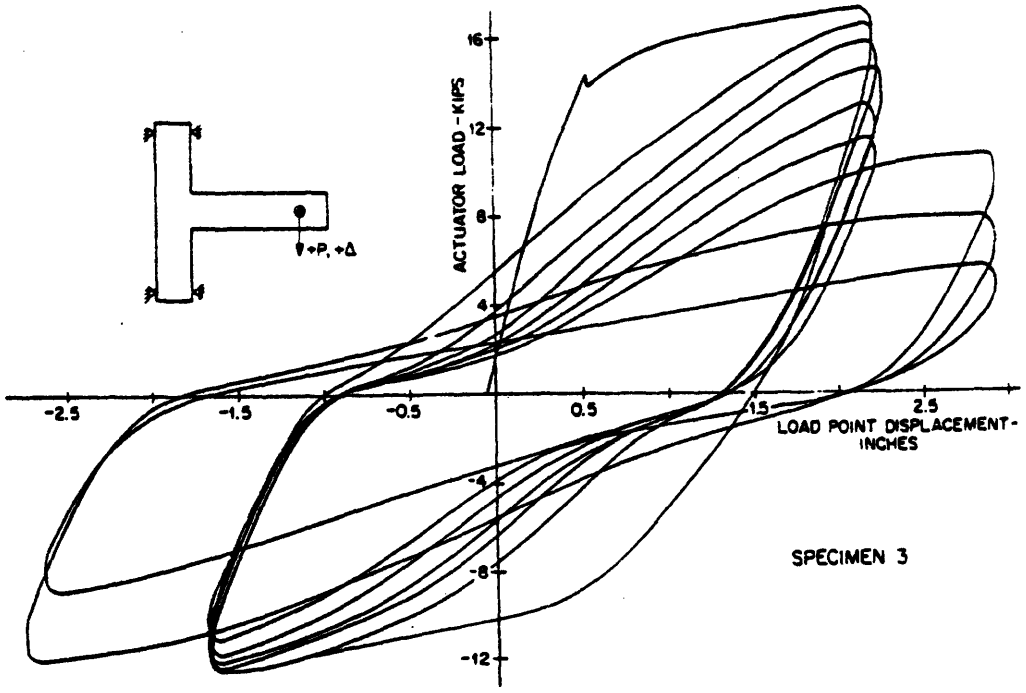

(a)

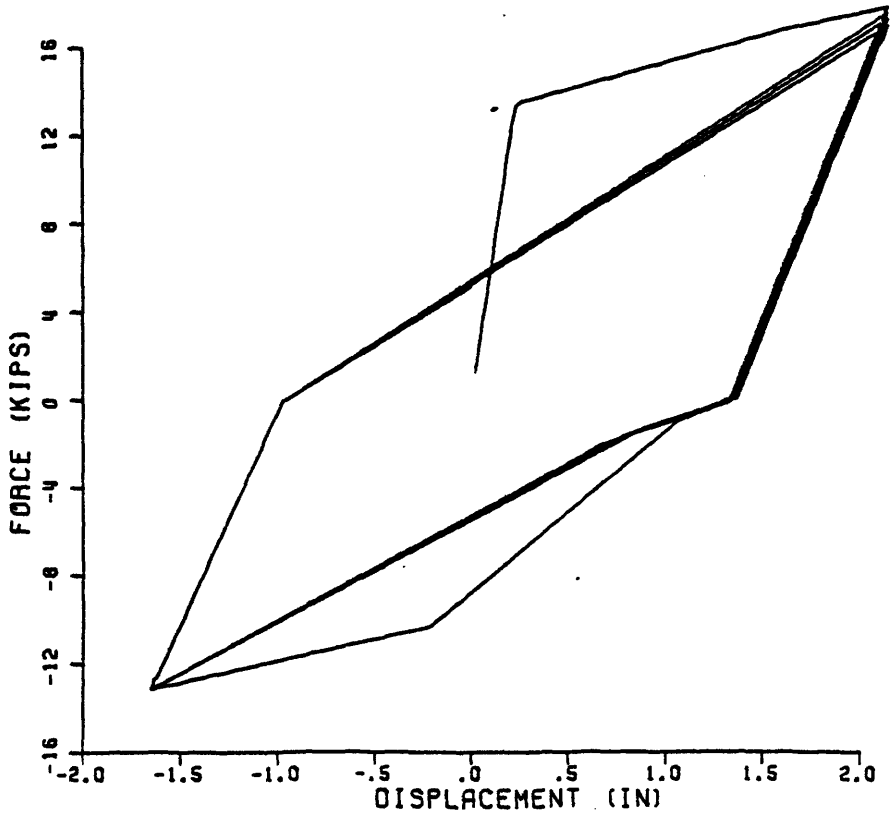

(b)

Fig. 3.29 - Experimental and Analytical Load-Deflection Curves for Specimen 3 in the Experiment by Scribner-Wight

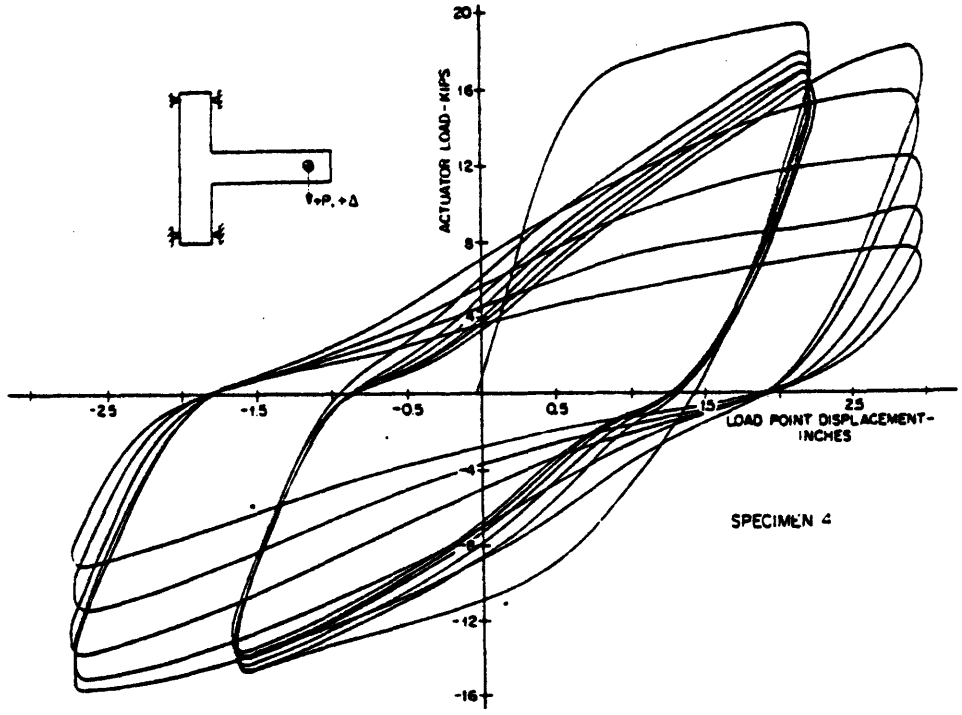

(a)

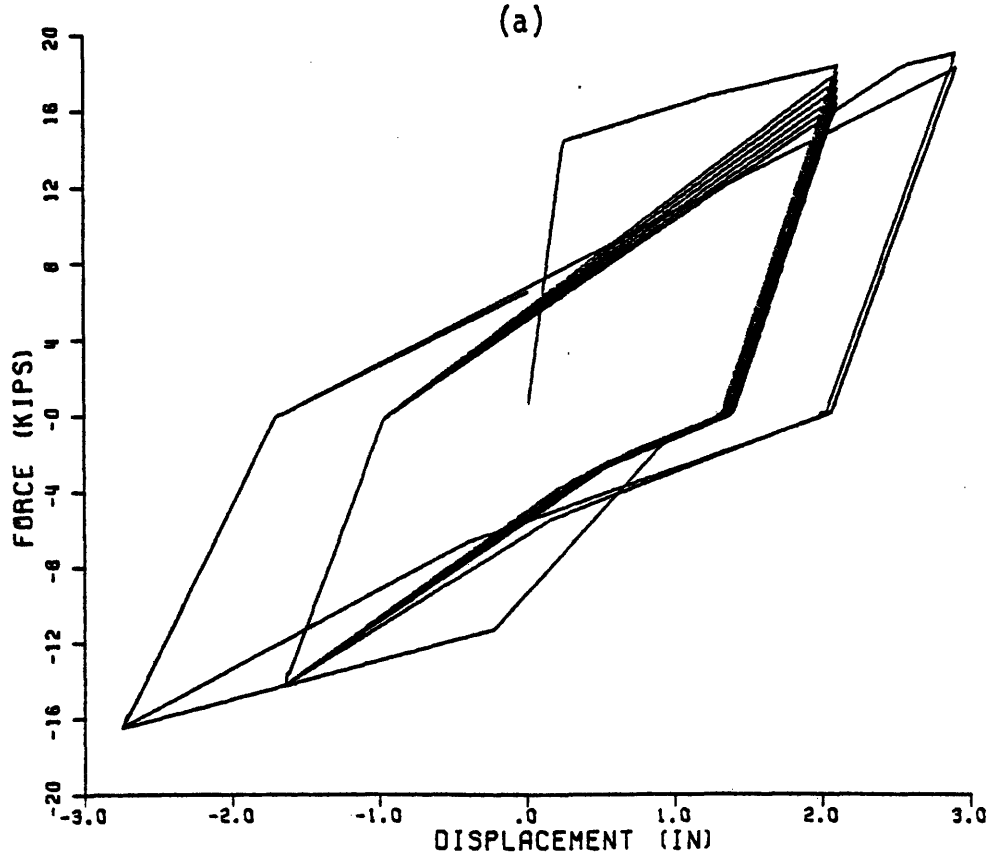

(b)

Fig. 3.30 - Experimental and Analytical Load-Deflection Curves for Specimen 4 in the Experiment by Scribner-Wight

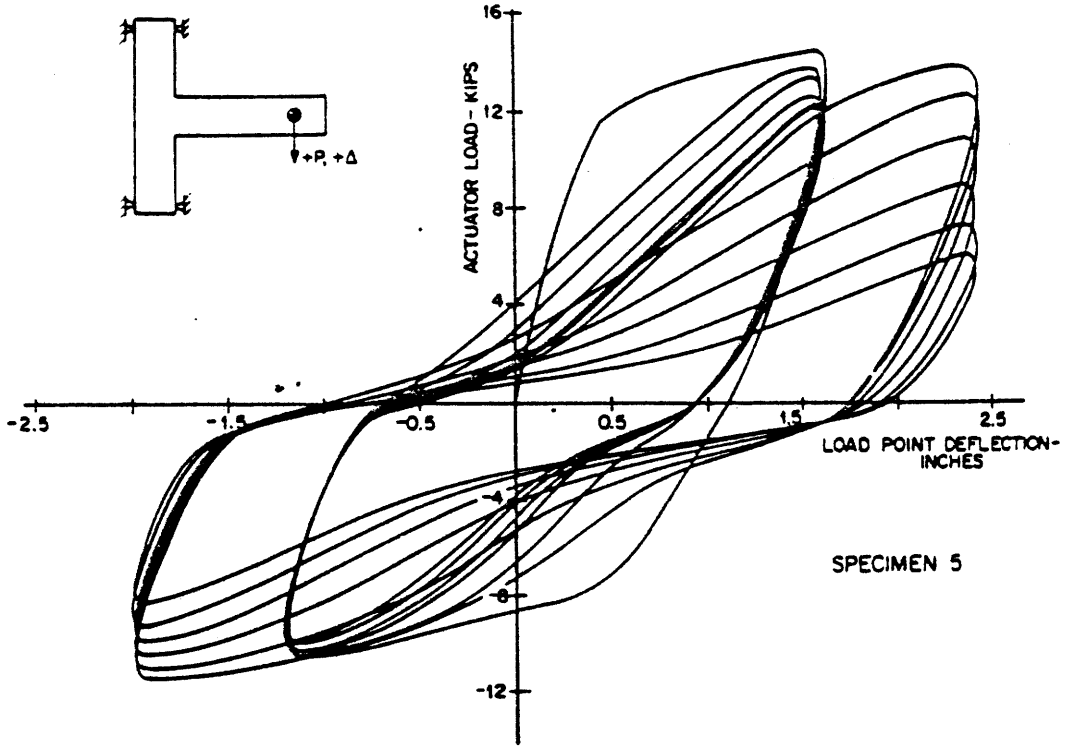

(a)

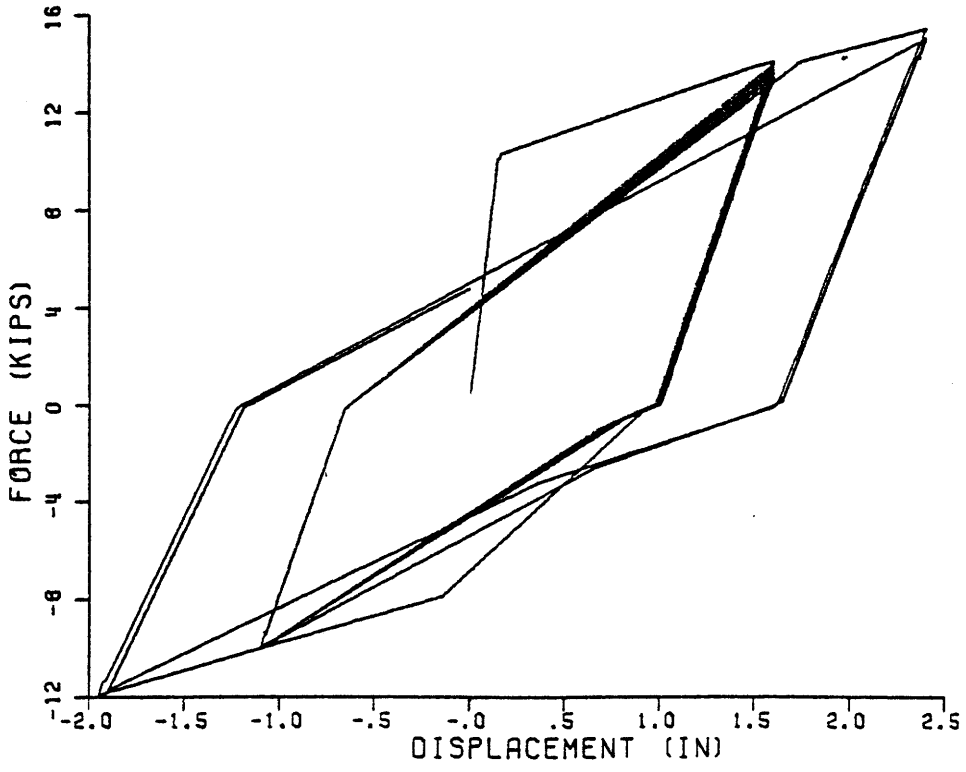

(b)

Fig. 3.31 - Experimental and Analytical Load-Deflection Curves for Specimen 5 in the Experiment by Scribner-Wight

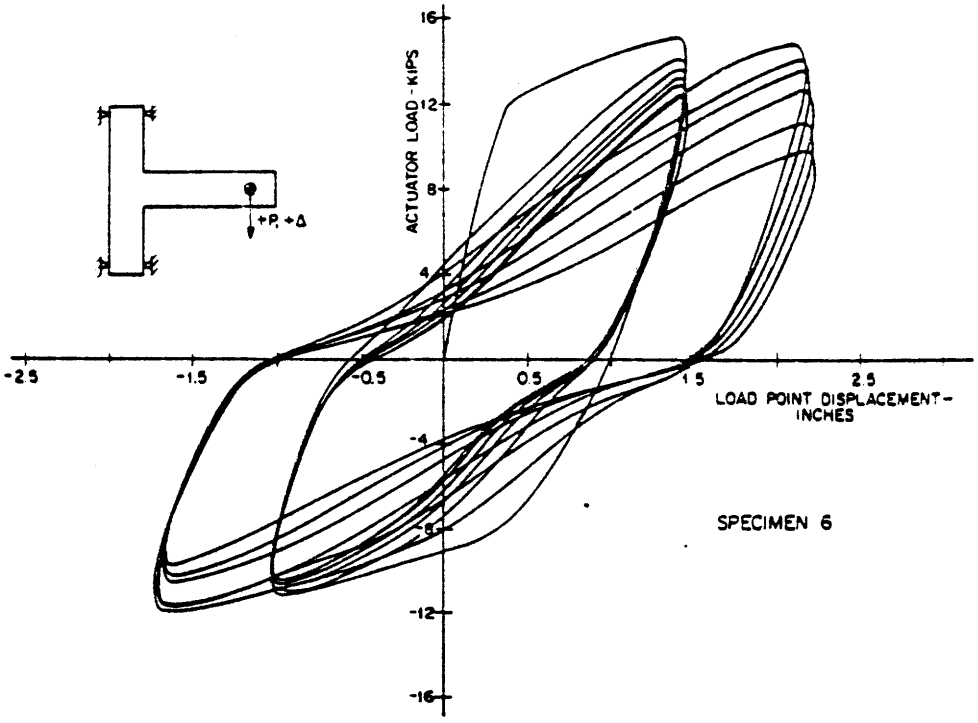

(a)

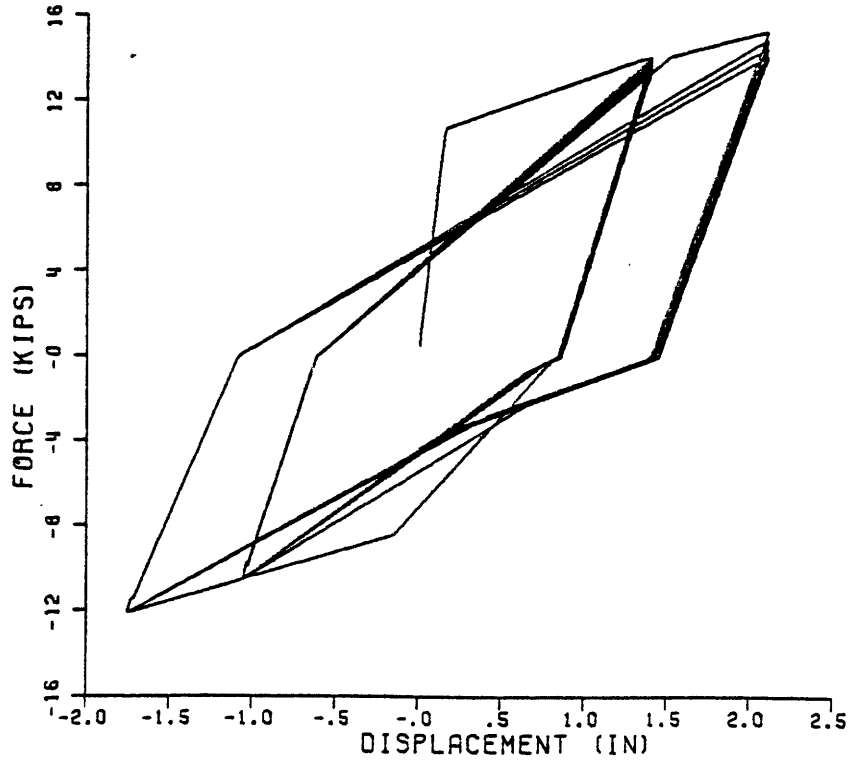

(b)

Fig. 3.32 - Experimental and Analytical Load-Deflection Curves for Specimen 6 in the Experiment by Scribner-Wight

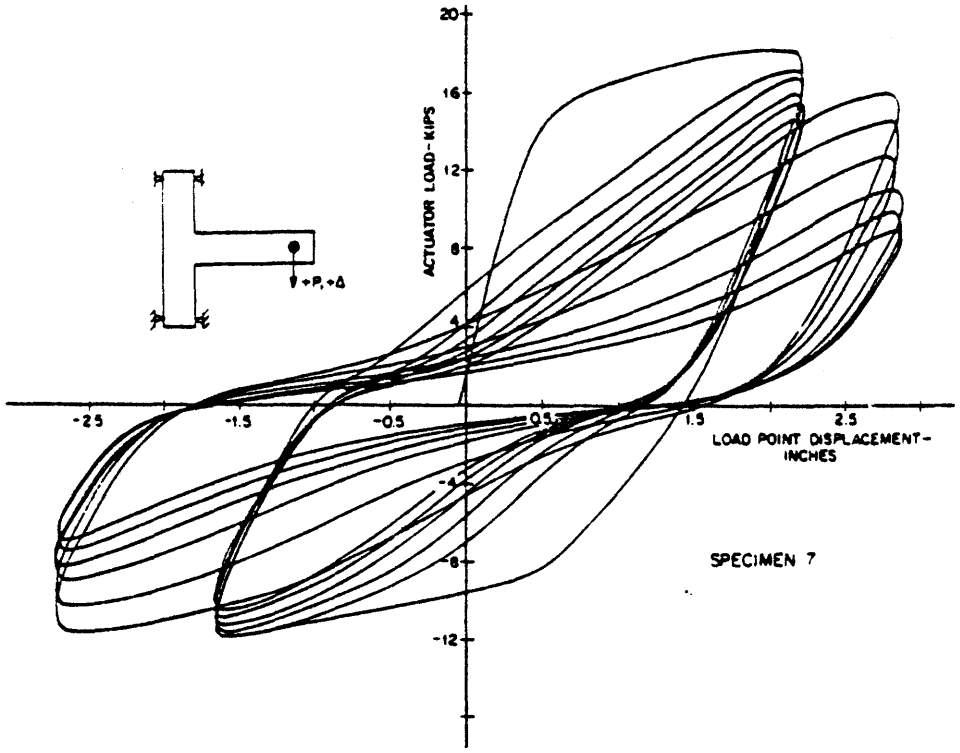

(a)

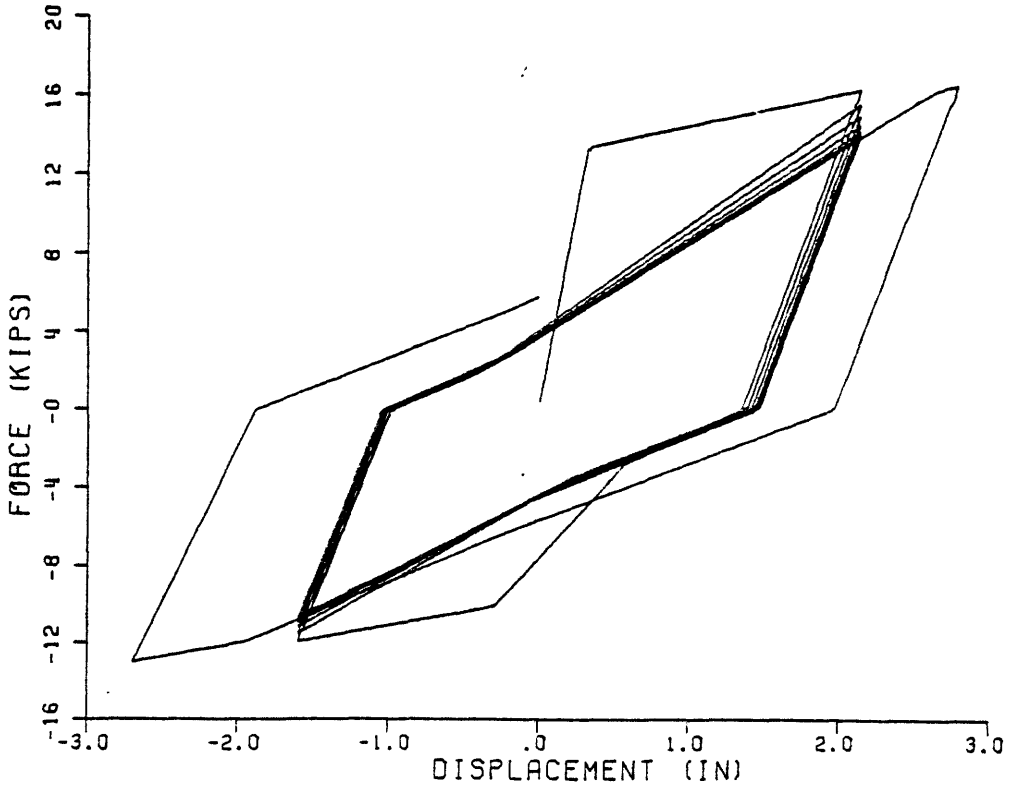

(b)

Fig. 3.33 - Experimental and Analytical Load-Deflection Curves for Specimen 7 in the Experiment by Scribner-Wight

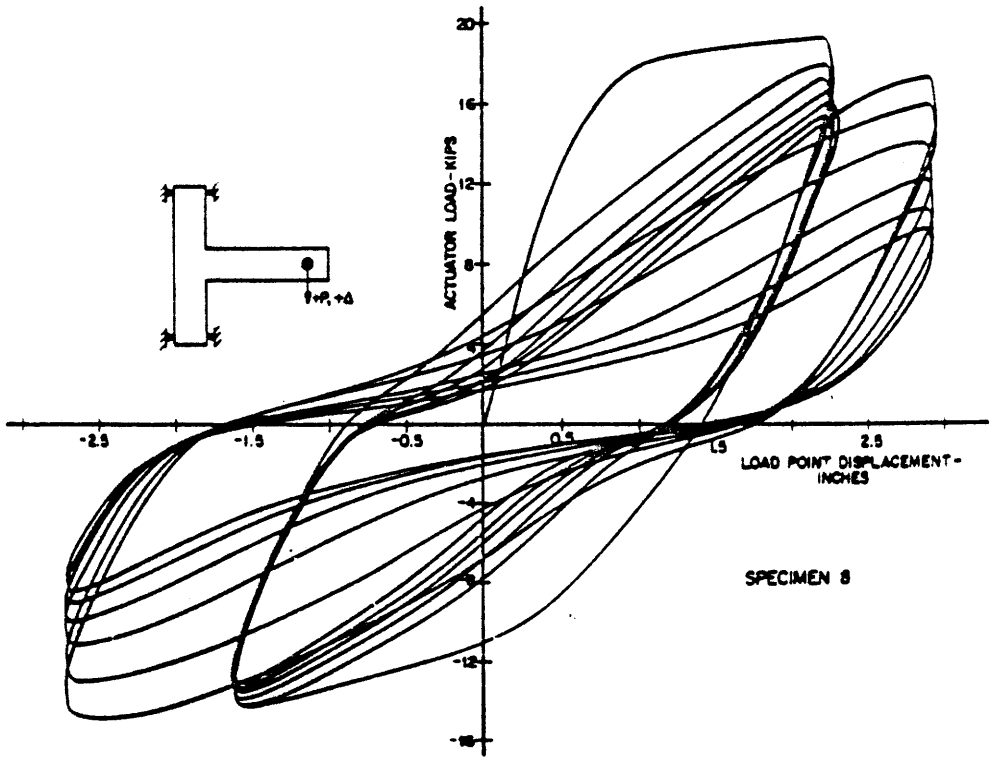

(a)

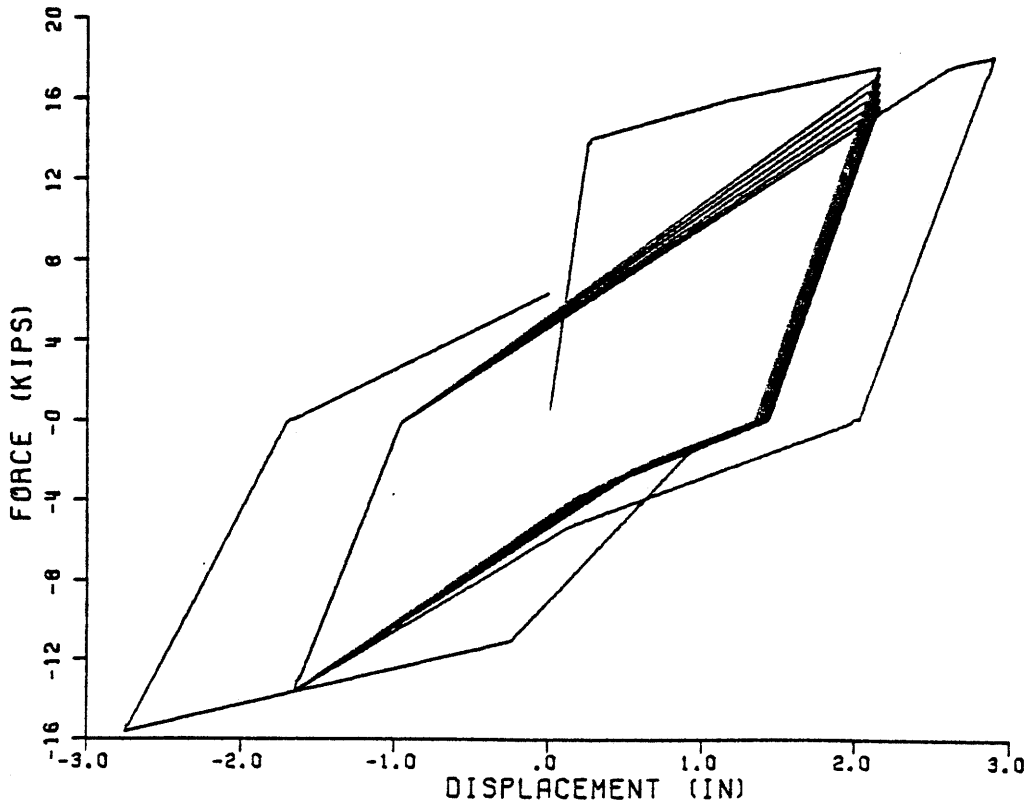

(b)

Fig. 3.34 - Experimental and Analytical Load-Deflection Curves for Specimen 8 in the Experiment by Scribner-Wight

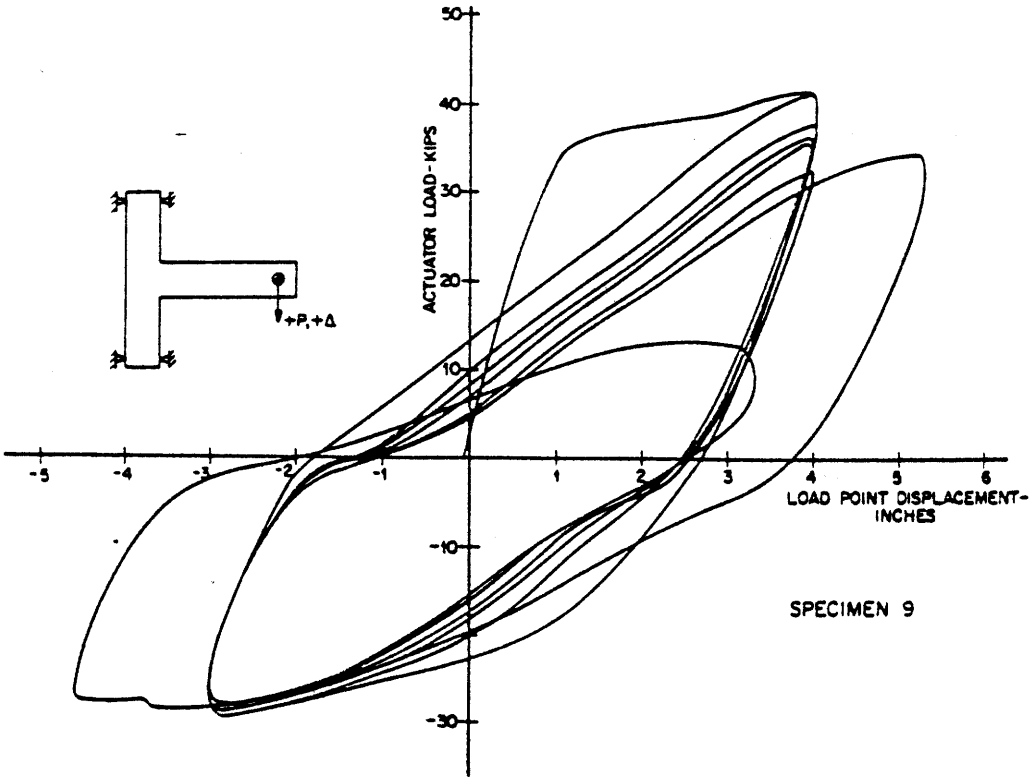

(a)

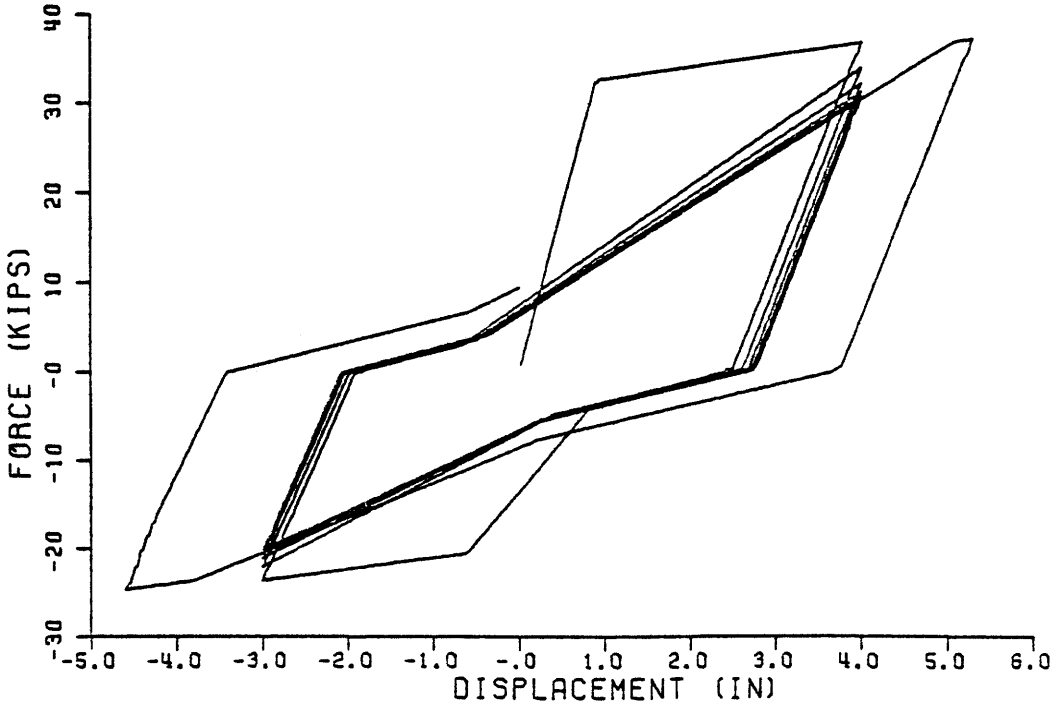

(b)

Fig. 3.35 - Experimental and Analytical Load-Deflection Curves for Specimen 9 in the Experiment by Scribner-Wight

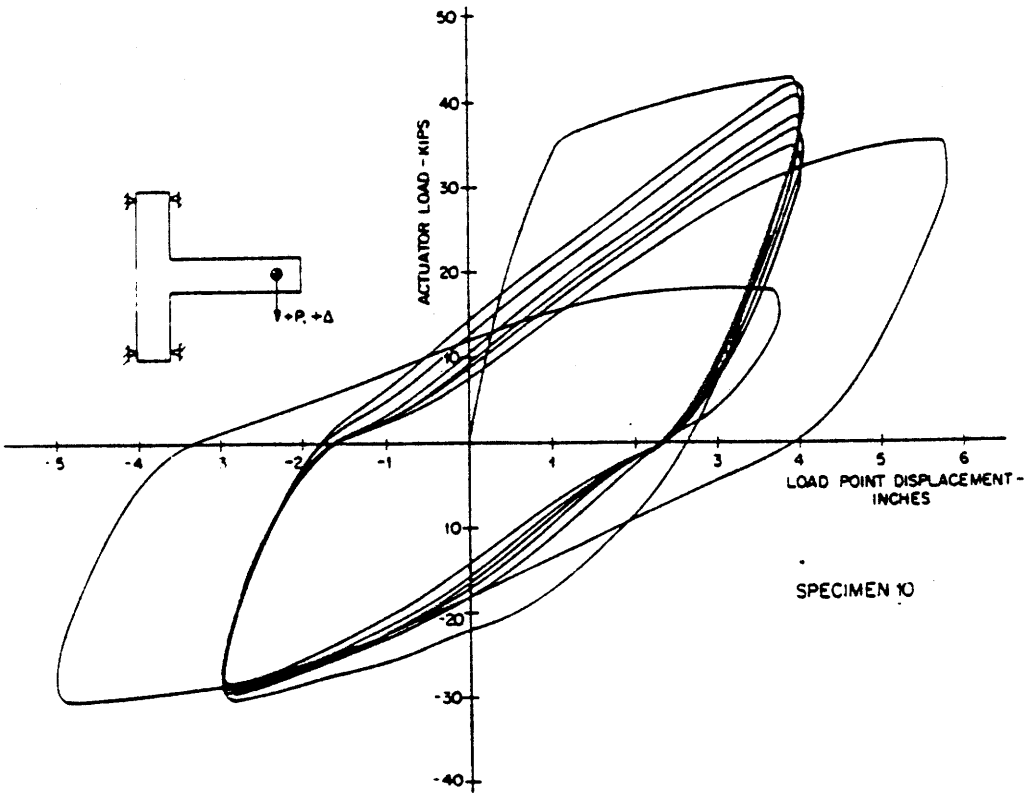

(a)

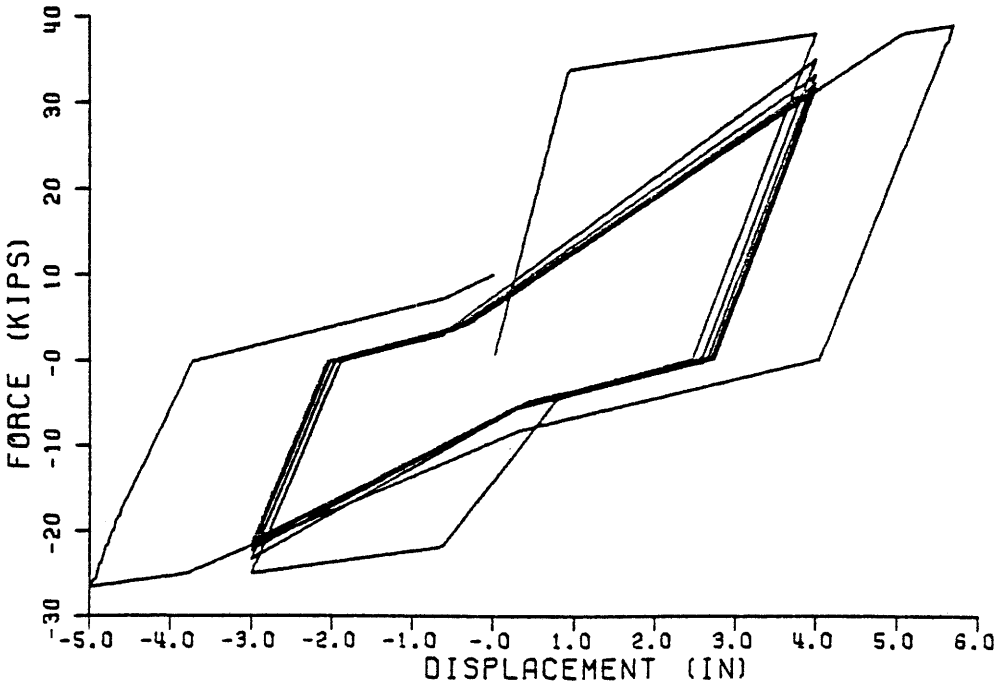

(b)

Fig. 3.36 - Experimental and Analytical Load-Deflection Curves for Specimen 10 in the Experiment by Scribner-Wight

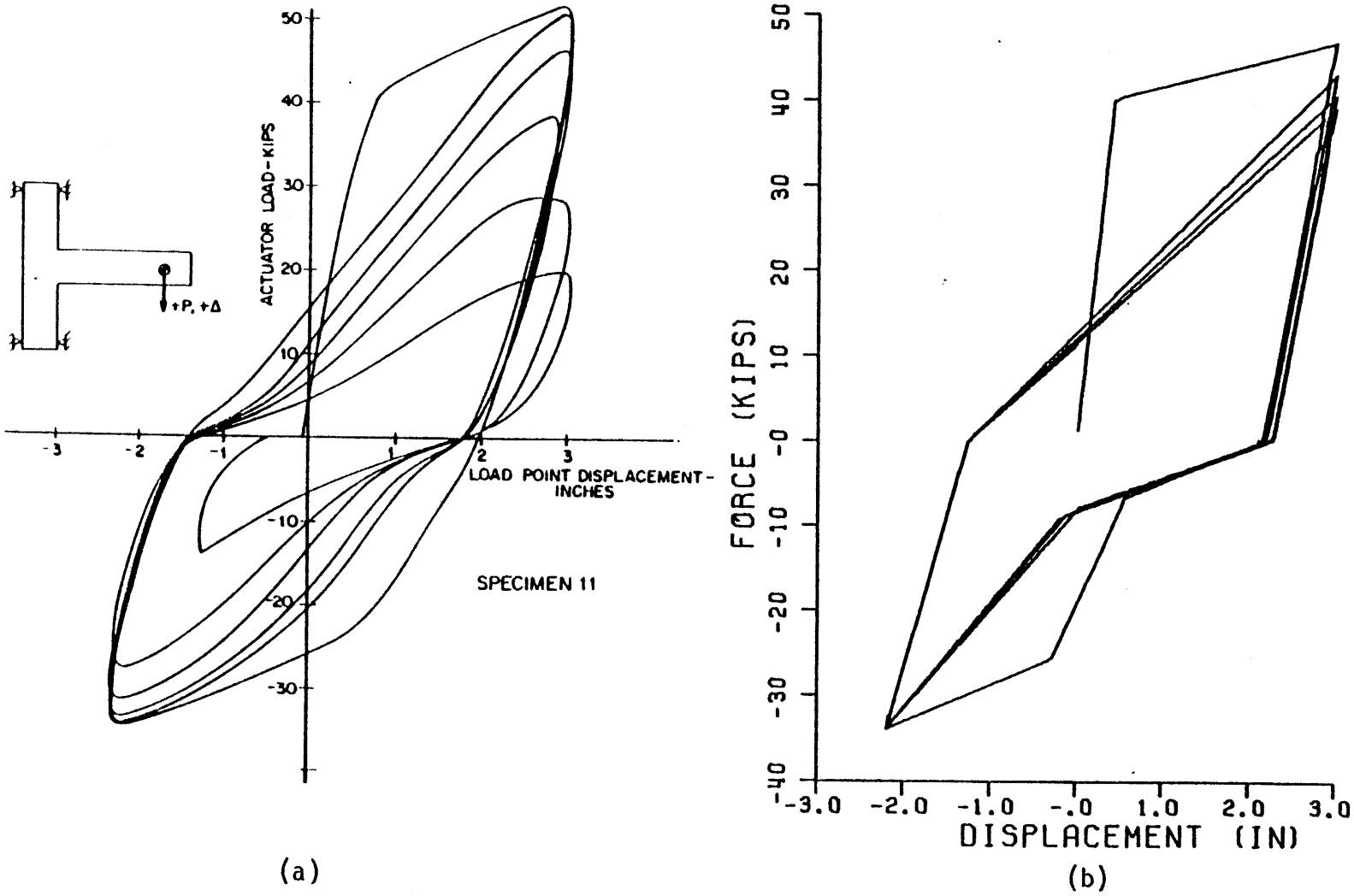

Fig. 3.37 - Experimental and Analytical Load-Deflection Curves for Specimen 11 in the Experiment by Scribner-Wight

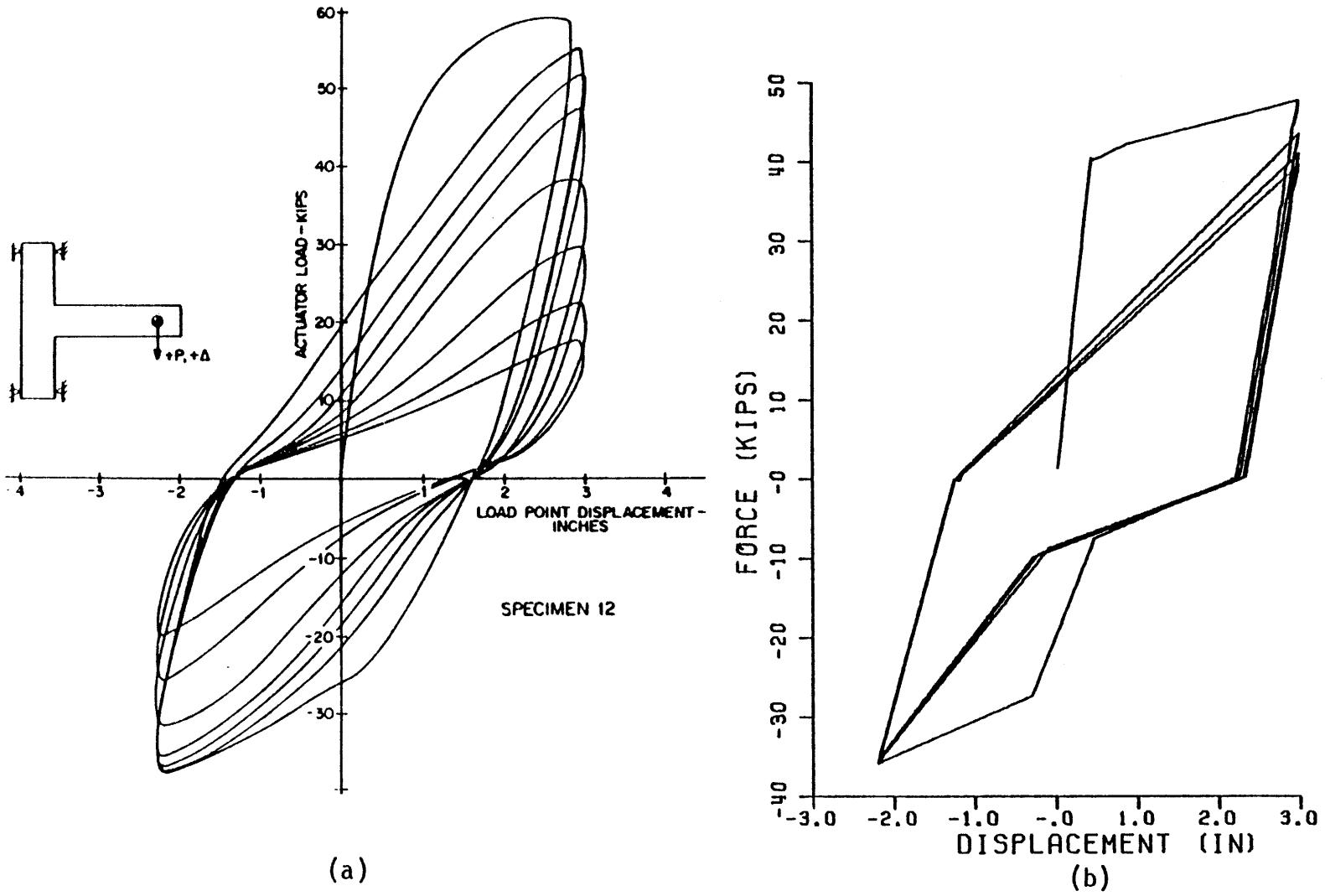

Fig. 3.38 - Experimental and Analytical Load-Deflection Curves for Specimen 12 in the Experiment by Scribner-Wight

did not fail, they were not considered in this study. The loading scheme consisted of six cycles of displacement ductility four in positive direction and ductility three in negative direction. If the specimen survived these loads, then more cycles of higher ductilities were also applied. Pinching behavior due to high shear forces and slippage may be observed in all of the specimens that were considered. Also, loss of strength is seen in all of the experimental curves. Most specimens in this experiment showed a gradual loss of load-carrying capacity, which finally led to their ultimate failure. However, failure in specimens 9 and 10 were more abrupt. Specimens 11 and 12 exhibited very drastic reduction in their load-carrying capacity after only a few cycles of inelastic rotations. This is in part due to very high shear forces acting on these two beams.

Table 3.2 is a comparison of dissipated energies measured in each test from the load-deflection curve and normalized values of energy computed from analytical models. Both of these values represent the energy loss in beams through flexural and shear deformations up to the theoretical failure point. There is very good agreement between the two values for Group I specimens, but results for Group II specimens differ by as much as 30 percent. This is mainly due to the fact that computed yield moments are lower than experimental yield values. Analytical yield displacements were all much lower than actual yield displacements, which means that computed ductility values are very high (specimen S3-S12 in Table 3.3). Overall match between the inelastic behavior of specimens and analytical results is good. As mentioned before, computed ductility values are always very sensitive to the modeling of the elastic stiffness of a member. On

the other hand, inelastic behavior of reinforced concrete members is rather insensitive to their elastic stiffnesses. A comparison of energy dissipation and flexural damage ratio for this set of experiments with the rest of the sample (Table 3.3) shows that these specimens dissipated less energy, but their flexural damage ratios were higher. High values of flexural damage ratio are a direct result of high ductilities and strength degradation in these specimens.

Results of these tests showed that intermediate longitudinal reinforcement increased the energy dissipation capacity of beams. This was partly due to better confinement of the concrete core by placing vertical ties around intermediate reinforcement. Intermediate reinforcement also improved the crack distribution in members, which also led to increased energy dissipation. Although such effects are not directly considered in analytical models, they are considered when failure of a member is modeled in a probabilistic sense. Buckling of compressive reinforcement was a significant factor in failure of these specimens. This again supports the idea that analytical models follow the behavior of the member until an unexpected event, such as buckling of compressive reinforcement, initiates the failure. This is described in more detail in the next chapter, where a stochastic model of excessive damage is presented.

h) Viwathanatepa, Popov, Bertero

These tests were designed to investigate differences in the behavior of reinforced concrete members in virgin state with repaired specimens (57). Two identical subassemblages, representing half-scale models of a section in the third floor of a 20-story building, were cast (Fig. 3.39). Beam sections were 9 x 16 inches and column sections were 17 x 17 inches.

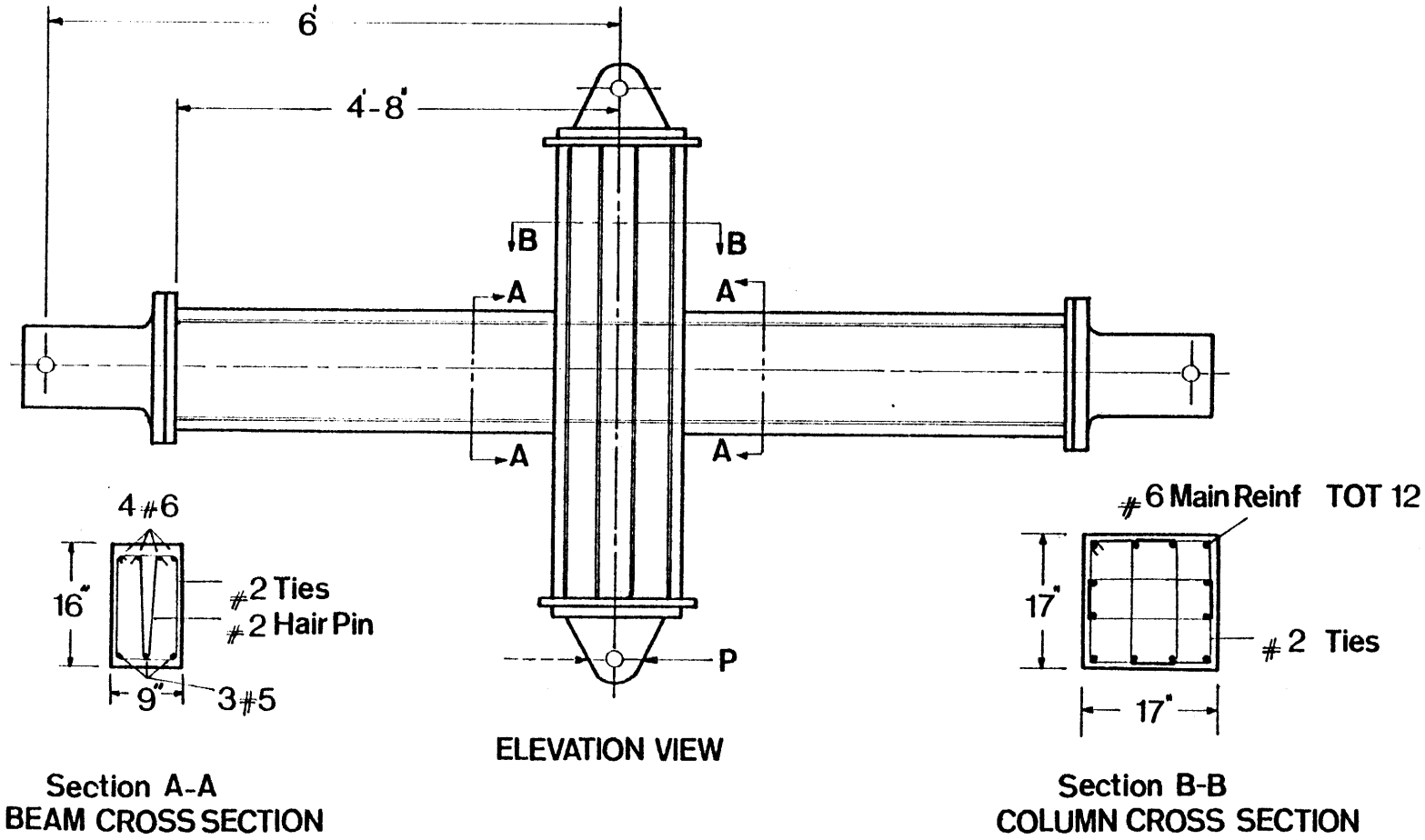

Fig. 3.39 - Test Set-up and Section Properties for the Experiment by Viwathanatepa-Popov-Bertero

Beams were reinforced with four #6 bars at top and three #5 bars at bottom, and columns were reinforced with twelve #6 bars at top and bottom (G60). Since the purpose of the present work is to study damage in members when they are first subjected to earthquake loads, the repaired specimen was not included in the sample. Concrete strength (f'_c) for the virgin specimen (Specimen BC3) was 4500 psi.

Test procedure consisted of first applying an axial load of 470 kips to columns, and then subjecting lower columns to displacement reversals (Fig. 3.39). Columns were modeled using the Single Component Model, and beams were modeled using the extended Non-Symmetric Single Component Model (Section 2.3c). Fixed end rotation due to slippage was considered only for the beams. Experimental and analytical load-deflection curves appear in Figure 3.40. The P-δ effect is clearly seen in both curves. Only beams had any inelastic behavior—the columns stayed elastic. Rotation ductility (μ_θ) measured along the first nine inches of the beam adjacent to the joint was 8, which is higher than $\mu_\theta = 7.1$ computed in the analysis. Pull-out stiffness for slippage mechanism was measured to be 2.58×10^5 and is in good agreement with computed value of 4.8×10^5 when one considers uncertainties in the slippage model. Total energy dissipated in the experiment was 400 k-in or 110 when normalized. This is in good agreement with the computed normalized energy (84 for specimen VBC3 in Table 3.3), which is calculated up to the theoretical failure point. There is rather poor agreement between yield loads and general shape of the hysteresis load-deflection curve (Fig. 3.40).

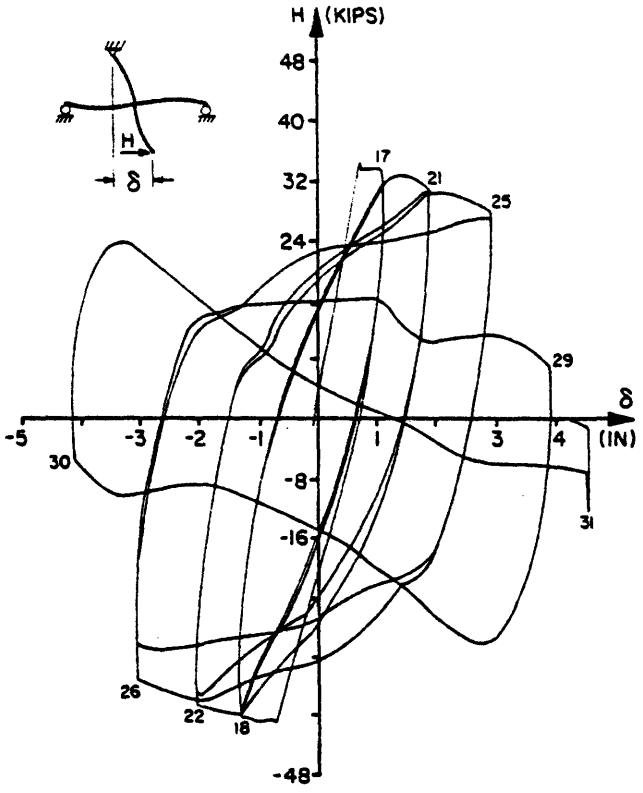

(a)

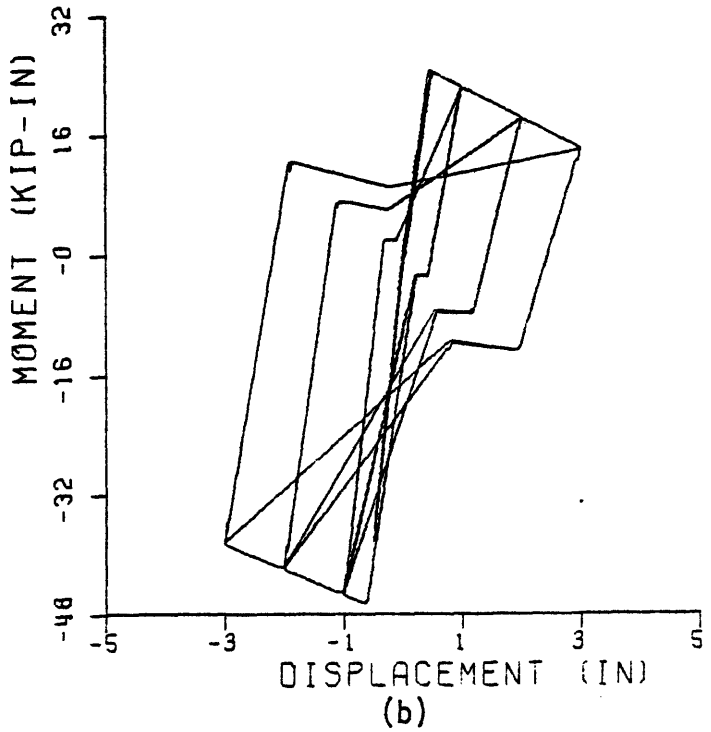

(b)

Fig. 3.40 - Experimental and Analytical Load-Deflection Curves for Specimen BC3 in the Experiment by Viwathanatepa-Popov-Bertero

3.3 Overall Comparison of Experimental and Analytical Results

Using the analytical models described in Chapter II, a total of 32 static cyclic load tests from eight sets of experiments were analyzed. Damage indicators, such as ductility, were computed for each specimen. All of the computed damage indicators are listed in Table 3.3. Since inelastic flexural and shear springs in a member act independently (see Chapter II), it is possible to isolate each one in an experiment. Figures 3.41 (a) and 3.41 (b) show analytical flexural and shear hysteresis loops for specimen R5 in the experiment by Ma, Bertero, and Popov (Section 3.2e). Figure 3.41 (c) is a plot of energy dissipation in flexure versus normalized cumulative rotation for the same specimen. These plots were produced for all specimens in the sample. Examination of energy dissipation plots showed that there is a nearly linear relationship in every case.

From the foregoing discussions of each test, it is apparent that the Single Component Model is accurate in predicting inelastic deformations of reinforced concrete specimens. The match between experimental and analytical results is especially good when flexural deformations are dominant. Although it is more difficult to model shear and slippage deformations in a reinforced concrete member, using the models described in Chapter II it was possible to obtain good prediction of inelastic behavior of members with high shear and slippage. On the other hand, some of the damage indicators could not be computed accurately. This is especially true for peak rotational ductility and peak curvature ductility. Since the definition of peak curvature ductility is based on inelastic deformation of a section, it is not suitable for the Single Component Model.

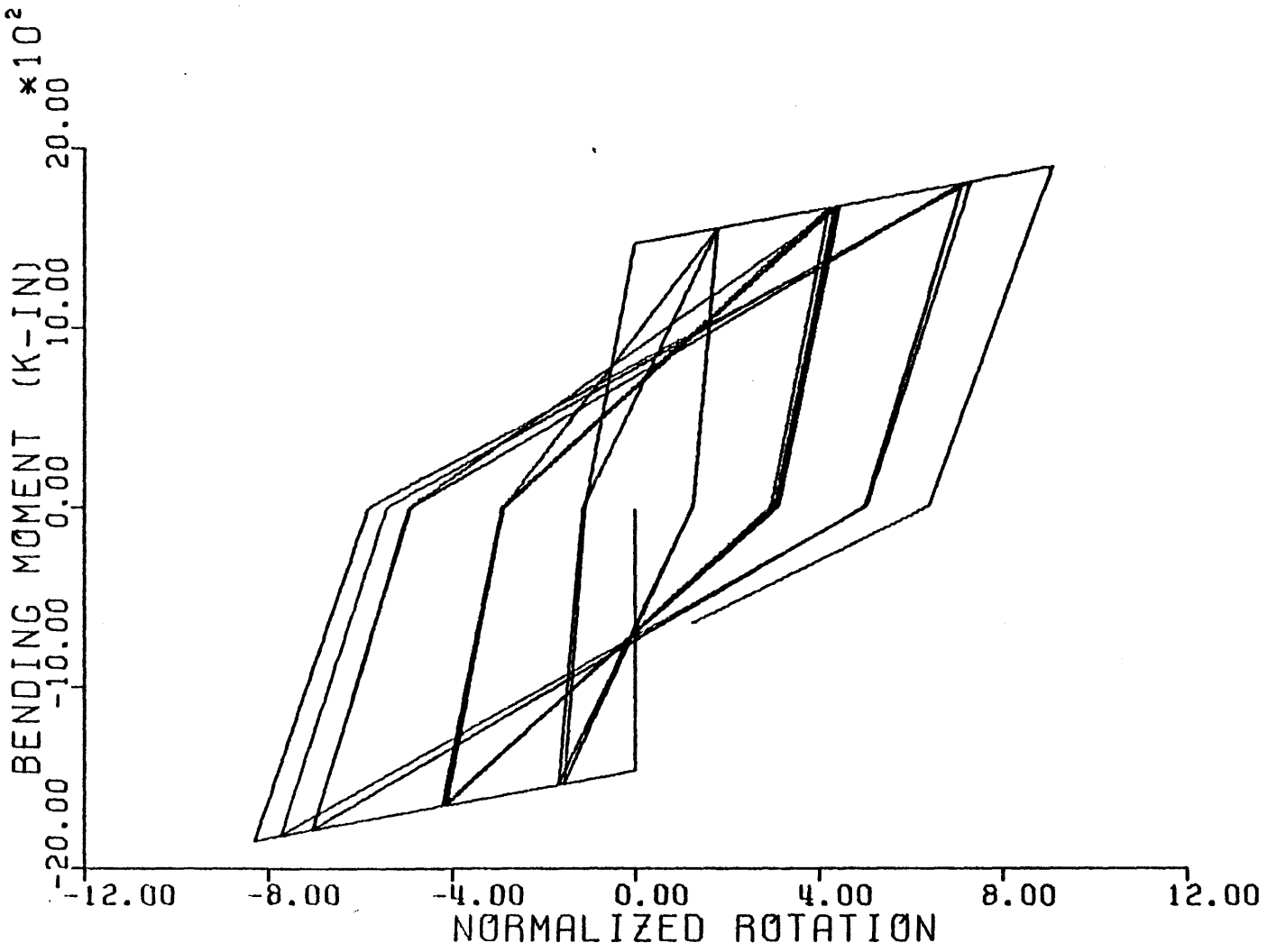

Fig. 3.41a - Moment-Rotation Relationship for Flexural Spring in Specimen R5

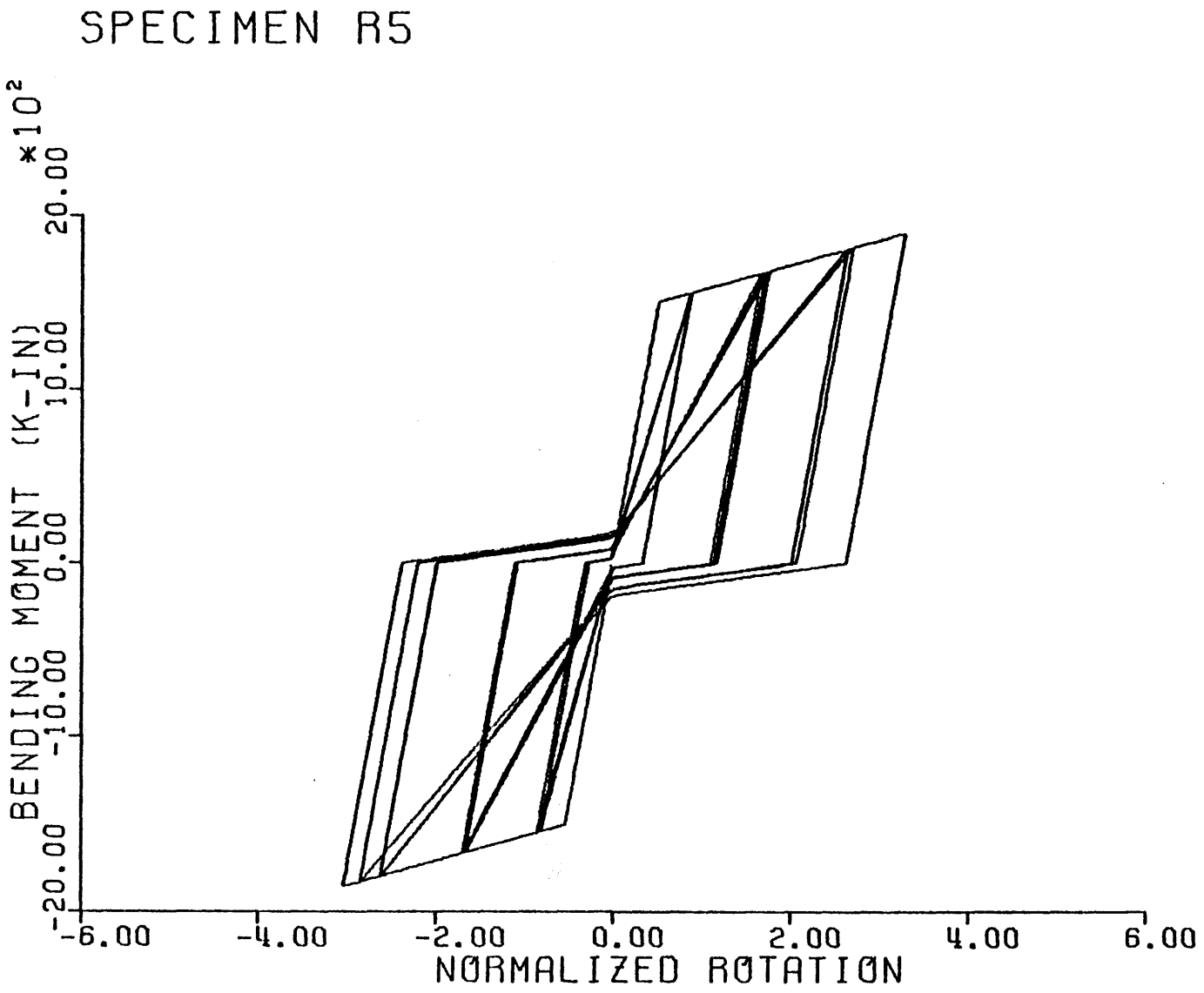

Fig. 3.41b - Moment-Rotation Relationship for Shear Spring in Specimen R5

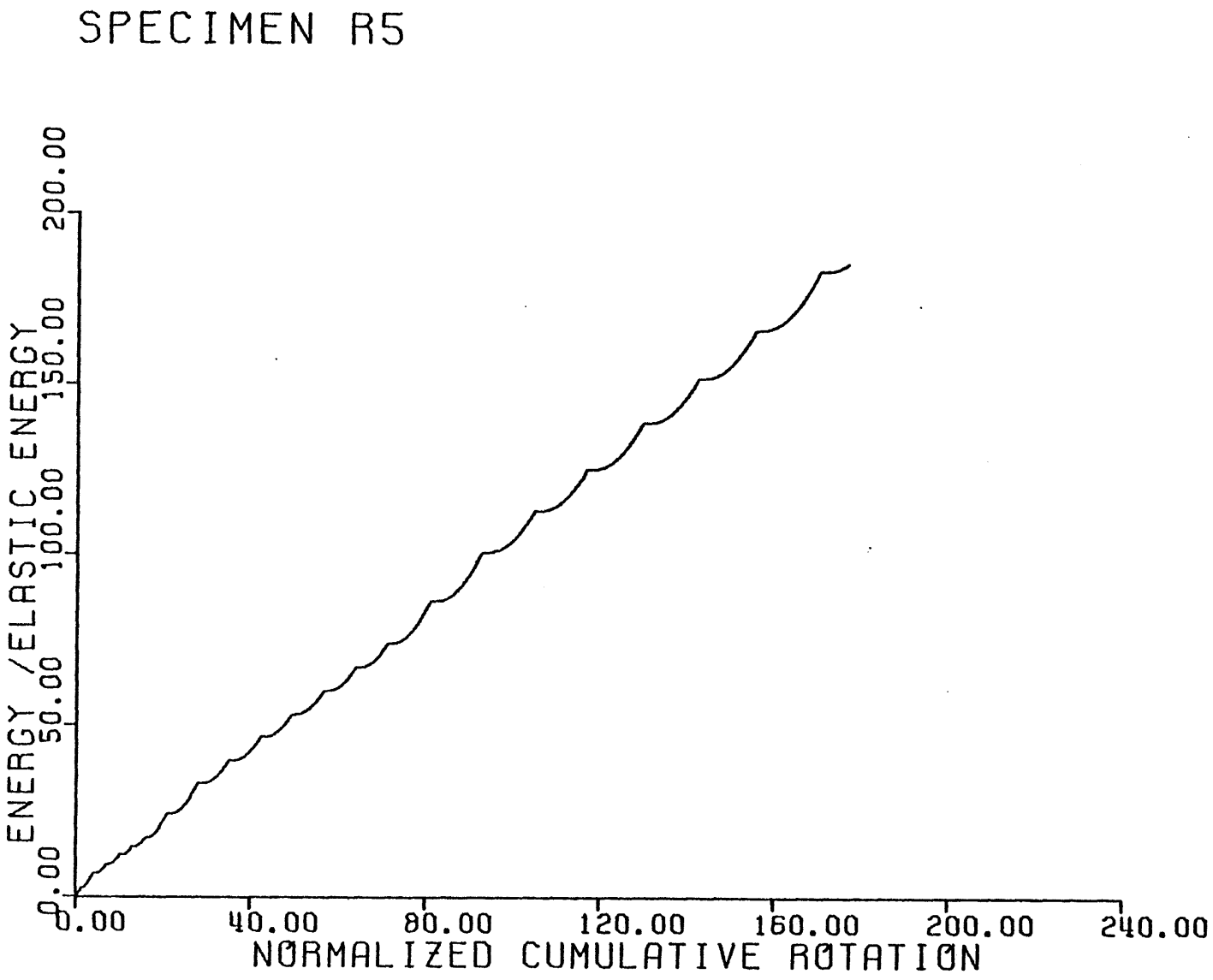

Fig. 3.41c - Energy Dissipation versus Normalized Cumulative Rotation for Flexural Spring in Specimen R5

Computed peak rotational ductilities were always higher than experimental rotational ductilities because computed elastic stiffnesses of members were always higher than their actual elastic stiffnesses. Comparison of other computed damage indicators with experimental results showed that dissipated energies and flexural damage ratios were accurate. Although peak rotational ductility is the most widely used parameter in practice, in view of the fact that it can not be accurately computed its use as a damage indicator is seriously questioned. Based on the results, flexural damage ratio seems to be a good substitute for peak ductility. These issues are discussed in more detail in the next chapter, where a stochastic model of damage based on damage indicators is developed.

Specimen	*Curvature Ductility (μ_ϕ)	**Rotation Ductility (μ_θ)	Energy	
			Kip-In.	Normalized
R1	8.3	4.3	335	123
R2	8.5	4.9	267	98
R3	8.3	4.9	583	215
R4	14.7	7.2	336	122
R5	10.5	4.4	349	160
R6	9.3	4.4	738	206
T1	8.6	4.1	519	181
T2	20.2	5.5	234	81
T3	11.2	4.2	803	222

* Average value over d/2 from beam support.

** δ_{max}/δ_y in the strong direction = μ_θ in the strong direction.

Table 3.1 - Experimental Values of Ductility and Energy for Specimens in the Test by Ma-Bertero-Popov (38).

Specimen	Experimental		Analytical
	Kip-In.	Normalized	
3	168	179	158
4	408	381	325
5	217	456	415
6	260	490	441
7	262	285	240
8	291	260	245
9	1267	290	197
10	1358	294	197
11	723	210	146
12	792	215	140

Table 3.2 - Comparison of Experimental and Analytical Energy Dissipations for the Tests by Scribner-Wight (52).

Specimen Specification	Rotation Ductility	Normalized Cumulative Rotation	Normalized Dissipated Energy	Curvature Ductility	Flexural Damage Ratio	$\tau/\sqrt{f'_c}$	P_a/P_b
R1	8.2	117.	116.	11.4	6.8	2.7	0.0
R2	8.9	113.	107.	10.5	7.8	2.7	0.0
R3	10.3	193.	199.	17.1	8.5	2.9	0.0
R4	13.9	70.	98.	24.0	10.6	3.3	0.0
R5	14.2	240.	220.	12.1	11.0	5.0	0.0
R6	8.9	187.	182.	9.7	7.4	3.1	0.0
T1	10.4	162.	169.	21.8	9.0	2.4	0.0
T2	14.6	36.	63.	31.2	11.4	2.7	0.0
T3	11.3	242.	249.	15.0	8.5	2.7	0.0
A4	7.8	282.	257.	9.0	8.7	1.2	0.25
A7	5.4	205.	180.	4.2	7.3	1.5	0.50
A8	5.4	168.	145.	4.2	7.3	1.5	0.50
A11	3.6	64.	60.	2.4	5.1	1.7	0.75
A12	3.0	60.	54.	2.1	4.0	1.7	0.75
H7	6.5	25.	24.	13.3	5.6	1.6	0.0
H9	10.5	84.	78.	26.9	8.3	1.9	0.0
W33	12.9	272.	269.	23.4	10.0	4.8	0.0
W35I	16.8	417.	457.	35.4	11.7	5.3	0.0
VBC3	8.1	96.	84.	23.4	8.2	3.0	0.0
F1	8.0	72.	64.	3.7	7.2	1.9	0.0
F4	11.7	162.	182.	8.0	9.4	2.2	0.0
P43	14.4	225.	227.	21.9	11.0	3.5	0.0
S3	13.0	142.	158.	11.1	10.4	2.6	0.0
S4	16.8	307.	325.	12.9	13.1	2.8	0.0
S5	22.0	356.	415.	15.2	14.6	3.1	0.0
S6	18.8	394.	441.	13.4	14.1	3.0	0.0
S7	15.1	249.	240.	9.2	13.1	2.7	0.0
S8	15.6	237.	245.	10.2	12.2	3.0	0.0
S9	15.3	245.	197.	11.8	14.1	3.8	0.0
S10	16.1	243.	197.	20.0	14.4	3.9	0.0
S11	14.2	157.	146.	12.7	11.4	4.7	0.0
S12	13.9	153.	140.	17.0	11.3	4.8	0.0

Table 3.3 - Damage Indicators for Specimens Tested in the Laboratory

CHAPTER IV - STOCHASTIC MODELING OF DAMAGE

4.1 Introduction

Previous chapters have focused on the modeling of reinforced concrete members using data from laboratory experiments. While the models are believed to be accurate up to small levels of damage, they become inaccurate as damage increases. Ordinarily, there is a level of damage beyond which the strength of the member is drastically reduced. We refer to this point as the "failure point" in this study. The goal of the present chapter is to calculate the probability that a member has reached such a failure point as a consequence of a certain amount of inelastic action. For this purpose, the experimental results are examined again to determine which set of damage parameters is the most indicative of the state of failure or survival of a member. A stochastic model of failure based on knowledge of these parameters are then developed.

4.2 Damage Parameters

The damage parameters which are listed below have been previously defined in Chapter II (Section 2.7). The present discussion is intended to describe the basis for choosing energy dissipation and damage ratio as the only parameters of the stochastic failure model.

Peak Rotation Ductility. This parameter is the one used most frequently as an indicator of damage. However, peak rotation ductility alone does not seem to be a good indicator of damage. For example, there are cases in which members fail after a large number of cycles at low ductility level. It should also be noted that peak rotation ductility conveys

information on inelastic rotation but not on strength. From comparison of experimental peak ductilities with analytical peak ductilities (Chapter III), it was observed that there is usually a very poor match between these two quantities. The reason is that the elastic stiffness of the analytical model was always higher than the initial stiffness of the actual member. On the other hand, the hysteretic behavior of the members was insensitive to this stiffness parameter.

Curvature (Moment) Ductility. The definition is based on a bilinear moment-curvature diagram (see Chapter II) which is inaccurate after the member has undergone a few inelastic cycles. The bilinear moment-curvature assumption may be relaxed, but then the Single Component Model cannot be used. Also, curvature ductility applies only to the member section with highest inelastic rotation, and provides no information about inelastic rotation along the member length. Therefore, it was decided not to use this parameter in the model.

Dissipated Energy. In this study, dissipated energy has been normalized with respect to the peak elastic energy that can be stored in the member while it is under antisymmetric bending. (Section 2.7). Although normalized dissipated energy is a good indicator of damage, it could be complemented with some other parameter. It is true, for example, that dissipated energy increases with the number of inelastic cycles, but members often fail due to a large rotation ductility even if very little energy is dissipated. Computed values of dissipated energy for the experiments (Chapter III) compare very favorably with analytical results.

Cumulative Plastic Rotation. A normalized value of cumulative plastic rotation as defined in Section 2.7 is used here. Figure 4.1 shows the relationship between this parameter and normalized energy for members tested in the laboratory. The high correlation (0.98) between these two parameters (to some degree due to the models of inelastic behavior) is not unexpected and indicates that one of the two parameters is redundant. In modeling failure, normalized dissipated enery has been retained, and cumulative plastic rotation has been deleted.

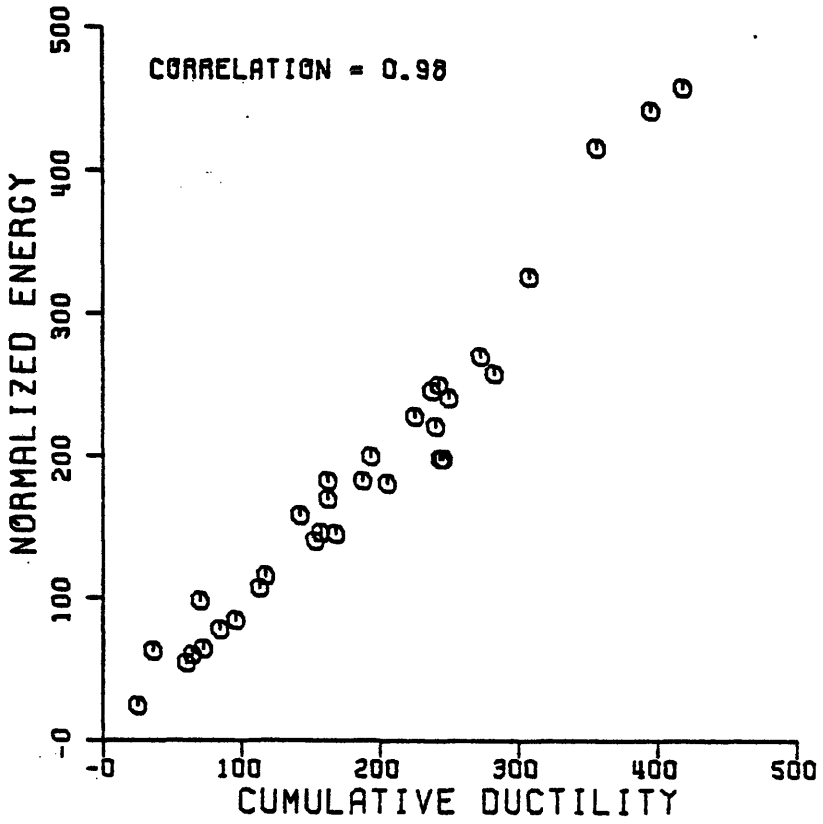

FIG. 4.1 - CORRELATION BETWEEN DISSIPATED ENERGY AND CUMULATIVE PLASTIC ROTATION FOR THE SAMPLE

Flexural Damage Ratio (defined in Chapter II, Section 2.7), depends both on peak inelastic rotation and on strength deterioration of a member. If one uses flexural stiffness of the member as a normalizing factor, then flexural damage ratio becomes independent of elastic stiffness. It is convenient to perform such a normalization because it is difficult to determine the elastic stiffness of a member with good accuracy. The advantage of using flexural damage ratio in place of peak rotation ductility is that the former parameter reflects strength degradation of the member.

All the above damage parameters are given in Table 3.3 for members tested in the laboratoy. The last two columns give the ratios $\tau/\sqrt{f'_c}$ and P_a/P_b: the former is the ratio of peak shear stress divided by concrete strength, and the latter is the ratio between axial load and the balanced point axial load. Data on shear stress was found to be inconclusive. For example, some members were able to dissipate large amounts of energy and attain high ductility levels even though they were subjected to high shear stresses (an indication of high overall strength). Although it is possible to fail members in shear, the frequent failure mode is a combination of flexure and shear. The assumption made here is that all members are designed to carry the ultimate shear load. Finally, data on axial load indicates that both energy dissipation capacity and flexural damage ratio decrease as the axial load in members increase. In spite of this trend and due to the small size of the sample (only five members tested with axial load), it was decided not to model this effect.

On the basis of the foregoing considerations, flexural damage ratio and normalized energy dissipation are chosen as the best pair of damage

indicators. Should one desire to include other parameters, the probabilistic models can be easily modified for that purpose.

4.3 Regression Model

Figure 4.2 displays all experimental failure data on a plane where the horizontal axis (D_1) is flexural damage ratio and the vertical axis (D_2) is normalized energy. Each point is the terminal point of a damage trajectory on the D_1D_2 plane. Trajectories start at ($D_1 = 1$, $D_2 = 0$) and are

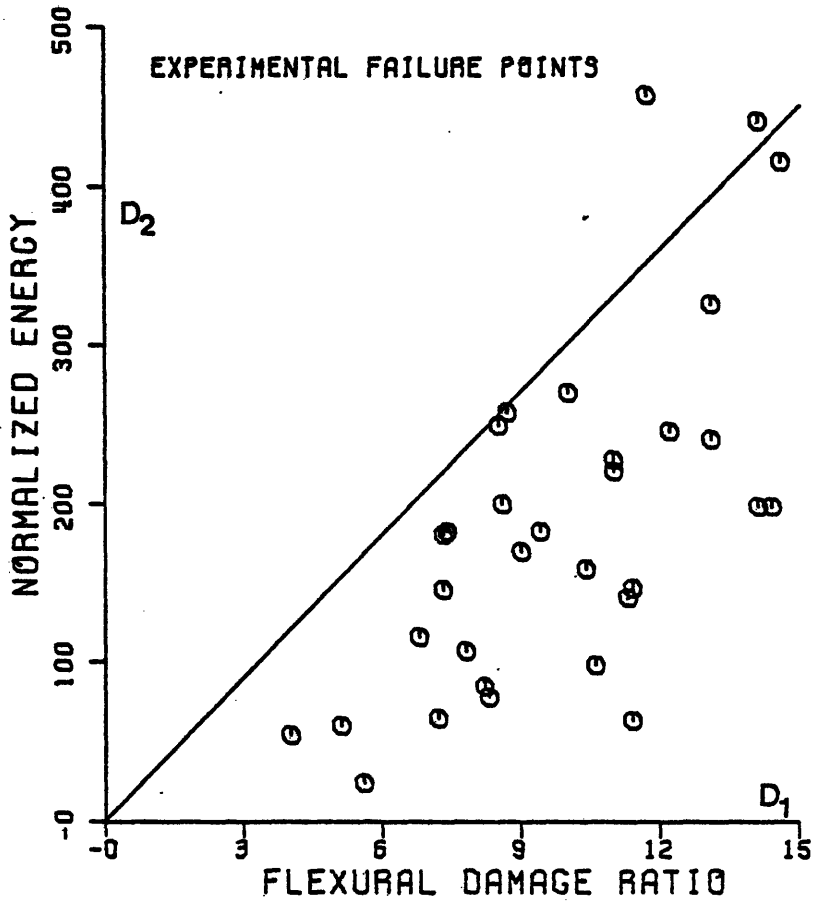

FIG. 4.2 - SAMPLE FAILURE POINTS ON THE D_1D_2 PLANE

such that D_1 and D_2 are non-decreasing functions of time. The trajectory is essentially controlled by the imposed displacement cycles, with some erraticity due to peculiarities of member and section properties. For each trajectory, one may define a failure indicator function $Z(D_1,D_2)$, as $Z(D_1,D_2) = 0$ if failure has not yet occurred at point (D_1,D_2) and $Z(D_1,D_2) = 1$ otherwise. In laboratory experiments, the trajectory can be traced only until Z first attains value 1. The two axes in figure 4.2 are scaled such that one unit of damage ratio corresponds to thirty units of energy. Most of the experimental failure points lie in the lower part of the figure, indicating that the sample does not include high-cycle fatigue experiments. Indeed, the purpose of the experiments was to produce failures at high levels of ductility, a condition that seems realistic in an earthquake environment. As a consequence, any extrapolation of the models described in this study to high-cycle fatigue (e.g., from wind or sea-wave loads) should be made with caution.

Within the present limitations on loading and failure paths, figure 4.3 represents a rather wide variety of cases. Specimen 8 in the experiment by Atalay and Penzien (A8) failed under high flexural and axial loads. Specimen R5 in the experiment by Ma, Bertero and Popov (38) was subjected to high shear and flexure. Specimen R4 in the same experiment was failed under flexure in just one cycle. Finally, specimen 43 in the experiment by Popov, Bertero, and Krawinkler (P43) failed in flexure after many cycles at increasing ductility levels. After examination of many experimental damage trajectories, and for the purpose of simplifying the analytical probabilistic model, it was decided to approximate each trajectory by a parabola of the type

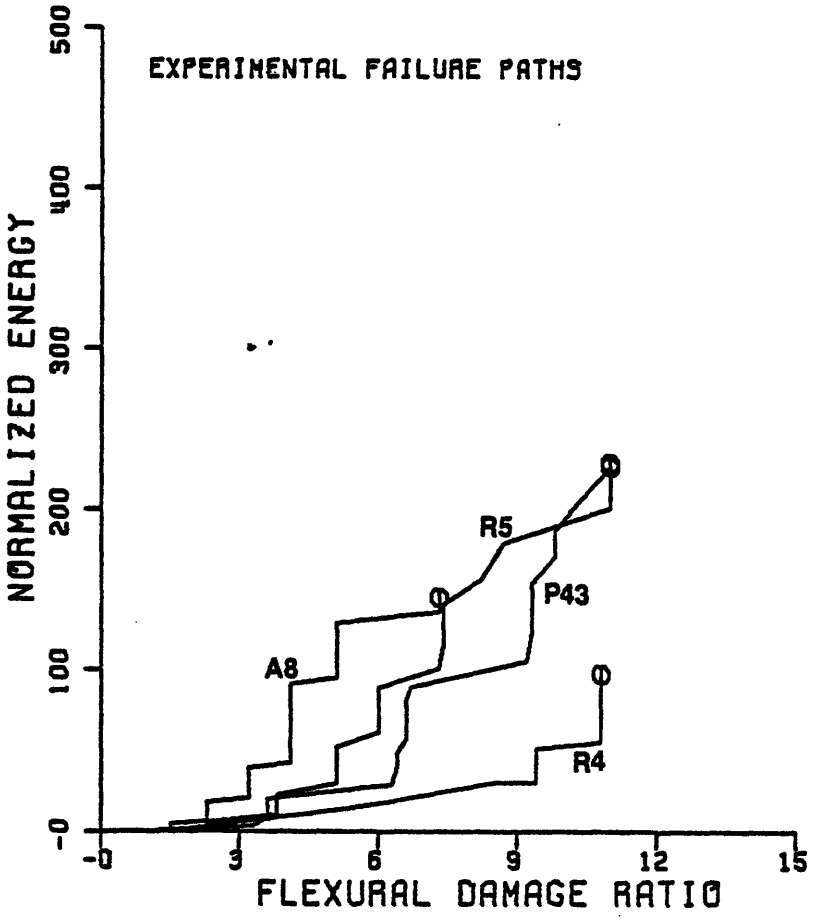

FIG. 4.3 - FAILURE TRAJECTORIES FOR SOME MEMBERS IN THE SAMPLE

$$D_2 = c(D_1 - 1)^2 \tag{4.1}$$

in which c is a constant parameter. An alternative representation of each failure point is in terms of X_1 = c and X_2 = length of the parabolic path, which is given by

$$X_2 = \int_1^{D_f} \sqrt{dD_1^2 + dD_2^2}\ dD_1 \tag{4.2}$$

where D_f = value of D_1 at failure. Figure 4.4 shows the distribution

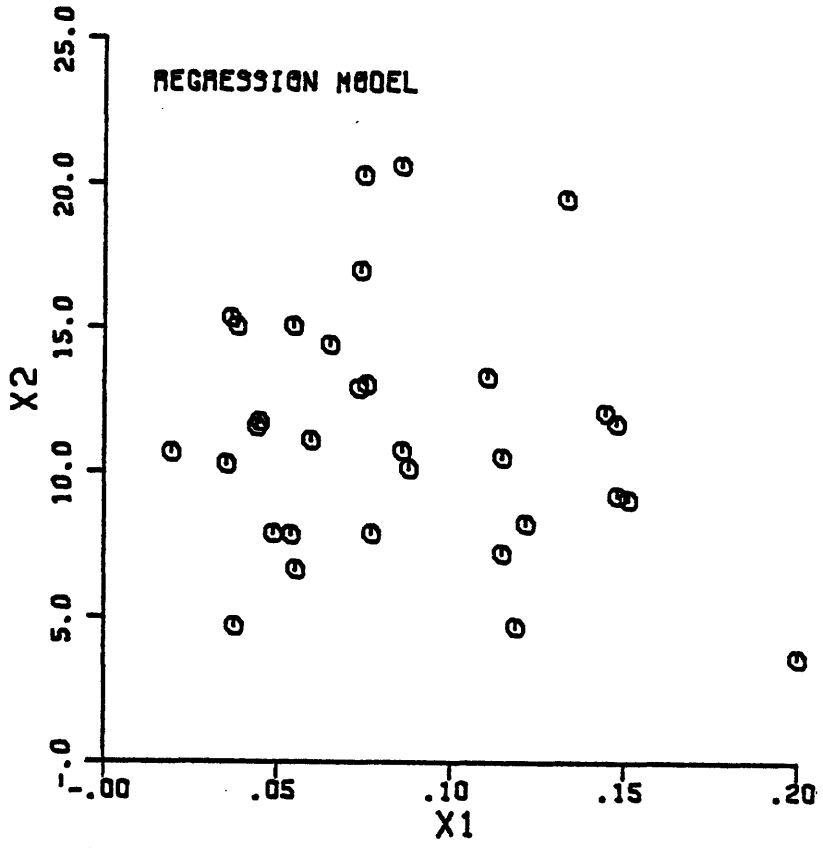

FIG. 4.4 - LENGTH OF FAILURE PATH (X_2) AS A FUNCTION OF DIRECTION PARAMETER X_1

of the experimental failure points on the X_1X_2 plane. For small values of X_2, the length of the failure path (X_2) is not sensitive to X_1. Therefore, for early failures, the distribution of distance to failure seems to be independent of path direction. On the other hand, the upper tail of the distribution of X_2 is sensitive to X_1. For example, if one excludes all values of X_2 smaller than 10 and runs a regression of X_2 on X_1, one finds

$$X_2 = 12.95 + 9.35\ X_1 \qquad (4.3)$$

The above regression is based on 21 data points. A regression with all values of X_2 larger than 13.0 gives

$$X_2 = 13.02 + 58.59\ X_1 \qquad (4.4)$$

The significance of the rapid increase in the coefficient of X_1 from Eq. (4.3) to Eq. (4.4) is that for longer damage paths, X_2 is more dependent on path direction. The positive value of the coefficient of X_1 also indicates that for a given length of damage path, the probability of failure is higher for high values of damage ratio than for high values of energy dissipation. This trend is clearly displayed by the experimental failure points in figure 4.2.

4.4 Stochastic Models of Damage

a) First Model

As mentioned earlier, the failure points in figure 4.2 mark the location of realizations of the damage process (Z) jump from value 0 to value 1. Let s denote distance along the damage path, and denote by $F_S(s)$ the cumulative distribution function (CDF) of distance to failure. If $f_S(s)$ is the probability density function (PDF) of s along a given damage path, then the "hazard function" (conditional failure rate) along that same path is defined as

$$\lambda_S(s) = \frac{f_S(s)}{1 - F_S(s)} \qquad (4.5)$$

Inversely, given λ_S, the CDF of s can be found from

$$F_S(s) = 1 - \exp\left[-\int_0^s \lambda_S(\xi)d\xi\right] \qquad (4.6)$$

In general, λ_S depends not only on the point $D = \begin{bmatrix} D_1 \\ D_2 \end{bmatrix}$ on the damage plane, but also on the local direction of the damage path and on the previous

trajectory. Fitting a nonparametric model to λ_S is clearly not possible because of too limited experimental data. However, one can restrict the family of functions λ_S by making parametric assumptions. First, we assume that, scaling the damage axes as in figure 4.2, λ_S depends only on $\underline{D}$ and not on path direction or past trajectory. Then with d and r as shown in figure 4.5 we generate models by making different assumptions about the form of $\lambda_S(\underline{D})$. Specifically, the first and simplest assumption is that the hazard function does not depend on r; hence that $\lambda_S(\underline{D}) = \lambda_S(d)$. This can be done by projecting the failure points on the 45° line shown in Fig. 4.5 and by then fitting a distribution to the projections.

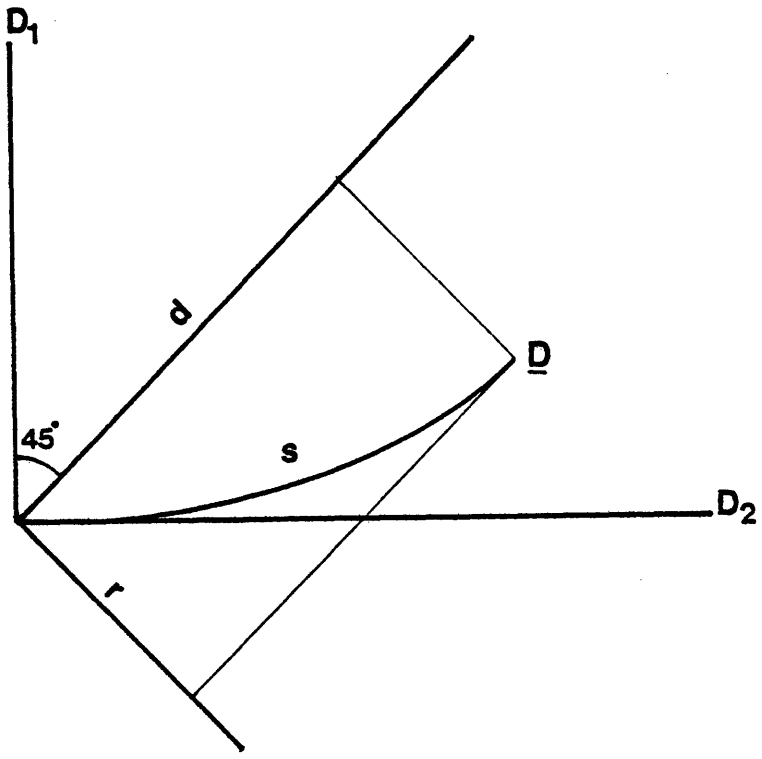

FIG. 4.5 - DEFINITIONS OF d AND r FOR HAZARD FUNCTION, $\lambda_S(\underline{D})$

Figure 4.6 shows the histogram of the projections. It may be noted that the minimin possible value of any projection is $\sqrt{2}/2$, which corresponds to the point at which all damage paths start. It has been judged desirable that the hazard function be an increasing function, i.e., that the conditional probability of failure given that a member has not failed increases as damage accumulates. A distribution model which satisfies this property and also fits well the data is the Extreme Type III with CDF,

$$F_D(d) = 1 - \exp\left[-\left(\frac{d - \sqrt{2}/2}{u - \sqrt{2}/2}\right)^k\right] \qquad (4.7)$$

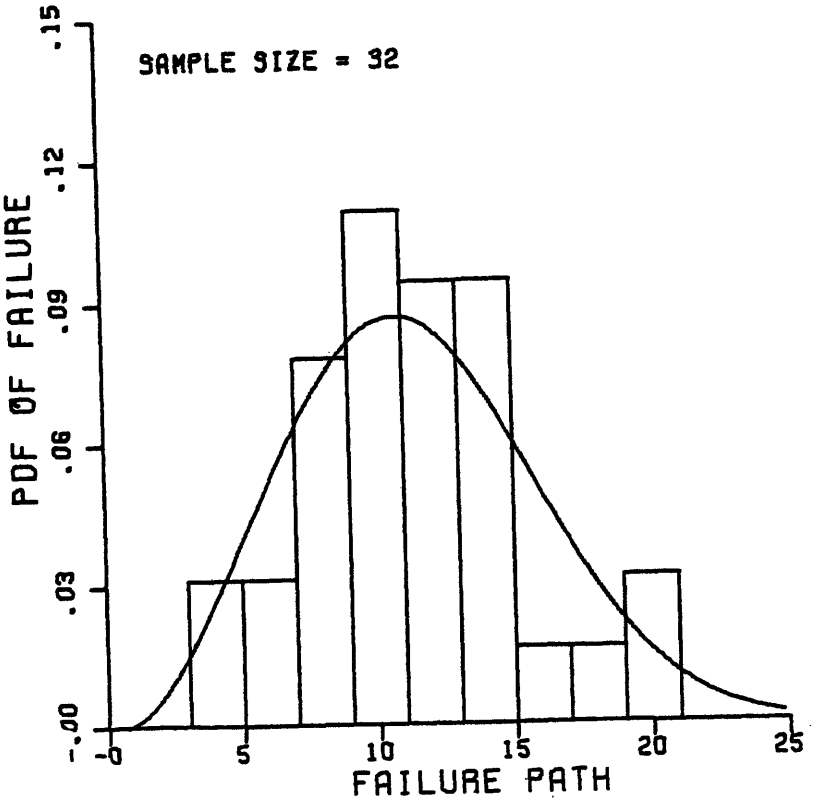

FIG. 4.6 - HISTOGRAM OF PROJECTIONS (d) AND PDF OF THE EXTREME TYPE III FIT

and parameters u and k. Taking twice the logarithm of both sides of Eq. (4.7) yields

$$\text{Ln}\left\{-\text{Ln}\left[1 - F_D(d)\right]\right\} = k\ \text{Ln}\ (d - \sqrt{2}/2) - k\ \text{Ln}\ (u - \sqrt{2}/2) \qquad (4.8)$$

The fitting of figure 4.7 refers to the last representation of the Extreme Type III distribution and gives k = 2.60 and u = 12.73. The associated hazard function has the form (20)

$$\lambda_D(d) = k\,\frac{(d - \sqrt{2}/2)^{k-1}}{(u - \sqrt{2}/2)^{k}} \qquad (4.9)$$

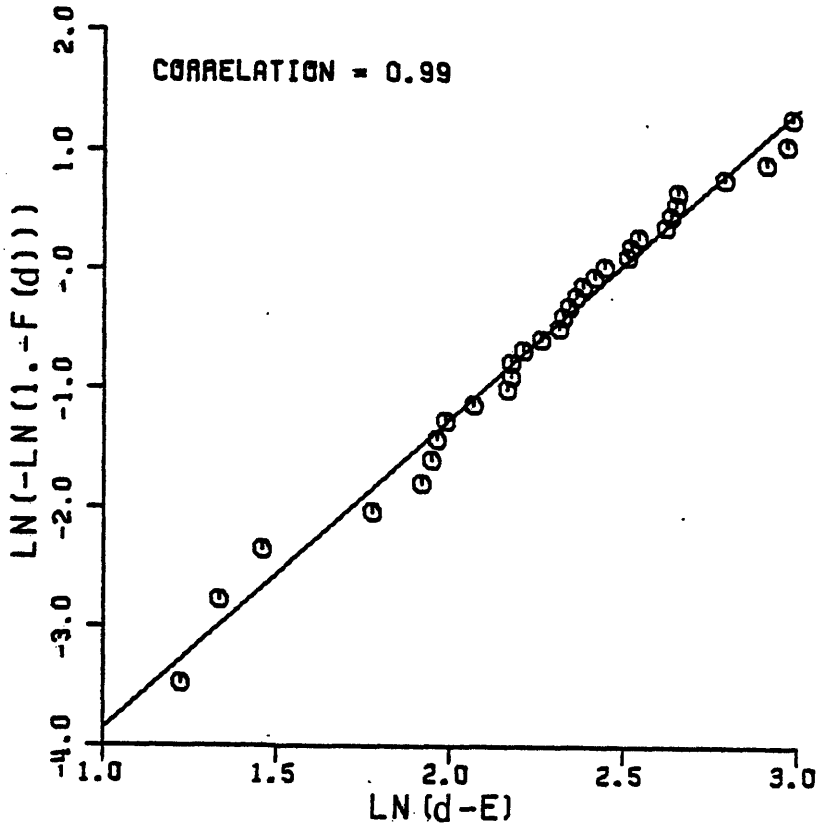

FIG. 4.7 - THE EXTREME TYPE III PROBABILITY DISTRIBUTION FIT, FIRST MODEL

(See Fig. 4.8). Using this result, contours of equal probability of failure in the damage plane are shown in figure 4.9.

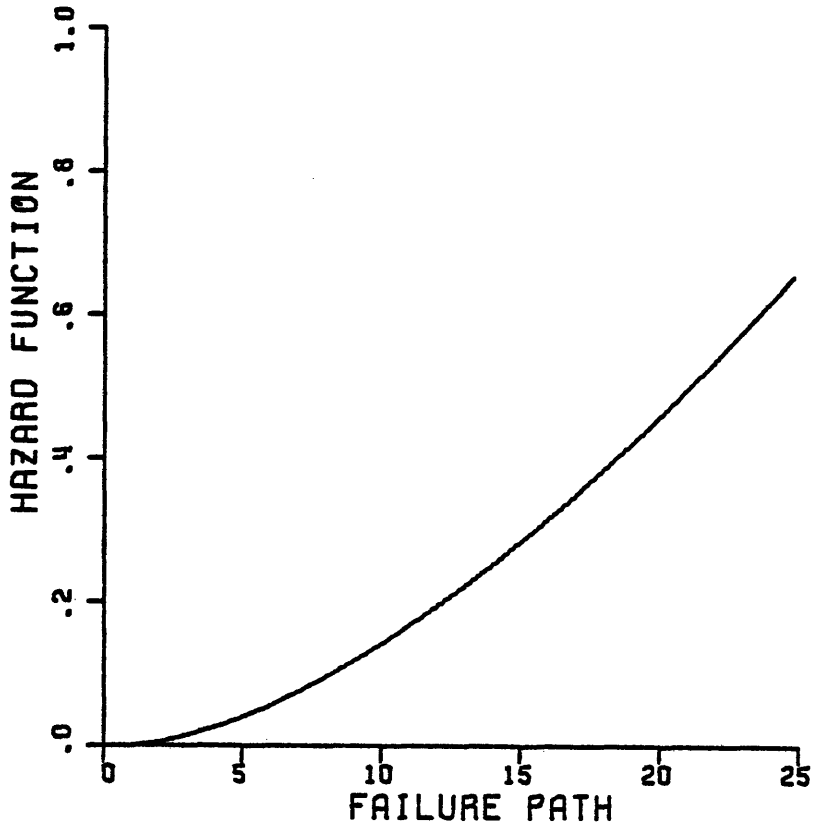

FIG. 4.8 - HAZARD FUNCTION FOR THE EXTREME TYPE III DISTRIBUTION FIT

b) Second Model

Assuming that the hazard function does not depend on r (see Fig. 4.5), results in erroneous calculation for the probability of failure if the stochastic process Z(0,1) is path dependent. The regression analysis in Section 4.3 suggests that this is in fact the case. In the model developed next, we retain the assumption that damage paths are parabolic and that the hazard function does not depend on the direction of the damage

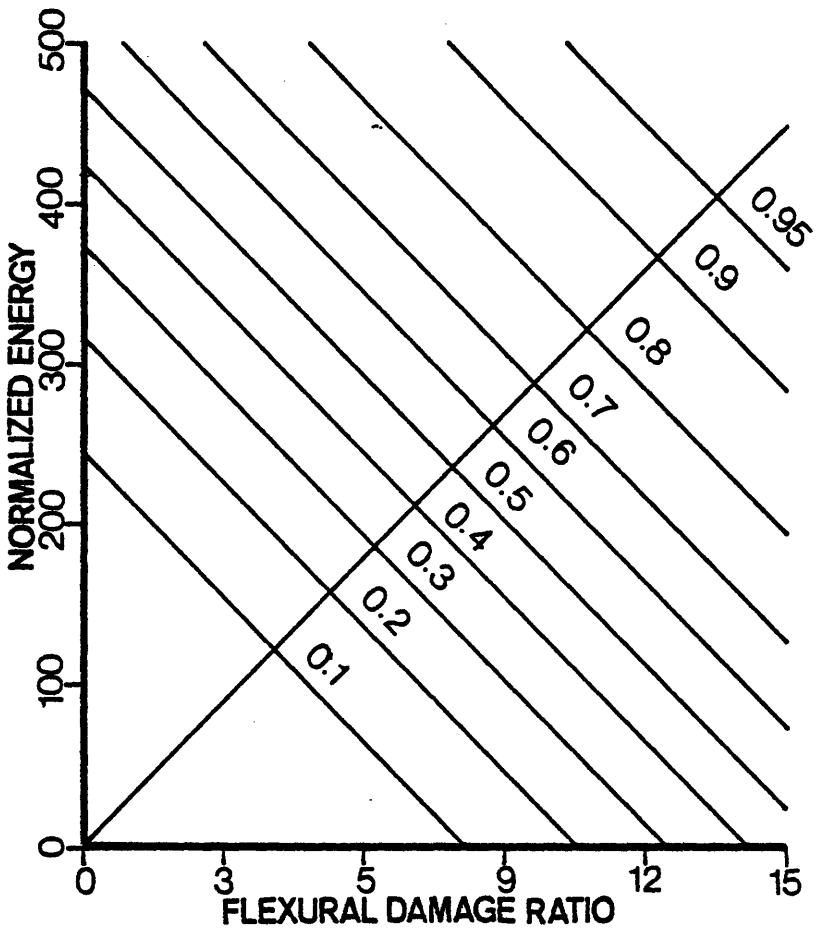

FIG. 4.9 - CONTOURS OF FAILURE PROBABILITY, FIRST MODEL

trajectory point. However, we assume that λ_S depends on both d and r in a multiplicative way:

$$\lambda_S(d,r) = \lambda_S(d) \cdot \lambda_S(r) \tag{4.10}$$

To be consistent with the first method, $\lambda_S(d)$ is taken to be the hazard function of the Type III Distribution, (Eq.(4.9)), and $\lambda_S(r)$ is parametrized as follows

$$\lambda_S(r) = e^{ar} \tag{4.11}$$

Hence, for a = 0 this model reduces to that studied previously. The probability density function of the location of failure is now

$$f_S(s|a) = \exp\left[-\int_0^s \lambda_S(\xi|a)d\xi\right] \lambda_S(s|a) \qquad (4.12)$$

where integration is along a given path in the damage plane.

If the method of maximum likelihood is used to estimate the parameter a, one needs to maximize the quantity

$$L(a,k,u \mid s_1, s_2, \ldots s_{32}) = \prod_{i=1}^{32} f_S\,(s_i|a,k,u) \qquad (4.13$$

In general, also the distribution parameters k and u may be estimated by the method of maximum likelihood. However, for the purpose of comparison, k and u are here fixed to the values found previously. The likelihood, now reduced to a function only of a, is shown in figure 4.10. The best

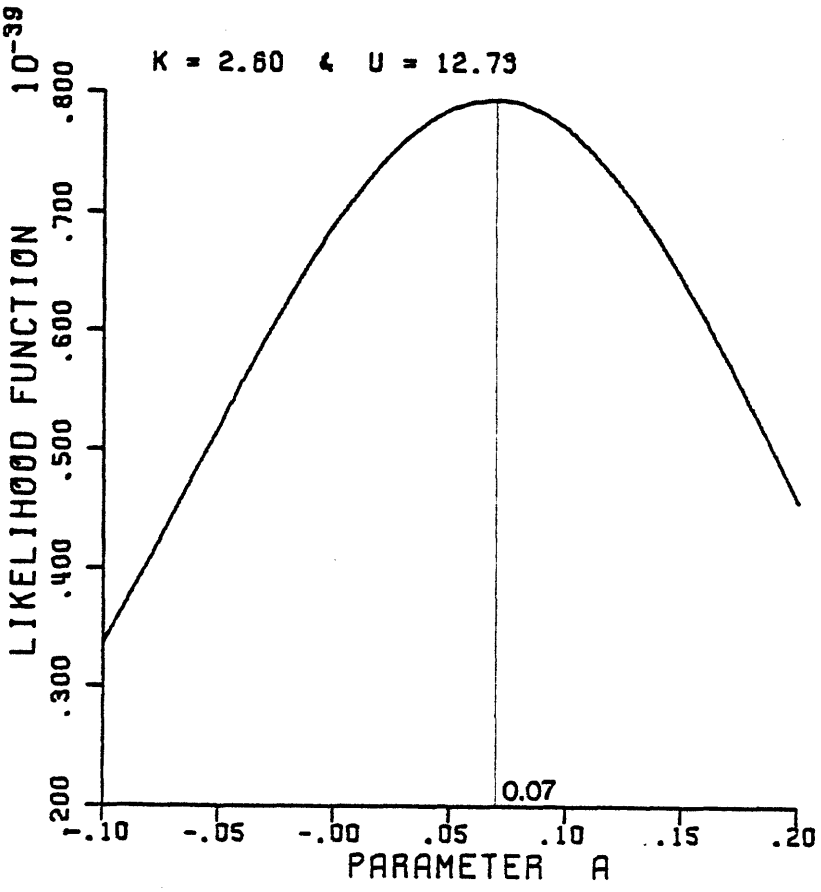

FIG. 4.10 - LIKELIHOOD AS A FUNCTION OF PARAMETER a

estimate of a is 0.07, and using this value one finds the contours of equal probability of failure in figure 4.11. Comparison with figure 4.9 shows that the present contours penalize higher flexural damage ratios. This characteristic of the present model is consistent with previous conclusions in Section 4.3, where damage ratio was found to be more important than energy in the case of long failure paths. In other words, the failure path is expected to be longer if the member is dissipating energy rather than undergoing higher ductility levels. Contours of the type in figure 4.11 can be used to estimate the probability of section failures in non-linear dynamic analysis of reinforced concrete frames.

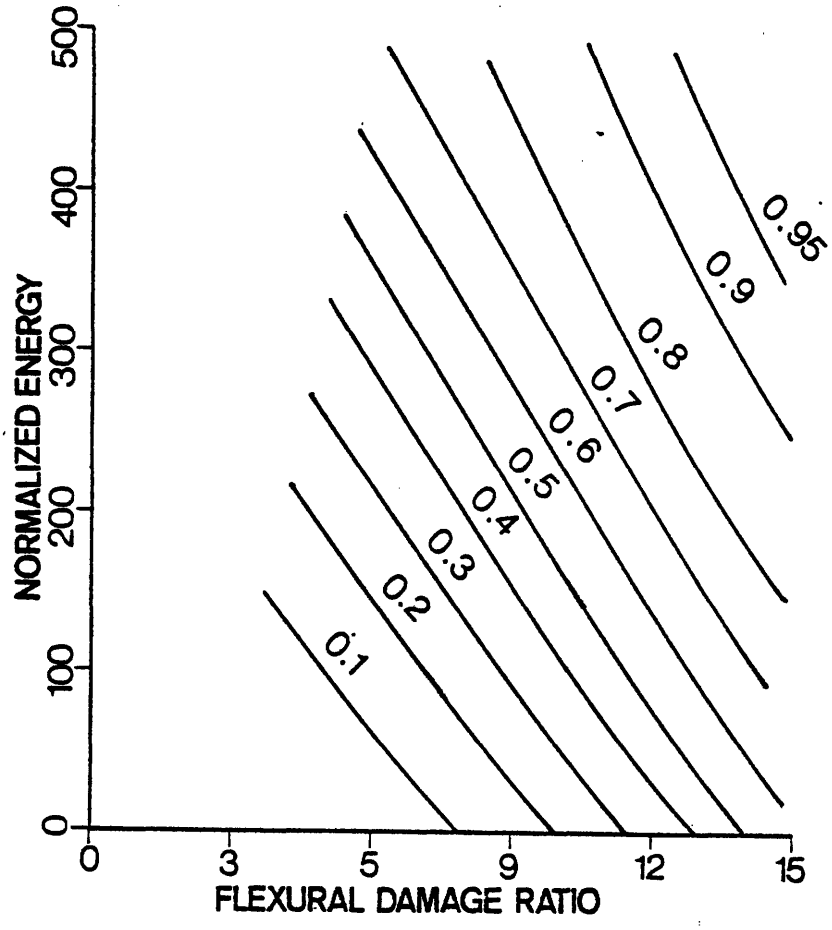

FIG. 4.11 - CONTOURS OF FAILURE PROBABILITY, SECOND MODEL

c) Bayesian Approach

The likelihood of figure 4.10 is a rather flat function of a, indicating that the maximum likelihood estimator is affected by large statistical uncertainty. A way to account for this uncertainty is by using a Bayesian procedure which treats a as a random variable. If a has prior noninformative flat distribution, then the posterior density is proportional to the likelihood function. From figure 4.10, one can see that in the neighbourhood of 0.07, the likelihood function behaves like a normal density function of the type

$$f_A(a) = \frac{1}{\sigma_a\sqrt{2\pi}} \exp\left[-\frac{1}{2}\left(\frac{a - m_a}{\sigma_a}\right)^2\right] \qquad (4.14)$$

The mean (m_a) and the standard deviation (σ_a) were found to be approximately 0.07 and 0.127. The posterior Bayesian distribution of the distance to failure along a given path can be found from the total probability theorem, which gives

$$F_S(s) = \int_{-\infty}^{\infty} F_S(s|a)\, f_A(a)\, da \qquad (4.15)$$

In order to investigate sensitivity to uncertainty in a, 9 points with probability of failure according to maximum likelihood $F_S(s|a=0.07)$ = 0.1, 0.5, and 0.9 were chosen and their Bayesian failure probabilities were calculated using Eq. (4.15). Table 4.1 summarizes the results. Points 2, 5 and 8 are on the damage path where λ_S is not a function of a (Fig. 4.5); therefore Bayesian and maximum likelihood results are the same in these cases. Figures 4.12 a, b, and c show the conditional CDF of failure, $F_S(s\ a)$ as a function of parameter a, for the points, with maximum likelihood failure probabilities of 0.1, 0.5, and 0.9, respectively. The

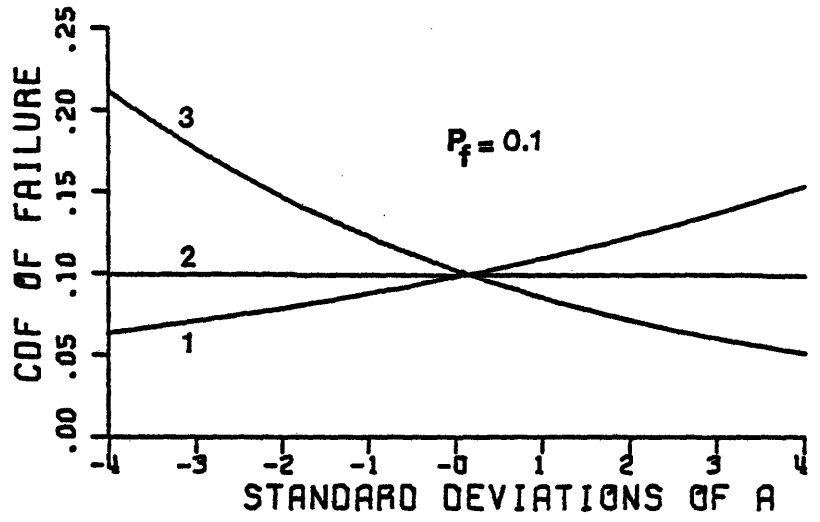

(a)

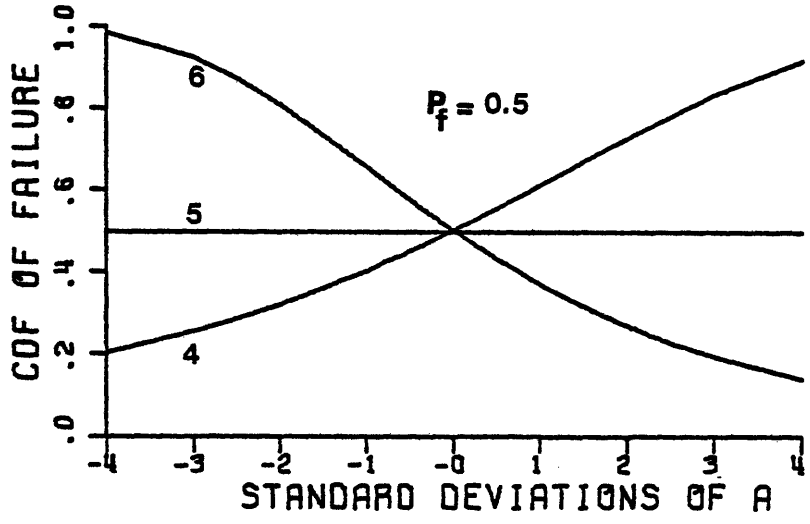

(b)

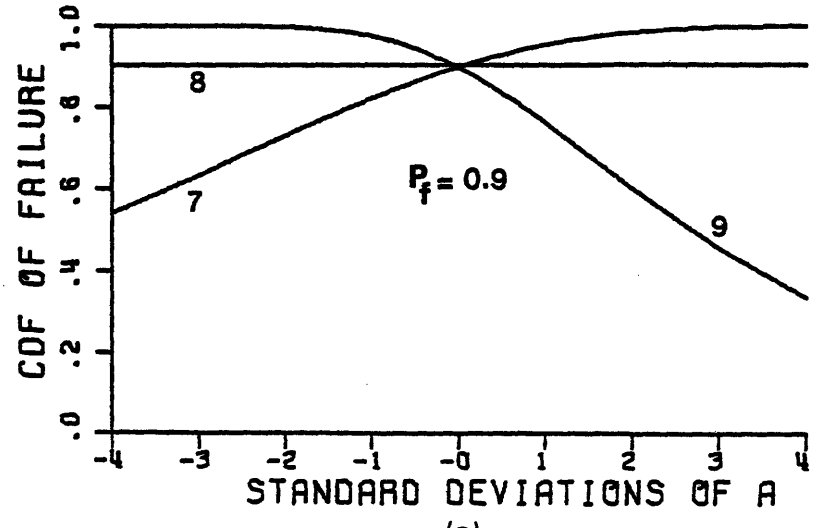

(c)

FIG. 4.12 - CONDITIONAL CDF OF FAILURE, $F_S(s|a)$, AS A FUNCTION OF PARAMETER a

curves show that if one uses the Bayesian approach one should expect an increase of failure probabilities over the maximum likelihood values if $F_S(s|a)$ is less than or equal to 0.5. However, for higher values of $F_S(s|a)$, Bayesian failure probabilities are expected to be smaller than the associated maximum likelihood probabilities. Overall, one may conclude that the probability of failure is not sensitive to uncertainty in a. This means that the maximum likelihood procedure may be employed with good accuracy.

Point	Damage Ratio	Energy	$F_S(s\|a)$	$F_S(s)$
1	7.0	27.8	0.10	0.10
2	6.1	60.2	0.10	0.10
3	4.8	111.4	0.10	0.104
4	11.9	90.5	0.50	0.513
5	9.8	177.3	0.50	0.50
6	7.2	299.9	0.50	0.516
7	14.9	245.7	0.90	0.896
8	13.2	340.6	0.90	0.90
9	10.4	493.5	0.90	0.878

TABLE 4.1 - MAXIMUM LIKELIHOOD PROBABILITIES OF FAILURE AND BAYESIAN PROBABILITIES OF FAILURE FOR 9 SELECTED POINTS

CHAPTER V - APPLICATION OF METHODS TO INELASTIC DYNAMIC ANALYSIS OF FRAMES

5.1 Introduction

A methodology for computing probabilities of member failure under inelastic load cycles is developed in Chapter IV. Applications of the model to inelastic dynamic analysis of building frames is discussed in this chapter. A 4-story and an 8-story building frame were chosen, and inelastic dynamic analyses of these frames under several different earthquake motions were carried out. Probabilities of local failure were computed for each case, and a method is also developed to compute the reliability of the system.

5.2 Design of Building Frames in Accordance with U.B.C. Specifications

The two building frames which are extensively analyzed in this chapter were designed by Lau(35). These are a 4-story frame and an 8-story frame designed according to the Uniform Building Code [1973 version]. Base shear for each frame is calculated by

$$V = ZKCW \tag{5.1}$$

where V = the total base shear

Z = seismic coefficient depending on site. This parameter is taken as 1 (Zone 3) in these designs.

K = seismic coefficient depending on the type of structure. $K = 0.67$ (moment-resisting frame) is used here.

$C = \frac{0.05}{\sqrt[3]{T}}$ where T is the fundamental period of the structure.

W = total weight.

Elevation and plan views of the two frames appear in figures 5.1 and 5.2. Once the base shear is calculated, it is distributed along the height, assuming a linear variation. In the 4-story frame, all girders have 12" x 20" sections, and all columns have 12" x 18" sections. All girders in the 8-story frame have 12" x 22" cross sections. Columns in the first three stories of the 8-story frame have 12" x 25" secions, and all other columns have 12" x 22" sections. A dead load of 120 psf is assumed for both frames; live loads for these frames were 40 psf for the 4-story frame and 50 psf for the 8-story frame. For dynamic analysis, 100 percent of dead load and 25 percent of live load were put on each floor.

Yield moment capacities of beams and columns for these frames are listed in Tables 5.1 and 5.2. Concrete strengths for both frames is 4000 psi. Since detailed member designs were not carried out, it was assumed that all beams and columns have equal stiffnesses in positive and negative loading directions. Furthermore, the effective stiffness of each beam and column is taken to be 45 percent and 60 percent of elastic stiffnesses, respectively. Using these assumptions, natural periods of the 4-story and 8-story frames were found to be 0.86 seconds and 2.0 seconds, respectively.

5.3 Prediction of Local Damage in Building Frames

A building frame which is designed according to seismic codes is expected to withstand moderate earthquakes without substantial damage. It is not only desirable to spread the damage in a reinforced concrete frame throughout the members, but also catastrophic failure of columns must be prevented. Damage prediction models developed in this study may be used to assess the overall safety of a building under a given earthquake.

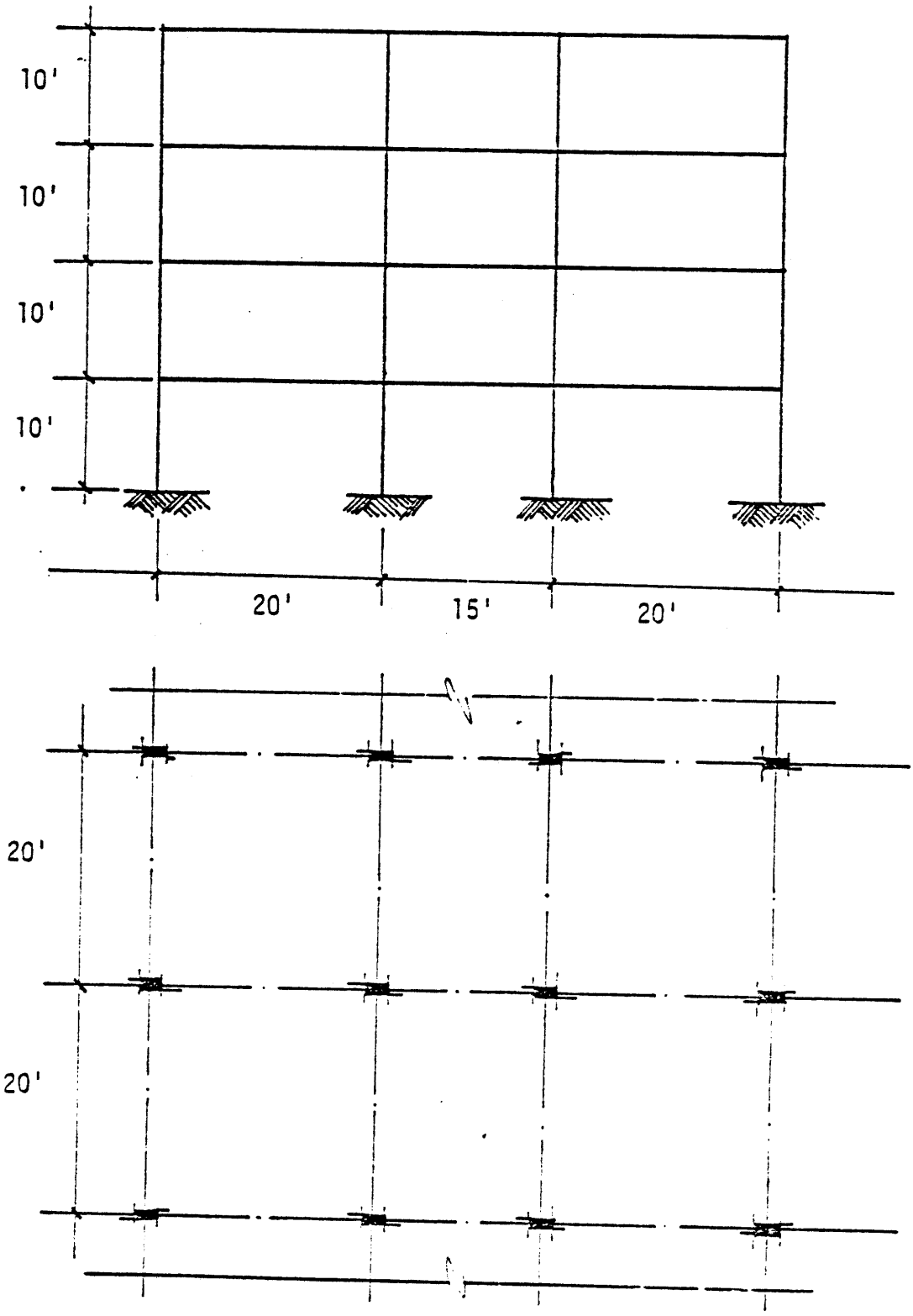

FIG. 5.1 - ELEVATION AND PLAN VIEW OF 4-STORY BUILDING FRAME

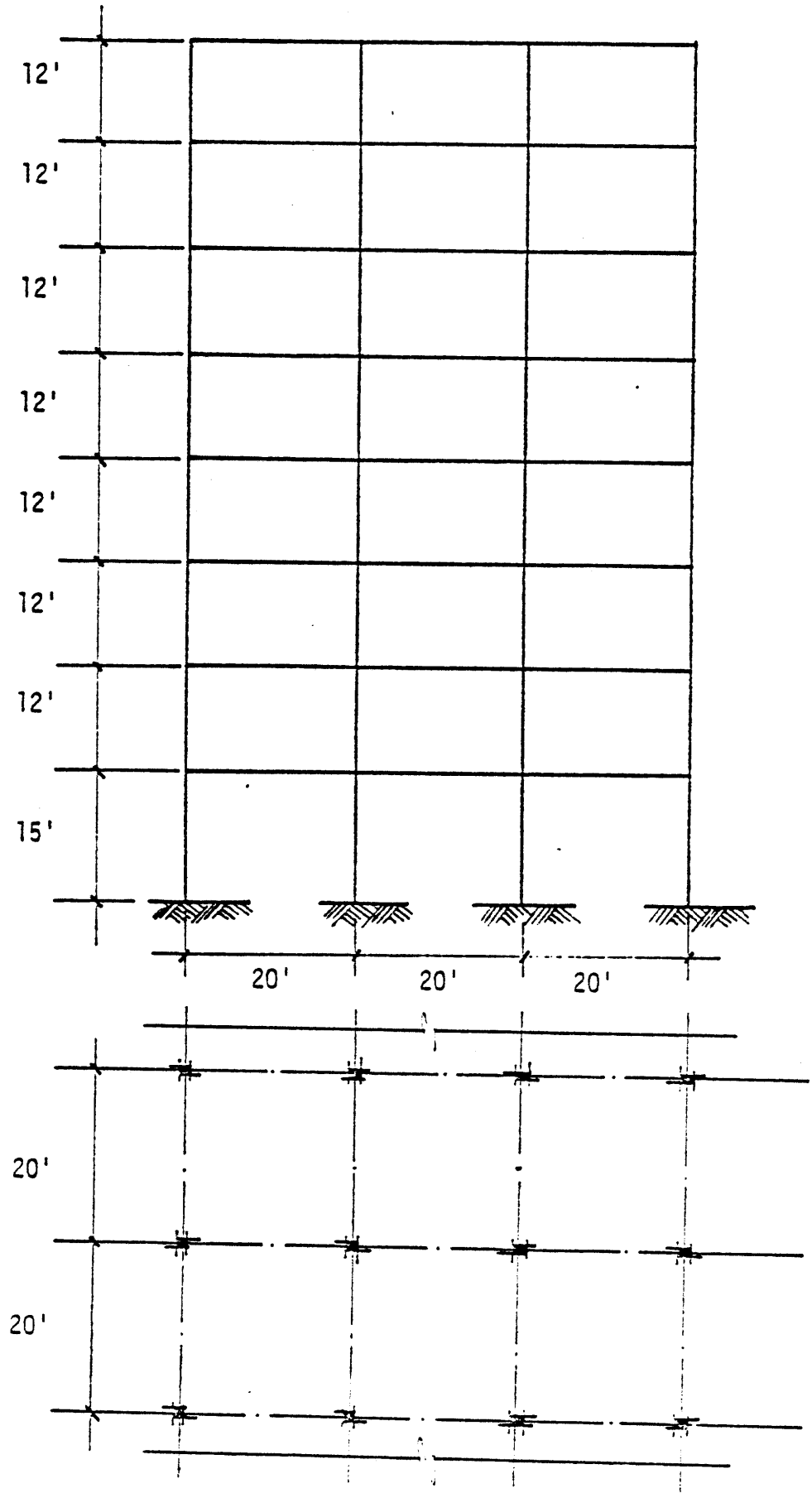

FIG. 5.2 - ELEVATION AND PLAN VIEW OF 8-STORY BUILDING FRAME

Figure 5.3 shows the hinges formed in the 4-story frame when it is subjected to the El Centro earthquake (Peak Acceleration = 0.35g). The number on each hinge indicates the probability of local failure in accordance with the second model presented in Chapter IV. For practical reasons, all probabilities less than 0.01 are omitted, because they are too small to be significant. Only one of the base columns and all three girders on the first floor exhibit appreciable damage. Figures 5.4a,b show the damage paths for one of the base columns and one of the girders on the D_1D_2 plane. It may be noted that far less energy was dissipated in these members compared to experimental cyclic load tests. Thus, most of the hazard

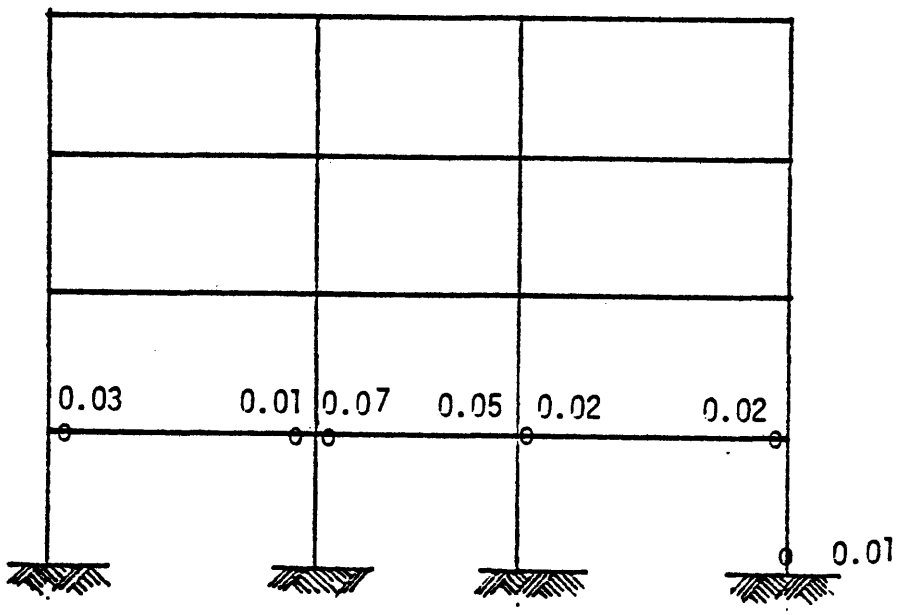

Fig. 5.3 - Member Failure Probabilities for El Centro Earthquake (Peak Acceleration = 0.35g)

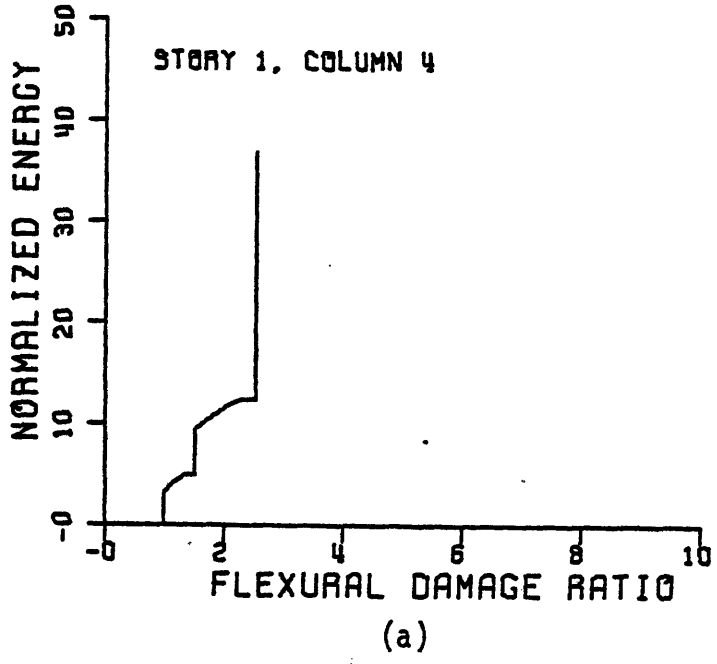

(a)

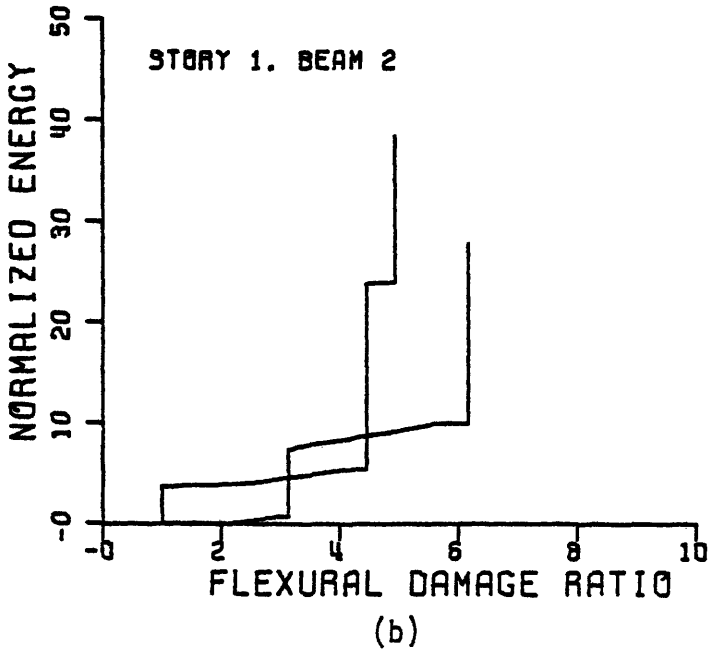

(b)

Fig. 5.4 - Damage Paths for Two Members of the 4-Story Frame Subjected to El Centro Earthquake

in local failures is due to damage ratio. If the same building frame is subjected to the Kern County (Olympia) earthquake scaled up to the same peak acceleration, only one of the girders is damaged (Fig. 5.5). However, if the same earthquake motion is scaled up to a peak acceleration of 0.5g, damage spreads over all the structure (Fig. 5.6). Figures 5.7a,b show the damage paths for two of the girders.

Local failure probabilities for the 8-story frame subjected to El Centro (Peak Acceleration = 0.35g) are shown in figures 5.8a,b. In this case there is a concentration of damage in stories 6 and 7. The reason is that the second mode of this frame is important when it is subjected to earthquake motions. Also, much higher probabilities of local failure are observed in the columns compared to the 4-story frame, which is not a desirable feature. Damage paths for one of the columns and one of the girders of this frame are shown in figures 5.9a,b.

5.4 System Reliability under Seismic Loads

If the probability of failure of each member of a system subjected to a given earthquake is known, then it is possible to calculate bounds on the probability P_s that all members will survive. If member resistances are independent, then the events (failure/survival) of various members are also independent and the probability that no failure occurs is simply

$$P_s^L = \prod_i (1 - P_i) \quad , \tag{5.2}$$

in which P_i = failure probability for the i^{th} member. On the other hand, for perfectly dependent member resistances, the reliability of the frame

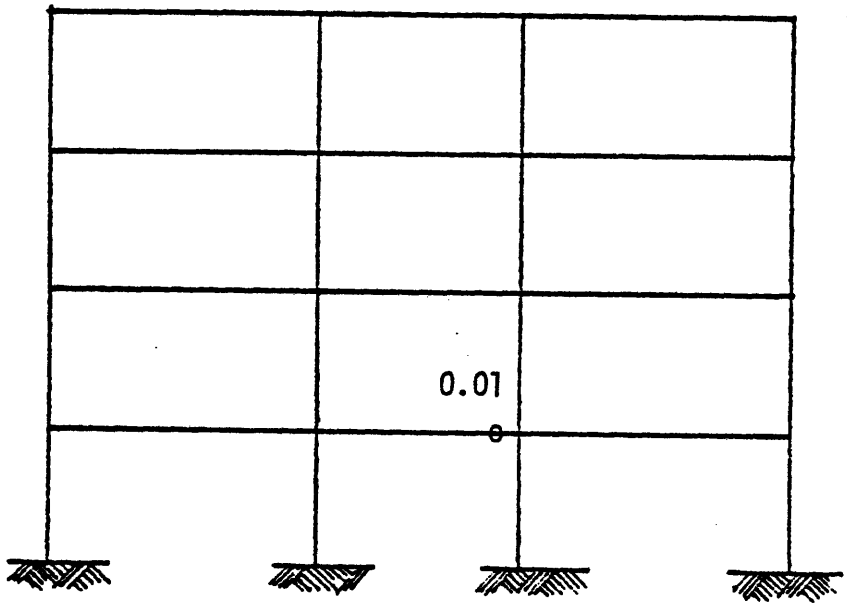

Fig. 5.5 - Member Failure Probabilities for Kern County Earthquake
(Peak Acceleration = 0.35g)

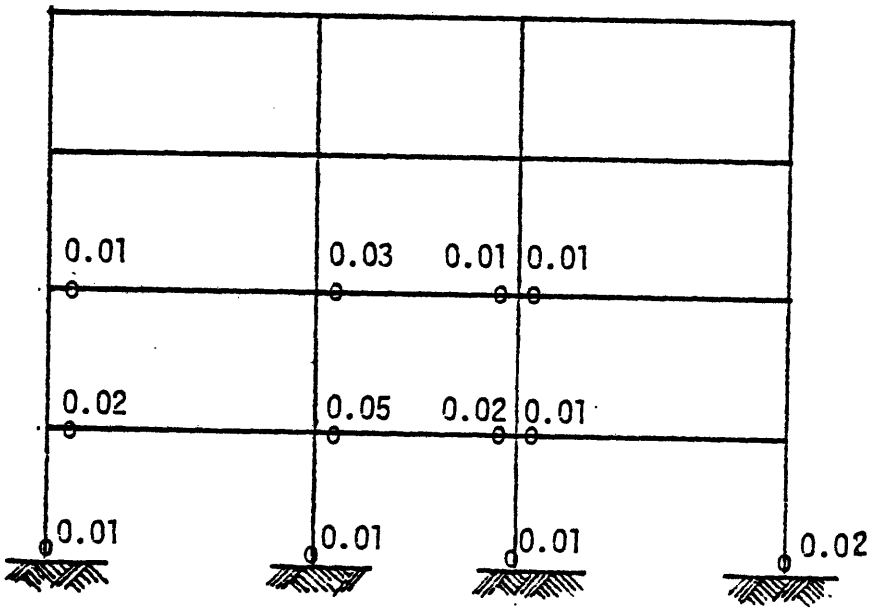

Fig. 5.6 - Member Failure Probabilities for Kern County Earthquake
(Peak Acceleration =0.50g)

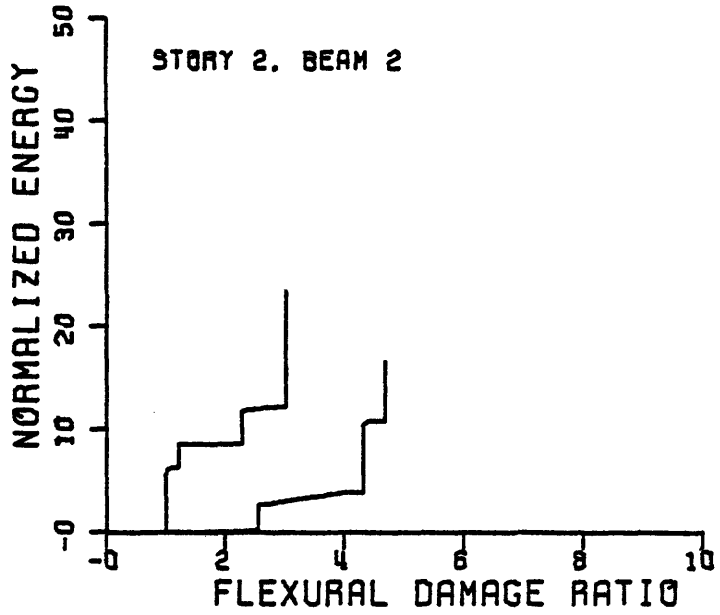

(a)

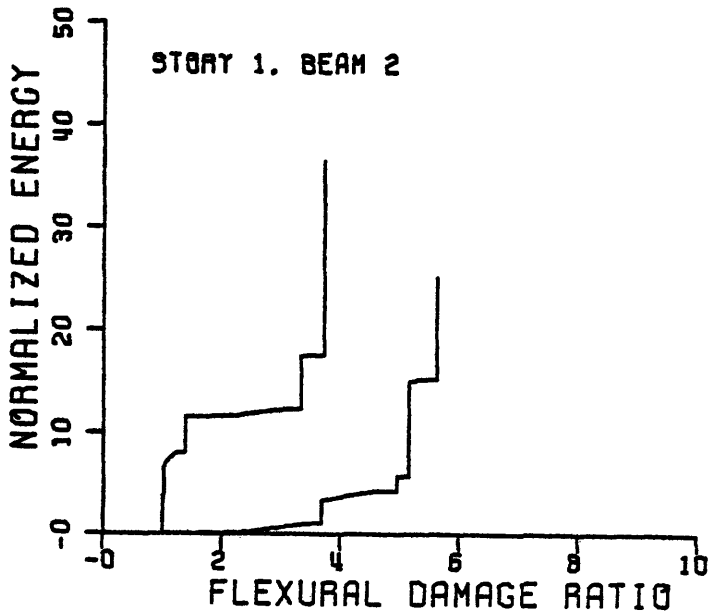

(b)

Fig. 5.7 - Damage Paths for Two Girders of the 4-Story Frame Subjected to Kern County Earthquake

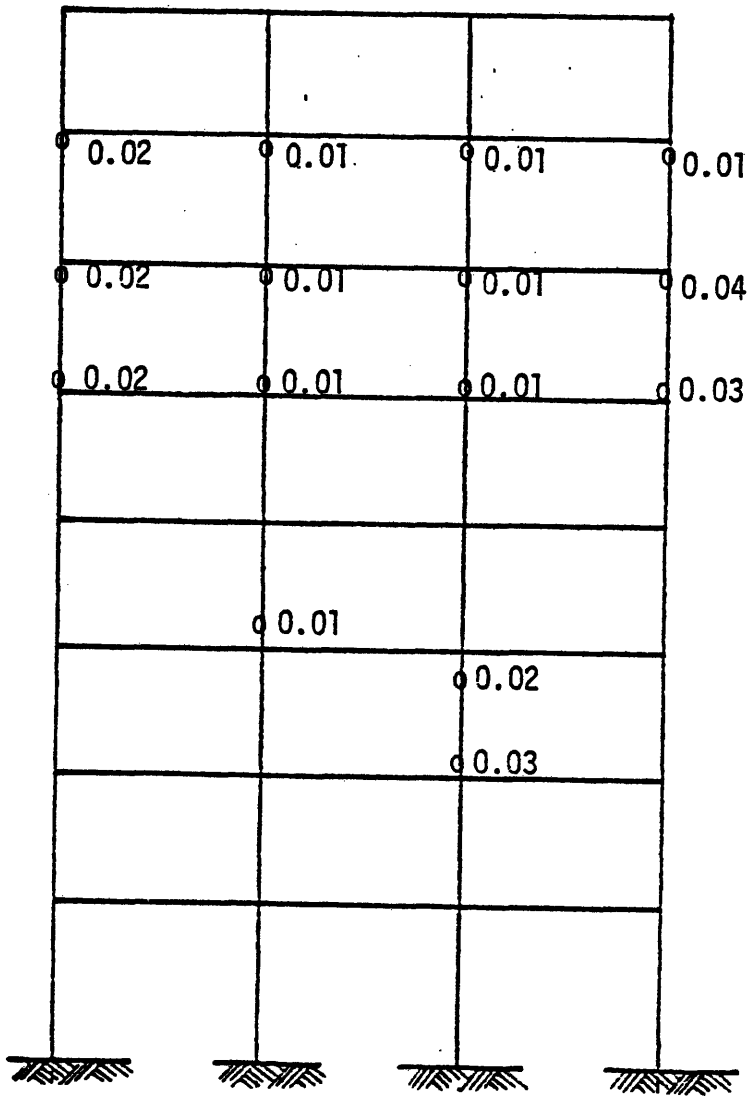

Fig. 5.8a - Column Failure Probabilities for El Centro Earthquake
(Peak Acceleration = 0.35g)

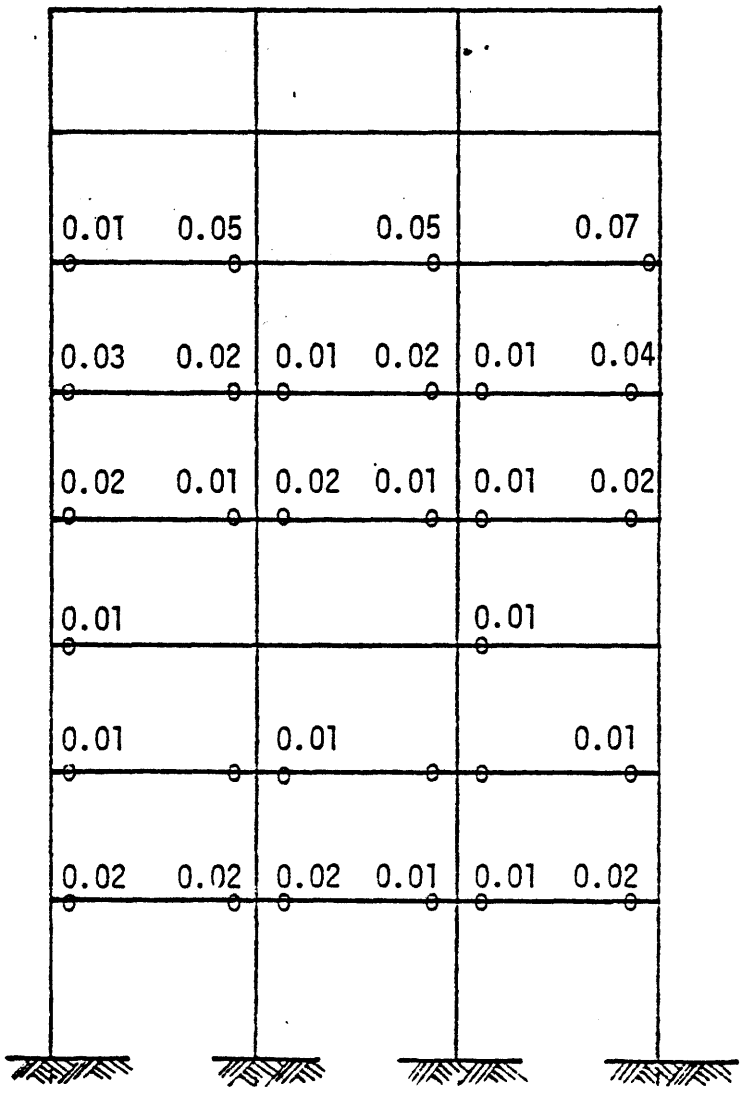

Fig. 5.8b - Girder Failure Probabilities for El Centro Earthquake (Peak Acceleration = 0.35g)

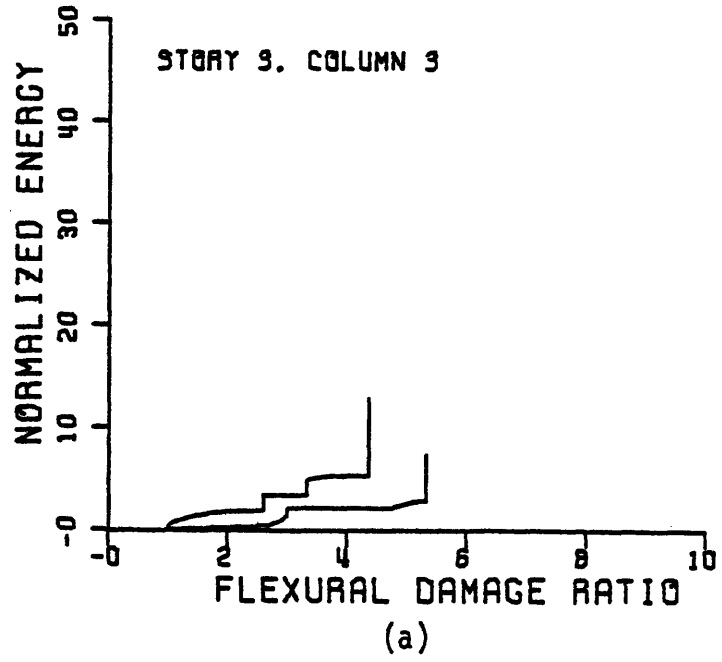

(a)

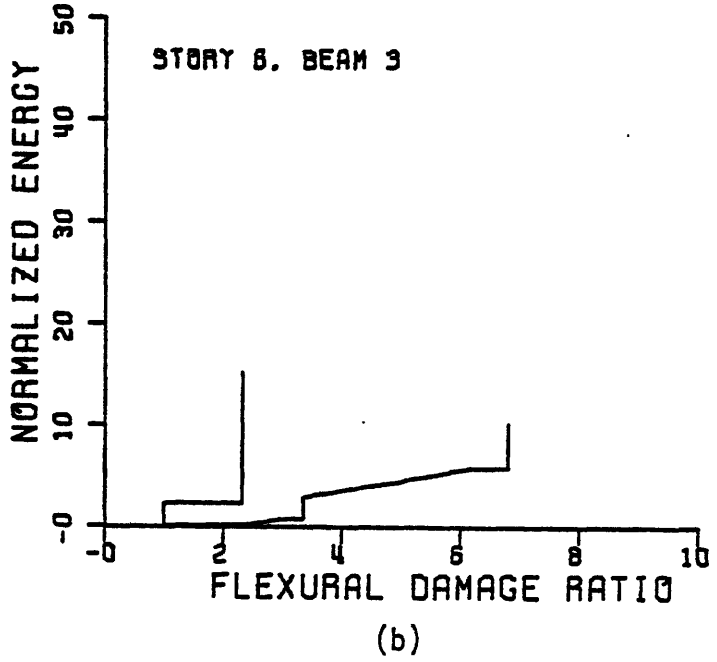

(b)

Fig. 5.9 - Damage Paths for Two Members of the 8-Story Frame Subjected to El Centro Earthquake

equals the probability that the most-loaded member survives. This probability is

$$P_s^u = \text{Min } (1 - P_i). \tag{5.3}$$

In practice, one may take P_s^L and P_s^u as lower and upper bounds to P_s, because in general member resistances display positive but not perfect dependence.

A model is developed next to calculate system reliability in the intermediate case of partial dependence. Using the first model of local failure in Chapter IV, the coordinate (d) of the failure point on the D_1D_2 plane can be taken to have the Extreme Type III distribution (Eq. 4.7). In order to introduce dependence between the values of d for different members, it is assumed here that the mean value of d_i is uncertain but identical for all i. It is further assumed that the mean value m_d has Extreme Type III distribution and, given m_d, the conditional quantities $(d_1|m_d)$, $(d_2|m_d)$... $(d_n|m_d)$ are independent, identical, Extreme Type III variables. Specifically, let m_d have mean m and variance $\sigma^2\rho$ and let $d_i|m_d$ have mean m_d and variance $\sigma^2(1-\rho)$. The parameters m and σ^2 are the mean value and the variance of the marginal distribution of d, as determined in Chapter IV. Quantity ρ measures the degree of dependence: in the extreme cases when $\rho = 0$ and $\rho = 1$ the resistances d_i have the same marginal distribution as d in Chapter IV (Extreme Type III) and are mutually independent and perfectly dependent respectively.

It is easy to show that ρ has indeed the meaning of correlation coefficient between any pair of resistances d_i, d_j, and that for any value of ρ, the marginal distributions of d_i have mean m and variance σ^2. In fact

$$E[d_i] = \underset{m_d}{E}\left\{\underset{d_i|m_d}{E}[d_i]\right\} = \underset{m_d}{E}[m_d] = m \tag{5.4a}$$

$$E[d_i^2] = \underset{m_d}{E}\left\{\underset{d_i|m_d}{E}[d_i^2]\right\} = \underset{m_d}{E}[m_d^2 + \sigma^2(1-\rho)] = m^2 + \sigma^2 \tag{5.4b}$$

$$E[d_i d_j] = \underset{m_d}{E}\left\{\underset{d_i|m_d}{E[d_i]} \cdot \underset{d_j|m_d}{E[d_j]}\right\} = \underset{m_d}{E}[m_d^2] = m^2 + \sigma^2\rho \ . \tag{5.4c}$$

Uncertainty in the parameter m_d may reflect physical variability in material properties; it is not unrealistic to assume that these factors affect the resistance of all structural members in the same way. The only unsatisfactory feature of the present model is that for $\rho \neq 0, 1$ the marginal distribution of d_i is not exactly Extreme Type III. On the other hand, available multivariate extreme models which preserve the marginal distribution are difficult to work with and express types of dependence among the d_i which are not compatible with the physical problem. According to the present model, survival of all members occurs with probability P_s, where

$$P_s = \int_0^\infty \left\{\prod_i [1 - \underset{d_i|m_d}{F}(\ell_i)]\right\} \underset{m_d}{f}(\xi)\, d\xi \tag{5.5}$$

where ℓ_i is the length of damage path along d for member i, as measured in the inelastic dynamic analysis. Figures 5.10 and 5.11 show the system reliability as a function of the correlation coefficient for the 4-story frame subjected to El Centro (Peak Acceleration = 0.35g) and Kern County

(Peak Acceleration = 0.5g) earthquakes. Figure 5.12 is a sketch of system reliability for the 8-story frame subjected to the El-Centro earthquake. It may be noted that system reliability for the first two cases shows a decreasing trend for lower correlations. This is in part due to the fact that the marginal distribution of d_i is not Extreme Type III for intermediate cases. Although this effect is not investigated, tentatively the curve may be assumed to be linear. This means that integration is avoided and reliability of the system is easily calculated.

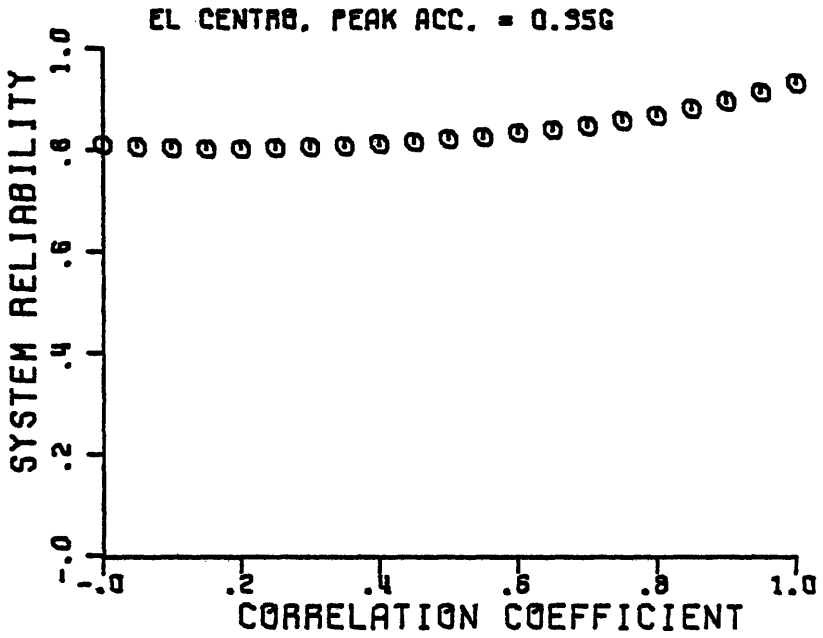

Fig. 5.10 - System Reliability as a Function of Correlation between Member Resistances for 4-Story Frame

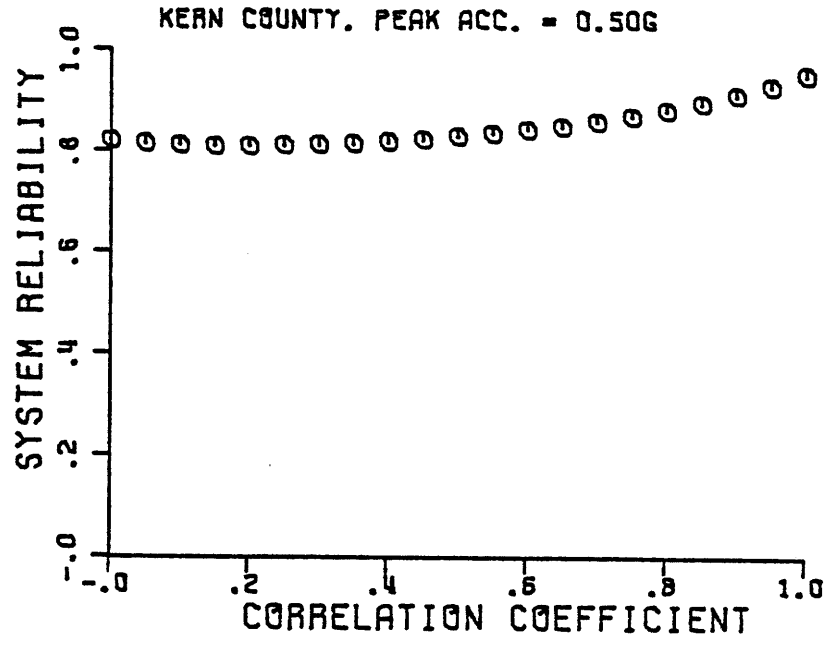

Fig. 5.11 - System Reliability as a Function of Correlation between Member Resistances for 4-Story Frame

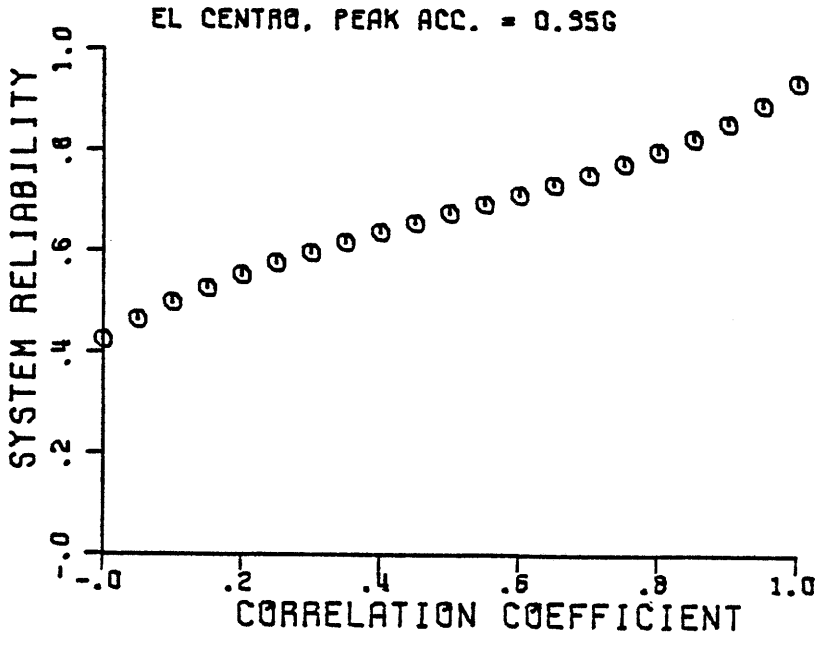

Fig. 5.12 - System Reliability as a Function of Correlation between Member Resistances for 3-Story Frame

5.5 Comparison of the Damage Model with Conventional Ductility Factors

Ductility demand has been the most widely used measure of damage in structures. One shortcoming of ductility as a damage indicator is that it is at best a qualitative measure. The second problem with peak ductility is that it could not always be accurately calculated in an inelastic dynamic analysis. Computed ductilities for the laboratory tests of members in Chapter III are much higher than actual peak ductilities measured in experiments. This is one reason why peak ductilities in the order of 10 or 15 may sometimes be computed in an inelastic dynamic analysis, and it is virtually impossible to achieve these high ductilities in laboratory tests of members.

Figure 5.13 shows ductility demand envelopes of the 4-story frame

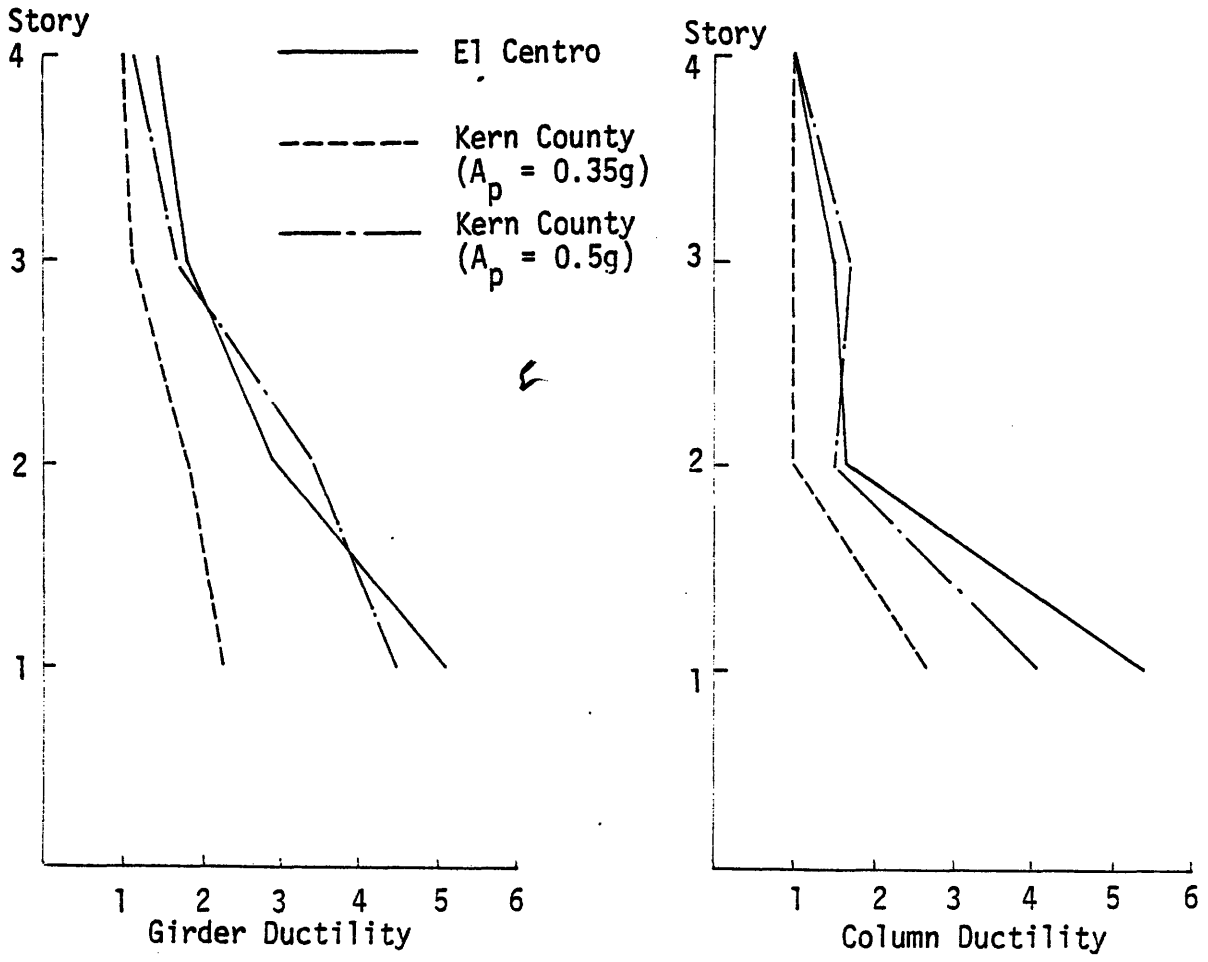

Fig. 5.13 - Ductility Demand Envelopes for the 4-Story Frame

subjected to three different input motions. It may be noted that ductility demands for the El Centro earthquake and the Kern County earthquake with peak acceleration scaled to 0.5g are comparable. On the other hand, much lower ductilities are observed in the third case (Kern County, Peak Acceleration = 0.35g). This figure may be compared with Figs. 5.3, 5.5 and 5.6, where local failure probabilities for critical members are shown. Although peak ductilities are comparable for girders and columns for each input motion, much higher failure probabilities are observed in the girders. As was mentioned before, not much energy is dissipated in these members compared to laboratory tests; thus most of the hazard in failure of members is due to damage ratio. This is the reason why the ductility demand envelope is a rather good predictor of concentration of damage in this case. However, if dissipated energy proves to be important in an earthquake, e.g., if the earthquake is a long duration stationary motion, then the ductility demand would be less effective in predicting damage. Figure 5.14 is a sketch of peak ductility envelopes for columns and girders in the 8-story building frame subjected to the El Centro earthquake. Again, comparison of this figure with Fig. 5.8 reveals that there is no clear relationship between ductility demands and probabilities of failure for the members. Although this investigation is not thorough, it seems to indicate that using ductility as a measure of damage would result in erroneous conclusions, i.e., two members with the same ductility demands do not necessarily have the same probability of failure.

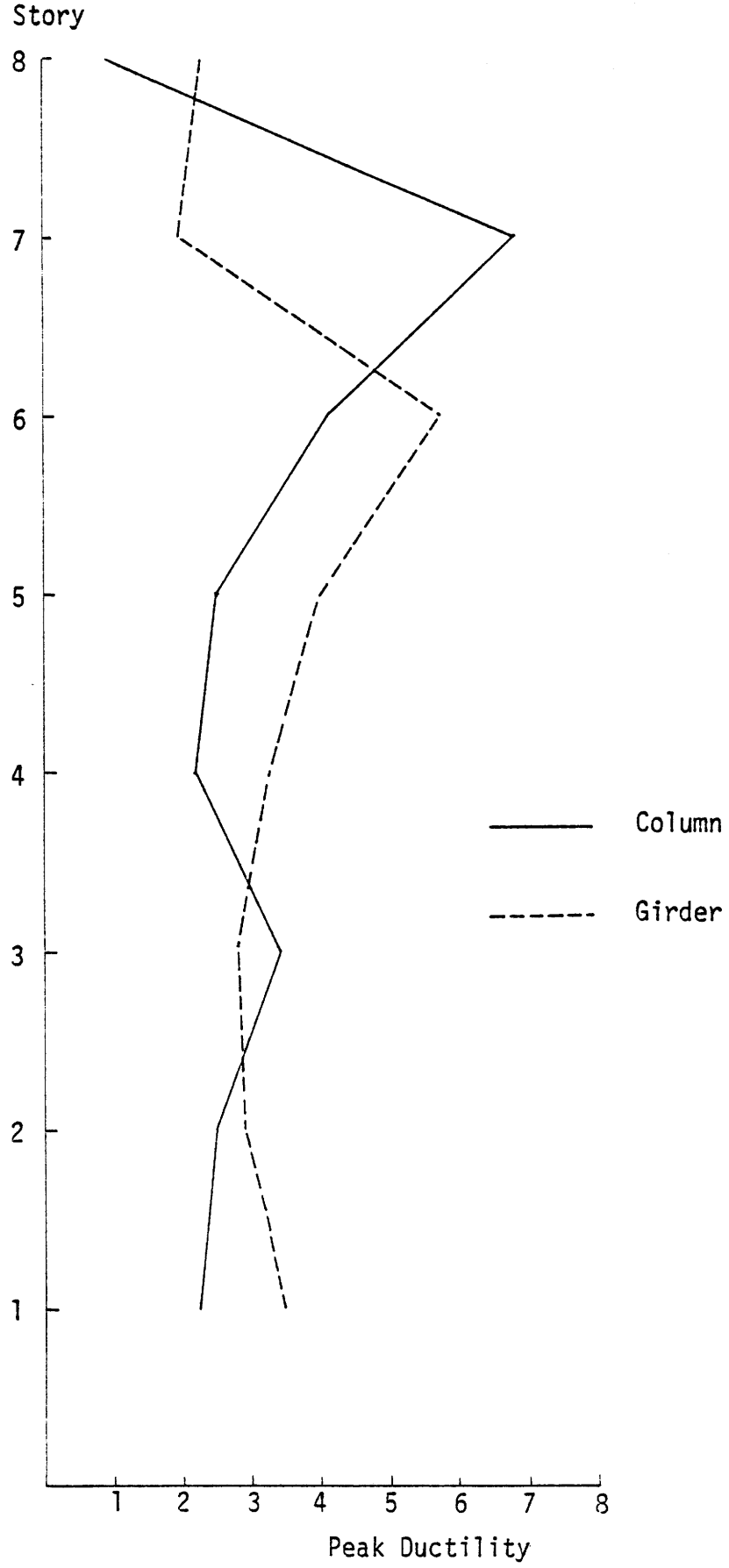

Fig. 5.14 - Ductility Demand Envelopes for the 8-Story Frame

Story Level	Column		Beam	
	Exterior	Interior	Edge	Interior
1	+ 1600 - 1600	+ 2000 - 2000	+ 2400 - 1200	+ 1800 - 900
2	+ 1900 - 1900	+ 2000 - 2000	+ 2400 - 1200	+ 1800 - 900
3	+ 1400 - 1400	+ 2000 - 2000	+ 2400 - 1200	+ 1800 - 900
4	+ 2100 - 2100	+ 2900 - 2900	+ 1800 - 900	+ 1300 - 650

Table 5.1 - Yield Moment Capacities of the 4-Story Frame Members

Story Level	Column		Beam	
	Exterior	Interior	Edge	Interior
1	+ 6200 - 6200	+ 5900 - 5900	+ 3600 - 1800	3600 - 1800
2	+ 5300 - 5300	+ 4000 - 4000	+ 3700 - 1850	3700 - 1850
3	+ 4000 - 4000	+ 3300 - 3399	+ 3700 - 1850	+ 3700 - 1850
4	+ 4000 - 4000	+ 3300 - 3300	+ 3600 - 1800	+ 3400 - 1700
5	+ 3000 - 3000	- 3000 - 3000	+ 3400 - 1700	- 3200 - 1600
6	+ 2500 - 2500	+ 3000 - 3000	+ 3200 - 1600	+ 3000 - 1500
7	+ 2000 - 2000	+ 2600 - 2600	+ 3000 - 1500	+ 2700 - 1350
8	+ 2500 - 2500	+ 3600 - 3600	+ 2000 - 1000	+ 2000 - 1000

Table 5.2 - Yield Moment Capacities of the 8-Story Frame Members

CHAPTER VI - CONCLUSIONS AND RECOMMENDATIONS

This work is a first attempt to develop a rigorous model of damage in reinforced concrete structures by integrating the reliability analysis with relatively conventional inelastic analysis. The model that is presented is based on actual laboratory tests of members and subassemblages chosen to represent realistic behavior of frames under earthquake loads. A uniform method of measuring damage is defined for all experiments, and damage indicators other than the conventionally used peak ductility are used to set up a stochastic model of damage. One advantage of this model is that it could easily be implemented in conventional inelastic dynamic analysis of reinforced concrete frames. Since the model is based on laboratory results, it is also expected to be accurate in predicting damage for individual members.

The mechanical model used in this work is the Single Component Model, in which all inelastic rotations along the member length are concentrated at its two end sections. Independent inelastic springs at the two ends of a beam element represent contributions of flexure, shear, and slippage to total member deformations. Flexural inelastic springs are assumed to follow a modified version of the Takeda model (54). The model of inelastic shear deformations is that originally proposed by Küstü (32), and it is based on physical characteristics of opening and closing of inclined shear cracks at member ends. Loss of bond between steel and concrete in the joint results in member free-body rotations which are known as slippage rotations. A model for slippage in reinforced concrete members is suggested here. It may be noted that inelastic deformations in shear and slippage are assumed to have the same hysteretic behavior. This inelastic

model is used to study a total of 32 laboratory tests of members and subassemblates from eight different sets of experiments. Although the sample is rather small, it represents a wide variety of loading conditions. Most of the members were failed under a combination of high flexural and shear loads. Five specimens in the sample were failed under combinations of flexural, shear, and axial loads. Each test is carefully chosen, so that they represent the realistic behavior of reinforced concrete buildings under earthquake loads. All specimens in the sample are large-scale specimens, and they were all tested to failure.

Comparison of experimental and analytical load-deflection curves show that the Single Component Model is indeed suitable for modeling inelastic behavior of reinforced concrete members. The match between experimental and analytical results is especially good when flexural deformations are dominant. In other studies also, the Takeda model has proved to be accurate in modeling inelastic flexural deformations of reinforced concrete members. However, the Takeda model does not reproduce the pinched behavior which is observed when high shear loads or slippage are present. Although inelastic models of shear and slippage are based on many assumptions, they proved to be successful in predicting the hysteretic behavior of laboratory tests in most cases. Interaction among flexure, shear, and slippage and the P-δ effect adds appreciably to the complexity of the physical problem, and makes the modeling more difficult. Overall, there is good agreement between experimental and analytical load-deflection curves. In light of the fact that inelastic models must also be practical for engineering practice, the use of the Single Component Model is recommended.

Member failure in this work is defined by setting a lower limit on the load-carrying capacity of a member. Although the definition is rather arbitrary, it is very useful in practice: i.e., the member behavior is of no interest if it does not contribute much to the overall stiffness. Various indicators of damage such as ductility, dissipated energy, and damage ratio were computed for each laboratory test. Although there is good agreement between load-deflection curves, computed peak ductilities are found to be much higher than measured peak ductilities in each experiment. On the other hand, computed dissipated energies are in good agreement with experimental results. Flexural damage ratio is defined as the ratio of elastic flexural stiffness to reduced secant stiffness. Since flexural damage ratio also accounts for strength deterioration, it is found to be a good substitute for peak ductility.

A stochastic model of damage using damage ratio and dissipated energy as a pair of damage indices is developed. Assuming that the conditional rate of failure (hazard function) on the plane of damage ratio-dissipated energy is known, and also knowing the exact path that the process follows on this plane, one can compute the probability of failure at each point on this plane. Next, a parametric form of the hazard function is assumed and, using the results of laboratory experiments, the model parameters are computed. It is obvious that the suggested multivariate probability model has many advantages over a univariate model. Dissipated energy in a reinforced concrete member is a useful measure of cumulative damage, and damage ratio is an indication of damage which is due to large deformations. If a large sample is available, more damage indicators may be included in the model. However, as the number of damage indices increases, the damage

model becomes more complicated and more difficult to work with. Curves showing contours of equal probability of failure on the plane of dissipated energy-damage ratio are presented. Thus, by computing dissipated energy and damage ratio for a reinforced concrete member, the probability of member failure can be easily estimated.

The model of damage can be easily implemented in conventional inelastic dynamic analysis of frames. A 4-story and an 8-story building frame, designed according to the UBC Code, are selected. These building frames are subjected to several earthquake motions, and probabilities of member failure for each case are computed. A model to evaluate system reliability is also presented. This model has the advantage that one can account for correlation between member resistances. Although the main purpose of the inelastic dynamic analysis has been to show the application of damage model in conventional analysis of building frames, some general conclusions may be drawn. Comparison of peak ductility demands with probabilities of member failure shows that there is no clear relationship between ductility demands and probabilities of member failure. The 4-story frame, when subjected to the El Centro earthquake, exhibits moderate damage. On the other hand, when the same frame is subjected to the Kern County (Olympia) earthquake scaled up to the same peak ground acceleration (0.35g), very little damage is observed. Damage spreads throughout the building when the Kern County earthquake is scaled up to 0.50g. Thus the importance of input motion is clearly seen in this investigation. Since the dissipated energy accumulates throughout the earthquake, the effect of earthquake duration on damage is accounted for. The 8-story building frame is subjected to the El Centro earthquake, and

it is found that the damage is concentrated in the 6^{th} and 7^{th} stories. This reflects the importance of higher modes in response of taller buildings.

Future research in this field may be pursued in any of the following areas:

- Better mechanical models for inelastic behavior of reinforced concrete members may be developed. There is an especial need for refinement of shear and slippage models.

- Definition of damage in this study is based on load-carrying capacity of the member. Other definitions of damage may be investigated in the future.

- The sample of laboratory tests of reinforced concrete members and subassemblages may be expanded. There are many more static cyclic load tests available in the literature. A large sample would result in better estimates of parameters of the damage model.

- Several minor refinements may be applied in the stochastic models presented in Chapter IV. For example, exact member failure paths may be used to evaluate parameters of the hazard function.

- The model of system reliability is restricted to a "series" system at the moment. One may think of applying the member failure model in a probabilistic progressive failure model. Knowing dissipated energy and damage ratio during each time step (Δt) of the (deterministic) dynamic analysis, one can calculate the probability of failure in Δt of each member. Then the failure/survival event of each member may be simulated by performing Bernoulli experiments (one for each member). If a member is failed, the global stiffness matrix is modified. One should repeat such an analysis a number of times to determine the probability of total collapse or probability distributions of desired quantities (deformations, member end forces, time of member failure).

APPENDIX A - NONLINEAR BEHAVIOR OF A CANTILEVER

One of the assumptions made in the Single Component Model is that the point of contraflexure of a member always stays at its mid-point. If the member is under anti-symmetric bending, each half of it may be viewed as a cantilever (Fig. 2.8). If the member has a bilinear moment-curvature relationship (Fig. 2.5), it is possible to find tip deflections of each half-length cnatilever at different loads. Using slope-deflection equations, tip deflections of the cantilever (length = $\frac{\ell}{2}$) at yield and ultimate conditions are

$$\delta_y = \frac{1}{3}\,\phi_y\,(\tfrac{\ell}{2})^2$$

$$\delta_u = \frac{1}{6}\,(\tfrac{\ell}{2})^2[(1+\gamma)\phi_y + (1-\gamma)(2+\gamma)\,\phi_u] \quad ,$$

where γ is the ratio M_y/M_u. The Single Component Model assumes that each cantilever is an elastic element with a rotational spring at its end. The rotational spring is initially infinitely stiff, and only becomes effective once the member yield moment is exceeded. Matching tip displacements of the real cantilever and the model cantilever at ultimate bending moment, post-yield stiffness of the hinge is computed.

$$K_S = \frac{M_u - M_y}{\frac{\delta_u - \delta_y}{\ell} - (M_u - M_y)\,\frac{\ell}{3EI}} \quad .$$

A typical load-deflection relationship for a cantilever with bilinear moment-curvature curve is shown in figure A.1. The curve is elastic up to the yield moment, and it has a decreasing stiffness past the yield. Thus a bilinear assumption for a P-δ curve introduces still another uncertainty into the model.

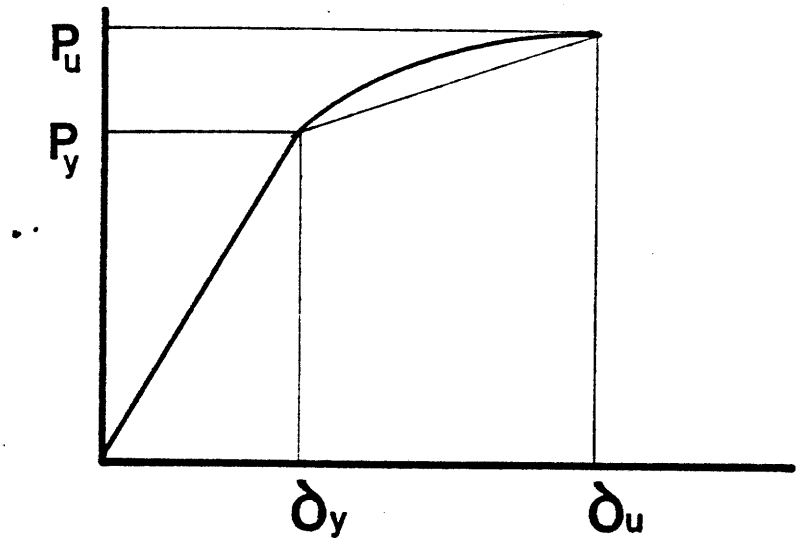

FIG. A.1 - LOAD-DEFLECTION OF A CANTILEVER WITH A BILINEAR MOMENT-CURVATURE RELATIONSHIP

APPENDIX B - TAKEDA MODEL

This model was first proposed by Takeda (54) based on experimental studies of reinforced concrete members. The original model has a trilinear primary curve for the hysteretic behavior of the member. The trilinear primary curve would be identified by cracking and yielding of the member. In addition, energy could be dissipated once the yield moment is exceeded. A simplified version of the Takeda model is used in this study. Litton (36) implemented this element in the computer program DRAIN-2D. The Moment-rotation relationship for the modified Takeda model is shown in figure B.1. Hysteretic behavior of the hinge is completely defined by eleven rules which are identified in figure B.1. The primary curve for the model is a bilinear curve which changes slope at the point of yielding. Two other modifications were also introduced by Litton. The first is for stiffness degradation in the unloading part. This is shown in figure B.2(a). Thus, instead of unloading with initial slope (K_o), parameter α is used to modify the unloading stiffness (K_u). The second modification is for reloading stiffness (K_ℓ) and is shown in figure B.2(b). Therefore, instead of loading towards the point of maximum (B), another point, such as A (which is set by parameter β), is aimed at. Parameter α decreases the unloading stiffness and parameter β increases the reloading stiffness. Values of $\alpha = 0.3$ and $\beta = 0$ were used throughout this study.

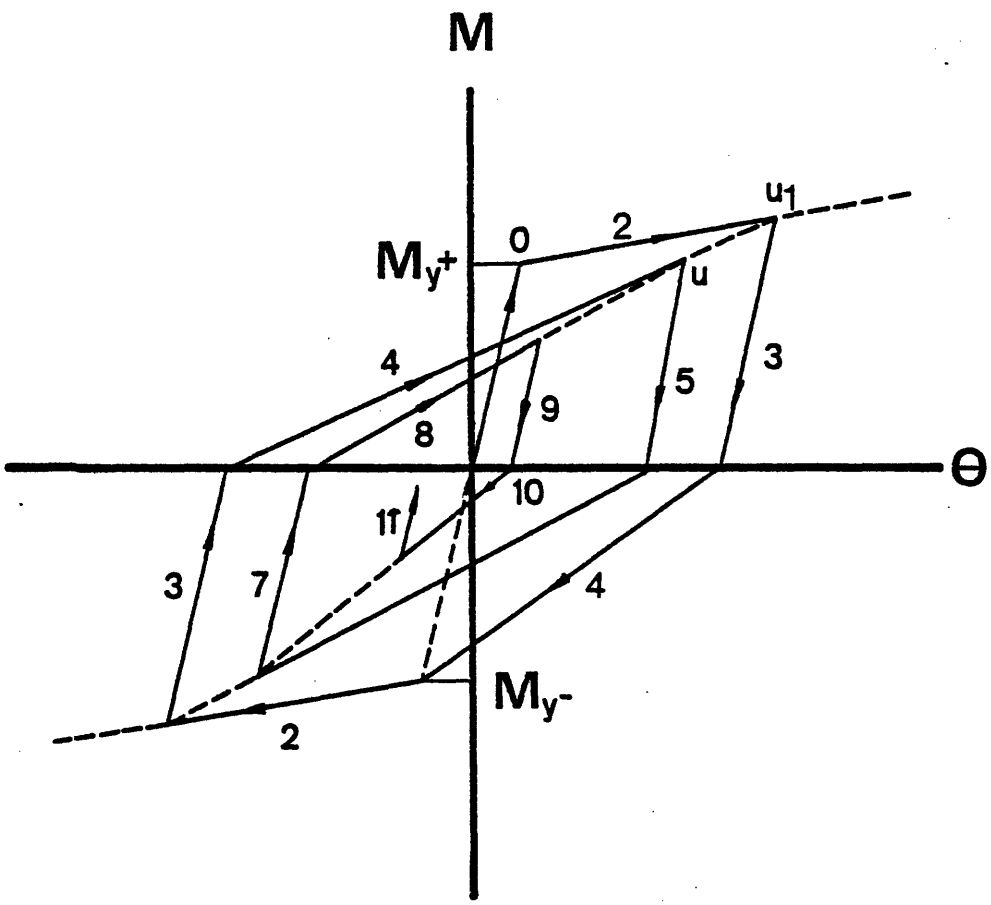

FIG. B.1 - MOMENT-ROTATION HYSTERESIS CURVE FOR THE MODIFIED TAKEDA MODEL

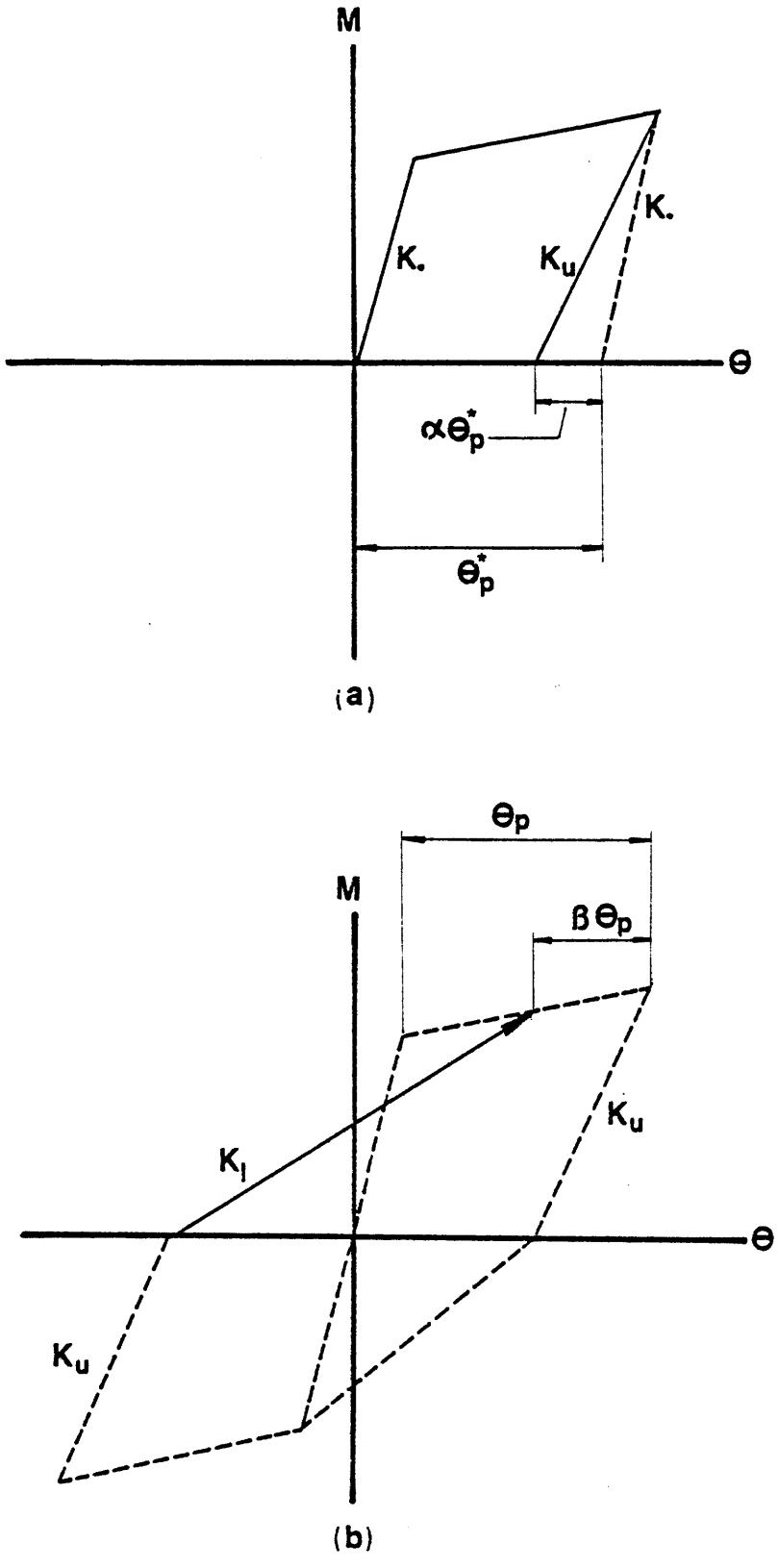

FIG. B.2 - DEFINITION OF PARAMETERS α AND β FOR THE MODIFIED TAKEDA MODEL

References

1. Anagnostopoulos, S.E., "Non-Linear Dynamic Response and Ductility Requirements of Building Structures Subjected to Earthquakes," Ph.D. Thesis, Department of Civil Engineering, M.I.T., September 1972.

2. Anderson, J.C. and Townsend, W.H., "Models for RC Frames with Degrading Stiffness," Journal of the Structural Division, ASCE, December 1977.

3. Atalay, M.B. and Penzien, J., "The Seismic Behavior of Critical Regions of Reinforced Concrete Components as Influenced by Moment, Shear, and Axial Force," EERC, University of California, Berkeley, December 1975.

4. Atkan, A.E., Pecknold, D.A. and Sozen, M.A., "R/C Column Earthquake Response in Two Dimensions," Journal of the Structural Division, ASCE, Oct. 1974.

5. Aziz, T., "Inelastic Dynamic Analysis of Building Frames," Ph.D. Thesis, Department of Civil Engineering, M.I.T., August 1976.

6. Benjamin, J.R. and Cornell, C.A., Probability, Statistics, and Decision for Civil Engineers, McGraw-Hill Book Company, 1970.

7. Bertero, V.V., Popov, E.P. and Wang, T.T., "Hysteresis Behavior of Reinforced Concrete Flexural Members with Special WEB Reinforcement," EERC, University of California, Berkeley, August 1974.

8. Bertero, V.V. and Popov, E.P., "Hysteresis Behavior of Ductile Moment-Resisting Reinforced Concrete Frame Components," EERC, University of California, Berkeley, April 1975.

9. Bertero, V.V. and Popov, E.P., "Seismic Behavior of Ductile Moment-Resisting Reinforced Concrete Frames," Symposium on Reinforced Concrete Structures in Seismic Zones, Publication SP-53, ACI, Detroit, 1977.

10. Blume, J.A. and Monroe, E.F., "The Spectral Matrix Method for Predicting Damage from Ground Motion," John A. Blume and Associates Research Division, Nevada Operations Office, United States Atomic Energy Commission, Las Vegas, Nevada, 1971.

11. Blume, J.A., Wang, E.C.W., Scholl, R.E. and Shah, E.C., "Earthquake Damage Prediction: A Technological Assessment," Department of Civil Engineering, Stanford University, October 1975.

12. Cheng, F.Y., Oster, K.B., and Kitipitayangkul, P., "Establishment of Ductility Factor Based on Energy Absorption and Evaluation of Present Methods," Proceedings of the Third Canadian Conference on Earthquake Engineering, Vol. 2, Montreal, June 1979.

13. Chopra, A.K. and Kan, C., "Effects of Stiffness Degradation on Ductility Requirements for Multistory Buildings," Earthquake Engineering and Structural Dynamics, Vol. 2, 1973.

14. Clough, R.W. and Johnston, S.B., "Effect of Stiffness Degradation on Earthquake Ductility Requirements," Proceedings, Japan Earthquake Engineering Symposium, Tokyo, October 1966.

15. Clough, R.W. and Benuska, "Nonlinear Earthquake Behavior of Tall Buildings," Journal of the Engineering Mechanics Division, ASCE, June 1967.

16. Clough, R.W. and Gidwani, J., "Reinforced Concrete Frame 2: Seismic Testing and Analytical Correlation," EERC, University of California, Berkeley, June 1976.

17. Clough, R.W., "Predicting the Earthquake Response of Reinforced Concrete Structures," Symposium on Reinforced Concrete Structures in Seismic Zones, Publication SP-53, ACI, Detroit, 1977.

18. Emori, K. and Schnobrich, W.C., "Analysis of Reinforced Concrete Frame-wall Structures for Strong Motion Earthquakes," Department of Civil Engineering, University of Illinois at Urbana-Champaign, December 1978.

19. Fenwick, R.C. and Irvine, H.M., "Reinforced Concrete Beam-Column Joints for Seismic Loading," Department of Civil Engineering, University of Auckland, New Zealand, March 1977.

20. Gertsbakh, I.B. and Kordonsky, Kh.B., Models of Failure, Translated from Russian, Springer-Verlag New York Inc., 1969.

21. Giberson, M.F., "Two Nonlinear Beams with Definitions of Ductility," Journal of the Structural Division, ASCE, February 1969.

22. Gulkan, P. and Sozen, M. A., "Inelastic Responses of Reinforced Concrete Structures to Earthquake Motions," Symposium on Reinforced Concrete Structures in Seismic Zones, Publication SP-53, ACI, Detroit,1977.

23. Hanson, N.W. and Conner, H.W., "Tests of Reinforced Concrete Beam-Column Joints under Simulated Seismic Loading," Portland Cement Association, Research and Development Bulletin RDD12, 1972.

24. Hawkins, N.M. and Lin, I.J., "Bond Characteristics of Reinforcing Bars for Seismic Loadings," Proceedings of Third Canadian Conference on Earthquake Engineering, Vol. 2, Montreal, June 1979.

25. Healey, T.J. and Sozen, M.A., "Experimental Study of the Dynamic Response of a Ten-Story Reinforced Concrete Frame with a Tall First Story" Department of Civil Engineering, University of Illinois at Urbana-Champaign, August 1978.

26. Hidalgo, P. and Clough, R.W., "Earthquake Simulator Study of a Reinforced Concrete Frame," EERC, University of California, Berkeley, December 1974.

27. Jimenez-Pérez, R., Gergeley, P. and White, R.N., "Shear Transfer Across Cracks in Reinforced Concrete," Department of Structural Engineering, Cornell University, August 1978.

28. Jirsa, J.O., Maruyama, K. and Ramirez, R., "Development of Loading System and Initial Tests - Short Columns under Bidirectional Loading," Department of Civil Engineering, The University of Texas, Austin, September 1978.

29. Kaldjian, M.J., "Moment-Curvature of Beams as Ramberg-Osgood Functions," Journal of the Structural Division, ASCE, October 1967.

30. Kanaan, A.E. and Powell, G.H., "General Purpose Computer Program for Dynamic Analysis of Inelastic Plane Structures," EERC, University of California, Berkeley, April 1973.

31. Kent, D.C. and Park, R., "Flexural Members with Confined Concrete," Journal of the Structural Division, ASCE, July 1971.

32. Küstü, C. and Bouwkamp, J.G., "Behavior of Reinforced Concrete Deep Beam-Column Subassemblages under Cyclic Loads," EERC, University of California, Berkeley, May 1975.

33. Lai, S.P., "Overall Safety Assessment of Multistory Steel Buildings Subjected to Earthquake Loads," Ph.D. Thesis, M.I.T., June 1980.

34. Latona, R.W., "Nonlinear Analysis of Building Frames for Earthquake Loading," Ph.D. Thesis, Department of Civil Engineering, M.I.T., September 1970.

35. Lau, W.K., "An Evaluation of Simplified Earthquake-Resistant Design Methods for Reinforced Concrete Frames," S.M. Thesis, Department of Civil Engineering, M.I.T., January 1979.

36. Litton, R.W., "A Contribution to the Analysis of Concrete Structures under Cyclic Loading," Ph.D. Thesis, Department of Civil Engineering, University of California, Berkeley, May 1975.

37. Lybas, J.M. and Sozen, M. A., "Effect of Beam Strength and Stiffness on Dynamic Behavior of Reinforced Concrete Coupled Walls," Department of Civil Engineering, University of Illinois at Urbana-Champaign, July 1977.

38. Ma, S.H., Bertero, V.V. and Popov, E.P., "Experimental and Analytical Studies on the Hysteresis Behavior of Reinforced Concrete Rectangular and T-Beams," EERC, University of California, Berkeley, May 1976.

39. Mark, K.M.S., "Nonlinear Dynamic Response of Reinforced Concrete Frames," Ph.D. Thesis, Department of Civil Engineering, M.I.T., August 1976.

40. Moehle, J.P. and Sozen, M.A., "Earthquake Simulation Tests of a Ten-Story Reinforced Concrete Frame with a Discontinued First-Level Beam," Department of Civil Engineering, University of Illinois at Urbana-Champaign, August 1978.

41. Otani, S. and Sozen, M.A., "Behavior of Multistory Reinforced Concrete Frames during Earthquakes," Department of Civil Engineering, University of Illinois at Urbana-Champaign, November 1972.

42. Otani, S., "Inelastic Analysis of R/C Frame Structures," Journal of the Structural Division, ASCE, July 1974.

43. Otani, S., "Nonlinear Dynamic Analysis of 2-D Reinforced Concrete Building Structures," Proceedings of the Third Canadian Conference on Earthquake Engineering, Vol. 2, Montreal, June 1979.

44. Otani, S., Cheung, W.T. and Lai, S.S., "Behavior and Analytical Models of Reinforced Concrete Columns under Biaxial Earthquake Loads," Proceedings of the Third Canadian Conference on Earthquake Engineering, Vol. 2, Montreal, June 1979.

45. Park, R., Kent, D.C. and Sampson, R.A., "Reinforced Conctete Members with Cyclic Loading," Journal of the Structural Division, ASCE, July 1972.

46. Park, R. and Paulay, T., Reinforced Concrete Structures, John Wiley and Sons Inc., 1975.

47. Parzan, E., Stochastic Processes, Holden-Day Inc., San Francisco, 1962.

48. Paulay, T., "Simulated Seismic Loading of Spandrel Beams," Journal of the Structural Division, ASCE, September 1971.

49. Piqué, J.R., "On the Use of Simple Models in Nonlinear Dynamic Analysis," Ph.D. Thesis, Department of Civil Engineering, M.I.T., September 1976.

50. Popov, E.P., Bertero, V.V. and Krawinkler, H., "Cyclic Behavior of Three R.C. Flexural Members with High Shear," EERC, University of California, Berkeley, October 1972.

51. Saiidi, M. and Sozen, M.A., "Simple and Complex Models for Nonlinear Seismic Response of Concrete Structures," Department of Civil Engineering, The University of Illinois at Urbana-Champaign, August 1979.

52. Scribner, C.F. and Wight, J.K., "Delaying Shear Strength Decay in Reinforced Concrete Flexural Members under Large Load Reversals," Department of Civil Engineering, The University of Michigan, May 1978.

53. Takayanagi, T. and Schnobrich, W.C., "Nonlinear Analysis of Coupled Wall Systems," Earthquake Engineering and Structural Dynamics, Vol. 7, January 1979.

54. Takeda, T., Sozen, M.A. and Nielson, N.N., "Reinforced Concrete Response to Simulated Earthquakes," Journal of the Structural Division, ASCE, December 1970.

55. Takizawa, H., "Nonlinear Models for Simulating the Dynamic Damping Process of Low-Rise Reinforced Concrete Buildings during Severe Earthquakes," Earthquake Engineering and Structural Dynamics, Vol. 4, 1975.

56. Uniform Building Code, International Association of Building Officials, California, 1973.

57. Viwathanatepa, S., Popov, E.P. and Bertero, V.V., "Seismic Behavior of Reinforced Concrete Interior Beam-Column Subassemblages," EERC, University of California, Berkeley, June 1979.

58. Whitman, R.V., Reed, J.W. and Hong, S.T., "Earthquake Damage Probability Matrices," Proceedings of the 5th World Conference on Earthquake Engineering, Paper No. 321, Rome, Italy, 1973.

59. Whitman, R.V., Biggs, J.M., Brennan, J.E., Cornell, C.A., DeNeufville, R.L. and Vanmarcke, E.H., "Seismic Design Decision Analysis," Journal of the Structural Division, ASCE, May 1975.